Document Version
Final published version

Citation (APA)
John, V. (2026). *Spin-Orbit Control of Spin Qubit Arrays in Germanium*. [Dissertation (TU Delft), Delft University of Technology]. https://doi.org/10.4233/uuid:7b452be2-534d-4d79-8770-0b84df0d8428

Spin-Orbit Control of Spin Qubit Arrays in Germanium

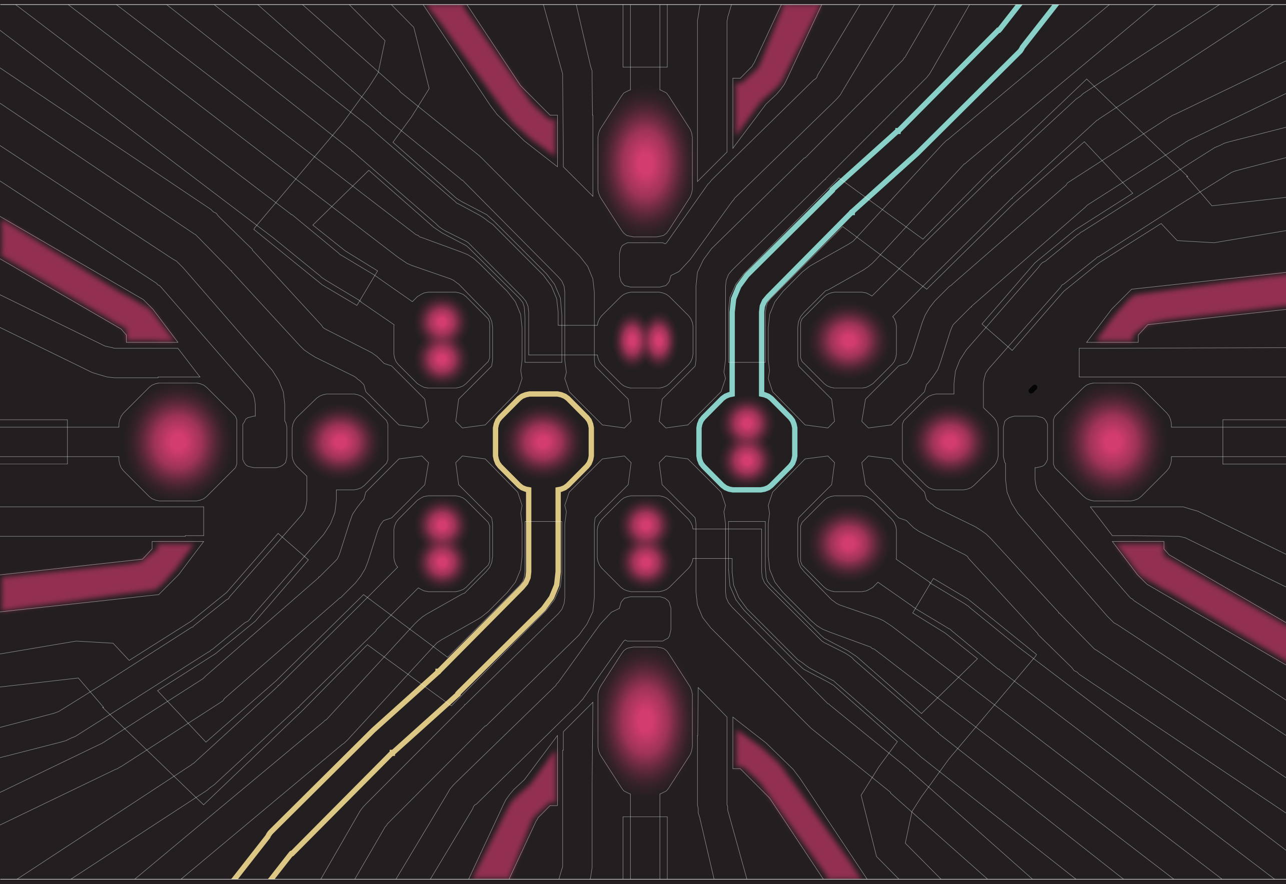

Valentin John

SPIN-ORBIT CONTROL OF SPIN QUBIT ARRAYS IN GERMANIUM

Dissertation

for the purpose of obtaining the degree of doctor
at Delft University of Technology
by the authority of the Rector Magnificus, prof. dr. ir. H. Bijl;
Chair of the Board for Doctorates
to be defended publicly on
Thursday, 16. April 2026 at 12:30 o'clock

by

Valentin JOHN

This dissertation has been approved by the promotors.

Composition of the doctoral committee:

Rector Magnificus,	chairperson
Prof. dr. ir. M. Veldhorst,	Technische Universiteit Delft, promotor
Dr. G. Scappucci,	Technische Universiteit Delft, promotor
Independent members:	
Prof. dr. ir. L.M.K. Vandersypen	Technische Universiteit Delft
Prof. dr. M. T. Wimmer	Technische Universiteit Delft
Prof. dr. K. De Greve	imec & Katholieke Universiteit Leuven, Belgium
Dr. N. Ares	New College, University of Oxford, UK
Dr. D. Kim	Seoul National University, South Korea

Keywords: quantum computing, spin qubits, quantum dots, germanium, semiconductor, spin-orbit, holes

Printed by: Gildeprint - www.gildeprint.nl

Front & Back: Design of a ten qubit array with highlighted edges and depicted wave functions; schematic of a quantum processor architecture

ISBN 978-94-6518-237-7

An electronic version of this dissertation is available at
`http://repository.tudelft.nl/`.

CONTENTS

1 Introduction **1**

2 Theory **15**
- 2.1 Origin of spin-orbit coupling 17
- 2.2 Zeeman splitting 17
- 2.3 Quantum bits 18
- 2.4 Electrons and holes in semiconductors 19
- 2.5 Material platform 21
- 2.6 Luttinger-Kohn formalism and g-tensor 23
  - 2.6.1 Crystalline Hamiltonians. 24
  - 2.6.2 Magnetic contributions 27
  - 2.6.3 Confinement and envelope functions 28
- 2.7 The g-tensor 28
  - 2.7.1 Analytical formulas 30
  - 2.7.2 Numerical example 32
  - 2.7.3 Larmor vector and spin quantisation axis 36
  - 2.7.4 Electric dipole spin resonance 39
  - 2.7.5 Rashba and Dresselhaus spin-orbit terms 41
  - 2.7.6 Spin in Double dots 42

3 Methods **57**
- 3.1 Device development 58
  - 3.1.1 Device design 59
  - 3.1.2 Device preparation and screening 59
- 3.2 Experimental setup 60
- 3.3 Fabrication 62
- 3.4 Gate virtualisation 62

4 Bichromatic Rabi control of semiconductor qubits **67**
- 4.1 Bichromatic EDSR spectroscopy 68
- 4.2 ACs in the bichromatic spectroscopy and Autler-Townes effect 71
- 4.3 Dependence on detuning energy of double quantum dot 73
- 4.4 Conclusions. 74
- 4.5 Supplementary 75
  - 4.5.1 Power dependence of anticrossing AC2 Q1$^{-P2,P4}$, Q2^{P4} 75
  - 4.5.2 EDSR spectroscopy map at zero detuning 76
  - 4.5.3 Exchange coupling at operation point 76
  - 4.5.4 Resonance line identification and Rabi rotations 77
  - 4.5.5 Attenuation 81
  - 4.5.6 Monochromatic Rabi frequencies 81

5 Shared control of a 16 semiconductor quantum dot crossbar array 87
5.1 A two-dimensional quantum dot crossbar array 88
5.2 Quantum dot occupancies 91
5.3 Interdot couplings control 94
5.4 Conclusions. 97
5.5 Methods 98
  5.5.1 Tune-up details 98
  5.5.2 Virtual matrix 98
  5.5.3 Quantum dot identification 99
  5.5.4 Tunnel coupling evaluation 105
5.6 Supplementary 106
  5.6.1 Rent's rule and gate count 106
  5.6.2 Practical device improvements. 107
  5.6.3 Addressable exchange operations with a double barrier design . . . 109
  5.6.4 Electron temperature extraction 115
  5.6.5 Detuning lever arm extraction 117
  5.6.6 Charge stability diagrams and applied gate voltages 118
  5.6.7 Characterisation of the variability of the quantum dot array 119

6 Operating semiconductor quantum processors with hopping spins 129
6.1 High-fidelity single-qubit operations and long qubit coherence times at low magnetic field. 130
  6.1.1 High-fidelity two-qubit exchange gate 134
6.2 Hopping spins to benchmark large and high-connectivity quantum dot architectures 137
6.3 Conclusion 138
6.4 Methods 139
6.5 Supplementary 140
  6.5.1 Power dissipation and scaling advantages of shuttling-based control 140
  6.5.2 Charge tuning and virtual gate control of the 10 quantum dot array . 142
  6.5.3 Hopping-induced oscillations in occupied quantum dots 147
  6.5.4 Timing precision of shuttling pulses 148
  6.5.5 Shuttling across multiple quantum dots: detuning and barrier voltage dependence 149
  6.5.6 Dephasing times and Larmor frequencies in the 10 quantum dot array 152

7 Robust and localised control of a 10-spin qubit array in germanium 161
7.1 The two-dimensional 10-spin qubit array. 162
7.2 Qubit drive efficiency and tunability 166
7.3 Modelling of single- and multi-hole quantum dots 167
7.4 Driving locality in extended qubit arrays 169
7.5 Conclusions. 171
7.6 Supplementary 172
  7.6.1 raw SEM image 172

7.6.2 Read-out visibilities . . . 173
7.6.3 Single-qubit gate randomised benchmark . . . 174
7.6.4 Qubit properties in the initial hole configuration . . . 177
7.6.5 Exchange interaction in the 10-qubit array . . . 178
7.6.6 LSES extraction . . . 181
7.6.7 Driving efficiency extraction . . . 184
7.6.8 Physical distance from gates to qubits . . . 189
7.6.9 Spatial locality of the electric field and qubit drive . . . 191
7.6.10 Frequency cross-talk . . . 193

8 Ge hole spin qubits with a room-temperature magnet 201
8.1 Experimental set-up . . . 203
8.2 Qubit frequency tunability . . . 204
8.3 Qubit coherence times . . . 206
8.4 Zero internal field operation . . . 207
8.5 Conclusion . . . 208
8.6 Methods . . . 208
8.7 Supplementary . . . 209
8.7.1 External magnet assembly . . . 209
8.7.2 Additional qubit data . . . 210
8.7.3 Qubit coherence times without the external magnet . . . 211
8.7.4 Driving efficiency . . . 212
8.7.5 Randomised Benchmarking . . . 213
8.7.6 Additional qubit coherence and fidelity data . . . 216
8.7.7 Hysteresis effect in the magnet movement . . . 219
8.7.8 Zero internal field data . . . 221

9 A gapless single-spin qubit 227
9.1 Architecture . . . 228
9.2 GS2 Qubit . . . 229
9.3 Qubit states and operations . . . 231
9.4 GS2 qubit in practice . . . 235
9.5 GS2 qubit architecture . . . 237
9.6 Conclusion . . . 237

10 Conclusion 247
10.1 g-tensor . . . 248
10.2 Advancing scalability . . . 248
10.3 Gapless spin qubit . . . 249
10.4 Spin qubits at crossroads . . . 249

Summary 253

Samenvatting 255

Data Availability 257

Acknowledgements 261

Curriculum Vitæ 269

List of Publications 271

1

INTRODUCTION

Civilization is a progress from an indefinite, incoherent homogeneity toward a definite, coherent heterogeneity. [1]

Herbert Spencer

THE natural sciences offer an exceptional framework for accurately describing the world around us. Physics, in particular, reaches closest to a fundamental account of nature because it is grounded in principles such as those of quantum mechanics. As we move from fundamental physics toward increasingly complex systems in materials science, chemistry and biology, the ability to express these systems in fully quantum-mechanical terms diminishes. Each discipline relies on its own level of abstraction: systems can be described accurately within that level, yet their connection to deeper layers of explanation becomes more opaque. Nevertheless, scientifically rigorous models remain capable of convincingly capturing the essential mechanisms that govern systems across this entire hierarchy[1]. The social sciences stand in sharp contrast, as they cannot rely on a universally valid set of fundamental laws governing human interactions. One could argue that conducting scientifically robust studies is therefore substantially more challenging, and many social theories reflect the intellectual climate of their time. This does not make the social sciences less significant. They are often indispensable for understanding and addressing the concerns and problems that shape the daily lives of individuals and communities.

Biological evolution produced Homo sapiens as a still-evolving species, with populations concentrating in regions that offered abundant resources and favourable environmental conditions. These stable and resource-rich areas formed the basis upon which societies could emerge and develop. Yet societal development itself must be studied through the social sciences. One influential framework is the evolutionary theory of society, to which Herbert Spencer contributed substantially. He argued that “the direction of social change is from the homogeneous to the heterogeneous”[2]. Simple societies consist of largely uniform groups performing similar tasks, whereas more complex societies naturally differentiate into increasingly specialised roles. This highlights complexity, progression and heterogeneity as central concepts for understanding how societies function.

It is instructive to compare the intricate evolution of human societies, which we encounter daily, with the development of quantum processing units, which may appear far more abstract. Ultimately, a quantum computing chip is an organised collection of components that process information to accomplish specific tasks. Viewed from a distance, this is not unlike the way societies themselves operate.

We begin with a foundation, a fertile land where crops can grow and sustain all who live there. History is full of societies that have risen and fallen depending on their ability, or failure, to nourish their people. Once the foundation is right, we must agree on a common language to communicate. Alternatively, in a multi-ethnic society, we need capable translators to mediate between groups that speak different tongues. With these two core principles in place, we can begin to build a functioning society.

To make such a society work, we must establish cultural norms that enable efficient interaction between its members. Every individual is different, so our rules and institutions must be flexible enough to work for most people most of the time. As the community grows, an economy takes shape and cities begin to rise, yet with increasing pop-

---

[1] Quantum computers may substantially improve our ability to simulate quantum systems, thereby clarifying how some lower-level physical processes give rise to higher-level behaviour that is inaccessible to classical computation.

ulation comes increasing complexity. Group dynamics become harder to control, and the demand for resources grows. Eventually, we cannot simply keep adding people to a single city; at some point, it becomes more practical to build a second city nearby and connect the two with roads. Of course, these roads must remain safe and stable so that people can move smoothly between cities. Step by step, the network expands until a whole territory emerges, a connected system of cities, each contributing to the strength of the whole. Smaller tasks can be handled locally, but greater challenges require the combined resources of the entire society. The larger the cities grow (while remaining sustainable) and the better they are interconnected (with reliable roads), the more advanced the problems this civilization can address.

In the realm of spin qubits, our inhabitants are rather selective when it comes to their definition of fertile land. They strongly prefer to live in materials with zero nuclear spin, which reduces the number of suitable materials to isotopically enriched group-IV materials, in particular silicon and germanium. To avoid ’noisy’ neighbours it is even better to further ban non-zero spin isotopes and materials from the close-by vicinity alltogether [3, 4]. This makes for a particularly promising location to build a highly complex spin qubit society. The language of our society is a bit-based language based on 0 and 1, that is highly contextual unlike in the classical realm. It comes in different dialects, of which the single spin dialect is the most common [5].

For the time being, our spin qubits live in small isolated villages, where all interactions happen within a small community. In that sense they are fairly homogeneous still since specialised roles are not yet typically assigned. While from an operational perspective the spin qubits are homogeneous, they are still all different (heterogeneous) in physical appearance and athleticism. The heterogeneity is uncontrolled and not the result of a desired evolution towards more complex tasks. Nonetheless, our villages slowly increase in size and first prototypes of roads connecting two villages are being explored. However, a society like this is not yet capable to address any complex problems and needs more time and resources to grow.

Wherever fertile ground exists though, it is no surprise that multiple competing societies may emerge. These societies might share the same foundation and even speak the same dialect, yet remain entirely detached from one another, each pursuing its own resources and financial interests. This competition becomes particularly visible once such societies fall under corporate rule. As so often in life, power and profit tend to breed tension, giving rise to dishonest or opportunistic actors. The realm of spin qubits is no exception. Only time will tell in which form these promised societies will endure.

The foundation of the spin qubit realm

The spin qubit realm is not particularly rich in terms of soil to pick from. First settlers have picked group-III-V materials, such as gallium and indium arsenide [6–9], but conditions for our inhabitants were non-ideal. Therefore, academic and industrial research focuses primarily on four different platforms all based on group-IV materials: silicon metal-oxide-semiconductor (SiMOS) [10], donors in SiMOS [11], Si/SiGe quantum wells [12], and Ge/SiGe quantum wells [13–15]. We also note that there have been efforts to realise spin qubits in carbon based devices [16, 17], and that germanium MOS has recently been suggested as an additional promising platform [18, 19]. Each of these platforms presents distinct advantages and disadvantages. We focus here exclusively on gate-defined quantum dot devices, but promising efforts are also conducted with implanted donor qubits such as phosphorus atoms in silicon [20–23].

SiMOS is, in principle, the platform most compatible with classical CMOS technology [24, 25]. However, integration into existing foundries remains challenging, as it requires small gate-to-gate pitches (30 nm and below) and isotopically purified silicon. Additional limitations include the small wave function size and confinement at the oxide interface, which is highly susceptible to disorder [26]. Recent studies on two-qubit SiMOS devices show high fidelity operation in multiple relevant metrics [27, 28], with attempts to now move to larger devices [29].

Si/SiGe platforms have a more constrained thermal budget, making them less compatible with advanced CMOS processes [30]. However, the quantum well confines the wavefunction away from the oxide interface, reducing sensitivity to interface disorder. As a result, this platform became the first to demonstrate a 6-qubit quantum processor [31] and a 12-qubit linear chain [32]. Some of the ongoing challenges include low valley splitting [33, 34], qubit addressability [25, 35] and the need for small pitch sizes [36].

The most recent platform, Ge/SiGe heterostructures [13, 37–39], has been pioneered in Delft since 2018 [19, 39–54]. While they share similar thermal budget constraints with Si/SiGe, germanium offers a major advantage in its lower effective mass [55]. This allows for significantly larger pitch sizes (>100 nm), which greatly simplifies fabrication and electrical fanout. In addition, holes in germanium do not have valley states and can be conveniently controlled through the intrinsic spin-orbit coupling. These benefits have enabled Ge/SiGe devices to quickly catch up to silicon based devices and to become one of the most dynamic spin qubit platforms to-date [41, 47, 56, 57]. One of the major drawbacks is the significantly more complicated physics of holes [58–68] that come with a large g-tensor anisotropy and variability [69–72].

Dialects of the spin quantum bit language family

The simplest way to define a spin qubit is by using the spin of a single electron, applying a magnetic field, and encoding the qubit in the resulting Zeeman-split spin states [5]. This is commonly referred to as a Loss-DiVincenzo (LD) qubit, named after its original inventors. In this configuration, the qubit state can be manipulated using an oscillating magnetic field. LD qubits can take different forms, particularly with respect to the method of control. Identifying the optimal control approach remains a central research question. While magnetic resonance is the most 'natural' method to control the LD qubit since it allows to couple to the magnetic moment of the spin directly [7], it is also technologically demanding. Alternative approaches involve coupling the spin to the motional degree of freedom via either intrinsic or engineered spin-orbit interaction [73, 74]. This enables spin control using electric fields and opens up a wide range of operation and manipulation protocols, challenging the traditional understanding of LD qubits. In addition to the LD qubit, which has dominated the scientific literature, multi-dot qubit implementations are also being explored. These include singlet-triplet qubits [6, 75, 76] and exchange-only qubits [77, 78], which require two and three quantum dots, respectively, to encode a single qubit. The latter is the approach pursued by HRL and Intel, as it eliminates the need for microwave control and allows for clock-free operation, despite the more complex encoding scheme [79–82].

Building a society

Having a single high-quality qubit is an important milestone, but ultimately meaningless in the broader context of building a quantum computer. What is needed are scalable solutions. This applies not only at the quantum chip level, where assigning a dedicated control line to each qubit may quickly become unmanageable, but also to the surrounding infrastructure. Addressing these challenges is closely linked to the ’foundation’ and ’dialect’. While the scaling requirements differ across platforms, certain constraints are shared.

The near-term approach to increasing the qubit count can be summarised as "more of the same", which covers all areas from quantum chips design to system hardware. Changing all components simultaneously is not a practical strategy. Instead, one must identify the bottlenecks that emerge under naive brute-force scaling, and trying to resolve one bottleneck after the next in a systematic and strategic way to make the overall system more and more extendable (with the end goal of reaching genuine scalability). For superconducting qubits this has meant, for now, packing all bulky high-frequency coax lines for 256 qubits into a single dilution refrigerator [83]. Spin qubit encoding schemes come with varying footprints in terms of number of control lines, complexity of control pulses, etc. Some of them can be operated at significantly lower frequencies, putting less strain on the high frequency control lines. In addition, superconducting magnets often occupy a large amount of precious space within the dilution fridge unit. In principle, spin qubits are small enough that large numbers of them can be integrated onto a single chip. Here, the major bottleneck arises from interconnects: how to control many qubits with a limited number of control lines. Possible solutions include shared control lines on-chip or performing multiplexing operations using a separate cryo-CMOS chip [84, 85].

Within this thesis, the focus is primarily on how to operate spin qubits and extended spin qubit array, which is addressed in chapter 4, 6, 7 and 9. Challenges for scalability in quantum processing unit design are covered separately in chapter 5 and system hardware development in chapter 8. Ideally, all mentioned considerations would be addressed simultaneously through a unified solution. However, as this remains an active area of research, we are still in the process of identifying the optimal trade-offs involved in tackling these challenges. Therefore, each chapter selectively addresses specific challenges, while keeping the broader context in mind. It is always valuable to reflect on how a proposed solution for one problem might perform with respect to other ones.

BIBLIOGRAPHY

[1] J. K. Hoyt and K. L. Roberts. *Hoyt's New Cyclopedia Of Practical Quotations.* New York and London: Funk & Wagnalls Company, 1922, p. 242. URL: `https://archive.org/details/hoytsnewcycloped000342mbp/page/242`.

[2] R. G. Perrin. "Herbert Spencer's Four Theories of Social Evolution". In: *Source: American Journal of Sociology* 81.6 (1976), pp. 1339–1359. URL: `https://www.jstor.org/stable/2777007`.

[3] B. E. Kane. "A Silicon-Based Nuclear Spin Quantum Computer". In: *Nature (London)* 393.6681 (1998), p. 133. ISSN: 0028-0836. DOI: `10.1038/30156`.

[4] A. M. Tyryshkin et al. "Electron Spin Coherence Exceeding Seconds in High-Purity Silicon". In: *Nat Mater* 11.2 (22012/02//print), pp. 143–147. DOI: `10.1038/nmat3182`.

[5] D. Loss and D. P. DiVincenzo. "Quantum computation with quantum dots". In: *Physical Review A* 57.1 (Jan. 1998), pp. 120–126. ISSN: 1050-2947. DOI: `10.1103/PhysRevA.57.120`. URL: `https://link.aps.org/doi/10.1103/PhysRevA.57.120`.

[6] J. R. Petta et al. "Coherent Manipulation of Coupled Electron Spins in Semiconductor Quantum Dots". In: *Science* 309.5744 (Sept. 2005), pp. 2180–2184. ISSN: 0036-8075. DOI: `10.1126/science.1116955`. URL: `https://www.science.org/doi/10.1126/science.1116955`.

[7] F. H. L. Koppens et al. "Driven Coherent Oscillations of a Single Electron Spin in a Quantum Dot". In: *Nature (London)* 442.7104 (2006), p. 766. ISSN: 0028-0836. DOI: `10.1038/nature05065`.

[8] S. Nadj-Perge et al. "Spin-Orbit Qubit in a Semiconductor Nanowire". In: *Nature (London)* 468.7327 (12 2010/12/23/print), pp. 1084–1087. DOI: `10.1038/nature09682`.

[9] M. D. Schroer et al. "Field Tuning the g Factor in InAs Nanowire Double Quantum Dots". In: *Physical Review Letters* 107.17 (Oct. 2011), p. 176811. ISSN: 0031-9007. DOI: `10.1103/PhysRevLett.107.176811`. URL: `https://link.aps.org/doi/10.1103/PhysRevLett.107.176811`.

[10] M. Veldhorst et al. "An Addressable Quantum Dot Qubit with Fault-Tolerant Control-Fidelity". In: *Nat. Nanotechnol.* 9.12 (2014), pp. 981–985. DOI: `10.1038/nnano.2014.216`.

[11] J. J. Pla et al. "A Single-Atom Electron Spin Qubit in Silicon". In: *Nature (London)* 489.7417 (92012/09/27/print), pp. 541–545. DOI: `10.1038/nature11449`.

[12] B. M. Maune et al. “Coherent Singlet-Triplet Oscillations in a Silicon-Based Double Quantum Dot”. In: *Nature (London)* 481.7381 (2012), p. 344. ISSN: 0028-0836. DOI: 10.1038/nature10707.

[13] H. Watzinger et al. “A germanium hole spin qubit”. In: *Nature Communications* 9.1 (Dec. 2018). ISSN: 20411723. DOI: 10.1038/S41467-018-06418-4.

[14] A. Sammak et al. “Shallow and Undoped Germanium Quantum Wells: A Playground for Spin and Hybrid Quantum Technology”. In: *Advanced Functional Materials* 29.14 (2019), p. 1807613. ISSN: 1616-3028. DOI: 10.1002/adfm.201807613.

[15] L. A. Terrazos et al. “Theory of Hole-Spin Qubits in Strained Germanium Quantum Dots”. In: *Phys. Rev. B* 103.12 (2021), p. 125201. DOI: 10.1103/PhysRevB.103.125201.

[16] E. A. Laird, F. Pei, and L. P. Kouwenhoven. “A valley–spin qubit in a carbon nanotube”. In: *Nature Nanotechnology 2013 8:8* 8.8 (July 2013), pp. 565–568. ISSN: 1748-3395. DOI: 10.1038/nnano.2013.140. URL: https://www.nature.com/articles/nnano.2013.140.

[17] L. M. Gächter et al. “Single-Shot Spin Readout in Graphene Quantum Dots”. In: *PRX Quantum* 3.2 (May 2022), p. 020343. ISSN: 2691-3399. DOI: 10.1103/PRXQuantum.3.020343. URL: https://link.aps.org/doi/10.1103/PRXQuantum.3.020343.

[18] L. Mauro et al. “Hole spin qubits in unstrained Germanium layers”. In: *npj Quantum Information 2025 11:1* 11.1 (Oct. 2025), pp. 167–. ISSN: 2056-6387. DOI: 10.1038/s41534-025-01108-8. URL: https://www.nature.com/articles/s41534-025-01108-8.

[19] D. Costa et al. “Buried unstrained germanium channels: a lattice-matched platform for quantum technology”. In: *arXiv* (July 2025). URL: http://arxiv.org/abs/2506.04724.

[20] M. T. Madzik et al. “Precision tomography of a three-qubit donor quantum processor in silicon”. In: *Nature* 601.7893 (Jan. 2022), pp. 348–353. ISSN: 14764687. DOI: 10.1038/s41586-021-04292-7.

[21] J. Reiner et al. “High-fidelity initialization and control of electron and nuclear spins in a four-qubit register”. In: *Nature Nanotechnology 2024 19:5* 19.5 (Feb. 2024), pp. 605–611. ISSN: 1748-3395. DOI: 10.1038/s41565-023-01596-9. URL: https://www.nature.com/articles/s41565-023-01596-9.

[22] I. Thorvaldson et al. “Grover’s algorithm in a four-qubit silicon processor above the fault-tolerant threshold”. In: *Nature Nanotechnology* 20.4 (Apr. 2025), pp. 472–477. ISSN: 1748-3387. DOI: 10.1038/s41565-024-01853-5. URL: https://www.nature.com/articles/s41565-024-01853-5.

[23] H. Edlbauer et al. “An 11-qubit atom processor in silicon”. In: *Nature* 648.8094 (Dec. 2025), pp. 569–575. ISSN: 0028-0836. DOI: 10.1038/s41586-025-09827-w. URL: https://www.nature.com/articles/s41586-025-09827-w.

[24] A. Elsayed et al. “Low charge noise quantum dots with industrial CMOS manufacturing”. In: *npj Quantum Information* 10.1 (July 2024), p. 70. ISSN: 2056-6387. DOI: 10.1038/s41534-024-00864-3.

[25] N. I. D. Stuyck et al. “Uniform Spin Qubit Devices in an All-Silicon 300 mm Integrated Process”. In: *IEEE Symposium on VLSI Circuits, Digest of Technical Papers* 2021-June (Aug. 2021). DOI: 10.23919/VLSICircuits52068.2021.9492427. URL: http://arxiv.org/abs/2108.11317%20http://dx.doi.org/10.23919/VLSICircuits52068.2021.9492427.

[26] B. Martinez and Y.-M. Niquet. “Variability of Electron and Hole Spin Qubits Due to Interface Roughness and Charge Traps”. In: *Physical Review Applied* 17.2 (Feb. 2022), p. 024022. ISSN: 2331-7019. DOI: 10.1103/PhysRevApplied.17.024022. URL: https://link.aps.org/doi/10.1103/PhysRevApplied.17.024022.

[27] J. Y. Huang et al. “High-fidelity spin qubit operation and algorithmic initialization above 1 K”. In: *Nature 2024 627:8005* 627.8005 (Mar. 2024), pp. 772–777. ISSN: 1476-4687. DOI: 10.1038/s41586-024-07160-2. URL: https://www.nature.com/articles/s41586-024-07160-2.

[28] P. Steinacker et al. “Industry-compatible silicon spin-qubit unit cells exceeding 99% fidelity”. In: *Nature 2025 646:8083* 646.8083 (Sept. 2025), pp. 81–87. ISSN: 1476-4687. DOI: 10.1038/s41586-025-09531-9. URL: https://www.nature.com/articles/s41586-025-09531-9.

[29] A. Nickl et al. “Eight-Qubit Operation of a 300 mm SiMOS Foundry-Fabricated Device”. In: (Dec. 2025). URL: https://arxiv.org/abs/2512.10174v1.

[30] W. I. Lawrie et al. *Quantum dot arrays in silicon and germanium.* Feb. 2020. DOI: 10.1063/5.0002013.

[31] S. G. J. Philips et al. “Universal control of a six-qubit quantum processor in silicon”. In: *Nature* 609.7929 (Sept. 2022), pp. 919–924. ISSN: 0028-0836. DOI: 10.1038/s41586-022-05117-x. URL: https://www.nature.com/articles/s41586-022-05117-x.

[32] H. C. George et al. “12-Spin-Qubit Arrays Fabricated on a 300 mm Semiconductor Manufacturing Line”. In: *Nano Letters* 25.2 (Jan. 2025), pp. 793–799. ISSN: 1530-6984. DOI: 10.1021/acs.nanolett.4c05205. URL: https://pubs.acs.org/doi/10.1021/acs.nanolett.4c05205.

[33] B. Paquelet Wuetz et al. “Atomic fluctuations lifting the energy degeneracy in Si/SiGe quantum dots”. In: *Nature Communications 2022 13:1* 13.1 (Dec. 2022), pp. 7730–. ISSN: 2041-1723. DOI: 10.1038/s41467-022-35458-0. URL: https://www.nature.com/articles/s41467-022-35458-0.

[34] M. P. Losert et al. “Practical strategies for enhancing the valley splitting in Si/SiGe quantum wells”. In: *Physical Review B* 108.12 (Sept. 2023), p. 125405. ISSN: 2469-9950. DOI: 10.1103/PhysRevB.108.125405. URL: https://link.aps.org/doi/10.1103/PhysRevB.108.125405.

[35] I. Hansen et al. “Pulse engineering of a global field for robust and universal quantum computation”. In: *Physical Review A* 104.6 (Dec. 2021), p. 062415. ISSN: 2469-9926. DOI: 10.1103/PhysRevA.104.062415.

[36] M. Veldhorst et al. “Silicon CMOS Architecture for a Spin-Based Quantum Computer”. In: *Nature Communications* 8.1 (2017), p. 1766. ISSN: 2041-1723. DOI: 10.1038/s41467-017-01905-6.

[37] D. Jirovec et al. “A singlet-triplet hole spin qubit in planar Ge”. In: *Nature Materials* 20.8 (Aug. 2021), pp. 1106–1112. ISSN: 1476-1122. DOI: 10.1038/s41563-021-01022-2. URL: https://www.nature.com/articles/s41563-021-01022-2.

[38] G. Xu et al. “Hole spin in tunable Ge hut wire double quantum dot”. In: *Applied Physics Express* 13.6 (May 2020), p. 065002. ISSN: 1882-0786. DOI: 10.35848/1882-0786/AB8B6D. URL: https://iopscience.iop.org/article/10.35848/1882-0786/ab8b6d.

[39] N. W. Hendrickx et al. “A Single-Hole Spin Qubit”. In: *Nat Commun* 11.1 (2020), p. 3478. ISSN: 2041-1723. DOI: 10.1038/s41467-020-17211-7.

[40] N. W. Hendrickx et al. “Fast Two-Qubit Logic with Holes in Germanium”. In: *Nature* 577.7791 (2020), pp. 487–491. ISSN: 1476-4687. DOI: 10.1038/s41586-019-1919-3.

[41] N. W. Hendrickx et al. “A Four-Qubit Germanium Quantum Processor”. In: *Nature* 591.7851 (2021), pp. 580–585. ISSN: 1476-4687. DOI: 10.1038/s41586-021-03332-6.

[42] W. I. L. Lawrie et al. “Simultaneous Single-Qubit Driving of Semiconductor Spin Qubits at the Fault-Tolerant Threshold”. In: *Nat Commun* 14.1 (2023), p. 3617. ISSN: 2041-1723. DOI: 10.1038/s41467-023-39334-3.

[43] F. van Riggelen et al. “Phase Flip Code with Semiconductor Spin Qubits”. In: *npj Quantum Inf* 8.1 (2022), pp. 1–7. ISSN: 2056-6387. DOI: 10.1038/s41534-022-00639-8.

[44] F. van Riggelen-Doelman et al. “Coherent Spin Qubit Shuttling through Germanium Quantum Dots”. In: *Nat Commun* 15.1 (2024), p. 5716. ISSN: 2041-1723. DOI: 10.1038/s41467-024-49358-y.

[45] C.-A. Wang et al. “Probing resonating valence bonds on a programmable germanium quantum simulator”. In: *npj Quantum Information* 9.1 (June 2023), p. 58. ISSN: 2056-6387. DOI: 10.1038/s41534-023-00727-3. URL: https://www.nature.com/articles/s41534-023-00727-3.

[46] V. John et al. “Bichromatic Rabi Control of Semiconductor Qubits”. In: *Physical Review Letters* 132.6 (Feb. 2024), p. 067001. ISSN: 0031-9007. DOI: 10.1103/PhysRevLett.132.067001.

[47] C.-A. Wang et al. “Operating semiconductor quantum processors with hopping spins”. In: *Science* 385.6707 (July 2024), pp. 447–452. ISSN: 0036-8075. DOI: 10.1126/science.ado5915. URL: https://www.science.org/doi/10.1126/science.ado5915.

[48] F. Borsoi et al. “Shared control of a 16 semiconductor quantum dot crossbar array”. In: *Nature Nanotechnology* 19.1 (Jan. 2024), pp. 21–27. ISSN: 1748-3387. DOI: 10.1038/s41565-023-01491-3. URL: https://www.nature.com/articles/s41565-023-01491-3.

[49] L. E. A. Stehouwer et al. “Exploiting strained epitaxial germanium for scaling low-noise spin qubits at the micrometre scale”. In: *Nature Materials* 24.12 (Dec. 2025), pp. 1906–1912. ISSN: 1476-1122. DOI: 10.1038/s41563-025-02276-w. URL: https://www.nature.com/articles/s41563-025-02276-w.

[50] D. Costa et al. “Reducing disorder in Ge quantum wells by using thick SiGe barriers”. In: *Applied Physics Letters* 125.22 (Nov. 2024), p. 222104. ISSN: 00036951. DOI: 10.1063/5.0242746/3322458.

[51] A. Tosato et al. “QARPET: A Crossbar Chip for Benchmarking Semiconductor Spin Qubits”. In: (Apr. 2025). URL: https://arxiv.org/abs/2504.05460v2.

[52] D. Jirovec et al. “Mitigation of exchange crosstalk in dense quantum dot arrays”. In: *Physical Review Applied* 24.3 (Sept. 2025), p. 034051. ISSN: 2331-7019. DOI: 10.1103/qgnt-n527. URL: https://link.aps.org/doi/10.1103/qgnt-n527.

[53] X. Zhang et al. “Universal control of four singlet–triplet qubits”. In: *Nature Nanotechnology* (Oct. 2024). ISSN: 1748-3387. DOI: 10.1038/s41565-024-01817-9. URL: https://www.nature.com/articles/s41565-024-01817-9.

[54] Z. Ademi et al. “Distributing entanglement between distant semiconductor qubit registers using a shared-control shuttling link”. In: (Oct. 2025). URL: http://arxiv.org/abs/2510.26860.

[55] G. Scappucci et al. “The Germanium Quantum Information Route”. In: *Nature Reviews Materials* (2020), pp. 1–18. ISSN: 2058-8437. DOI: 10.1038/s41578-020-00262-z.

[56] H. Watzinger et al. “A Germanium Hole Spin Qubit”. In: *Nat Commun* 9.1 (2018), p. 3902. ISSN: 2041-1723. DOI: 10.1038/s41467-018-06418-4.

[57] V. John et al. “Robust and localised control of a 10-spin qubit array in germanium”. In: *Nature Communications* 16.1 (Nov. 2025), p. 10560. ISSN: 2041-1723. DOI: 10.1038/s41467-025-65577-3. URL: https://www.nature.com/articles/s41467-025-65577-3.

[58] J. Danon and Y. V. Nazarov. “Pauli spin blockade in the presence of strong spin-orbit coupling”. In: *Physical Review B* 80.4 (July 2009), p. 041301. ISSN: 1098-0121. DOI: 10.1103/PhysRevB.80.041301. URL: https://link.aps.org/doi/10.1103/PhysRevB.80.041301.

[59] L. A. Terrazos et al. “Theory of hole-spin qubits in strained germanium quantum dots”. In: *Physical Review B* 103.12 (Mar. 2021), p. 125201. ISSN: 24699969. DOI: 10.1103/PHYSREVB.103.125201/FIGURES/7/MEDIUM. URL: https://journals.aps.org/prb/abstract/10.1103/PhysRevB.103.125201.

[60] E. A. Rodríguez-Mena et al. "Linear-in-momentum spin orbit interactions in planar Ge/GeSi heterostructures and spin qubits". In: *Physical Review B* 108.20 (Nov. 2023), p. 205416. ISSN: 2469-9950. DOI: 10.1103/PhysRevB.108.205416. URL: https://link.aps.org/doi/10.1103/PhysRevB.108.205416.

[61] E. A. Rodríguez-Mena et al. "Sweet-spot protection of hole spins in sparse arrays via spin-dependent magneto-tunneling". In: (Oct. 2025). URL: http://arxiv.org/abs/2510.25857.

[62] C.-A. Wang et al. "Modeling of planar germanium hole qubits in electric and magnetic fields". In: *npj Quantum Information* 10.1 (Oct. 2024), p. 102. ISSN: 2056-6387. DOI: 10.1038/s41534-024-00897-8.

[63] J. C. Abadillo-Uriel et al. *Hole Spin Driving by Strain-Induced Spin-Orbit Interactions.* 2022. DOI: 10.48550/arXiv.2212.03691. eprint: arxiv:2212.03691.

[64] A. Sen et al. "Classification and Magic Magnetic Field Directions for Spin-Orbit-Coupled Double Quantum Dots". In: *Phys. Rev. B* 108.24 (2023), p. 245406. DOI: 10.1103/PhysRevB.108.245406.

[65] B. Martinez et al. "Hole Spin Manipulation in Inhomogeneous and Nonseparable Electric Fields". In: *Phys. Rev. B* 106.23 (2022), p. 235426. DOI: 10.1103/PhysRevB.106.235426.

[66] P. M. Mutter and G. Burkard. "Natural heavy-hole flopping mode qubit in germanium". In: *Physical Review Research* 3.1 (Feb. 2021), p. 013194. ISSN: 2643-1564. DOI: 10.1103/PhysRevResearch.3.013194. URL: https://link.aps.org/doi/10.1103/PhysRevResearch.3.013194.

[67] S. Bosco et al. "Squeezed hole spin qubits in Ge quantum dots with ultrafast gates at low power". In: *Physical Review B* 104.11 (Sept. 2021), p. 115425. ISSN: 2469-9950. DOI: 10.1103/PhysRevB.104.115425. URL: https://link.aps.org/doi/10.1103/PhysRevB.104.115425.

[68] B. Venitucci et al. "Electrical Manipulation of Semiconductor Spin Qubits within the g-Matrix Formalism". In: *Phys. Rev. B* 98.15 (2018), p. 155319. DOI: 10.1103/PhysRevB.98.155319.

[69] B. Martinez and Y.-M. Niquet. "Variability of Electron and Hole Spin Qubits Due to Interface Roughness and Charge Traps". In: *Phys. Rev. Appl.* 17.2 (2022), p. 024022. DOI: 10.1103/PhysRevApplied.17.024022.

[70] B. Martinez, S. de Franceschi, and Y.-M. Niquet. "Mitigating variability in epitaxial-heterostructure-based spin-qubit devices by optimizing gate layout". In: *Physical Review Applied* 22.2 (Aug. 2024), p. 024030. ISSN: 2331-7019. DOI: 10.1103/PhysRevApplied.22.024030. URL: https://link.aps.org/doi/10.1103/PhysRevApplied.22.024030.

[71] E. Valvo et al. "Electrically Tuneable Variability in Germanium Hole Spin Qubits". In: (Dec. 2025). URL: https://arxiv.org/abs/2512.12702v1.

[72] I. Seidler et al. "Spatial uniformity of g-tensor and spin-orbit interaction in germanium hole spin qubits". In: (Oct. 2025). URL: http://arxiv.org/abs/2510.03125.

[73] Y. Tokura et al. "Coherent Single Electron Spin Control in a Slanting Zeeman Field". In: *Phys. Rev. Lett.* 96.4 (2006), p. 047202. DOI: 10.1103/PhysRevLett.96.047202.

[74] S. Nadj-Perge et al. "Spin–orbit qubit in a semiconductor nanowire". In: *Nature* 468.7327 (Dec. 2010), pp. 1084–1087. ISSN: 0028-0836. DOI: 10.1038/nature09682. URL: https://www.nature.com/articles/nature09682.

[75] R. M. Jock et al. "A Silicon Metal-Oxide-Semiconductor Electron Spin-Orbit Qubit". In: *Nat. Commun.* 9.1 (2018), p. 1768.

[76] D. Jirovec et al. "A Singlet-Triplet Hole Spin Qubit in Planar Ge". In: *Nat. Mater.* 20.8 (2021), pp. 1106–1112. ISSN: 1476-4660. DOI: 10.1038/s41563-021-01022-2.

[77] D. P. DiVincenzo et al. "Universal quantum computation with the exchange interaction". In: *Nature* 408.6810 (Nov. 2000), pp. 339–342. ISSN: 0028-0836. DOI: 10.1038/35042541. URL: https://www.nature.com/articles/35042541.

[78] J. Medford et al. "Quantum-Dot-Based Resonant Exchange Qubit". In: *Phys. Rev. Lett.* 111.5 (2013), p. 050501. DOI: 10.1103/PhysRevLett.111.050501.

[79] K. Eng et al. "Isotopically enhanced triple-quantum-dot qubit". In: *Science Advances* 1.4 (May 2015). ISSN: 23752548. DOI: 10.1126/SCIADV.1500214/SUPPL{_}FILE/1500214{_}SM.PDF. URL: https://www.science.org/doi/abs/10.1126/sciadv.1500214.

[80] R. W. Andrews et al. "Quantifying Error and Leakage in an Encoded Si/SiGe Triple-Dot Qubit". In: *Nat. Nanotechnol.* 14.8 (2019), pp. 747–750. ISSN: 1748-3395. DOI: 10.1038/s41565-019-0500-4.

[81] A. J. Weinstein et al. "Universal Logic with Encoded Spin Qubits in Silicon". In: *Nature* 615.7954 (2023), pp. 817–822. ISSN: 1476-4687. DOI: 10.1038/s41586-023-05777-3.

[82] M. T. Madzik et al. "Operating two exchange-only qubits in parallel". In: *Nature 2025 647:8091* 647.8091 (Nov. 2025), pp. 870–875. ISSN: 1476-4687. DOI: 10.1038/s41586-025-09767-5. URL: https://www.nature.com/articles/s41586-025-09767-5.

[83] Google Quantum AI. *Go inside the Google Quantum AI lab*. Dec. 2024. URL: https://blog.google/technology/research/behind-the-scenes-google-quantum-ai-lab/.

[84] L. M. K. Vandersypen et al. "Interfacing spin qubits in quantum dots and donors—hot, dense, and coherent". In: *npj Quantum Information* 3.1 (Dec. 2017), p. 34. ISSN: 2056-6387. DOI: 10.1038/s41534-017-0038-y. URL: http://www.nature.com/articles/s41534-017-0038-y.

[85] M. Veldhorst et al. "Silicon CMOS architecture for a spin-based quantum computer". In: *Nature Communications* 8.1 (Dec. 2017), p. 1766. ISSN: 2041-1723. DOI: 10.1038/s41467-017-01905-6. URL: http://www.nature.com/articles/s41467-017-01905-6.

2

THEORY

cubit [noun]: an ancient unit of measurement for length based on the distance from a man's elbow to the end of the middle finger, usually about 45-50 centimetres. [1]

Cambridge Dictionary

THE foundation of quantum mechanics in the early twentieth century was strongly influenced by studies of the hydrogen atom, which represents one of the most elementary and experimentally accessible quantum systems. There are many good entry-level textbooks covering this scientific era. A large part of the first chapters is based on Ref. [2–4]. The filling of the hydrogen atom's orbital shells can be described using discrete quantum numbers: the principal quantum number $n = 1, 2, 3, \ldots$, the orbital angular momentum quantum number $l = 0, 1, \ldots, n-1$, the spin quantum number $s = \frac{1}{2}$, and the total angular momentum quantum number $j = |l-s|, l+s$. The latter becomes relevant whenever the atomic number is large and $l \neq 0$ because electrons experience spin-orbit interaction that couples orbital angular momentum to spin. This interaction arises from relativistic effects and scales with the atomic number, which implies that heavier elements exhibit stronger spin-orbit coupling. To facilitate the discussion of these effects, it is convenient to use the standard spectroscopic notation nl_j such as $1s_{1/2}$, $2s_{1/2}$, $2p_{1/2}$, $2p_{3/2}$, …. In the following, the principal quantum number n will be omitted whenever it is not essential.

With this notation clarified, we recall the meaning of the quantum numbers for the s and p orbitals, which will play a central role in the remainder of the thesis. The s orbital is defined by $l = 0$, and $m_l = 0$. The total angular momentum is therefore solely determined by the spin $s = \frac{1}{2}$, implying the absence of spin-orbit coupling. This yields the two eigenstates $|j, m_j\rangle = |s, m_s\rangle$

$$|\tfrac{1}{2}, \pm\tfrac{1}{2}\rangle_s \;\Big\}\quad s_{1/2}.$$

In contrast, the p orbital is characterized by $l = 1$, leading to a threefold degeneracy with $m_l = -1, 0, 1$. For sizeable spin-orbit coupling, incorporating the electron spin $s = \frac{1}{2}$ results in total angular momentum values $j = |l \pm s|$ and six corresponding eigenstates $|j, m_j\rangle$.

$$\left.\begin{matrix} |\tfrac{3}{2}, \pm\tfrac{3}{2}\rangle_p \\ |\tfrac{3}{2}, \pm\tfrac{1}{2}\rangle_p \end{matrix}\right\}\quad p_{3/2}$$
$$|\tfrac{1}{2}, \pm\tfrac{1}{2}\rangle_p \;\Big\}\quad p_{1/2}$$

The magnetic moments associated with orbital and spin angular momentum give rise to interactions with magnetic fields. The electron possesses a magnetic moment analogous to its classical counterpart in electromagnetism. In a semi-classical picture of an electron orbiting the nucleus with angular momentum, the corresponding quantum operator is

$$\mathbf{M}_L = \frac{\mu_B}{\hbar}\hat{\mathbf{L}}, \qquad \mu_B = \frac{e\hbar}{2m_e}, \tag{2.1}$$

with $\hat{\mathbf{L}}$ the angular momentum operator and μ_B the Bohr magneton.

In addition to orbital angular momentum, the electron carries intrinsic spin that contributes an additional magnetic moment. Its operator takes a similar form but includes the intrinsic spin g-factor $g_s \approx 2$ and spin operator $\hat{\mathbf{S}}$,

$$\mathbf{M}_S = \frac{g_s \mu_B}{\hbar}\hat{\mathbf{S}}. \tag{2.2}$$

2.1. ORIGIN OF SPIN-ORBIT COUPLING

Following Ref. [2] the fundamental origin of the spin-orbit coupling term comes from the relativistic Dirac equation, which can be evaluated for an electron placed in a nuclear potential and expanded in v/c as a power series. For a semi-classical analogy we can consider the magnetic field that an electron feels in the electron frame within the electrostatic field **E** created by the nucleus with potential $V(r)$:

$$B' = -\frac{1}{c^2}\mathbf{v}\times\mathbf{E} = \frac{1}{em_ec^2}\frac{1}{r}\frac{dV(r)}{dr}\underbrace{\mathbf{p}\times\mathbf{r}}_{-\mathbf{L}}, \qquad \mathbf{E} = -\frac{1}{e}\frac{dV(r)}{dr}\frac{\mathbf{r}}{r} \tag{2.3}$$

The spin-orbit interaction energy comes from the interaction of the intrinsic magnetic moment of the spin (keeping in mind that we are in the electron frame) with the effective magnetic field it feels because of its relative motion[1]

$$H_{SO} = -\mathbf{M}_s\cdot B' = \frac{1}{m_e^2c^2}\frac{1}{r}\frac{dV(r)}{dr}\mathbf{L}\cdot\mathbf{S}. \tag{2.4}$$

For the hydrogen atom it is possible to get the energy correction corresponding to Equation 2.4 analytically from the Dirac equation, which is only dependent on quantum numbers n and j [2].

$$\Delta E_{SO,H}^{n,j} = -\frac{m_ec^2}{2n^4}\left(\frac{n}{j+1/2}-\frac{3}{4}\right)\alpha^4 \qquad \alpha \approx \frac{1}{137} \tag{2.5}$$

For the hydrogen atom this means that the $2s_{1/2}$ and $2p_{1/2}$ energy levels are split from $2p_{3/2}$. This serves as an illustration how the spin-orbit interaction shifts degenerate energy levels on the atomic level already, only dependent on quantum numbers n and j.

2.2. ZEEMAN SPLITTING

The Zeeman Hamiltonian H_z arises from the interaction of the total magnetic moment $M = M_L + M_S$ with an external magnetic field $\mathbf{B} = B_0\mathbf{b}$ with $\mathbf{b}$ the magnetic field unit vector, and B_0 the magnetic field amplitude.

$$H_z = -B_0M = -B_0(M_L+M_S) = -\frac{\mu_BB_0}{\hbar}(\hat{L}+g_s\hat{S}) \tag{2.6}$$

Defining the magnetic field direction along z, the Zeeman Hamiltonian can be written as

$$H_z = -\frac{\mu_BB_0}{\hbar}(\hat{L}_z+g_s\hat{S}_z) \tag{2.7}$$

For obtaining the Zeeman splitting one has to project the Zeeman Hamiltonian on the bases states, which yields considering significant spin-orbit coupling:

$$\Delta E_z^{j,m_j} = \mu_BB_0\underbrace{\frac{\langle j,m_j|\hat{L}_z|j,m_j\rangle + g_s\langle j,m_j|\hat{S}_z|j,m_j\rangle}{\hbar}}_{g^*} = \hbar\omega_L \qquad \omega_L = \frac{g^*\mu_BB_0}{\hbar}, \tag{2.8}$$

---

[1] A relativistic effect that has been ignored in the derivation of Equation 2.4 is Thomas precession, which adds a factor of 1/2 to the final equation[5].

where we can define an effective g-factor g^* and Larmor frequency ω_L that characterise the Zeeman splitting. In atomic physics the effective g-factor in a weak magnetic field is expressed by the Landé g-factor, which is only dependent on the quantum numbers j, s and l [2].

2.3. QUANTUM BITS

Quantum information theory is a rich discipline at the intersection of quantum physics and information theory. A comprehensive review is provided in Ref. [6], from which only the most relevant concepts are introduced here. Classical information theory is based on encoding information in two states denoted 1 and 0. Quantum information follows an analogous structure but uses two quantum mechanical basis states $|1\rangle$ and $|0\rangle$. A single quantum bit (qubit) can therefore be written as

$$|\theta\rangle = \alpha\,|0\rangle + \beta\,|1\rangle\,, \tag{2.9}$$

where α and β are complex scalars that satisfy $|\alpha|^2 + |\beta|^2 = 1$. The spin degree of freedom in an applied magnetic field provides a natural realization of a qubit, with the two spin states corresponding to $|0\rangle$ and $|1\rangle$. This two level system can be visualized on the Bloch sphere, where the north and south poles represent $|0\rangle$ and $|1\rangle$. Any superposition of these states corresponds to a point on the sphere's surface and is parametrised by the angles θ and ϕ,

$$|\Psi\rangle = \cos\left(\frac{\theta}{2}\right)|0\rangle + \exp(i\phi)\,\sin\left(\frac{\theta}{2}\right)|1\rangle\,. \tag{2.10}$$

The angle θ determines the statistical probability of measuring either state. Over time the system relaxes to the ground state (in the 0 K-limit) through energy exchange with the environment, characterized by the relaxation time T_1. The angle ϕ encodes the relative phase, which is essential for quantum algorithms. Loss of phase coherence is known as decoherence, which is quantified by the coherence time T_2. It is important to note that T_2 is affected not only by pure dephasing of ϕ but also by population relaxation of θ, since relaxation to the ground state destroys all phase information [7].

The principles of quantum mechanics extend naturally to systems of multiple qubits, where entanglement becomes central. Instead of two isolated qubits that can each be represented by a Bloch sphere, the combined system can occupy entangled states in which the state of one qubit depends on that of the other. A general two qubit state takes the form

$$|\Psi\rangle = \alpha_{00}\,|00\rangle + \alpha_{01}\,|01\rangle + \alpha_{10}\,|10\rangle + \alpha_{11}\,|11\rangle\,, \tag{2.11}$$

with the normalisation condition

$$|\alpha_{00}|^2 + |\alpha_{01}|^2 + |\alpha_{10}|^2 + |\alpha_{11}|^2 = 1.$$

These properties do not have a classical analogue, and can be exploited to construct quantum algorithms that outperform classical approaches.

There are five general accepted conditions to build a quantum computer known as the DiVincenzo criteria [8]:

1. A scalable physical system with well characterised qubits

2. The ability to initialise the state of the qubits to a simple fiducial state
3. Long relevant decoherence times, much longer than the gate operation time
4. A “universal” set of quantum gates
5. A qubit-specific measurement capability

We have established that the Zeeman splitting provides a platform for defining an isolated two level system that can be manipulated using an electric dipole field. A universal gate must allow full control over all states on the Bloch sphere and must support the implementation of a two qubit operation. To address the remaining requirements it is necessary to distinguish between the various existing and emerging qubit platforms. In this thesis we focus on hole spins confined in gate defined germanium quantum dots.

2.4. ELECTRONS AND HOLES IN SEMICONDUCTORS

While the roots of solid-state physics date back to the 19th century and classical mechanics of earlier centuries, its modern form only took shape with the theoretical quantum mechanical foundation of electronic band structure starting in the late 1920s [9]. Unlike atomic orbitals, where electrons are strictly confined within a certain area, electronic band structures in solids reveal bands (as the name suggests), on which electrons can freely move unless they are fully occupied. This gave a theoretical understanding of the position and isolation of these bands that distinguish insulators, semiconductors, and metals from each other [9]. Over the years, various theoretical methods have been employed in studying band structures in solids. They range from atomistic models that can re-construct the band structure of the full Brillouin zone, to mesoscopic models that are based on effective parameters [9–11]. For all these models, there is always a trade-off between accuracy and computational cost. Within the scope of this thesis, we are interested in the following: How to create a well-defined qubit system, *i.e.* an isolated 2-level system.

A good intuitive picture on the nature of the conduction and valence band states is given by the tight binding model, which relies on the linear combination of atomic orbitals (LCAO) [11]. Considering the electronic configuration of a germanium atom $[\mathrm{Ar}]3d^{10}4s^{2}4p^{2}$, it has deep core electrons (represented here by [Ar]), shallow core electrons in the 3d orbital, and valence electrons in the 4s and 4p orbitals. Ignoring the shallow core electrons with a binding energy of 29.2 eV, the valence electrons in the $3s$ and $3p$ orbitals form the electronic bands as LCAO.

It is possible to evaluate the contributions of each orbital to the electronic band structure by defining the overlap of the corresponding wave functions and analysing them according to the crystal symmetries. In germanium the crystal structure follows the face-centred cubic diamond lattice with a body-centred cubic Brillouin zone in reciprocal space as depicted in Figure 2.1a and b. The full 8×8 Hamiltonian, which contains one s orbital and three p orbitals for each of the two adjacent atoms, is omitted here. Its derivation is given in Ref. [11]. The resulting band structure, evaluated as a function of the crystal momentum k, is shown in Figure 2.1d, where an energy splitting between the valence and conduction bands appears, with the top of the valence band located at the Γ point at $k = 0$. At the Γ point the LCAO Hamiltonian simplifies substantially due to the high symmetry of the system (see Figure 2.1c and e). It separates into an s like Hamiltonian $H^{\Gamma,s}_{TBA}$ and a threefold degenerate p like Hamiltonian $H^{\Gamma,p}_{TBA}$, which take the form assuming negligible magnetic field

$$H^{\Gamma,s}_{TBA} = \begin{pmatrix} E_S & V_{ss} \\ V_{ss} & E_S \end{pmatrix}, \qquad V_{ss} = 4V_{ss\sigma} \tag{2.12}$$

$$H^{\Gamma,p}_{TBA} = \begin{pmatrix} E_p & V_{xx} \\ V_{xx} & E_p \end{pmatrix}, \qquad V_{xx} = 4V_{pp\sigma}/3 + 8V_{pp\pi}/3. \tag{2.13}$$

The quantities $V_{ss\sigma}$, $V_{pp\sigma}$ and $V_{pp\pi}$ denote the overlap parameters between neighbouring orbitals and are real. The term $V_{ss\sigma}$ describes the overlap of two adjacent s orbitals, $V_{pp\sigma}$ corresponds to the overlap of two p orbitals aligned along the axis of displacement, and $V_{pp\pi}$ represents the overlap of two p orbitals oriented orthogonal to the displacement axis. This shows that at the Γ point we have s-like states from the linear combination of neighbouring s-orbitals and p-like states from the linear combination of the p-like orbitals. All contributions from the *sp* hybridised orbitals are cancelled out at the Γ point.

The precise contribution from each orbital to each eigenfunction ψ_n is visualised in Figure 2.1e, where the full LCAO Hamiltonian has been solved as a function of the crystal wave vector **k**. At the Γ point the cubic symmetry enforces eigenstates with pure orbital character. The lowest state carries only s weight, while the three degenerate valence states carry only p weight. As k moves away from Γ, this symmetry constraint is lost. The eigenstates no longer remain strictly s-like or p-like, and the plot shows how the orbital weights of each state evolve with k.

For further consideration, it is common practice to focus on the band extrema of the valence and conduction band, which is usually sufficient to describe transport phenomena. Since the top valence band is p like and the bottom conduction band is s type, electrons and holes must be treated differently, particularly when spin is included. Within the effective mass approximation the dispersion relation is expanded to second order around its extremum, which yields an associated effective mass. For holes several models of varying complexity exist, depending on how many eigenstates are explicitly retained. Adding the spin degree of freedom to the eight band states that we have already seen in the tight-binding model, gives us up to 16 states. The extended Kane model includes 14 of the 16 states and neglects only the bonding $|1/2,1/2\rangle_s$ state. It also introduces material dependent parameters that describe the coupling to remote bands beyond the explicitly considered states. Following the notation in Ref. [12], these parameters are C_r and $C_{r'}$ for the conduction bands, and γ_1', γ_2', γ_3', κ' and q' for the valence band. Simpler models incorporate fewer states and treat the omitted ones as part of the remote band contributions. The Kane model retains eight states, namely all p like valence band states together with the s type conduction band state. The most reduced description is the Luttinger Kohn model, which includes only the four $|3/2,1/2\rangle_p$ and $|3/2,3/2\rangle_p$ valence band states, which is depicted in Figure 2.2. Consequently the effective parameters for remote band contributions differ across these models.

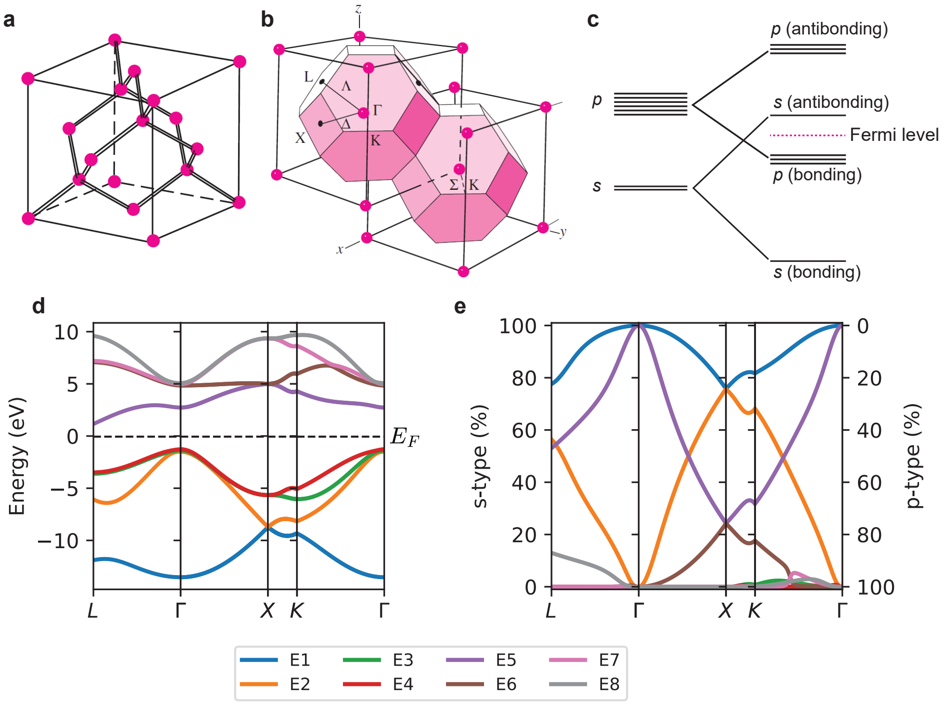

Figure 2.1: **Bulk energy diagram for germanium, a.** Diamond lattice structure (subfigure taken from Ref. [11]), **b.** corresponding Wigner unit cell with indicated symmetry points (Γ, L, X, K) (subfigure taken from Ref. [11]), **c.** simplified depiction how orbitals hybridise, **d** Band diagram and **e** eigenfunctions obtained from solving the LCAO Hamiltonian as a function of **k** ignoring spin-orbit coupling. Energy levels are labelled E1 to E8. The Fermi energy is indicated as E_F.

2.5. MATERIAL PLATFORM

Before introducing the Hamiltonian that describes our system, we present the material platform used throughout this thesis. We employ Ge/SiGe heterostructures with a germanium quantum well buried 55 nm below the surface and metallic gate electrodes on top. Patterned gates define the electrostatic landscape that enables quantum-dot formation and the confinement of single hole spins. Because germanium has a larger lattice constant than silicon (5.66 Å versus 5.43 Å [13]), the Ge quantum well is under biaxial compressive strain, as illustrated in Figure 2.3a. In this work the well is encapsulated by $Si_{0.2}Ge_{0.8}$, which permits a quantum-well width of 16 nm before reaching the critical thickness [14, 15]. The critical thickness represents the maximum layer thickness, at which it becomes energetically favourable for a strained layer to relax and form misfit dislocations. Experimentally a biaxial strain of $(6.9 \pm 0.2) \times 10^{-3}$ [16] has been obtained. To obtain a virtual $Si_{0.2}Ge_{0.8}$ substrate one typically starts from a commercial Si or Ge wafer and grows a reverse-graded $Si_{0.2}Ge_{0.8}$ buffer. The lattice mismatch at the substrate-virtual-substrate interface produces misfit dislocations that aggregate

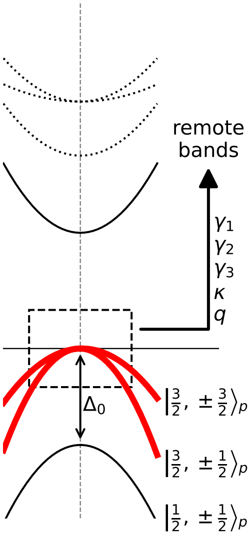

Figure 2.2: Energy bands commonly considered when approximating typical semiconductors around the Γ-point. The Luttinger-Kohn model only considers the four $p_{3/2}$ bands indicated here in red. The Kane model also includes the black continuous bands, and the extended Kane model includes all depicted bands. The black arrow indicates all the parameters that are determined from integrating out the remote bands.

into line-like features at the two-dimensional interface and, after propagating along the [110] crystallographic direction, form threading dislocations along the [111] direction. Threading dislocations can intersect the quantum well and appear at the top surface with a characteristic density. Their presence affects charge-carrier mobility and introduces local strain fluctuations in the quantum well, both of which are relevant for device performance. Metallic gate electrodes are patterned on top of the heterostructure and are separated from the semiconductor by a dielectric. Common gate materials are aluminium and palladium, with thermal expansion coefficients of $23.1\,\mu\mathrm{m\,m^{-1}\,K^{-1}}$ and $11.8\,\mu\mathrm{m\,m^{-1}\,K^{-1}}$, respectively. These values exceed those of silicon and germanium ($2.6\,\mu\mathrm{m\,m^{-1}\,K^{-1}}$ and $6.0\,\mu\mathrm{m\,m^{-1}\,K^{-1}}$) [17, 18]. Extrapolating from fabrication temperatures around 600 K [19] to device operation at 100 mK, and accounting for the non-linear low-temperature thermal expansion, gives approximate contractions of 0.1% for silicon, 0.3% for germanium, 0.6% for palladium, and 1.1% for aluminium [17, 18]. Consequently, cooldown induces stress from the metal gates that is accommodated either by plastic relaxation in the dielectric or by inhomogeneous strain imposed on the underlying heterostructure, the latter being sketched in Figure 2.3c. Because germanium lacks a high-quality native oxide [20], we employ a thin silicon cap and Al_2O_3 as the gate dielectric. The Ge/SiGe quantum well forms a type-I heterostructure capable of hosting both electrons and holes, but the Fermi level is pinned close to the valence band. This results in ohmic p-type contacts with most metals and a large Schottky barrier for n-type contacts [21]. The band alignment therefore makes the platform particularly suitable for

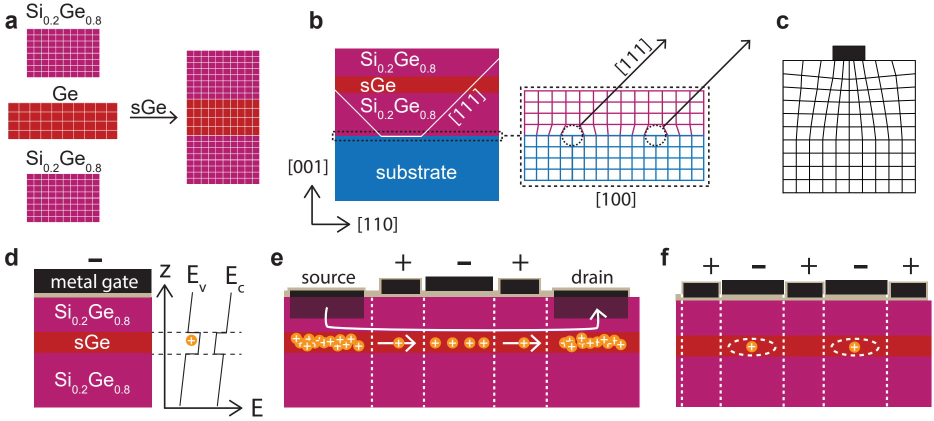

Figure 2.3: **Material platform, a.** Epitaxial growth of a Ge/SiGe quantum well giving a compressively strained quantum well, **b.** Mismatch between the SiGe and the substrate leading to misfit dislocations that propagate towards the quantum well as threading dislocations. **c.** Metal gates contracting upon cooldown leading to inhomogeneous strain in the heterostructure underneath. **d.** Negative potential on the gate allowing accumulation of holes in the quantum well. **e.** Typical structure of a single hole transistor, where charges can tunnel one-by-one from source to the centre island and further to the drain. **f.** Typical double quantum dot structure, where two holes are trapped underneath a plunger gate and seperated from one another by barrier gates.

hole-based devices, where a negative voltage applied to a dedicated gate accumulates holes near the top of the quantum well. Quantum processing units typically contain two device types depicted in Figure 2.3e and f. The first is the quantum dot, defined by plunger and barrier gates [22–24]. Plunger gates create the confining potential by applying negative voltages, while barrier gates between plungers are biased more positively to control tunnelling and the coupling between neighbouring dots. Single-hole-spin qubits are localized at these dots under an applied magnetic field. The second device type is the single-hole transistor, which comprises source and drain contacts, a central plunger gate, and barrier gates separating the ohmic contacts from the central island [25, 26]. The electrostatic potentials on the plunger and barrier gates can be tuned so that only a single charge at a time tunnels from the source to the central gate and then to the drain. This produces Coulomb peaks as a function of the plunger voltage, and their slope serves as a highly sensitive charge sensor.

2.6. LUTTINGER-KOHN FORMALISM AND G-TENSOR

In this section we are going to derive and get a basic understanding of the Hamiltonian of our system that is based on the Luttinger-Kohn Hamiltonian [10, 12]. The full Hamiltonian has the following contributions

$$H = \underbrace{H^0_{LK} + H^0_{BP}}_{\text{crystalline}} + \underbrace{H^0_z}_{\text{magnetic}} + \underbrace{V(x,y,z)\mathbb{1}_{4\times 4}}_{\text{confinement}} \underbrace{(+H^0_{SO})}_{\text{SO correction}} \tag{2.14}$$

LK parameter (from [12])	silicon	germanium
γ_1	4.285	13.38
γ_2	0.339	4.24
γ_3	1.446	5.69
κ	-0.42	3.41
q	0.01	0.06
Δ_{SO} (eV) (from [27])	0.044	0.29

Table 2.1: Luttinger-Kohn parameters arising from integrating out remote bands. The parameters κ and q represent the linear Zeeman term and the cubic correction thereof.

with the Luttinger-Kohn (LK) Hamiltonian H^0_{LK}, the Bir-Pikus correction due to strain H^0_{BP}, the Zeeman Hamiltonian H^0_Z, the confinement potential $V(x,y,z)$ with the 4×4 identity matrix $\mathbb{1}_{4\times4}$, and an additional spin-orbit correction term H^0_{SO} if applicable. We note that the LK Hamiltonian is also directly dependent on the confinement potential.

2.6.1. CRYSTALLINE HAMILTONIANS

Semiconductors, such as silicon and germanium, are typically grown along the high symmetry [001] crystallographic axis direction, and the Luttinger Kohn Hamiltonian is typically expressed in the corresponding $([100],[010],[001])$-coordinate system. In bulk germanium these three axes are equivalent, such that we do not have a preferential spin quantisation axis, i.e. J_x, J_y, J_z all commute with the system Hamiltonian. We know, however, that this symmetry is going to be broken along the growth direction, once we confine or apply an electric field along z. Due to the axial symmetry around z, the system Hamiltonian is approximately invariant under rotations about z. Therefore, J_z remains a good quantum number, whereas J_x and J_y do not. As result, it makes sense to write down the LK Hamiltonian with a quantisation axis along z. Only later we perturb it by breaking the symmetry around z, and it is possible to re-calculate the new spin quantisation axis.

The Luttinger-Kohn (LK) Hamiltonian can be expressed in the basis set $\{|3/2,+3/2\rangle, |3/2,-3/2\rangle, |3/2,+1/2\rangle, |3/2,-1/2\rangle\}$ as

$$H^0_{\mathrm{LK}} = \begin{bmatrix} P+Q & 0 & S & R \\ 0 & P+Q & R^\dagger & -S^\dagger \\ S^\dagger & R & P-Q & 0 \\ R^\dagger & -S & 0 & P-Q \end{bmatrix}, \tag{2.15}$$

where P represents the monopole contribution and Q the quadrupolar contribution along z. With the spin quantisation axis along z, the corresponding eigenvalues of $J_z|j,m_j\rangle = m_j|j,m_j\rangle$ vary between HH with $m_j = 3/2$ and LH with $m_j = 1/2$. As result the quadrupolar contribution acts differently on these two states, which splits them in energy. Thus, $P+Q$ represents the energy of $|3/2,\pm3/2\rangle$, $P-Q$ represents the energy of $|3/2,\pm1/2\rangle$, and S and R representing the heavy hole-light hole (HH-LH) coupling terms with spin conservation and spin flip, respectively. The corresponding relations are

$$P = \frac{\hbar^2}{2m_0}\gamma_1(k_x^2 + k_y^2 + k_z^2) \tag{2.16}$$

$$Q = \frac{\hbar^2}{2m_0}\gamma_2(k_x^2 + k_y^2 - 2k_z^2) \tag{2.17}$$

$$S = -\sqrt{3}\frac{\hbar^2}{2m_0}\gamma_3[(k_x - ik_y)k_z + k_z(k_x - ik_y)] \tag{2.18}$$

$$R = \sqrt{3}\frac{\hbar^2}{2m_0}[-\gamma_2(k_x^2 - k_y^2) + i\gamma_3 k_x k_y + i\gamma_3 k_y k_x]. \tag{2.19}$$

We can also see directly from the LK Hamiltonian that we can define an effective mass for HHs and LHs from $P \pm Q$, which depends whether its direction is along the spin quantisation axis or orthogonal towards it.

$$m_{x,y}^{\mathrm{HH}} = \frac{m_0}{\gamma_1 + \gamma_2} \approx 0.057 m_0 \tag{2.20}$$

$$m_z^{\mathrm{HH}} = \frac{m_0}{\gamma_1 - 2\gamma_2} \approx 0.204 m_0 \tag{2.21}$$

$$m_{x,y}^{\mathrm{LH}} = \frac{m_0}{\gamma_1 - \gamma_2} \approx 0.109 m_0 \tag{2.22}$$

$$m_z^{\mathrm{LH}} = \frac{m_0}{\gamma_1 + 2\gamma_2} \approx 0.046 m_0 \tag{2.23}$$

Contrary to what the name suggests, the HH-states have a smaller in-plane effective mass than the LH-states. Off-diagonal terms originate from the coupling of the $p_{3/2}$-states to remote bands. The Luttinger parameters γ_2 and γ_3 quantify the strength of these anisotropic contributions, which enter the Hamiltonian through the S and R terms. Their symmetry is expressed in how S and R depend on the momentum components k_x, k_y, and k_z. In cubic crystals, this symmetry forbids direct coupling between $|3/2, +3/2\rangle$ and $|3/2, -3/2\rangle$ as well as between $|3/2, +1/2\rangle$ and $|3/2, -1/2\rangle$. Nevertheless, indirect processes via virtual intermediate states remain possible, and can be exploited when operating a qubit within the heavy hole (HH) subspace.

strain parameters	Ge	comments
$\epsilon_{\|\|,110}$	$(6.9 \pm 0.2) \cdot 10^{-3}$ [16]	Ge/SiGe on Si wafer
a_v	2.1 eV [28]	hydrostatic deformation potential
b_v	−2.16 eV [28]	uniaxial deformation potential
d_v	−6.06 eV [28]	shear deformation potential

Table 2.2: Strain parameters entering the Bir-Pikus correction for the Luttinger-Kohn Hamiltonian.

Since crystal symmetries play such a major role in determining the overall band structure, confinement and strain have a massive impact on the $p_{3/2}$ energy levels and their mixing. The former is already accounted for in the LK Hamiltonian with its dependence on k. Confinement along z by applying an electric field and/or utilising quantum wells splits the $|3/2, \pm 3/2\rangle$ and $|3/2, \pm 1/2\rangle$ apart.

Strain, however, is not yet properly taken into account. This is done by defining a similar Hamiltonian like H^0_{LK}, and is referred to as the Bir-Pikus correction. Since they share the same crystal symmetry it can be expressed using the same notation as

$$H^0_{\mathrm{BP}} = \begin{bmatrix} P_\epsilon + Q_\epsilon & 0 & S_\epsilon & R_\epsilon \\ 0 & P_\epsilon + Q_\epsilon & R^\dagger_\epsilon & -S^\dagger_\epsilon \\ S^\dagger_\epsilon & R_\epsilon & P_\epsilon - Q_\epsilon & 0 \\ R^\dagger_\epsilon & -S_\epsilon & 0 & P_\epsilon - Q_\epsilon \end{bmatrix}, \tag{2.24}$$

with a_v, b_v, and d_v the deformation potentials, which are given for germanium in Table 2.2. The quantities P_ϵ, Q_ϵ, R_ϵ and S_ϵ are given by

$$P_\epsilon = -a_v(\epsilon_{xx} + \epsilon_{yy} + \epsilon_{zz}) \tag{2.25}$$

$$Q_\epsilon = -\frac{1}{2} b_v(\epsilon_{xx} + \epsilon_{yy} - 2\epsilon_{zz}) \tag{2.26}$$

$$S_\epsilon = \frac{\sqrt{3}}{2} b_v(\epsilon_{xx} - \epsilon_{yy}) - i d_v \epsilon_{xy} \tag{2.27}$$

$$R_\epsilon = -d_v(\epsilon_{xz} - i\epsilon_{yz}). \tag{2.28}$$

It is difficult to obtain realistic values for the full strain tensor from experiment. However, the growth of the Ge/SiGe heterostructure stack leads to a visible cross-hatch pattern caused by misfit dislocations between the substrate and the buffer layer. These relaxations occur along the [110] and [1$\bar{1}$0] crystallographic axes, which indicates that tensile and compressive strain primarily develop along these two directions [16, 29]. Without any gate electrodes, all strain components with respect to [110] and [1$\bar{1}$0] are therefore expected to be negligible. Once gate electrodes are added, the different thermal contraction of the metal and the semiconductor introduces additional inhomogeneous strain, which can affect all strain tensor components depending on how the gate retracts and how much plastic relaxation occurs in the oxide. Ignoring inhomogeneous strain, we can approximate the strain tensor as

$$\epsilon_{110} = \begin{pmatrix} \epsilon_{xx,110} & 0 & 0 \\ 0 & \epsilon_{yy,110} & 0 \\ 0 & 0 & \epsilon_{zz,110} \end{pmatrix}, \tag{2.29}$$

which needs to be converted into the [100] reference frame, in which the LK Hamiltonian is expressed:

$$\epsilon_{100} = R^T \epsilon_{110} R = \frac{1}{\sqrt{2}} \begin{pmatrix} \epsilon_{xx,110} + \epsilon_{yy,110} & -\epsilon_{xx,110} + \epsilon_{yy,110} & 0 \\ -\epsilon_{xx,110} + \epsilon_{yy,110} & \epsilon_{xx,110} + \epsilon_{yy,110} & 0 \\ 0 & 0 & \sqrt{2}\epsilon_{zz,110} \end{pmatrix} \tag{2.30}$$

We can immediately see that the HH-LH coupling terms simplify to

$$S_\epsilon = -i d_v(-\epsilon_{xx,110} + \epsilon_{yy,110}) \qquad R_\epsilon = 0. \tag{2.31}$$

Therefore, one major contribution of HH-LH mixing from the BP correction comes from a planar mismatch in strain, which can occur particularly if crossing one of the misfit dislocation in either [110] or [1$\bar{1}$0] direction.

strain tensor	22 nm deep Ge/SiGe QW on Si [29]	55 nm deep Ge/SiGe QW on Ge [16]
$\epsilon_{\parallel,110}$	$-7(2)\times 10^{-3}$	$-6.9(2)\times 10^{-3}$
$\epsilon_{\perp,110}$	$5.1(1)\times 10^{-3}$	-
$\epsilon_{ij,110}$ for $i \neq j$	$\pm 0.15\times 10^{-3}$	-

Table 2.3: Strain parameters entering the Bir-Pikus correction for the Luttinger-Kohn Hamiltonian.

2.6.2. MAGNETIC CONTRIBUTIONS

The Zeeman coupling in the LK formalism relates the interaction of angular momentum and magnetic field to the Zeeman splitting and can be written as [12, 30]

$$H_Z = \underbrace{-2\frac{\mu_B\kappa}{\hbar}(J_xB_x + J_yB_y + J_zB_z)}_{H_\kappa}\underbrace{-2\frac{\mu_B q}{\hbar}(J_x^3B_x + J_y^3B_y + J_z^3B_z)}_{H_q}. \tag{2.32}$$

We can see from the equation that we have a linear isotropic contribution H_κ, whose strength is characterised by the parameter κ, and a small cubic correction term H_q, whose strength is characterised by the parameter q, where $|q| \ll |\kappa|$.

The J_z-matrix simply carries the eigenvalues of $J_z|j=3/2, m_j\rangle = m_j\hbar|j=3/2, m_j\rangle$ along the diagonal, i.e.

$$J_z = \begin{pmatrix} 3/2 & 0 & 0 & 0 \\ 0 & -3/2 & 0 & 0 \\ 0 & 0 & 1/2 & 0 \\ 0 & 0 & 0 & -1/2 \end{pmatrix}. \tag{2.33}$$

If a magnetic field is thus applied along z, the HH and LH states are split directly, yielding a pure HH Zeeman splitting of

$$E_{Z,HH,B_\perp} = \left|-2\frac{\mu_B\kappa}{\hbar}\Delta J_{z,HH}B_z - 2\frac{\mu_B q}{\hbar}\Delta J_{z,HH}^3 B_z\right| = (6\kappa + \frac{27}{2}q)\cdot\frac{\mu_B}{\hbar}B_z, \tag{2.34}$$

with $\Delta J_{z,HH} = |3/2 - (-3/2)| = 6/2$ and $\Delta J_{z,HH}^3 = |(3/2)^3 - (-3/2)^3| = 27/4$.

For magnetic fields orthogonal to z we need the angular momentum operators J_x and J_y (expressed in the z-basis), which can be constructed using corresponding ladder operators as shown in [2]. Note that these matrices are fundamental, and can be applied to any system that contains a quantum number of $j = 3/2$. As result the J_x and J_y matrices are defined as follows:

$$J_x = \begin{pmatrix} 0 & 0 & \sqrt{3}/2 & 0 \\ 0 & 0 & 0 & \sqrt{3}/2 \\ \sqrt{3}/2 & 0 & 0 & 1 \\ 0 & \sqrt{3}/2 & 1 & 0 \end{pmatrix}, \quad J_y = i\begin{pmatrix} 0 & 0 & -\sqrt{3}/2 & 0 \\ 0 & 0 & 0 & \sqrt{3}/2 \\ \sqrt{3}/2 & 0 & 0 & -1 \\ 0 & -\sqrt{3}/2 & 1 & 0 \end{pmatrix} \tag{2.35}$$

Physically, this implies that when a magnetic field is applied orthogonal to the quantization axis z, it does not split the HH and LH doublets directly. Instead, it mixes them through these off-diagonal couplings, leading to an indirect energy splitting once the system is diagonalized. The resulting eigenstates are therefore no longer pure HH or LH states, but mixtures defined by the interplay of the Zeeman and Luttinger-Kohn Hamiltonians. As result the corresponding Zeeman splitting becomes strongly dependent on confinement and strain as both modulate the HH-LH mixing. While the linear κ-term exclusively couples the HH ground states via HH-LH mixing, the cubic q-term has a small direct coupling contribution between $p_{+3/2}$ and $p_{-3/2}$ coming from cubing the J_x and J_y matrices.

$$J_x^3 = \begin{pmatrix} 0 & 3/4 & 7\sqrt{3}/8 & 0 \\ 3/4 & 0 & 0 & 7\sqrt{3}/8 \\ 7\sqrt{3}/8 & 0 & 0 & 5/2 \\ 0 & 7\sqrt{3}/8 & 5/2 & 0 \end{pmatrix}, \quad J_y^3 = i \begin{pmatrix} 0 & 3/4 & -7\sqrt{3}/8 & 0 \\ -3/4 & 0 & 0 & 7\sqrt{3}/8 \\ 7\sqrt{3}/8 & 0 & 0 & -5/2 \\ 0 & -7\sqrt{3}/8 & 5/2 & 0 \end{pmatrix} \tag{2.36}$$

This coupling term is therefore independent of the HH-LH coupling and becomes significant when HH-LH mixing is weak. To get the pure HH Zeeman splitting we can calculate the eigenvalues of the isolated HH-block in J_x^3 and J_y^3 respectively, which return eigenvalues of ±3/4. We can thus approximate the pure HH in-plane Zeeman splitting as

$$E_{Z,HH,B_\parallel} = 2\left|2\frac{\mu_B q}{\hbar}(\Delta J^3_{x,HH}B_x + \Delta J^3_{y,HH}B_y)\right| = 6q\cdot\frac{\mu_B}{\hbar}(B_x + B_y), \tag{2.37}$$

with $\Delta J^3_{x,HH} = \Delta J^3_{y,HH} = |3/4 - (-3/4)| = 3/2$.

We therefore have our characteristic pure HH g-factors, which are $6q$ for in-plane magnetic fields and $6\kappa + \frac{27}{2}q$ for out-of-plane magnetic fields.

2.6.3. CONFINEMENT AND ENVELOPE FUNCTIONS

To obtain numerical estimates and explore the behaviour of our system, we start from the confinement potentials, from which we construct a set of envelope wave functions to evaluate the crystalline contributions of the Luttinger-Kohn Hamiltonian. At this stage, it is sufficient to note that we impose strong confinement along one direction and weak confinement in the other two. We therefore assume a hard-wall potential along z with eigenfunctions $\chi^m(z)$, and a harmonic potential in the x, y plane with eigenfunctions $\phi^n(x, y)$, all separable. From these textbook potentials, the total envelope functions read

$$\Psi^{ij}(x,y,z) = \phi^i(x,y)\chi^j(z) \quad \text{for} \quad i,j \in [0,1,2,...] \tag{2.38}$$

The number of orbitals taken into account ($n = \max(i)$, $m = \max(j)$) determines the dimension of the final Hamiltonian's Hilbert space. The orbital wave functions are projected onto the 4 × 4 LK Hamiltonian, yielding a total Hamiltonian H^{nm} of dimension $4(1+n+m)\times 4(1+n+m)$, with matrix elements

$$H^{nm}_{ijkl} = \langle\Psi^{ij}|H^0|\Psi^{kl}\rangle \quad \text{for} \quad i,k \in [0,1,..,n] \text{ and } j,l \in [0,1,...,m] \tag{2.39}$$

2.7. THE G-TENSOR

To determine the precise impact of the HH-LH mixing terms in the LK Hamiltonian on the HH ground state, it is convenient to reduce the problem to a two-level system describing only the effective HH ground state. This can be done by treating the HH-LH mixing perturbatively, relative to the HH-LH splitting, and block-diagonalizing the Hamiltonian, thereby isolating a 2×2 HH Hamiltonian that incorporates second-order contributions from virtual HH-LH transitions.[31, 32]. As such it is feasible to get an effective HH 2×2 Hamiltonian, where the Zeeman anistropy, confinement, and higher order $p_{+3/2} \leftrightarrow p_{-3/2}$ transitions via the LH-states are represented within the g-tensor $\mathbf{G}$. This Hamiltonian takes the form [33]:

$$H = \frac{1}{2}\mu_B \vec{\sigma}\mathbf{G}\vec{B} \tag{2.40}$$

The HH subspace is obtained from projecting the envelope wavefunction on the Hamiltonian $H_{\mathrm{LKBP}} = H_{\mathrm{LK}} + H_{\mathrm{BP}}$ and obtaining the two lowest eigenstates.

The Zeeman operators corresponding to magnetic fields along the principal axes are defined as

$$O_i = \frac{H_{Z,i}}{\mu_B B_0},$$

where $H_{Z,i}$ the Zeeman term for a magnetic field applied along the i-direction and B_0 the reference magnetic-field amplitude. Projection onto the HH subspace yields the effective operators

$$\tilde{O}_i = \Psi_{\mathrm{HH}}^{\dagger} O_i \Psi_{\mathrm{HH}}.$$

To remove the overall shift due to any trace component, we define the traceless operators

$$\tilde{O}'_i = \tilde{O}_i - \frac{\mathrm{Tr}(\tilde{O}_i)}{2}\mathbb{1}.$$

Each operator $\tilde{O}'_i$ can be expressed in terms of Pauli matrices,

$$\tilde{O}'_i = \frac{1}{2}\sum_{j\in\{x,y,z\}} g_{ji}\sigma_j,$$

where the coefficients g_{ji} are obtained as

$$g_{ji} = \mathrm{Tr}(\sigma_j \tilde{O}'_i).$$

The resulting matrix

$$\mathbf{G} = \begin{pmatrix} g_{xx} & g_{xy} & g_{xz} \\ g_{yx} & g_{yy} & g_{yz} \\ g_{zx} & g_{zy} & g_{zz} \end{pmatrix}$$

defines the effective G-tensor of the HH subspace.

It is important to recognise that the g-tensor $\mathbf{G}$ is not uniquely defined. It can be decomposed as $G = U\mathbf{G_d}V$, where $\mathbf{G_d}$ is a diagonal matrix, V defines the magnetic axes, and U specifies the qubit basis. Consequently, $\mathbf{G}$ depends on the choice of qubit basis. Considering the strong out-of-plane anisotropy and the absence of a preferential in-plane direction, it is reasonable to adopt the device axes with z aligned along the growth direction. In practice, the g-tensor is typically asymmetric following this convention. For isolated qubits, one can alternatively align the qubit axes along the magnetic axes, which makes $\mathbf{G}$ symmetric.

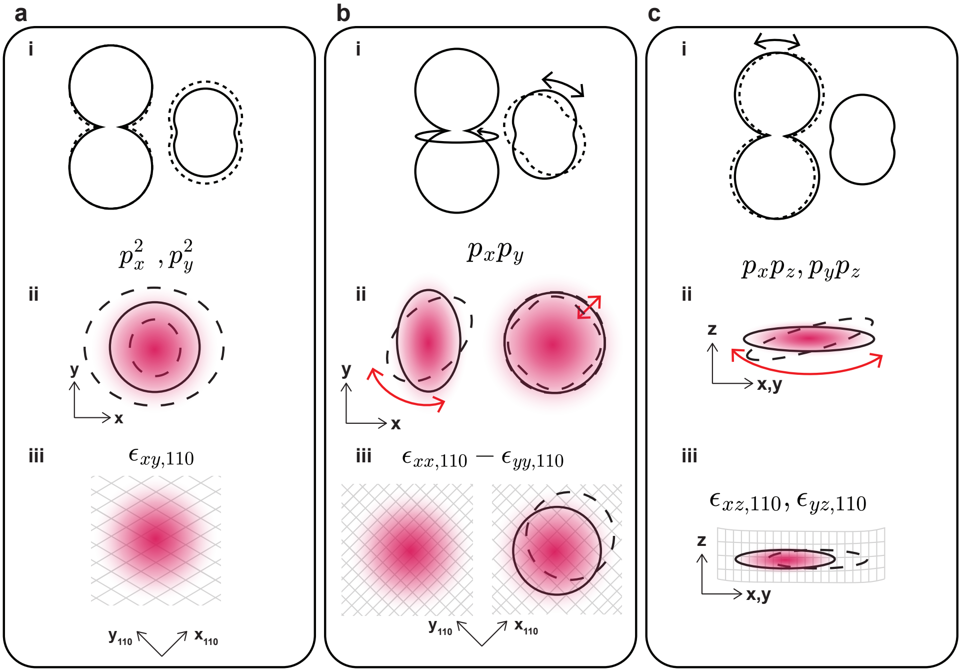

Figure 2.4: **Sources of g-tensor variability and tunability, a.** 'Breathing' of the g-tensor dependent on the harmonic confinement and shear strain. **b.** Change of in-plane principal g-tensor axes by rotating elongated wavefunction, introducing anharmonic potential, or biaxial strain mismatch. **c.** Out-of-plane tilt of the g-tensor by an inhomogeneous electric field or inhomogeneous strain.

2.7.1. ANALYTICAL FORMULAS

The corresponding g-tensor components can be analytically obtained as in [34]:

$$g_{xx} \approx 3q - \frac{6\tilde{\kappa} b_v(\langle\epsilon_{xx}\rangle - \langle\epsilon_{yy}\rangle)}{\Delta_{HL}} - \frac{6(\lambda\langle p_x^2\rangle - \lambda'\left\langle p_y^2\right\rangle)}{m_0\Delta_{HL}} \tag{2.41}$$

$$g_{yy} \approx -3q - \frac{6\tilde{\kappa} b_v(\langle\epsilon_{xx}\rangle - \langle\epsilon_{yy}\rangle)}{\Delta_{HL}} + \frac{6(\lambda\left\langle p_y^2\right\rangle - \lambda'\langle p_x^2\rangle)}{m_0\Delta_{HL}} \tag{2.42}$$

$$g_{xy,yx} \approx \pm\frac{4\sqrt{3}\kappa d_v\langle\epsilon_{xy,yx}\rangle}{\Delta_{HL}} \mp \frac{12\tilde{\lambda}\langle p_x p_y\rangle}{m_0\Delta_{HL}}, \tag{2.43}$$

$$g_{xz,zx} \approx g_{yz,zy} \approx 0 \tag{2.44}$$

$$g_{zz} = 6\kappa - \frac{27}{2}q - 2\gamma_h \tag{2.45}$$

where the average $\langle\cdot\rangle$ represents the average in respect to the ground wavefunction ψ_0, i.e. $\langle\psi_0|\cdot|\psi_0\rangle$, and material dependent scaling parameters

$$\lambda = -\kappa\gamma_2 + \underbrace{2\tilde{\eta}_h\gamma_2\gamma_3 + 2\eta_h\gamma_3^2}_{\text{higher LH orbital correction}} \tag{2.46}$$

$$\lambda' = -\kappa\gamma_2 + \underbrace{2\tilde{\eta}_h\gamma_2\gamma_3 + 2\eta_h\gamma_2\gamma_3}_{\text{higher LH orbital correction}} \tag{2.47}$$

$$\tilde{\lambda} = -\kappa\gamma_3 + \underbrace{2\tilde{\eta}_h\gamma_3^2 + 2\eta_h(\gamma 2\gamma 3 + \gamma_3^2)}_{\text{higher LH orbital correction}} \tag{2.48}$$

$$\tilde{\kappa} = \kappa \qquad \underbrace{-2\tilde{\eta}_h\gamma_3}_{\text{higher LH orbital correction}} \qquad . \tag{2.49}$$

We find back the pure HH g-factors, which appear as constant offsets, whereas the Luttinger-Kohn (LK) Hamiltonian and the Bir-Pikus (BP) correction introduce confinement- and strain-dependent contributions, whose magnitude is determined by the degree of HH-LH coupling. The three key parameters describing this coupling are γ_h, η_h, and $\tilde{\eta}_h$, obtained by integrating out the remote LH bands. Table 2.4 lists theoretical values reported in the literature. The precise values depend on the heterostructure design, strain, and the separability of the electric field [35]. For in-plane magnetic fields, the isotropic Zeeman term H_κ couples via the light-hole (LH) states and therefore gives a highly sensitive contribution to the in-plane g-factors in terms of strain and confinement. For out-of-plane fields, the Zeeman Hamiltonian has no off-diagonal components, and its value is primarily determined by κ and q, with corrections from γ_h, which accounts for the coupling of the HH ground state to LH subbands mediated by k_z. This assumes separability of in-plane and out-of-plane motion, which is not strictly valid in practice [32].

LH parameters	unstrained Ge	strained Ge[2]
γ_h	$\sim 3.6\,\mathrm{eV}$ [31]	$\sim 2.59\,\mathrm{eV}$ [31]
η_h	$\sim 0.2\,\mathrm{eV}$ [31]	$\sim 0.42\,\mathrm{eV}$ [31]
$\tilde{\eta}_h$	$\sim -0.5\,\mathrm{eV}$[3]	-

Table 2.4: Parameters arising from integrating out the the light-hole states from the vertical motion. The given values should only be interpreted as orders of magnitude.

Figure 2.4 illustrates the influence of wave-function shape and strain on the g-tensor. Both effects act, on the one hand, as sources of variability and, on the other, as resources that can be exploited for qubit manipulation. Broadly, the impact of momentum and strain parameters can be grouped into three categories. We begin by assuming a harmonic confinement potential along the [100] and [010] crystallographic directions. Modulating the confinement length leads to a ’breathing’ of the g-tensor (Figure 2.4a.i), in which the principal components along the [100] and [010] directions are modulated (Figure 2.4a.ii). A similar effect arises from the strain component $\epsilon_{xy,110}$, which may fluctuate

---

[2] Biaxial strain for Ge/SiGe quantum well with $\epsilon_{||} = -0.61\%$ and $\epsilon_\perp = +0.45\%$, $L_w = 16\,\mathrm{nm}$

[3] Value coming from preliminary results from E. Valvo *et al.*

around zero in space and can contribute to small dot-to-dot variations (Figure 2.4a.iii). The magnetic axes of the g-tensor can be rotated towards the [110] crystallographic directions (Figure 2.4b.i) by introducing anharmonic confinement, rotating an elongated wave function in space (Figure 2.4b.ii), or through a biaxial strain mismatch between $\epsilon_{xx,110}$ and $\epsilon_{yy,110}$ (Figure 2.4b.iii). This biaxial strain mismatch can reasonably be assumed to be the dominant source of strain-induced variability and may have a significant impact on qubit manipulation [32], particularly when the strain sampled by the wave function varies strongly with its shape and position. For sufficiently large biaxial strain differences, the magnetic axes fully align along the [110] direction, such that further modulation primarily results in breathing behaviour, effectively inverting the roles of the effects shown in Figure 2.4a and b. So far, we have focused on variability and modulation of the in-plane g-tensor. Owing to the strong out-of-plane anisotropy, even small tilts of the g-tensor out of the plane can have pronounced effects (Figure 2.4c.i). For instance, the non-separability of in- and out-of-plane electric fields when applying an oscillating gate voltage modulates the $p_x p_z$ and $p_y p_z$ terms, leading to strong driving via out-of-plane rocking of the g-tensor [35]. Similarly, inhomogeneous strain can introduce shear components that tilt the g-tensor differently in each quantum dot. Physical displacement of the wave function within a spatially varying strain field may therefore also constitute an efficient driving mechanism.

Experimentally, only the magnitude of the Zeeman splitting is typically measured.

$$E_z = \mu_B |\mathbf{G}\vec{B}| = g^* \mu_B B. \tag{2.50}$$

In experiment, the effective g-factor g^* can be measured as a function of magnetic field direction [36–39], which reveals the magnitude of the g-tensor components.

We conclude this subsection by summarising the key considerations when working with the g-tensor.

1. The cubic Zeeman term gives a constant offset for the in-plane g-tensor components of $\pm 3q$ that vary in sign between x- and y-direction.
2. Modifying the confinement potential induces opposite changes in g_{xx} and g_{yy}. Because the cubic Zeeman term also has opposite signs along these directions, it produces a comparable change in magnitude.
3. The difference in biaxial strain $\langle \epsilon_{xx} \rangle - \langle \epsilon_{yy} \rangle$ introduces a constant shift of equal sign for g_{xx} and g_{yy}.

2.7.2. NUMERICAL EXAMPLE

To better understand the g-tensor formalism and familiarise ourselves with the orders of magnitude at play, we can run through a simple numerical example. To do so, we make the following assumptions:

1. The wavefunction is separable along x, y, and z such that we can use Equation 2.38.
2. The strong confinement along z can be approximated with an infinite well potential. Since electric fields heavily tilt the potential in the quantum well, we define an effective confinement length that corresponds to half the quantum well thickness $L_z \approx L_{\mathrm{QW}}/2 = 8\,\mathrm{nm}$

3. The confinement along x and y can be approximated by a 2D harmonic potential
4. We approximate the in-plane wavefunctions of the ground state as $\phi^0 \approx \phi^0_{\mathrm{HH}} \approx \phi^0_{\mathrm{LH}}$, such that the HH and LH envelope functions are the same and $\langle\phi^0_{\mathrm{HH}}|p^2_{x,y}|\phi^0_{\mathrm{HH}}\rangle \approx \langle\phi^0_{\mathrm{HH}}|p^2_{x,y}|\phi^0_{\mathrm{LH}}\rangle$
5. We assume a confinement length of $L_x \approx 19\,\mathrm{nm}$ along x and $L_y \approx 20\,\mathrm{nm}$ along y, which gives a HH orbital splitting of $\sim 50\,\mathrm{meV}$ for ϕ^0_{HH} using the eigenvalues of the harmonic oscillator.
6. We assume that we have isotropic biaxial strain $\epsilon_{\parallel} = \epsilon_{xx} = \epsilon_{yy}$ and $\epsilon_{ij} = 0$ for $i \neq j$

For practical numerical evaluations, we can include a finite number of orbital states for each confinement direction. For simplicity, however, we only consider the minimal case, including only the HH/LH ground state

$$\Psi^{00}(x,y,z) = \phi^0(x,y)\,\chi^0(z),$$

and later apply corrections arising from the coupling of χ^0 to higher z-orbitals $\chi^{i>0}$.

For harmonic confinement, the momentum operator $p_{x,y}$ is related to the spatial extent of the ground wave function as

$$\langle\phi^0|p^2_{x,y}|\phi^0\rangle = \frac{\hbar^2}{2L^2_{x,y}} \Rightarrow \begin{cases} p_x^2 = 1.385 \times 10^{15}\,(\hbar/\mathrm{m})^2 \\ p_y^2 = 1.250 \times 10^{15}\,(\hbar/\mathrm{m})^2 \end{cases} \tag{2.51}$$

$$\langle\phi^0|p_i p_j|\phi^0\rangle_{i\neq j} \approx 0 \tag{2.52}$$

For an infinite potential well along z, the corresponding matrix element reads

$$\langle\chi^n|p_z^2|\chi^n\rangle = \left(\frac{n\pi}{2L_z}\right)^2 \Rightarrow p_z^2 = 3.855 \times 10^{16}\,(\hbar/\mathrm{m})^2 \tag{2.53}$$

Analytical expressions for mixed terms such as $\langle\chi_i|p_z|\chi_j\rangle$, $\langle\chi_i|z|\chi_j\rangle$, $\langle\chi_i|p_z z|\chi_j\rangle$, and $\langle\chi_i|z p_z|\chi_j\rangle$ (including the ground state χ_0 and excited orbitals $\chi_{j>0}$) exist and become relevant once higher orbital states are included. All coupling terms between z and x, y vanish due to the separability of the chosen wave functions. Projecting the ground state Ψ^{00} on the LK Hamiltonian we thus get:

$$H_{\mathrm{LK}}^{(\Psi^{00})}(\mathrm{meV}) = \langle\Psi^{00}|H^0_{LK}|\Psi^{00}\rangle \approx \begin{bmatrix} 8.97 & 0. & 0 & -0.04 \\ 0 & 8.97 & -0.04 & 0 \\ 0 & -0.04 & 33.03 & 0 \\ -0.04 & 0 & 0 & 33.03 \end{bmatrix}, \tag{2.54}$$

We thus obtain a HH-LH splitting of $\Delta_{HH-LH} \approx 24.1\,\mathrm{meV}$, which is almost exclusively determined by the much stronger z-confinement, i.e. $\Delta_{HH-LH} \sim 2\frac{\hbar^2}{2m_0}\gamma_2 2k_z^2 \approx 24.9\,\mathrm{meV}$.

We consider here only isotropic biaxial strain with $\epsilon_{xx,110} = \epsilon_{yy,110} = -6.9\,\mathrm{meV}$, $\epsilon_{zz,110} = 5.2\,\mathrm{meV}$, and negligible shear strain, i.e. $\epsilon_{ij,110} \approx 0$ for $i \neq j$. For more complex and inhomogeneous strain due to gate contraction upon cooldown, the strain fields need to be sampled across the full wave function. When projecting the ground state on the BP Hamiltonian we obtain:

$$H_{\mathrm{BP}}^{(\Psi^{00})}(\mathrm{meV}) = \langle \Psi^{00} | H_{BP}^{0} | \Psi^{00} \rangle \approx \begin{bmatrix} -8.08 & 0. & 0 & 0 \\ 0 & -8.08 & 0 & 0 \\ 0 & 0 & 44.2 & 0 \\ 0 & 0 & 0 & 44.2 \end{bmatrix}, \tag{2.55}$$

The contribution of the strain on the HH-LH splitting is ~ 52 meV and thus further splits them apart on top of the confinement splitting. Here, we assumed to have isotropic biaxial strain, therefore no off-diagonal elements arise. However, mismatch in the biaxial strain can potentially be quite significant as a function of space due to the strain-relaxed buffer that imprints a misfit dislocation network along the [110] and [1$\bar{1}$0] crystal direction.

We can evaluate the Zeeman Hamiltonian for a magnetic field along $\hat{x}$ and $\hat{z}$. We use a magnetic field of $B_0 = 100\,\mathrm{mT}$ along $\hat{x}$ and $\hat{z}$ respectively. Projecting the ground state on the Zeeman Hamiltonian $H_{\mathrm{z}}^{(\Psi^{00})} = \langle \Psi^{00} | H_{\mathrm{z}}^{0} | \Psi^{00} \rangle$ we obtain:

$$H_{\mathrm{z}}^{(\Psi^{00})}(\vec{B} = B_0 \hat{z})(\mathrm{meV}) = \begin{bmatrix} -0.062 & 0 & 0 & 0 \\ 0 & 0.062 & 0 & 0 \\ 0 & 0 & -0.020 & 0 \\ 0 & 0 & 0 & 0.020 \end{bmatrix}, \tag{2.56}$$

$$H_{\mathrm{z}}^{(\Psi^{00})}(\vec{B} = B_0 \hat{x})(\mathrm{meV}) = \begin{bmatrix} 0 & 0.001 & -0.035 & 0 \\ -0.001 & 0 & 0 & -0.035 \\ -0.035 & 0 & 0 & -0.041 \\ 0 & -0.035 & -0.041 & 0 \end{bmatrix}, \tag{2.57}$$

From diagonalising $H_{LK} + H_{BP}$ we can get the HH eigenvectors

$$\Psi_{\mathrm{HH}} \approx \begin{pmatrix} 1.0000 & 0 \\ 0 & 1.0000 \\ 0 & 0.0005 \\ 0.0005 & 0 \end{pmatrix}, \tag{2.58}$$

which have been rounded here to the fifth digit.

Projecting the Zeeman Hamiltonian for a B-field along the x, y and z direction on the HH subspace and expressing it in terms of Pauli matrices, we can thus extract the g-tensor:

$$\mathbf{G}_{\mathrm{numerical}} = \begin{pmatrix} 0.192 & 0 & 0 \\ 0 & -0.168 & 0 \\ 0 & 0 & 21.27 \end{pmatrix}$$

Since we assumed isotropic biaxial strain and only introduced an asymmetry between the x and y-confinement, we obtain a g-tensor without any off-diagonal terms. The principal g-factors are all quite similar to the pure HH g-factors, only deviating from it by the small difference in x- and y-confinement.

We can also compare this result, to the one of the analytical formulas. Plugging in the same values yields

$$\mathbf{G}_{\text{analytical}} = \begin{pmatrix} 0.094 & 0 & 0 \\ 0 & -0.156 & 0 \\ 0 & 0 & 16.09 \end{pmatrix}.$$

We can see that the analytical result differs substantially from the naive result one would obtain when only considering the ground state. Indeed, we have seen before that the analytical equations contain correction terms due to the mixing of the ground HH state to excited LH states. We can estimate these correction terms using the known matrix elements of the coupling between ground and higher orbitals states in the infinite well potential [40].

$$\langle n|z|m\rangle = \begin{cases} -\frac{8L_z}{\pi^2}\frac{nm}{(n^2-m^2)^2} & n+m \text{ odd}, \\ 0 & n+m \text{ even}(n \neq m), \\ L_z/2 & n=k, \end{cases} \tag{2.59}$$

$$\langle n|k_z|m\rangle = \begin{cases} \frac{4}{iL_z}\frac{nm}{n^2-m^2} & n+m \text{ odd}, \\ 0 & n+m \text{ even}(n \neq m), \end{cases} \tag{2.60}$$

$$\langle n|k_z z|m\rangle = \sum_l \langle n|k_z|l\rangle\,\langle l|z|m\rangle, \qquad \langle n|z k_z|m\rangle = \sum_l \langle n|z|l\rangle\,\langle l|k_z|m\rangle. \tag{2.61}$$

The correction terms (given in Ref. [31]) then become:

$$\gamma_h = \frac{6\gamma_3^2\hbar}{m_0}\sum_l \frac{\langle HH_0|k_z|LH_l\rangle^2}{E_{LH,l}-E_{HH,0}} \approx 2.234 \tag{2.62}$$

$$\eta_h = -\Delta_{\text{LH}}\sum_l \frac{2i\,\text{Im}\left(\langle HH_0|z|LH_l\rangle\,\langle LH_l|k_z|HH_0\rangle\right)}{E_{LH,l}-E_{HH,0}} \approx -0.377 \tag{2.63}$$

$$\tilde{\eta}_h = \Delta_{\text{LH}}\sum_l \frac{\text{Im}\left(\langle HH_0|k_z z + z k_z|LH_l\rangle\,\langle LH_l|HH_0\rangle\right)}{E_{LH,l}-E_{HH,0}} \approx 0 \tag{2.64}$$

Both γ_h and η_h saturate quickly after taking two excited LH states into account. Note that Ref. [41] shows that for a more realistic potential the higher LH states contribute significantly, since they start to leak out of the quantum well and further reduce the out-of-plane principal g-tensor component. As a first approximation, we can use the analytical equations to compute the expected correction coming from γ_h and η_h on our numerical result, which only took into account the HH and LH ground states.

$$\mathbf{G}_{\text{numerical, corrected}} = \begin{pmatrix} 0.102 & 0 & 0 \\ 0 & -0.16 & 0 \\ 0 & 0 & 16.801 \end{pmatrix}$$

Including the correction for the excited LH states coming from our infinite well approximation, we finally get principal g-factor components that are very close to the analytical ones.

2.7.3. LARMOR VECTOR AND SPIN QUANTISATION AXIS

Now that we have a basic understanding, where the g-tensor is coming from, we can move further to look on the implications that the g-tensor has on the spin qubit operation and dynamics. We can re-write Equation 2.40 as [33]

$$H = \frac{\hbar}{2}\mathbf{\Omega}_L \cdot \sigma, \tag{2.65}$$

with the Larmor vector $\mathbf{\Omega}_L$ and spin quantisation axis $\hat{n}_{\text{spin}}$ defined as

$$\mathbf{\Omega}_L = \frac{\mu_B}{\hbar}\mathbf{GB} = \omega_L \cdot \hat{n}_{\text{spin}}, \qquad \hat{n}_{\text{spin}} = \frac{\mathbf{GB}}{|\mathbf{GB}|}. \tag{2.66}$$

The Larmor vector specifies the natural alignment of the spin, represented by the spin quantisation axis $\hat{n}_{\text{spin}}$, as well as the amplitude of the Zeeman splitting, represented by the corresponding Larmor frequency. Figure 2.5b visualises the Larmor vector, using the angles $\theta_{\hat{n}_{\text{spin}}}$ and $\phi_{\hat{n}_{\text{spin}}}$ to describe its direction. The Larmor vector depends on the magnetic field orientation. Using the analytical g-tensor expressions, Figure 2.5c shows the effective g-factor and the two angles of the spin quantisation axis as functions of the magnetic field direction. The g-factor increases rapidly for out-of-plane fields due to the strong g-tensor anisotropy. The spin quantisation axis rotates nearly uniformly for in-plane magnetic fields, depending on additional in-plane anisotropies in confinement, and tilts abruptly out of plane once the magnetic field deviates from the in-plane direction.

We can also examine the difference between two Larmor vectors that correspond to distinct confinement conditions, as shown in Figure 2.5d. Figure 2.5e displays the resulting change in the g-factor and the angle between the two quantisation axes when the x-y confinement is interchanged between the two Larmor vectors. Since the principal axes remain unchanged, the maximum variation in the g-factor occurs when the magnetic field aligns with one of these axes. This variation is largest for in-plane fields and decreases as the field approaches the out-of-plane direction. The angle between the two quantisation axes is minimal when the magnetic field is aligned with a principal axis and is maximised for in-plane orientations between these axes. For out-of-plane magnetic fields both spins align along z, which causes the difference between the quantisation axes to vanish.

Now that we have seen that g-factor and quantisation axes can differ between different spin qubits, we can estimate using the analytical expressions what kind of variability we can expect. Figure 2.6 shows the variability of the g-factor and the difference in quantisation axis for different configurations including varying confinement and strain. Depending on the dominant contribution we can expect sharp or washed-out in-plane features. But generally, we can only see large differences in g-factor and quantisation axis for angles close to in-plane. Already a couple of degree out-of-plane removes all patterns since it aligns all quantisation axes along z and normalises the g-factors. This should be kept in mind when considering the desired operation regime.

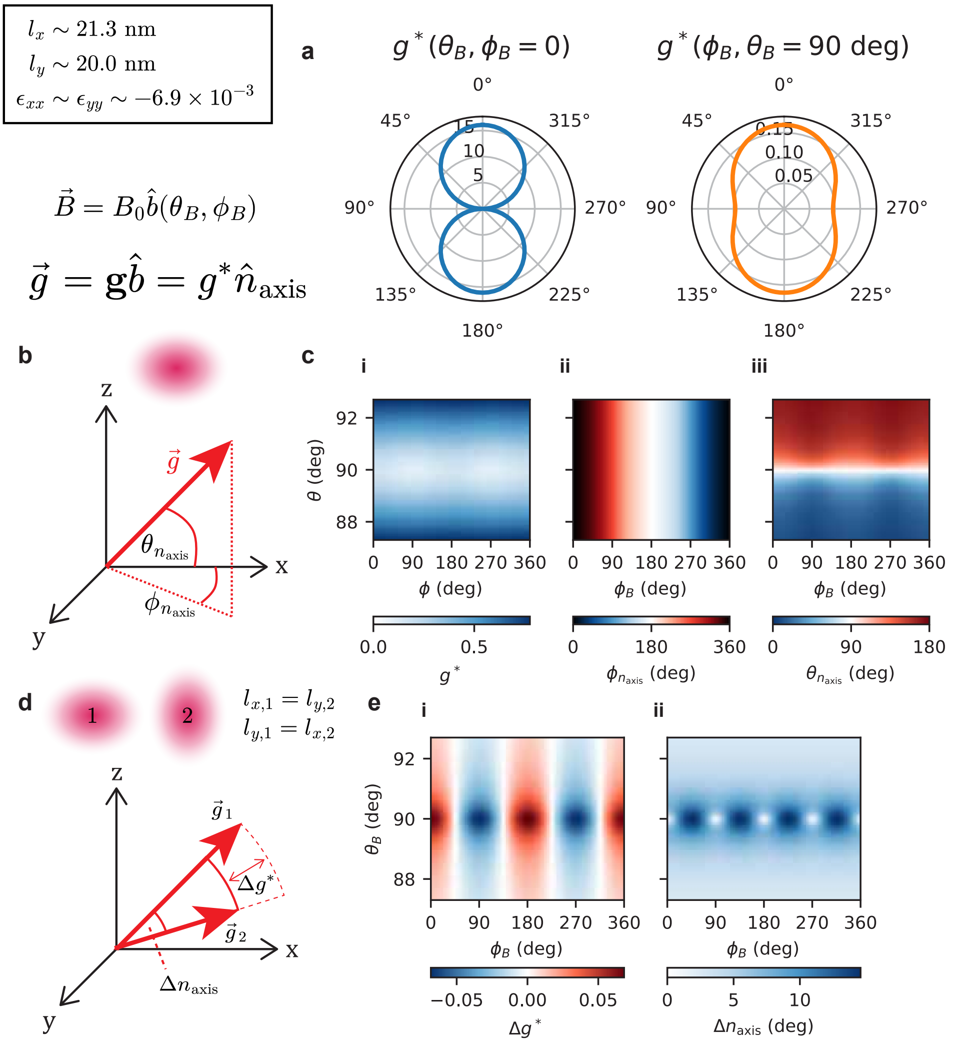

Figure 2.5: **Larmor vector** for a confined spin in a Ge/SiGe quantum well for a slightly elongated dot and matched biaxial strain **a.** g-factor as a function of magnetic field direction, **b.** Visualisation of the g-vector characterised by the magnitude g^* and the two angles $\phi_{n_{\mathrm{axis}}}$ and $\theta_{n_{\mathrm{axis}}}$, which are plotted as a function of the magnetic field direction in **c**. **d.** g-vector mismatch between two different g-vectors characterised by the difference in magnitude Δg^* and the angle difference Δn_{axis}, which is plotted in **e.** for two oppositely elongated quantum dots.

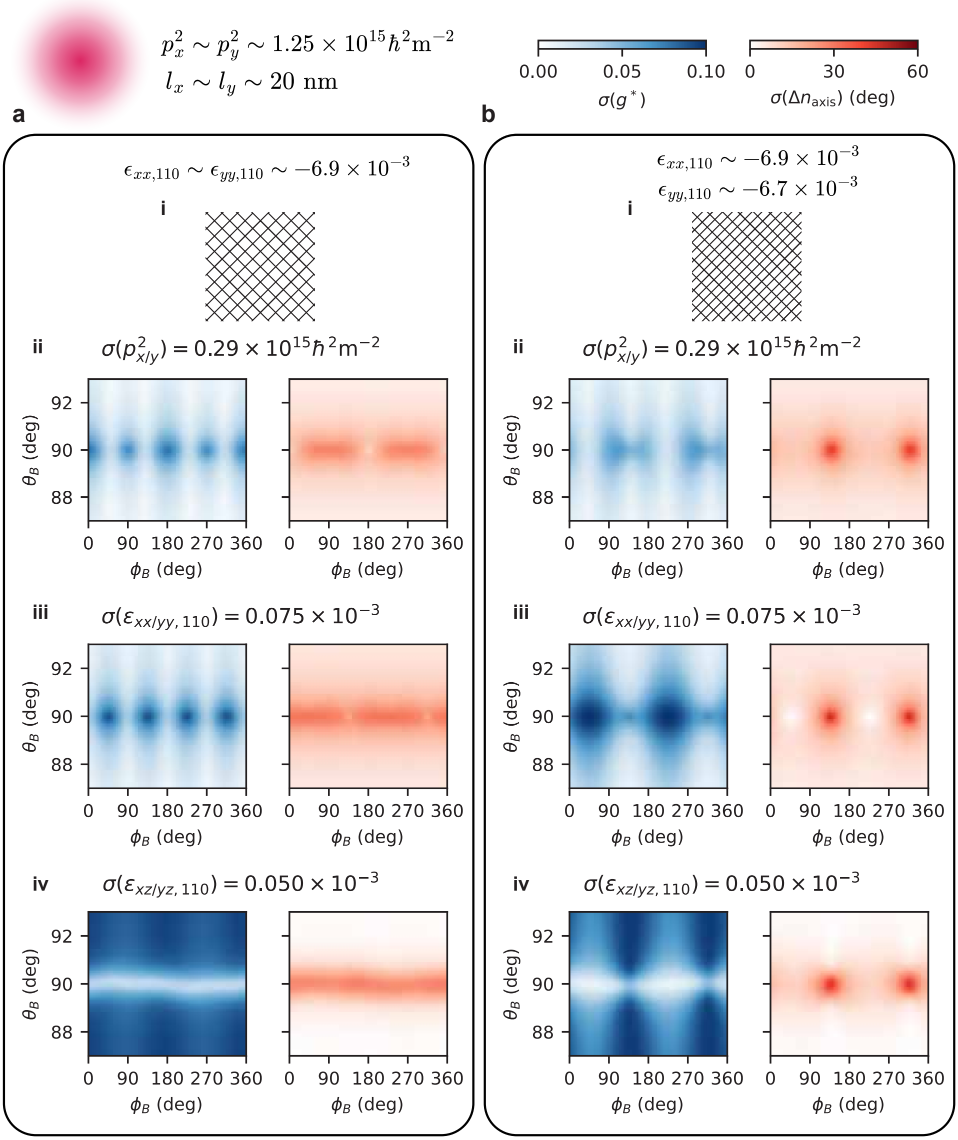

Figure 2.6: **Variability of the g-factor and quantisation axis** for an isotropic harmonic wavefunction assuming an isolated variability of one parameter per plot. We assume the variability to be normally distributed with standard deviation σ, which is chosen such that all plots return similar magnitude. **a.** Variability for matched biaxial strain for variability of **(ii)** $p^2_{x/y}$, **(iii)** $\epsilon_{xx/yy,110}$, and **(iv)** $\epsilon_{xz/yz,110}$. **b.** Same as **a.** but for mismatched biaxial strain.

2.7.4. Electric dipole spin resonance

Electric dipole spin resonance is a general framework describing the electric excitation of a spin via the spin-orbit interaction [42]. In quantum dots, two commonly used descriptions of EDSR can be distinguished. The first is g-tensor modulation resonance (GTMR), which relies on a time-dependent modulation of the Larmor vector [33], and has been used to investigate EDSR in systems with g-tensor anisotropy [36, 37, 39, 43–45]. The second one is iso-Zeeman EDSR, which is based on the effective magnetic field experienced by a spin as it moves through the spin-orbit field [46]. The latter framework allows the extraction of an effective spin-orbit length. In bulk and two-dimensional systems, the spin-orbit length denotes the distance over which an unconfined spin undergoes a π rotation due to the spin-orbit field [47]. Although this picture breaks down in zero-dimensional systems, it remains a useful effective metric for comparing spin-orbit strengths across different platforms [48–52]. Attempts have been made to unify these two contributions within a single theoretical framework by relating EDSR to gate-induced modulation of the g-tensor [53, 54]. Owing to its close connection to the original GTMR formulation, we refer to this unified approach as the generalised g-tensor modulation resonance, which has been shown to describe well the spin qubit dynamics in planar Ge/SiGe heterostructures [39].

Generalised g-tensor modulation resonance

In the previous chapters we analysed in detail how the confinement potential affects the g-tensor. Since the confinement can be modulated with electrical pulses, it becomes possible to modulate the g-tensor and therefore the Larmor vector by applying an oscillating electric field to a gate electrode. We can decompose this modulation of the Larmor vector into a longitudinal component $\mathbf{\Omega}_{L,\parallel}$ and an orthogonal component $\mathbf{\Omega}_{L,\perp}$. In particular, the modulation of $\mathbf{\Omega}_{L,\perp}$ can drive spin flips because it acts orthogonally to the spin quantisation axis. As a result, the Rabi frequency that quantifies the rotation strength can be written as [54]

$$f_{\text{Rabi}} = \frac{1}{2\pi}\left|\frac{d\mathbf{\Omega}_{L,\perp}}{dV}\right| V_{\text{ac}} = \frac{\mu_B B V_{\text{ac}}}{2hg^*}\left\|\left[(\mathbf{G}\mathbf{b})\times\left(\frac{d\mathbf{G}}{dV}\mathbf{b}\right)\right]\right\|. \tag{2.67}$$

We can again consider a numerical example using the analytical g-tensor formulas. Assuming isotropic confinement, we simulate the modulation of different g-tensor components. In Figure 2.7a we use isotropic biaxial strain and modulate the in-plane confinement in (ii). From the resulting g-tensor derivatives we evaluate Equation 2.67 to obtain the Rabi frequency as a function of magnetic field direction. The same procedure applies to modulating the off diagonal components in (iii) and (iv). The drive amplitudes are adjusted to yield comparable effective driving strengths and are not intended to be realistic. The purpose is to illustrate how different driving mechanisms depend on the magnetic field orientation. For GTMR at a fixed Larmor frequency operation close to in-plane is essential. At the same time the approach to the in-plane configuration increases the diversity of patterns across the driving mechanisms, which complicates the identification of an optimal operating point. Additional anisotropies such as mismatched biaxial strain (Figure 2.7b) alter the maps further. In general, isotropic modulation of the in-plane confinement is far less effective than modulating the off diagonal g-tensor

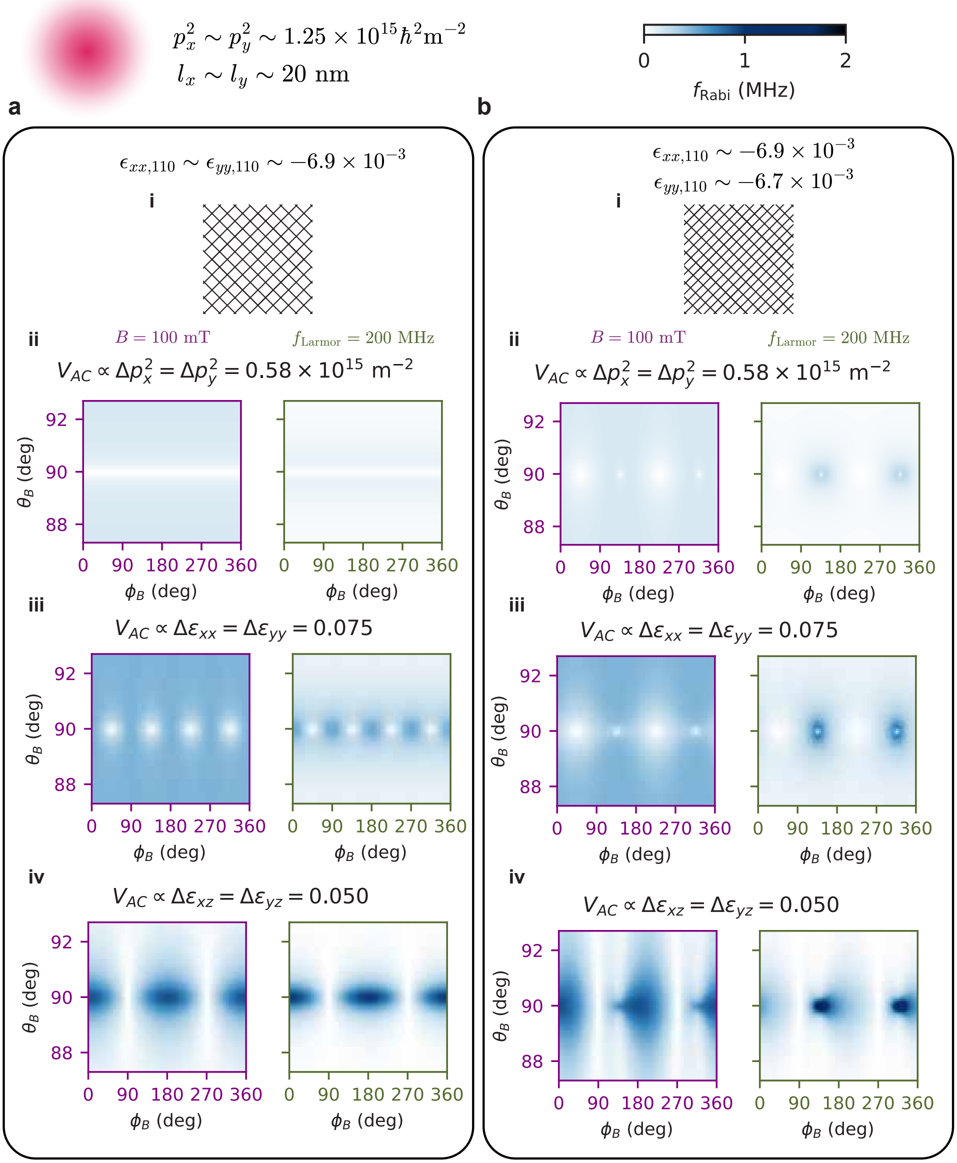

Figure 2.7: **Rabi frequency** for an isotropic harmonic wavefunction assuming an isolated modulation of one parameter per plot. We choose the modulation amplitude such that all plots return similar magnitude. **a.** Rabi frequency for matched biaxial strain for modulation of **(ii)** $p^2_{x/y}$, **(iii)** $\epsilon_{xx/yy,110}$, and **(iv)** $\epsilon_{xz/yz,110}$. **b.** Same as **a.** but for mismatched biaxial strain.

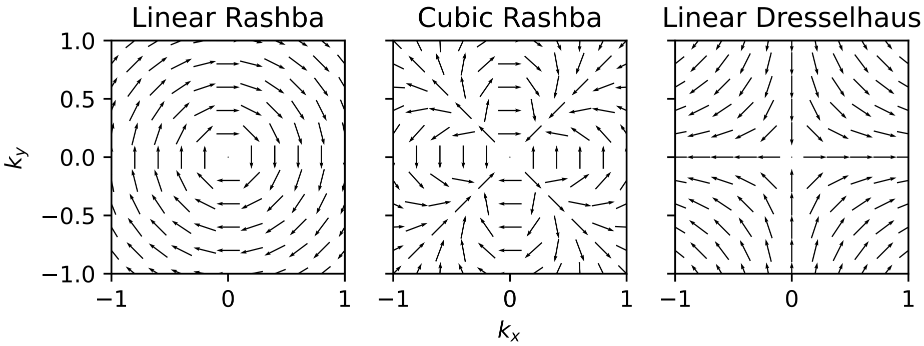

Figure 2.8: **Typical spin-obit fields** characterised by their varying degree of symmetry. The winding direction is determined by the sign of the Rashba and Dresselhaus coefficient. Real-world materials can have an admixture of all these SO fields.

components, for example through displacement in an inhomogeneous strain field. This is why the drive amplitude for the in-plane modulation must be chosen unrealistically high in this example.

2.7.5. RASHBA AND DRESSELHAUS SPIN-ORBIT TERMS

Symmetry and symmetry breaking generate distinct spin-orbit interactions, each associated with a characteristic spin-orbit field. This field is the effective magnetic field experienced by a spin moving along a given direction. Three relevant types are shown in Figure 2.8. First, Rashba spin-orbit interaction originates from structural inversion asymmetry, for example an electric field along z. The linear Rashba term has radial symmetry in the (k_x, k_y) plane, with the spin-orbit vector lying in-plane and orthogonal to the direction of motion, as shown in Figure 2.8a. A loop around the origin in momentum space causes the spin-orbit field to rotate once. The cubic Rashba term is anisotropic: it has an in-plane orthogonal component along the k_x and k_y axes and becomes parallel in between, rotating three times when traversing such a loop, see Figure 2.8b. Depending on the wavefunction geometry either contribution can dominate. In one dimensional confinement the linear term can be strongest, while in zero dimensional confinement the cubic term usually dominates [52]. Second, Dresselhaus spin-orbit interaction typically arises from bulk inversion asymmetry, present in III-V and II-VI compound semiconductors due to the two atom basis. The linear Dresselhaus field is anisotropic: it is parallel along the k_x and k_y axes and orthogonal in between, but it rotates only once when encircling the origin, see Figure 2.8c. Because Ge/SiGe heterostructures lack true bulk inversion asymmetry, Rashba SOI was long assumed to dominate [12]. Recent experiments in Ge/SiGe quantum dots, however, indicate that Dresselhaus SOI may be the leading term [55]. Numerical simulations likewise show that a sharp Ge/SiGe interface can generate a strong Dresselhaus contribution [56]. This contribution is highly sensitive to interface sharpness and is rapidly suppressed by interdiffusion.

Our previous considerations and numerical calculations only considered atomic spin-orbit contributions which are intrinsically represented within the LK Hamiltonian. However, there are additional extrinsic spin-orbit contributions that can emerge when breaking the crystal symmetry. These can be manually added to Equation 2.14 as part of the term H^0_{SO}. In Ref. [56] they find through numerical simulation that the contribution of the linear Rashba and Dresselhaus terms are minor for describing the single-hole dynamics for magnetic fields in-plane. Instead the GTMR formalism from the LKBP Hamiltonian is largely dominant for electric dipole spin resonance. The additional Rashba and Dresselhaus contributions only slightly shift the sweet and hot spot operation points around the in-plane angle. For magnetic fields out-of-plane the relative contribution of the Rashba and Dresselhaus terms increase, and become critical when describing the spin dynamics.

2.7.6. SPIN IN DOUBLE DOTS

Up to now, we have evaluated the single-particle Hamiltonian for a single quantum dot, which can be accurately described by its effective g-tensor. The g-tensor determines the local spin quantisation axis, which can vary across a quantum-dot array.

It may be tempting to describe a multi-dot system (for instance, two dots denoted $|L\rangle$ and $|R\rangle$) using only the projected 2×2 effective Hamiltonian of each dot. However, the mixing terms that arise from inter-band coupling within an individual dot, which are responsible for the local g-tensor and quantisation-axis variations, are not equivalent to the couplings originating from the spatial overlap of neighbouring orbitals [57]. Therefore, the full Hamiltonian must be evaluated in the extended double-dot subspace, as this can generate additional spin-orbit-induced, spin-flip tunnelling matrix elements [58]. It is also good to keep in mind that depending on the dominant type of SOI, the axis along which the quantum dots are arranged may matter due to the different symmetries of the spin-orbit fields [12, 55].

When a spin is transferred diabatically between dots (while remaining adiabatic with respect to charge), two distinct mechanisms can lead to spin rotation. The first is the difference in local quantisation axes, which results in a frame-induced spin rotation [59] and a geometric (Berry) phase if shuttling in a closed loop [60]. The second is the genuine spin-flip tunnelling term, which arises from spin-orbit coupling irrespective of the local bases [58].

In contrast to holes in silicon, the spin-flip tunnelling term in germanium is expected to be comparatively small due to the large HH-LH splitting, with an estimated ratio of $|\vec{t}_{SO}|/t_c \approx 10^{-5}$ [61]. We therefore neglect it in our conceptual description of the double-dot system. However, spin-orbit effects can still play an important role, as they renormalise the effective g-factor when tunnel coupling exceeds the Zeeman splitting. Consequently, spin-orbit interactions may still influence initialisation, readout, and hopping processes [61].

From microscopic models, it is possible to extract a spin-orbit tunnelling vector [58]

$$\vec{t}_{SO} = \begin{pmatrix} t_x & t_y & t_z \end{pmatrix} = t_{\mathrm{SO}}\hat{n}_{\mathrm{SO}}, \tag{2.68}$$

where $\hat{n}_{\mathrm{SO}}$ is the direction of the spin-orbit field around which the spin flips, and t_{SO} is the corresponding magnitude. For planar confinement, the spin-orbit field typically lies in-plane [12], so we can set $t_z \approx 0$ and neglect the t_z term from now on.

We can then define the off-diagonal tunnelling block T of the single-particle Hamiltonian H_t in the basis $\{|L\uparrow\rangle, |L\downarrow\rangle, |R\uparrow\rangle, |R\downarrow\rangle\}$ [62],

$$H_t = \begin{pmatrix} 0 & T \\ T^\dagger & 0 \end{pmatrix}, \qquad T = t_c\mathbb{I} + i\vec{t}_{SO}\cdot\vec{\sigma} \approx t_c\mathbb{I} + i t_x\sigma_x + i t_y\sigma_y,$$

where t_c represents spin-conserving tunnelling, and t_x, t_y are spin-flip components.

In addition to spin-orbit effects, there may be a difference in the local spin quantisation axes between the two dots. We denote the angle between the axes by Δn_{axis} and choose it as a rotation about the y-axis. The rotation of the right-dot spin into the left-dot basis is

$$R(\Delta n_{\text{axis}}) = \cos\frac{\Delta n_{\text{axis}}}{2}\mathbb{1}_{2\times 2} - i\sin\frac{\Delta n_{\text{axis}}}{2}\sigma_y.$$

The single-particle tunnelling matrix in the common (left-dot) basis is then

$$T' = TR(\Delta n_{\text{axis}}) = t'_c\mathbb{1}_{2\times 2} + i t'_x\sigma_x + i t'_y\sigma_y + i t'_z\sigma_z,$$

with

$$t'_c(\Delta n_{\text{axis}}) = t_c\cos\frac{\Delta n_{\text{axis}}}{2} - i t_y\sin\frac{\Delta n_{\text{axis}}}{2}, \tag{2.69}$$

$$t'_x(\Delta n_{\text{axis}}) = t_x\cos\frac{\Delta n_{\text{axis}}}{2}, \tag{2.70}$$

$$t'_y(\Delta n_{\text{axis}}) = -i t_c\sin\frac{\Delta n_{\text{axis}}}{2} + t_y\cos\frac{\Delta n_{\text{axis}}}{2}, \tag{2.71}$$

$$t'_z(\Delta n_{\text{axis}}) = t_x\sin\frac{\Delta n_{\text{axis}}}{2}. \tag{2.72}$$

There are two interesting findings in these equations of the effective tunnelling matrix elements. Firstly, even if all spin-orbit tunnelling matrix elements are zero, we can have an effective spin flip element coming from the difference in the quantisation axis. Secondly, we obtain a finite t'_z component if $t_x \neq 0$. This means that unlike predicted from purely in-plane SOI fields, there can be an effective out-of-plane tunnelling term, resulting from the difference in quantisation axis.

To construct the two-spin Hamiltonian, we project the single-particle tunnelling into the two-spin singlet-triplet basis [58, 63]. Using the eigenstates

$$\left\{S(2,0),\quad S(0,2),\quad \downarrow\uparrow,\quad \uparrow\downarrow,\quad \uparrow\uparrow,\quad \downarrow\downarrow\right\}$$

and the effective tunnelling elements (Equation 2.69-2.72), the Hamiltonian becomes

$$H_{2Q,\text{local}} = \begin{pmatrix} U_c+\epsilon & 0 & t'_c - i t'_z & -t'_c - i t'_z & -t'_y + i t'_x & -t'_y - i t'_x \\ 0 & U_c-\epsilon & t'_c - i t'_z & -t'_c - i t'_z & -t'_y + i t'_x & -t'_y - i t'_x \\ t'_c + i t'_z & t'_c + i t'_z & E_{Z-} & 0 & 0 & 0 \\ -t'_c + i t'_z & -t'_c + i t'_z & 0 & -E_{Z-} & 0 & 0 \\ -t'_y - i t'_x & -t'_y - i t'_x & 0 & 0 & E_{Z+} & 0 \\ -t'_y + i t'_x & -t'_y + i t'_x & 0 & 0 & 0 & -E_{Z+} \end{pmatrix}.$$

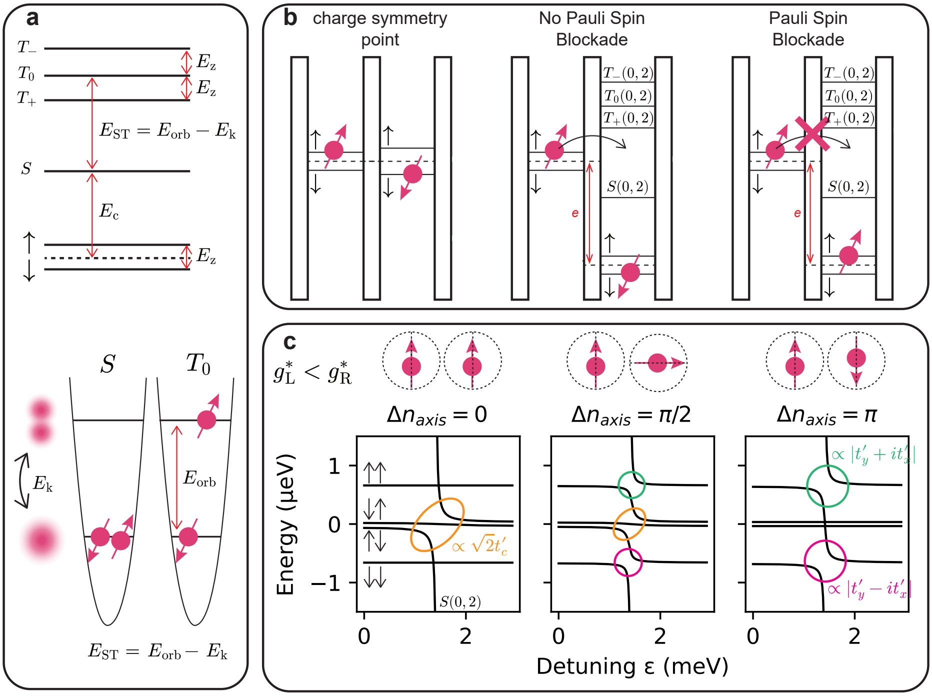

Figure 2.9: **Energy diagrams for the single and double quantum dot, a.** Energy levels of a single quantum dot. The singlet-triplet energy spacing is determined by the orbital splitting E_orb and the single quantum dot exchange energy E_k that arises from occupying a different orbital wavefunction. **b.** Simplified representation of the operation and read-out point, where spin-to-charge conversion via Pauli spin blockade is performed. **c.** Double dot energy diagram for mismatched g-factors, and three distinct cases for the quantisation axis mismatch: aligned, orthogonal and anti-aligned.

with $E_{Z+} = (g_L + g_R)\mu B$ and $E_{Z-} = (g_R - g_L)\mu B$.

The Hamiltonian has been evaluated numerically for $t_c = 1\,\mathrm{GHz}$, $t_\mathrm{SO} = 0$, and several quantisation axis differences, see Figure 2.9c. The results show that the charge and spin-orbit anticrossings can invert depending on the relative quantisation axes. For most magnetic field angles the axes are nearly aligned, which leads to a negligible spin-orbit anticrossing. For in-plane fields, however, there can be field directions that produce substantial misalignment of the quantisation axes, which in turn modifies the anticrossings in the singlet-triplet spectrum.

INITIALISATION

One of the DiVincenzo criteria requires the ability to initialise a well defined fiducial state [8]. For spin qubits this is achieved by moving along the detuning axis ϵ of the energy diagram of the double quantum dot [64]. As shown in Figure 2.9c, sufficiently strong detuning makes the singlet $S(0,2)$ the ground state. If the tunnel coupling is large and the detuning deep enough, all singlet and triplet $(1,1)$ states relax rapidly into $S(0,2)$. The detuning can then be pulsed back to the charge symmetry point at $\epsilon = 0$. The required ramp times depend on the sizes of the relevant anticrossings, which are set by the tunnel coupling and by the mismatch of the quantisation axes [58, 65]. In principle one either maximises the spin-orbit anticrossing by increasing the relative angle of the quantisation axes and preparing the system adiabatically in $\Downarrow$, or suppresses the spin-orbit anticrossing entirely and ramps adiabatically into $\uparrow\downarrow$. If the spin-orbit anticrossing remains sizable a non-uniform ramp may be needed, starting fast to cross the first anticrossing diabatically and then slowing down to remain adiabatic with respect to the $\mathrm{S}(0,2)$-$\mathrm{T}_0(1,1)$ anticrossing.

READ-OUT

For read out we need to determine the spin state of a specific spin qubit. Direct detection of the magnetic moment is impractical, so the spin state is mapped onto a charge configuration [47, 66]. A nearby single hole transistor (SHT) can then sense this charge state through shifts of the Coulomb peaks [25].

Spin to charge conversion relies on Pauli spin blockade (PSB) [67]. A simplified picture is shown in Figure 2.9a and b. Each quantum dot has an energy level structure in which the singlet is separated from the single spin level by the charging energy E_c. The singlet-triplet splitting is set by the orbital level spacing and by the intradot exchange energy E_k. The exchange energy reflects the reduced Coulomb repulsion for the triplet, since the two spins occupy different orbitals. The ordering of these states is illustrated in Figure 2.9a. At the charge symmetry point the single spin levels of the two dots align. By detuning the levels one can reach the PSB configuration, where the single spin level of one dot lies between the S(0,2) and the (0,2) triplet states. Depending on the spin configuration, tunnelling to form S(0,2) is either allowed or forbidden [68].

Spin-orbit coupling in germanium complicates this picture because the spin can rotate during tunnelling [58]. It is therefore necessary to consider the detuning dependent spectrum shown in Figure 2.9c, where the mapping of $\Downarrow$ or $\uparrow\downarrow$ to S(0,2) depends on the relative quantisation axes. The same considerations as for initialisation apply. The required ramp profile is set by the sizes of the anticrossings, and may need to be adiabatic, diabatic, or a combination of both. A larger tunnel coupling supports adiabaticity but also increases charge hybridisation, which in turn reduces the charge contrast between the (1,1) and (0,2) states sensed by the SHT. A more detailed analysis on the impact of different quantisation axes on read-out can be found in Ref. [65].

TWO-QUBIT GATES

In the previous section we introduced the intradot. In addition to this contribution there is an interdot exchange energy J [57], defined analogously but using the energies of the $S(1,1)$and $T_0(1,1)$ states. In the simple case where the quantisation axes are aligned and spin flip tunnelling is negligible, J can be read off directly from the energy difference between the $\widetilde{\uparrow\downarrow}$ and $\widetilde{\downarrow\uparrow}$ states [57, 69]. The tilde indicates that these states are not necessarily exact eigenstates. If these conditions are not satisfied, extracting J from the diagrams in Figure 2.9c becomes more involved [70]. Here, we define it as the conditional energy splitting

$$J = \left|(E_{\widetilde{\uparrow\uparrow}} - E_{\widetilde{\downarrow\uparrow}}) - (E_{\widetilde{\uparrow\downarrow}} - E_{\widetilde{\downarrow\downarrow}})\right|, \tag{2.73}$$

which depends on both the detuning ϵ and the tunnel coupling t_c, and is a common way to extract it from experiment [64, 71–73]. The interdot exchange energy becomes

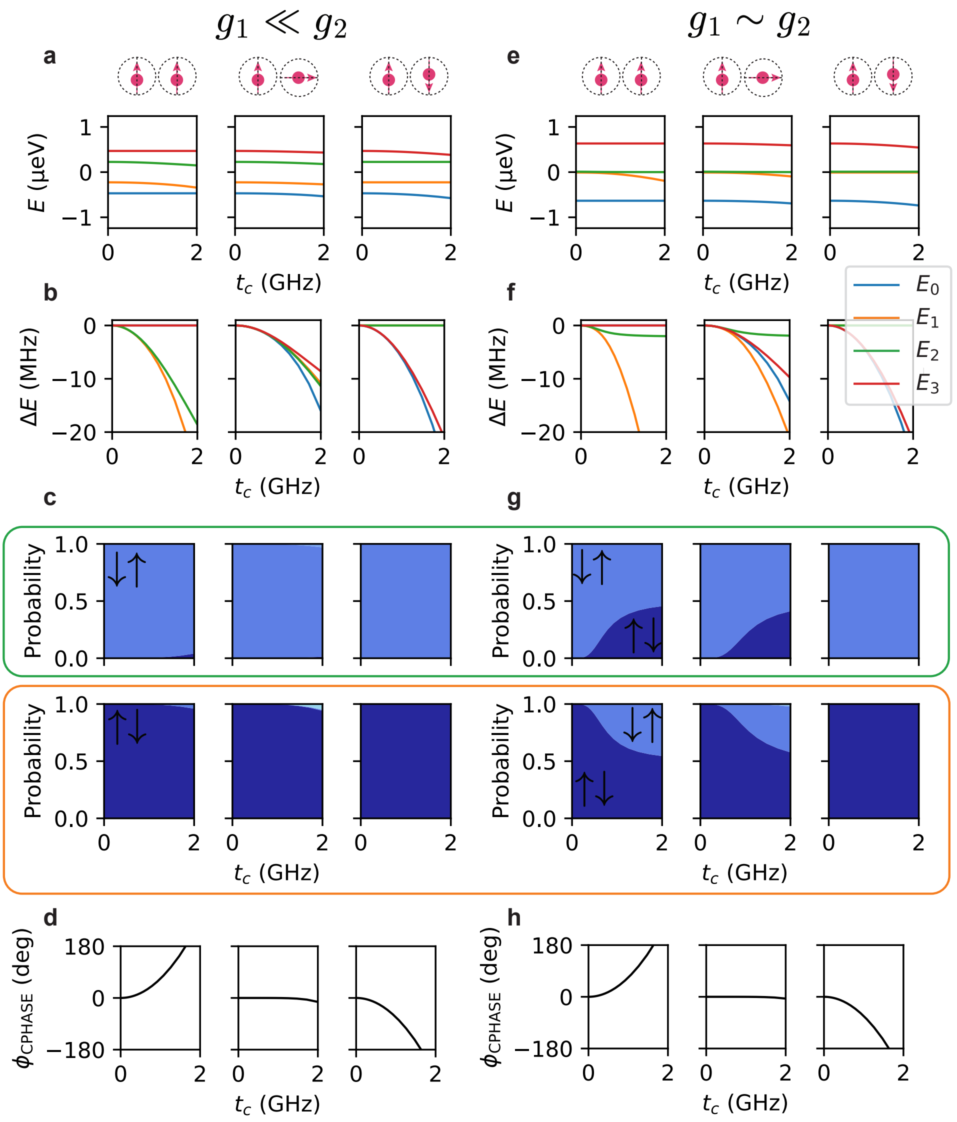

Figure 2.10: **Two-qubit gates, a.** Energy diagram at the charge symmetry point as a function of the tunnel coupling t_c for different quantisation axis mismatch and a significant g-factor mismatch ($g_1 = 0.07, g_2 = 0.20$). **b.** Energy difference of all states when pulsing from $t_c = 0$ to a finite t_c. **c.** Eigenstates of ↓↑ and ↑↓ as a function of the tunnel coupling. Dark-blue refers to ↑↓, mid-blue to ↓↑, and light-blue to ↓↓. **d.** Accumulated phase at $t_c = 1$ GHz during 100 ns. **e.-h.** show the same as **a.-d.** but for almost identical g-factors ($g_1 = 0.180, g_2 = 0.185$).

anisotropic with respect to the magnetic field because the field direction controls the relative spin quantisation axes. Any sizeable spin-orbit tunnelling component enhances this anisotropy, since it shifts the $S(0,2)-\downarrow\downarrow$ and $S(0,2)-\uparrow\uparrow$ anticrossings in opposite directions. Before discussing two qubit gate schemes, it is necessary to distinguish the $S(1,1)-T_0(1,1)$ basis from the $\uparrow\downarrow-\downarrow\uparrow$ basis at the charge symmetry point. In an isolated double dot the latter form the natural eigenstates. Once the tunnel coupling is switched on they compete with the singlet-triplet manifold. The dominant factor determining the outcome is the g-factor difference between the two dots. A g-factor mismatch skews the singlet-triplet mixing and suppresses the formation of pure singlet-triplet eigenstates. Reaching the true singlet-triplet regime then requires very large tunnel couplings, often beyond what is experimentally feasible. If the g-factor mismatch is large enough the $\uparrow\downarrow$ and $\downarrow\uparrow$ states remain good eigenstates for practical tunnel couplings. This behaviour is visible in Figure 2.10c and g, where singlet-triplet formation is strongly delayed for mismatched g-factors, while for nearly identical g-factors it emerges at $t_c \approx 2\,\mathrm{GHz}$. Two baseband approaches exist for implementing a two qubit gate. The first relies on pulsing any control parameter that distorts the energy spectrum in a non-uniform way. Figure 2.10a and e show the eigenenergies for g-factor and quantisation axis mismatch. If the eigenstate changes along the pulse trajectory, the ramp must be slow to stay adiabatic. This becomes increasingly important the smaller the g-factor difference. Suitable control parameters are the detuning ϵ or the tunnel coupling t_c. Each eigenstate i accumulates a dynamical phase [74]

$$\phi_i = \Delta E_i(t) \cdot t_{\mathrm{ramp,wait,ramp}}/\hbar, \tag{2.74}$$

where $\Delta E_i(t)$ is the energy difference with respect to $E_i(t=0)$, which is plotted in Figure 2.10b and f. These phase pick-ups in the two-qubit space can be used to calibrate a two-qubit phase gate with the state evolution following the unitary

$$U_{\mathrm{phase}} = \begin{pmatrix} e^{-i\phi_0} & 0 & 0 & 0 \\ 0 & e^{-i\phi_1} & 0 & 0 \\ 0 & 0 & e^{-i\phi_2} & 0 \\ 0 & 0 & 0 & e^{-i\phi_3} \end{pmatrix}. \tag{2.75}$$

By picking the phase of $|00\rangle$ for reference, and factoring out the single-qubit phases, the unitary can be decomposed into

$$U_{\mathrm{phase}} = \left(\begin{pmatrix} 1 & 0 \\ 0 & e^{-i\Delta\phi_{02}} \end{pmatrix} \otimes \begin{pmatrix} 1 & 0 \\ 0 & e^{-i\Delta\phi_{01}} \end{pmatrix} \right) \begin{pmatrix} 1 & 0 & 0 & 0 \\ 0 & 1 & 0 & 0 \\ 0 & 0 & 1 & 0 \\ 0 & 0 & 0 & e^{-i(\Delta\phi_{03}-\Delta\phi_{02}-\Delta\phi_{01})} \end{pmatrix}, \tag{2.76}$$

which is a controlled phase operation and contains the accumulated phase differences $\Delta\phi_{0i} = \phi_i - \phi_0$. Figure 2.10d and h show the accumulated two qubit phase after a wait time of 100 ns. For orthogonal axes the phase is strongly reduced because all levels bend downward and the relevant energy differences shrink. The CPHASE gate is effective when the neighbouring g-factors are sufficiently different [74]. In that regime the $\uparrow\downarrow$ and $\downarrow\uparrow$ states remain the eigenstates throughout the pulse, and fast ramps are possible. When the g-factors are too similar the states acquire singlet-triplet character and slow ramps are required to maintain adiabaticity and suppress unwanted oscillations. If the g-factors are nearly identical adiabatic ramps become impossible. In that limit it is feasible to exploit a diabatic pulse to implement a SWAP gate [57, 75]. By pulsing from $t_c = 0$ to a large tunnel coupling, the instantaneous eigenstates become the pure singlet and triplet, which induces singlet-triplet oscillations. These oscillations implement a SWAP between $\uparrow\downarrow$ and $\downarrow\uparrow$. Any residual g-factor mismatch perturbs the ideal symmetry and skews the oscillation weights. Due to the g-factor variability CPHASE gates are typically easier to implement than SWAP gates.

BIBLIOGRAPHY

[1] Cambridge Advanced Learner's Dictionary & Thesaurus. *Meaning of cubit in English.* URL: https://dictionary.cambridge.org/dictionary/english/cubit.

[2] C. Cohen-Tannoudji et al. *Quantum mechanics.* Wiley-VCH Verlag GmbH & Co., 2020. ISBN: 9783527345533.

[3] J. Sakurai and J. Napolitano. *Modern Quantum Mechanics.* Addison-Wesley, 2011. ISBN: 978-0-8053-8291-4.

[4] D. J. Griffiths. *Introduction to quantum mechanics.* Cambridge University Press, 2017, p. 468. ISBN: 9781107179868.

[5] J. D. Jackson. *Classical electrodynamics.* Wiley, 1975, p. 848. ISBN: 047143132X.

[6] M. A. Nielsen and I. L. Chuang. *Quantum computation and quantum information.* Cambridge University Press, 2010, p. 676. ISBN: 9781107002173.

[7] P. Krantz et al. "A quantum engineer's guide to superconducting qubits". In: *Applied Physics Reviews* 6.2 (June 2019). ISSN: 19319401. DOI: 10.1063/1.5089550.

[8] D. P. DiVincenzo. "The Physical Implementation of Quantum Computation". In: *Fortschritte der Physik* 48.9-11 (Sept. 2000), pp. 771–783. ISSN: 00158208. DOI: 10.1002/1521-3978(200009)48:9/11<771::AID-PROP771>3.0.CO;2-E. URL: https://onlinelibrary.wiley.com/doi/10.1002/1521-3978(200009)48:9/11%3C771::AID-PROP771%3E3.0.CO;2-E.

[9] N. W. Ashcroft and N. D. Mermin. *Solid state physics.* Cengage, 2012. ISBN: 8131500527.

[10] J. M. Luttinger and W. Kohn. "Motion of Electrons and Holes in Perturbed Periodic Fields". In: *Physical Review* 97.4 (Feb. 1955), p. 869. ISSN: 0031899X. DOI: 10.1103/PhysRev.97.869. URL: https://journals.aps.org/pr/abstract/10.1103/PhysRev.97.869.

[11] P. Y. Yu and M. Cardona. *Fundamentals of Semiconductors.* Berlin, Heidelberg: Springer Berlin Heidelberg, 2010. ISBN: 978-3-642-00709-5. DOI: 10.1007/978-3-642-00710-1.

[12] R. Winkler. *Spin—Orbit Coupling Effects in Two-Dimensional Electron and Hole Systems.* Vol. 191. Springer Tracts in Modern Physics. Berlin, Heidelberg: Springer Berlin Heidelberg, 2003. ISBN: 978-3-540-01187-3. DOI: 10.1007/b13586. URL: https://link.springer.com/10.1007/b13586.

[13] O. Madelung. *Semiconductors. Group IV elements and III-V compounds.* Springer-Verlag, 1991, p. 164. ISBN: 3540531505.

[14] J. Matthews and A. Blakeslee. “Defects in epitaxial multilayers”. In: *Journal of Crystal Growth* 27 (Dec. 1974), pp. 118–125. ISSN: 00220248. DOI: 10.1016/S0022-0248(74)80055-2.

[15] R. People and J. C. Bean. “Calculation of critical layer thickness versus lattice mismatch for Ge_x Si_(1x) Si strained-layer heterostructures”. In: *Applied Physics Letters* 47.3 (Aug. 1985), pp. 322–324. ISSN: 0003-6951. DOI: 10.1063/1.96206.

[16] L. E. A. Stehouwer et al. “Germanium wafers for strained quantum wells with low disorder”. In: *Applied Physics Letters* 123.9 (Aug. 2023), p. 92101. ISSN: 0003-6951. DOI: 10.1063/5.0158262. URL: https://doi.org/10.1063/5.0158262.

[17] Y. S. Touloukian. *Thermophysical properties of matter. Vol. 12: Thermal expansion.* IFI/Plenum, 1970. ISBN: 0306670321.

[18] Y. S. Touloukian. *Thermal expansion : nonmetallic solids.* IFI/Plenum, 1977, p. 1786. ISBN: 030667033X.

[19] W. I. Lawrie et al. *Quantum dot arrays in silicon and germanium.* Feb. 2020. DOI: 10.1063/5.0002013.

[20] Y. Kamata. “High-k/Ge MOSFETs for future nanoelectronics”. In: *Materials Today* 11.1-2 (Jan. 2008), pp. 30–38. ISSN: 1369-7021. DOI: 10.1016/S1369-7021(07)70350-4.

[21] A. Dimoulas et al. “Fermi-level pinning and charge neutrality level in germanium”. In: *Applied Physics Letters* 89.25 (Dec. 2006), p. 252110. ISSN: 0003-6951. DOI: 10.1063/1.2410241. URL: https://aip.scitation.org/doi/abs/10.1063/1.2410241.

[22] L. P. Kouwenhoven et al. “Electron transport in quantum dots”. In: *Mesoscopic Electron Transport.* Ed. by L. Sohn, L. Kouwenhoven, and G. Schön. Advanced Study Institute, 1997.

[23] M. Ciorga et al. “Addition spectrum of a lateral dot from Coulomb and spin-blockade spectroscopy”. In: *Physical Review B* 61.24 (June 2000), R16315. ISSN: 1550235X. DOI: 10.1103/PhysRevB.61.R16315. URL: https://journals.aps.org/prb/abstract/10.1103/PhysRevB.61.R16315.

[24] L. P. Kouwenhoven, D. G. Austing, and S. Tarucha. “Few-Electron Quantum Dots”. In: *Reports on Progress in Physics* 64.6 (2001), p. 701.

[25] M. Field et al. “Measurements of Coulomb blockade with a noninvasive voltage probe”. In: *Physical Review Letters* 70.9 (Mar. 1993), p. 1311. ISSN: 00319007. DOI: 10.1103/PhysRevLett.70.1311. URL: https://journals.aps.org/prl/abstract/10.1103/PhysRevLett.70.1311.

[26] R. J. Schoelkopf et al. “The Radio-Frequency Single-Electron Transistor (RF-SET): A Fast and Ultrasensitive Electrometer”. In: *Science* 280.5367 (May 1998), pp. 1238–1242. ISSN: 0036-8075. DOI: 10.1126/science.280.5367.1238. URL: https://www.science.org/doi/10.1126/science.280.5367.1238.

[27] J. C. Phillips. *Bonds and Bands in Semiconductors.* Elsevier, 1973, p. 288. ISBN: 9780125533508. DOI: 10.1016/B978-0-12-553350-8.X5001-5. URL: https://linkinghub.elsevier.com/retrieve/pii/B9780125533508X50015.

[28] M. V. Fischetti and S. E. Laux. “Band structure, deformation potentials, and carrier mobility in strained Si, Ge, and SiGe alloys”. In: *Journal of Applied Physics* 80.4 (Aug. 1996), pp. 2234–2252. ISSN: 0021-8979. DOI: 10.1063/1.363052. URL: https://pubs.aip.org/jap/article/80/4/2234/2840/Band-structure-deformation-potentials-and-carrier.

[29] C. Corley-Wiciak et al. “Nanoscale Mapping of the 3D Strain Tensor in a Germanium Quantum Well Hosting a Functional Spin Qubit Device”. In: *ACS Applied Materials & Interfaces* 15.2 (Jan. 2023), pp. 3119–3130. ISSN: 1944-8244. DOI: 10.1021/acsami.2c17395.

[30] J. M. Luttinger. “Quantum Theory of Cyclotron Resonance in Semiconductors: General Theory”. In: *Physical Review* 102.4 (May 1956), pp. 1030–1041. ISSN: 0031-899X. DOI: 10.1103/PhysRev.102.1030. URL: https://link.aps.org/doi/10.1103/PhysRev.102.1030.

[31] V. P. Michal, B. Venitucci, and Y.-M. Niquet. “Longitudinal and transverse electric field manipulation of hole spin-orbit qubits in one-dimensional channels”. In: *Physical Review B* 103.4 (Jan. 2021), p. 045305. ISSN: 2469-9950. DOI: 10.1103/PhysRevB.103.045305. URL: https://link.aps.org/doi/10.1103/PhysRevB.103.045305.

[32] J. C. Abadillo-Uriel et al. “Hole-Spin Driving by Strain-Induced Spin-Orbit Interactions”. In: *Physical Review Letters* 131.9 (Sept. 2023), p. 097002. ISSN: 0031-9007. DOI: 10.1103/PhysRevLett.131.097002. URL: https://link.aps.org/doi/10.1103/PhysRevLett.131.097002.

[33] Y. Kato et al. “Gigahertz Electron Spin Manipulation Using Voltage-Controlled g-Tensor Modulation”. In: *Science* 299.5610 (Feb. 2003), pp. 1201–1204. ISSN: 0036-8075. DOI: 10.1126/science.1080880. URL: https://www.science.org/doi/10.1126/science.1080880.

[34] M. Rimbach-Russ et al. “Gapless Single-Spin Qubit”. In: *Physical Review Letters* 135.19 (Nov. 2025), p. 197001. ISSN: 0031-9007. DOI: 10.1103/mvtj-zhrl. URL: https://link.aps.org/doi/10.1103/mvtj-zhrl.

[35] B. Martinez et al. “Hole spin manipulation in inhomogeneous and nonseparable electric fields”. In: *Physical Review B* 106.23 (Dec. 2022), p. 235426. ISSN: 2469-9950. DOI: 10.1103/PhysRevB.106.235426. URL: https://link.aps.org/doi/10.1103/PhysRevB.106.235426.

[36] M. D. Schroer et al. “Field Tuning the g Factor in InAs Nanowire Double Quantum Dots”. In: *Physical Review Letters* 107.17 (Oct. 2011), p. 176811. ISSN: 0031-9007. DOI: 10.1103/PhysRevLett.107.176811. URL: https://link.aps.org/doi/10.1103/PhysRevLett.107.176811.

[37] B. Voisin et al. “Electrical control of g-factors in a few-hole silicon nanowire MOSFET”. In: *Nano Letters* 16.1 (Nov. 2015), pp. 88–92. DOI: 10.1021/acs.nanolett.5b02920. URL: http://arxiv.org/abs/1511.08003%20http://dx.doi.org/10.1021/acs.nanolett.5b02920.

[38] S. D. Liles et al. “Electrical control of the g tensor of the first hole in a silicon MOS quantum dot”. In: *Physical Review B* 104.23 (Dec. 2021), p. 235303. ISSN: 2469-9950. DOI: 10.1103/PhysRevB.104.235303. URL: https://link.aps.org/doi/10.1103/PhysRevB.104.235303.

[39] N. W. Hendrickx et al. “Sweet-spot operation of a germanium hole spin qubit with highly anisotropic noise sensitivity”. In: *Nature Materials* 23.7 (July 2024), pp. 920–927. ISSN: 1476-1122. DOI: 10.1038/s41563-024-01857-5. URL: https://www.nature.com/articles/s41563-024-01857-5.

[40] J. Prentis and B. Ty. “Matrix mechanics of the infinite square well and the equivalence proofs of Schrödinger and von Neumann”. In: *American Journal of Physics* 82.6 (June 2014), pp. 583–590. ISSN: 0002-9505. DOI: 10.1119/1.4864740. URL: https://pubs.aip.org/ajp/article/82/6/583/1057813/Matrix-mechanics-of-the-infinite-square-well-and.

[41] C.-A. Wang et al. “Modeling of planar germanium hole qubits in electric and magnetic fields”. In: *npj Quantum Information* 10.1 (Oct. 2024), p. 102. ISSN: 2056-6387. DOI: 10.1038/s41534-024-00897-8.

[42] E. Rashba and V. Sheka. “Electric-Dipole Spin Resonances”. In: 1991, pp. 131–206. DOI: 10.1016/B978-0-444-88535-7.50011-X. URL: https://linkinghub.elsevier.com/retrieve/pii/B978044488535750011X.

[43] J. Pingenot, C. E. Pryor, and M. E. Flatté. “Electric-field manipulation of the Landé g tensor of a hole in an In 0.5Ga0.5As/GaAs self-assembled quantum dot”. In: *Physical Review B* 84.19 (Nov. 2011), p. 195403. ISSN: 1098-0121. DOI: 10.1103/PhysRevB.84.195403. URL: https://link.aps.org/doi/10.1103/PhysRevB.84.195403.

[44] S. Takahashi et al. “Electrically tunable three-dimensional <math display="inline"> <mi>g</mi> </math> -factor anisotropy in single InAs self-assembled quantum dots”. In: *Physical Review B* 87.16 (Apr. 2013), p. 161302. ISSN: 1098-0121. DOI: 10.1103/PhysRevB.87.161302. URL: https://link.aps.org/doi/10.1103/PhysRevB.87.161302.

[45] N. Ares et al. “SiGe Quantum Dots for Fast Hole Spin Rabi Oscillations”. In: *Applied Physics Letters* 103.26 (2013), p. 263113. ISSN: 0003-6951. DOI: 10.1063/1.4858959.

[46] E. I. Rashba and A. L. Efros. “Orbital mechanisms of electron-spin manipulation by an electric field”. In: *Physical Review Letters* 91.12 (Sept. 2003), p. 126405. ISSN: 10797114. DOI: 10.1103/PHYSREVLETT.91.126405/FIGURES/1/MEDIUM. URL: https://journals.aps.org/prl/abstract/10.1103/PhysRevLett.91.126405.

[47] R. Hanson et al. “Spins in Few-Electron Quantum Dots”. In: *Rev. Mod. Phys.* 79.4 (2007), p. 1217. DOI: 10.1103/RevModPhys.79.1217.

[48] C. Fasth et al. “Direct Measurement of the Spin-Orbit Interaction in a Two-Electron InAs Nanowire Quantum Dot”. In: *Physical Review Letters* 98.26 (June 2007), p. 266801. ISSN: 0031-9007. DOI: 10.1103/PhysRevLett.98.266801. URL: https://link.aps.org/doi/10.1103/PhysRevLett.98.266801.

[49] V. F. Maisi et al. “Spin-Orbit Coupling at the Level of a Single Electron”. In: (2015). DOI: 10.1103/PhysRevLett.116.136803.

[50] F. N. M. Froning et al. “Strong Spin-Orbit Interaction and g-Factor Renormalization of Hole Spins in Ge/Si Nanowire Quantum Dots”. In: *Phys. Rev. Research* 3.1 (2021), p. 013081. DOI: 10.1103/PhysRevResearch.3.013081.

[51] G. Xu et al. “Hole spin in tunable Ge hut wire double quantum dot”. In: *Applied Physics Express* 13.6 (May 2020), p. 065002. ISSN: 1882-0786. DOI: 10.35848/1882-0786/AB8B6D. URL: https://iopscience.iop.org/article/10.35848/1882-0786/ab8b6d.

[52] S. Bosco et al. “Squeezed hole spin qubits in Ge quantum dots with ultrafast gates at low power”. In: *Physical Review B* 104.11 (Sept. 2021), p. 115425. ISSN: 2469-9950. DOI: 10.1103/PhysRevB.104.115425. URL: https://link.aps.org/doi/10.1103/PhysRevB.104.115425.

[53] A. Crippa et al. “Electrical spin driving by g-matrix modulation in spin-orbit qubits”. In: *Physical Review Letters* 120.13 (Oct. 2017). DOI: 10.1103/PhysRevLett.120.137702. URL: http://dx.doi.org/10.1103/PhysRevLett.120.137702.

[54] B. Venitucci et al. “Electrical manipulation of semiconductor spin qubits within the g -matrix formalism”. In: *Physical Review B* 98.15 (Oct. 2018), p. 155319. ISSN: 24699969. DOI: 10.1103/PHYSREVB.98.155319/FIGURES/16/MEDIUM. URL: https://journals.aps.org/prb/abstract/10.1103/PhysRevB.98.155319.

[55] I. Seidler et al. “Spatial uniformity of g-tensor and spin-orbit interaction in germanium hole spin qubits”. In: (Oct. 2025). URL: http://arxiv.org/abs/2510.03125.

[56] E. A. Rodríguez-Mena et al. “Linear-in-momentum spin orbit interactions in planar Ge/GeSi heterostructures and spin qubits”. In: *Physical Review B* 108.20 (Nov. 2023), p. 205416. ISSN: 2469-9950. DOI: 10.1103/PhysRevB.108.205416. URL: https://link.aps.org/doi/10.1103/PhysRevB.108.205416.

[57] G. Burkard, D. Loss, and D. P. DiVincenzo. “Coupled Quantum Dots as Quantum Gates”. In: *Phys. Rev. B* 59.3 (1999), p. 2070. DOI: 10.1103/PhysRevB.59.2070.

[58] J. Danon and Y. V. Nazarov. “Pauli Spin Blockade in the Presence of Strong Spin-Orbit Coupling”. In: *Phys. Rev. B* 80.4 (2009), p. 041301. DOI: 10.1103/PhysRevB.80.041301.

[59] F. van Riggelen-Doelman et al. “Coherent spin qubit shuttling through germanium quantum dots”. In: *Nature Communications* 15.1 (July 2024), p. 5716. ISSN: 2041-1723. DOI: 10.1038/s41467-024-49358-y. URL: https://www.nature.com/articles/s41467-024-49358-y.

[60] M. V. Berry. “Quantal phase factors accompanying adiabatic changes”. In: *Proceedings of the Royal Society of London. A. Mathematical and Physical Sciences* 392.1802 (Mar. 1984), pp. 45–57. ISSN: 0080-4630. DOI: 10.1098/RSPA.1984.0023. URL: https://dx.doi.org/10.1098/rspa.1984.0023.

[61] E. A. Rodríguez-Mena et al. “Sweet-spot protection of hole spins in sparse arrays via spin-dependent magneto-tunneling”. In: (Oct. 2025). URL: http://arxiv.org/abs/2510.25857.

[62] C.-A. Wang. “Interacting and hopping spin qubits in germanium”. PhD thesis. Delft University of Technology, Feb. 2025.

[63] P. M. Mutter and G. Burkard. “All-Electrical Control of Hole Singlet-Triplet Spin Qubits at Low-Leakage Points”. In: *Phys. Rev. B* 104.19 (2021), p. 195421. DOI: 10.1103/PhysRevB.104.195421.

[64] J. R. Petta et al. “Coherent Manipulation of Coupled Electron Spins in Semiconductor Quantum Dots”. In: *Science* 309.5744 (Sept. 2005), pp. 2180–2184. ISSN: 0036-8075. DOI: 10.1126/science.1116955. URL: https://www.science.org/doi/10.1126/science.1116955.

[65] A. Sen et al. “Classification and Magic Magnetic Field Directions for Spin-Orbit-Coupled Double Quantum Dots”. In: *Phys. Rev. B* 108.24 (2023), p. 245406. DOI: 10.1103/PhysRevB.108.245406.

[66] J. M. Eizerman et al. “Single-shot read-out of an individual electron spin in a quantum dot”. In: *Nature 2004 430:6998* 430.6998 (July 2004), pp. 431–435. ISSN: 1476-4687. DOI: 10.1038/nature02693. URL: https://www.nature.com/articles/nature02693.

[67] K. Ono et al. “Current Rectification by Pauli Exclusion in a Weakly Coupled Double Quantum Dot System”. In: *Science* 297.5585 (Aug. 2002), pp. 1313–1317. ISSN: 0036-8075. DOI: 10.1126/science.1070958. URL: https://www.science.org/doi/10.1126/science.1070958.

[68] R. Hanson et al. “Spins in few-electron quantum dots”. In: *Reviews of Modern Physics* 79.4 (Oct. 2007), pp. 1217–1265. ISSN: 0034-6861. DOI: 10.1103/RevModPhys.79.1217. URL: https://link.aps.org/doi/10.1103/RevModPhys.79.1217.

[69] J. R. Petta et al. “Coherent Manipulation of Coupled Electron Spins in Semiconductor Quantum Dots”. In: *Science* 309.5744 (2005), p. 2180. DOI: 10.1126/science.1116955.

[70] K. V. Kavokin. “Anisotropic exchange interaction of localized conduction-band electrons in semiconductors”. In: *Physical Review B* 64.7 (July 2001), p. 075305. ISSN: 1550235X. DOI: 10.1103/PhysRevB.64.075305. URL: https://journals.aps.org/prb/abstract/10.1103/PhysRevB.64.075305.

[71] M. Veldhorst et al. “A two-qubit logic gate in silicon”. In: *Nature* 526.7573 (Oct. 2015), pp. 410–414. ISSN: 0028-0836. DOI: 10.1038/nature15263. URL: https://www.nature.com/articles/nature15263.

[72] T. F. Watson et al. “A Programmable Two-Qubit Quantum Processor in Silicon”. In: *Nature (London)* 555 (22018/02/14/online), p. 633. DOI: 10.1038/nature25766.

[73] N. W. Hendrickx et al. “Fast Two-Qubit Logic with Holes in Germanium”. In: *Nature* 577.7791 (2020), pp. 487–491. ISSN: 1476-4687. DOI: 10.1038/s41586-019-1919-3.

[74] T. Meunier, V. E. Calado, and L. M. K. Vandersypen. “Efficient controlled-phase gate for single-spin qubits in quantum dots”. In: *Physical Review B* 83.12 (Mar. 2011), p. 121403. ISSN: 1098-0121. DOI: `10.1103/PhysRevB.83.121403`. URL: `https://link.aps.org/doi/10.1103/PhysRevB.83.121403`.

[75] D. Loss and D. P. DiVincenzo. “Quantum computation with quantum dots”. In: *Physical Review A* 57.1 (Jan. 1998), pp. 120–126. ISSN: 1050-2947. DOI: `10.1103/PhysRevA.57.120`. URL: `https://link.aps.org/doi/10.1103/PhysRevA.57.120`.

3

METHODS

The design of the Master Cook must be the fine and dependable method produced by experience, of which he should have acquired such knowledge that he could serve rather in the Office of Steward than the Steward could serve as Cook. [1]

Bartolomeo Scappi

THE development and electrical characterisation of spin qubit devices includes multiple steps and techniques. This chapter gives a general introduction into the methods used within the thesis. Further specifications can also be found in the respective experimental chapters.

3.1. DEVICE DEVELOPMENT

University research typically focuses on developing proof-of-concept devices in cleanroom facilities that provide substantial freedom for experimentation. This contrasts with industry, where processes are considerably more restrictive and yield is paramount. We typically use coupons containing either nine or sixteen chips, of which at least one serves as a witness chip. The target yield is therefore to have the majority of devices on a single coupon functional, since proof-of-concept experiments require only a single working device, often referred to as the "hero device." As device complexity increases, fabrication quality must improve accordingly to maintain such yield. All device development in this thesis was carried out in close collaboration with a dedicated fabrication engineer. The ten-quantum-dot array described in chapter 6, 7, and 8 required five fabrication rounds to achieve a satisfactory yield that enabled more extensive device characterization. Sub-optimal design choices necessitated the further development of generations 6 and 7, which are nearly identical.

Typical fabrication rules followed in electron beam lithography were:

1. a minimum spacing of 30 nm between adjacent elements within the same layer
2. elements in close proximity within the same layer should, where possible, be fabricated in two steps
3. avoid running fanout lines in parallel over extended distances when they are in close proximity
4. after ohmic contact diffusion, up to three additional layers can be fabricated, each separated by a sufficiently thick oxide
5. elements in higher layers can cross those in lower layers at a 90° angle to reduce the risk of discontinuities
6. all bonding pads should be placed on a SiN bond pad to prevent contacting the 2D hole gas during bonding
7. ohmic bond pads should not be placed on SiN pads, as these can facilitate leakage currents
8. screening gates at the device edges are required to prevent the formation of stray dots

These rules are not set in stone and have evolved over time through efforts to diagnose failure and mitigate low yield. Some can already be considered partially obsolete, such as restrictions on parallel fanout lines and limiting the design to three additional layers. It is therefore necessary to reassess these rules when deviating from them offers clear advantages. Nevertheless, it remains important to begin from a rule set that has proven effective in the past, even if the initial reasoning behind these rules have become unclear.

3.1.1. DEVICE DESIGN

Designing a device requires the creation of a GDS file that contains all elements assigned to corresponding processing layers. Typically, GDS files are created manually using tools such as KLayout. As device complexity increases, there is a growing need to automate the design process. This introduces a trade-off in terms of flexibility and user interface, both of which are maximized in KLayout. An alternative approach for creating GDS files is the use of dedicated Python modules, such as Gdstk, the successor to Gdspy. Gdstk is a powerful and flexible Python library that enables the creation of arbitrary shapes, their placement and grouping into cells, and hierarchical cell design. For complete documentation, refer to `https://heitzmann.github.io/gdstk`.

As part of this PhD, a wrapper module has been developed based on Gdstk, tailored specifically to the design requirements of research groups working on spin qubits. This module, named *QuantumDotDesigner*, is available as open-source software at `https://github.com/valentinjohn/quantum-dot-designer`. *QuantumDotDesigner* retains the core structure of Gdstk, including the ability to create cells and place elements and cell instances within them. In addition, it tracks all elements and their positions, which simplifies the addition of fanout structures at the final stage of the design process. The module provides predefined elements such as plungers, barriers, and screening gates, as well as predefined components, implemented as separate cells containing multiple elements. An example is a sensor component comprising a plunger, two barriers, and two ohmic contacts. To ensure flexibility, the module also includes an `ArbitraryPolygon` class, which allows the creation of custom shapes by specifying vertex coordinates. New predefined elements can be added with minimal effort, as each element and component is implemented in a separate file. After cloning the repository, additional files can be placed in the appropriate directory. Further details are provided in the full documentation at `https://valentinjohn.github.io/quantum-dot-designer`.

3.1.2. DEVICE PREPARATION AND SCREENING

After processing in the cleanroom, the coupons are diced into individual chips and inspected optically and by scanning electron microscopy. Mechanical failures, such as discontinuities or disconnected lines, can thus be identified. The devices are then removed from the cleanroom and handed over by the fabrication engineer, packaged in a gel box and an ESD-protected bag. The next step is electrical screening, which requires gluing and bonding the device onto a printed circuit board (PCB).

All samples studied in this thesis are mounted on the same PCB, which provides 100 direct current (DC) lines. Thirty of these lines incorporate a resistive bias network that combines alternating current (AC) and DC signals. The AC input is capacitively coupled (100 nF) and referenced to ground through 100 kΩ, with a 1 MΩ resistor linking the AC and DC nodes. The DC bias is decoupled to ground via 100 pF. All plunger, barrier, and sensor plunger gates are bonded to AC lines.

For gluing, vacuum grease and Gvarnish have primarily been used. Vacuum grease is

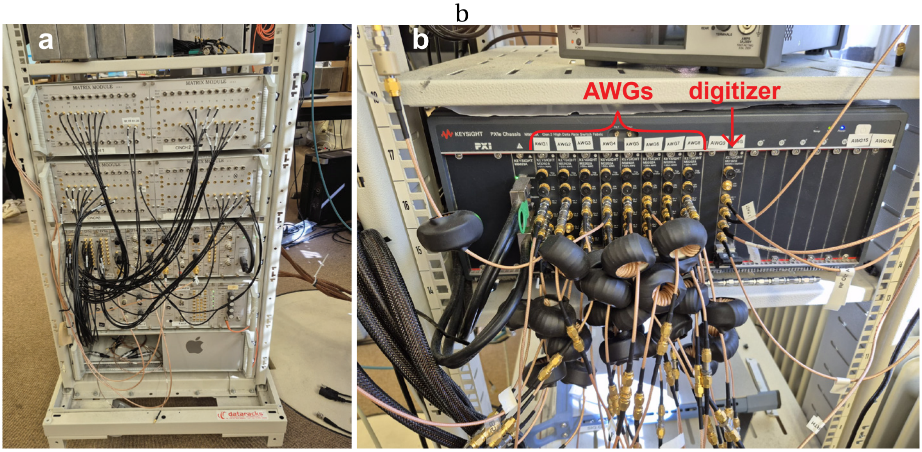

Figure 3.1: Room temperature electronic setup. **a.** SPI rack providing the dc voltages; **b.** Keysight M3202A AWGs for applying AC pulses up to 400 MHz and M3102A digitizer demodulating the read-out signal.

resilient to thermal cycling and was used for all 3-4-3 quantum dot devices, but it complicates bonding since it does not harden and the chip can slide or tilt. Gvarnish was therefore adopted in later stages. As the PCB was optimized for a different device design [2], in which all fast lines fan out on the top side, bonding required a significant number of wires crossing over the chip to the opposite side of the PCB.

After bonding, the device is tested in a 4 K dipstick setup using direct current. The device is immersed in liquid helium, reaching temperatures down to 4 K. At this stage, it is verified whether the 2DHG is insulating and whether a current can be established between ohmic contacts by using the intermediate gates to control the conduction path. Turn-on is typically observed well before $-1000\,\text{mV}$, although this can depend on the design, fabrication run and wafer.

3.2. EXPERIMENTAL SETUP

Experiments are performed in a Bluefors LD400 dilution refrigerator with a base temperature of a few tens of millikelvin. A superconducting solenoid magnet operated in driven mode provided an axial magnetic field.

DC lines are filtered at multiple stages of the refrigerator and connected outside the cryostat to a battery-powered SPI rack for voltage control `https://qtwork.tudelft.nl/~mtiggelman/spi-rack/chassis.html`. AC lines are attenuated within (9–15 dB) and outside (~ 10 dB) the dilution fridge, and connected to a Keysight M3202A arbitrary waveform generator cluster. The room and cryogenic temperature setup can be seen in Figure 3.1 and 3.2 respectively. Instrument control is implemented using pulselib (pulselib.readthedocs.io) and internal qconstruct libraries.

Charge sensing employs reflectometry. The PCB feedline is coupled to four LC tank circuits (100 pF capacitors with off-chip inductors of a few µH). A 5 kΩ shunt resistor sets an RC constant $\tau = 0.5\,\mu\text{s}$. The input RF tone is attenuated by 43 dB in the fridge and by a similar amount at room temperature. Reflected signals are amplified 35 dB by

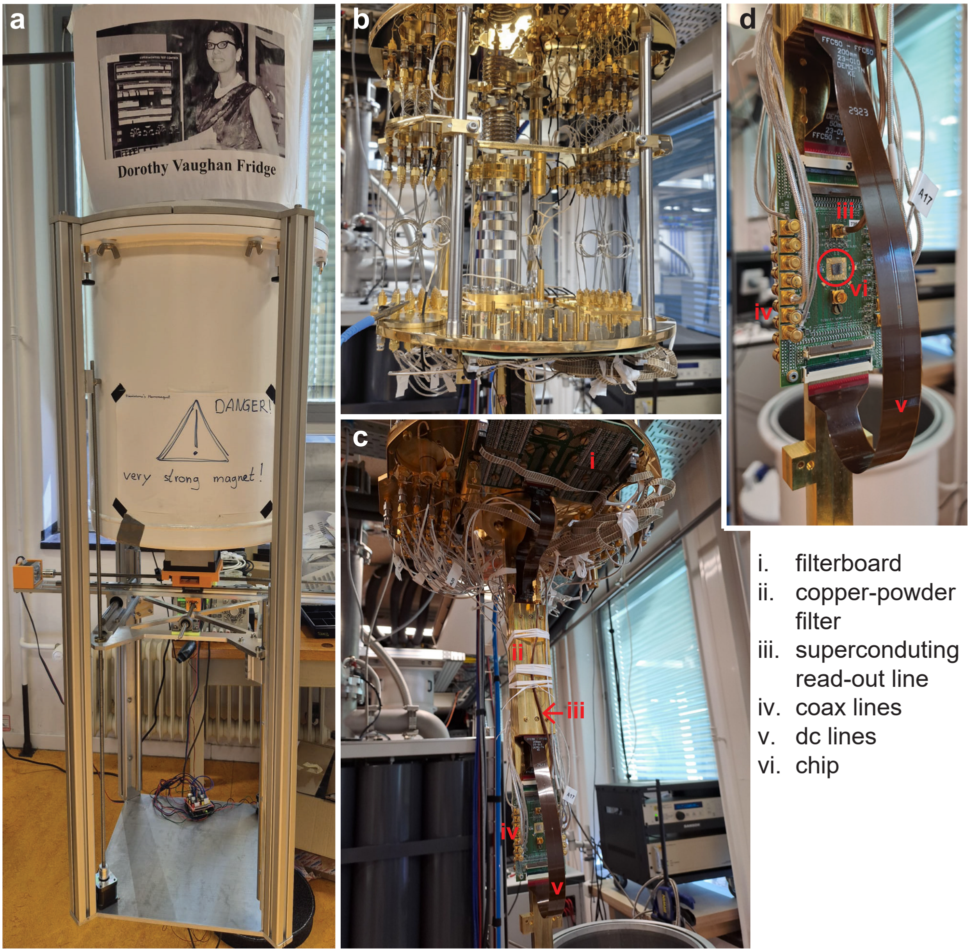

Figure 3.2: Cryogenic setup. **a.** Bluefors LD400 dilution fridge from the outside when closed. An additional external magnet has been installed and utilised in chapter 8. All other experiments use a superconducting solenoid magnet inside the dilution fridge. **b.** Inside of the dilution fridge showing the mixing chamber and still flange. **c.** Cold finger that is attached to the mixing chamber plate to place the sample in the magnetic field centre of the solenoid magnet. **d.** The quantum chip is mounted on a PCB and connected to the required AC lines via coaxial cables and to DC lines via flex flat cables (FFC).

a cryogenic low-noise amplifier at 4 K and 30 dB at room temperature, after which it is digitized with a Keysight M3102A module with 500 MSa/s, and demodulated using its FPGA.

The source of each single hole transistor is bonded to one tank circuit, with the drain grounded. Resonance frequencies can range from 70–200 MHz. The RF phase is chosen to maximize sensitivity.

Single-shot readout is performed by repeating pulse sequences n times and assigning binary outcomes depending on whether the measured amplitude crossed a calibrated threshold.

3.3. FABRICATION

The devices presented in this thesis are fabricated on a Ge/SiGe heterostructure featuring a 16 nm germanium quantum well located 55 nm below the semiconductor–oxide interface, as introduced in section 2.5. The device gate stack is realized using a multilayer of Pd gates and Al_2O_3 gate oxide grown by atomic layer deposition.

Ohmic contacts are formed via diffusion of 30 nm aluminium or platinum. Prior to contacting, the oxidized silicon cap is etched. The gates are composed of Pd with a 3 nm Ti adhesion layer. Table 3.1 contains all additional fabrication details of the used devices within the thesis.

Table 3.1: Differences in the fabrication details between the utilised devices

Device	**2x2**	**4x4**	**3-4-3 (6gen)**	**3-4-3 (7gen)**	**GS2**
Chapters	4	5	6	7, 8	9
Substrate	silicon	silicon	silicon	germanium	silicon
Ti/Pd thickness (nm)	20-40	20-30-30	20-30-40	20-30-40	20-30-40
Ohmic material	Al	Pt	Pt	Pt	Pt
Al_2O_3 thickness (nm)	7-7	7-5-5	7-5-5	7-5-5	7-5-5
plunger size (nm)	100	100	130	130	80
plunger pitch (nm)	130	160	165	165	80
barrier size (nm)	30	30	50	50	-

3.4. GATE VIRTUALISATION

For the experiments conducted in this thesis, a set of virtual gates defined in software is used, as outlined in Table 3.2. The first layer of virtualisation compensates for crosstalk between gates and sensors, as well as interactions between nearby quantum dots. This ensures that adjustments to plunger or barrier gates do not shift the position of the charge sensor's Coulomb peak or alter the potentials of nearby dots. In the second layer, the charging voltage of each dot is normalized by rescaling the strength of its corresponding plunger gate. Finally, the third layer virtualizes the barrier gates, enabling independent tuning of the exchange interaction between dots without affecting their charge states. For a complete description of the gate virtualisation method, see Ref. [3].

Table 3.2: Layers of the virtualization approach. **S** denotes sensor plunger gates, **P** (**B**) quantum dot plunger (barrier) gates.

Virt. layer	**Description**	**Notation**
1	Charge sensor and QD compensations	$[\mathbf{vS}, \mathbf{vP}, \mathbf{vB}] = \mathbf{M_1} \cdot [\mathbf{S}, \mathbf{P}, \mathbf{B}]$
2	Normalisation of plungers with uniform charging voltages	$\mathbf{N} = \mathbf{M_2} \cdot \mathbf{vP}$
3	Barriers to QDs	$\mathbf{J} = \mathbf{M_3} \cdot [\mathbf{vB}, \mathbf{N}]$

BIBLIOGRAPHY

[1] B. Scappi and T. Scully. *The Opera of Bartolomeo Scappi (1570) : l'arte et prudenza d'un maestro cuoco*. University of Toronto Press, 2008, p. 99. ISBN: 9780802096241.

[2] S. G. J. Philips et al. "Universal Control of a Six-Qubit Quantum Processor in Silicon". In: *Nature* 609.7929 (2022), pp. 919–924. ISSN: 1476-4687. DOI: `10.1038/s41586-022-05117-x`.

[3] A. S. Rao et al. "Modular Autonomous Virtualization System for Two-Dimensional Semiconductor Quantum Dot Arrays". In: *Physical Review X* 15.2 (Apr. 2025), p. 021034. ISSN: 2160-3308. DOI: `10.1103/PhysRevX.15.021034`. URL: `https://link.aps.org/doi/10.1103/PhysRevX.15.021034`.

4

BICHROMATIC RABI CONTROL OF SEMICONDUCTOR QUBITS

In all fighting, the direct method may be used for joining battle, but indirect methods will be needed in order to secure victory. [1]

From *The Art of War* by Sun Tzu

Electrically-driven spin resonance is a powerful technique for controlling semiconductor spin qubits. However, it faces challenges in qubit addressability and off-resonance driving in larger systems. We demonstrate coherent bichromatic Rabi control of quantum dot hole spin qubits, offering a spatially-selective approach for large qubit arrays. By applying simultaneous microwave bursts to different gate electrodes, we observe multichromatic resonance lines and resonance anticrossings that are caused by the ac Stark shift. Our theoretical framework aligns with experimental data, highlighting interdot motion as the dominant mechanism for bichromatic driving.

Parts of this chapter have been published in **Valentin John**, Francesco Borsoi, Zoltán György, Chien-An Wang, Gábor Széchenyi, Floor van Riggelen-Doelman, William I. L. Lawrie, Nico W. Hendrickx, Amir Sammak, Giordano Scappucci, András Pályi, and Menno Veldhorst, Bichromatic Rabi control of semiconductor qubits, Phys. Rev. Lett. 132, 067001

SPIN qubits based on semiconductor quantum dots represent a promising platform for quantum computing owing to their small qubit footprint, long coherence times, and compatibility with semiconductor manufacturing techniques [2, 3]. However, the present control of spin qubit devices relies on a brute force approach, where each qubit is individually connected to at least one control line. This approach poses a significant challenge for scaling to larger systems and is affecting current progress [4, 5]. Multiplexing strategies will most likely become essential and this has been the motivation for various proposals, such as crossbar arrays with shared control [6, 7]. Executing quantum algorithms requires selective quantum control, but its implementation in large qubit arrays poses significant challenges. Recently, the concept of bichromatic spin resonance has been proposed to offer addressable microwave control in qubit crossbar architectures [8]. In this approach, two microwave tones with frequencies f_w and f_b are utilized. These tones are applied to the word and the bit line of the crossbar array, respectively. By exploiting the nonlinearity of electric dipole spin resonance (EDSR) [9–17], rotations of a qubit with Larmor frequency of $|f_\mathrm{w} \pm f_\mathrm{b}|$ at the intersection of the two lines [Fig. 4.1(a)] can be targeted. This operation scheme presents new opportunities for both spatially selective qubit addressing and gate parallelization [8]. Analogous two-photon processes have been utilized in Rydberg-atom processors [18, 19] and superconducting qubits [20] to optimize qubit performance.

Here, we investigate experimentally and theoretically the bichromatic driving of semiconductor spin qubits in a 2-qubit system defined in a strained germanium quantum well. We find that both qubits can be coherently driven by mixed frequency signals, including the sum and difference of the corresponding frequencies. We investigate the occurrence of resonance anticrossings in EDSR spectroscopy maps, which originate from the Autler-Townes (also known as ac Stark) shift of a photon-dressed spin transition. Additionally, we introduce a model that reveals the importance of spin-conserving and spin-flip tunneling terms in bi- and monochromatic EDSR.

We investigate bichromatic driving of spin qubits in a two-qubit system within a four-qubit germanium quantum processor (Figs.4.1b, c) [21, 22]. By tuning the electrostatic potential using plunger and barrier gates, we confine a single-hole quantum dot underneath each of the four plungers P1-P4, and define virtual gate voltages vP1-vP4 based on P1-P4 to achieve independent control ([23], Supplementary Note 1). We focus on the spin qubits Q1 and Q2, while Q3 and Q4 remain in their ground state. We furthermore define the detuning voltage $\epsilon_{12} = \mathrm{vP1} - \mathrm{vP2}$ [24].

4.1. BICHROMATIC EDSR SPECTROSCOPY

Fig.4.1d displays the charge stability diagram of the double quantum dot system, obtained through rf-reflectometry charge sensing [25]. The device is operated in an in-plane magnetic field of 0.675 T, resulting in qubit frequencies of $f_{\mathrm{Q1}} = 1.514$ GHz and $f_{\mathrm{Q2}} = 2.649$ GHz. To investigate the bichromatic driving approach, we follow the pulse protocol outlined in Fig.4.2a. We initialise the Q1, Q2 qubits in the $|{\downarrow\downarrow}\rangle$ state by adiabatically pulsing ϵ_{12} from the (0, 2) to the (1, 1) charge state via the spin-orbit induced anticrossing. Next, we manipulate the spins by two simultaneous microwave pulses on plunger gates P2 and P4, with a duration t_p and microwave frequencies f_{P2} and f_{P4}. We perform such two-tone qubit manipulation at the voltage point indicated in Fig.4.1c cor-

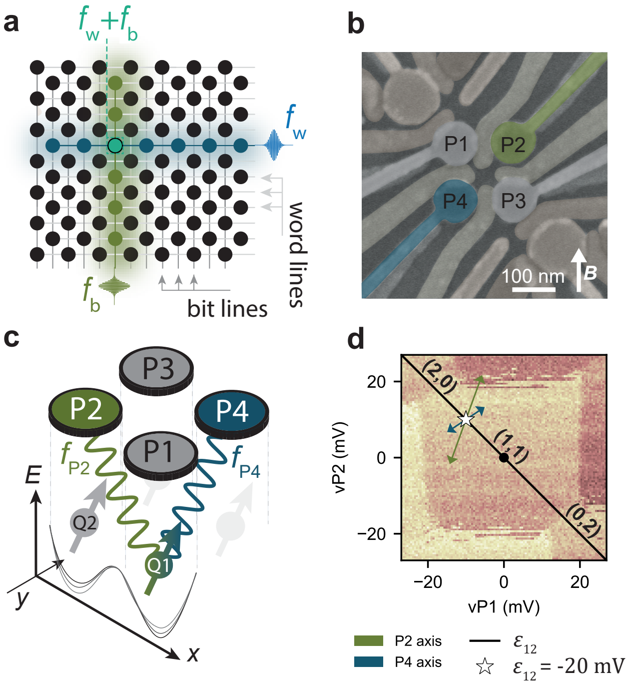

Figure 4.1: **Bichromatic control of a spin qubit. a,** Bichromatic driving in a crossbar architecture. **b,** False-color scanning electron microscopy of a 2x2 germanium quantum dot device, nominally identical to the one used here. **c,** Illustration of the four-qubit processor. We operate Q1 and Q2 with microwave bursts applied to P2 and P4. We model qubit rotations via AC detuning modulation (sketched potential). **d,** Charge stability diagram of the double quantum dot illustrating the (1, 1) charge sector and the detuning ϵ_{12} axis (black line). The white star indicates the gate voltages used for the qubit manipulation stage. The green and blue arrows indicate the displacement within the vP1, vP2 framework, when applying a microwave burst on P2 and P4, showcasing the different orientation of the driving fields. The displayed length of the arrows is proportional to the amplitude of the signal at the device, amplified by a factor of 5 for visibility.

responding to $\epsilon_{12} = -20$ mV. Finally, we return to the (0, 2) charge sector and perform read-out using latched Pauli spin blockade [21].

The 2D EDSR spectroscopy in Fig.4.2b reveals resonance lines from monochromatic and bichromatic spin excitations. Monochromatic qubit transitions labelled as $Q1^{P2}$, $Q1^{P4}$, $Q2^{P2}$, $Q2^{P4}$ (with the superscript defining the driving plunger gate) are observed as vertical and horizontal lines at the corresponding Larmor frequencies. Bichromatic excitations appear as tilted resonance lines, with negative (positive) slopes indicating the frequency sum (difference) matching the qubit Lamor frequency. Three-photon bichromatic excitations can also be observed when a combination of two photons with the same frequency, and a third one with a different frequency match the qubit Larmor frequency.

Figs. 4.2c, d depict the expected resonance lines considering the individual resonance frequencies of the two qubits. The qubits exchange interaction resulting from

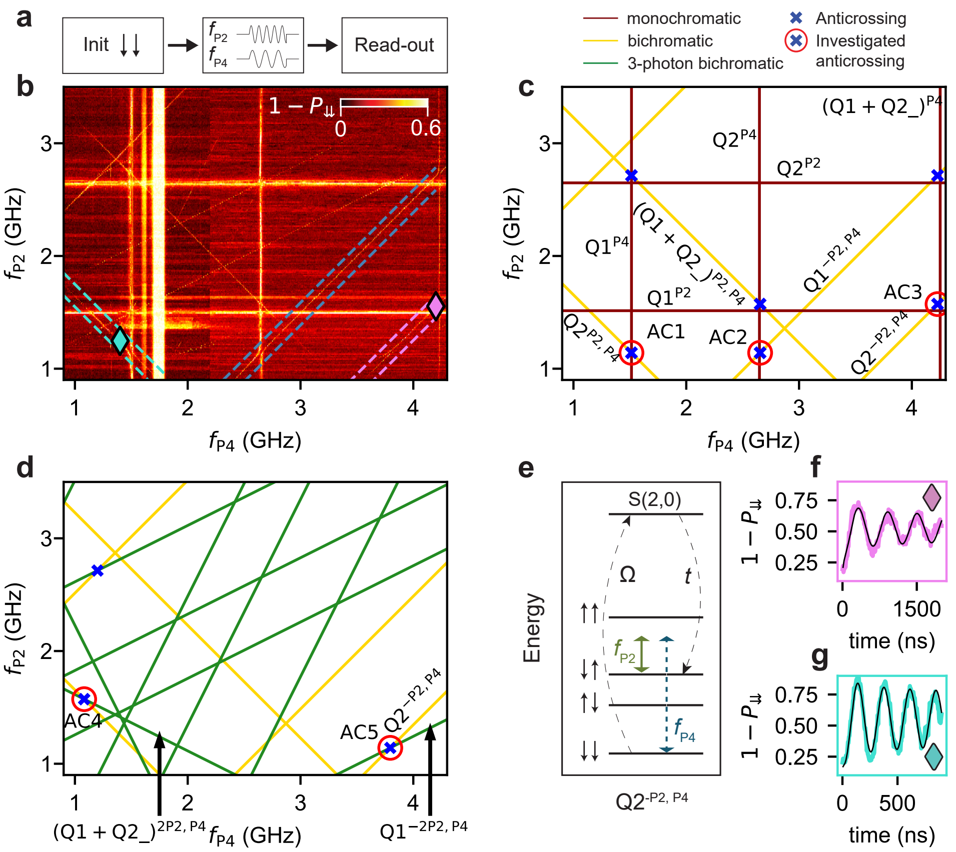

Figure 4.2: **Bichromatic EDSR spectroscopy. a,** Bichromatic control sequence. **b,** Single-shot probability versus f_{P4} and f_{P2}, at $\epsilon_{12} = -20$ mV. We include three turquoise, blue and purple dotted lines to enclose the bichromatic resonances of $\mathrm{Q2}^{\mathrm{P2,P4}}$, $\mathrm{Q1}^{-\mathrm{P2,P4}}$ and $\mathrm{Q2}^{-\mathrm{P2,P4}}$ respectively. The broad vertical excitation at $f_{\mathrm{P4}} \sim 1.8$ GHz is associated to a transmission resonance in the lines, and not to a spin transition. **c, d** Monochromatic, bichromatic and three-photon bichromatic excitations in the 2D frequency plane, as predicted by theory. **e,** Energy diagram of a two-spin system with finite exchange and finite magnetic field. The green and blue arrows represent the applied microwave frequencies f_{P2} and f_{P4}, when driving the $\mathrm{Q2}^{-\mathrm{P2,P4}}$ transition. Driven spin-flipping processes originate from higher order processes via the S(2,0) state involving the spin-conserving tunneling term t and spin-flip tunneling term Ω. **f, g** Coherent Rabi oscillations of the $\mathrm{Q2}^{-\mathrm{P2,P4}}$ and $\mathrm{Q2}^{\mathrm{P2,P4}}$ bichromatic transition. The corresponding f_{P2} and f_{P4} frequencies are indicated with the purple and turquoise diamonds in **b**.

interdot tunnelling (55 MHz at $\epsilon_{12} = -20$ mV, see Section 4.5.3) is taken into account. To label the Larmor frequency of qubit i when qubit j is in the excited state, we use the notation Qi_ (with $i, j \in \{1,2\}$ and $i \neq j$). The monochromatic transition from $|{\downarrow\downarrow}\rangle$ to $|{\uparrow\uparrow}\rangle$ driven by P4 is then denoted as $(\mathrm{Q1}+\mathrm{Q2\_})^{\mathrm{P4}}$. A bichromatic transition can be visualised as a two-step process via a virtual state, as illustrated in Fig.4.2e. Following perturbation theory, bichromatic spin transitions are activated thanks to spin-conserving (t) and spin-flipping (Ω) tunnelling terms, which hybridize the four possible spin states with the S(2,0) state, as discussed below and in Suppl. Note 8 [23].

We analyze three resonance lines (dashed lines in Fig.4.2b) resulting from bichromatic rotation of Q1 and Q2. The bichromatic Q1 spin resonance ($Q1^{-P2,P4}$) occurs when the frequency difference matches the Q1 Larmor frequency. Similarly, Q2 exhibits bichromatic resonance lines from both frequency difference ($Q2^{-P2,P4}$) and frequency sum ($Q2^{P2,P4}$). The bichromatic spin resonance $Q1^{P2,P4}$ is not investigated due to the presence of a high-pass filter (Section 4.5.5). The conditions for the three studied bichromatic qubit rotations are: $Q1^{-P2,P4}$: $f_{P4} - f_{P2} = f_{Q1}$, $Q2^{-P2,P4}$: $f_{P4} - f_{P2} = f_{Q2}$ and $Q2^{P2,P4}$: $f_{P4} + f_{P2} = f_{Q2}$. At these frequency combinations, we also achieve coherent bichromatic qubit rotations with a Rabi frequency exceeding 1 MHz, as we demonstrate in Figs. 4.2f, g as well as Fig. 4.8, Fig. 4.9, and Fig. 4.10.

4.2. ACs IN THE BICHROMATIC SPECTROSCOPY AND AUTLER-TOWNES EFFECT

At the intersection of specific resonance lines (see Fig.4.2b), we also observe anticrossings (labelled as ACn with $n \in \{1,\ldots,5\}$ in Figs. 4.2c and d). In Fig.4.3, we analyse the evolution of the two bichromatic spin resonances, $Q2^{-P2,P4}$ and $Q2^{P2,P4}$, in the frequency plane. We vary the two microwave frequencies together to follow the two resonance lines, using Δf_{P2} in the range of [-40, 40] MHz centered around the bichromatic resonance. This procedure allows to monitor in detail the Q2 bichromatic spin resonance

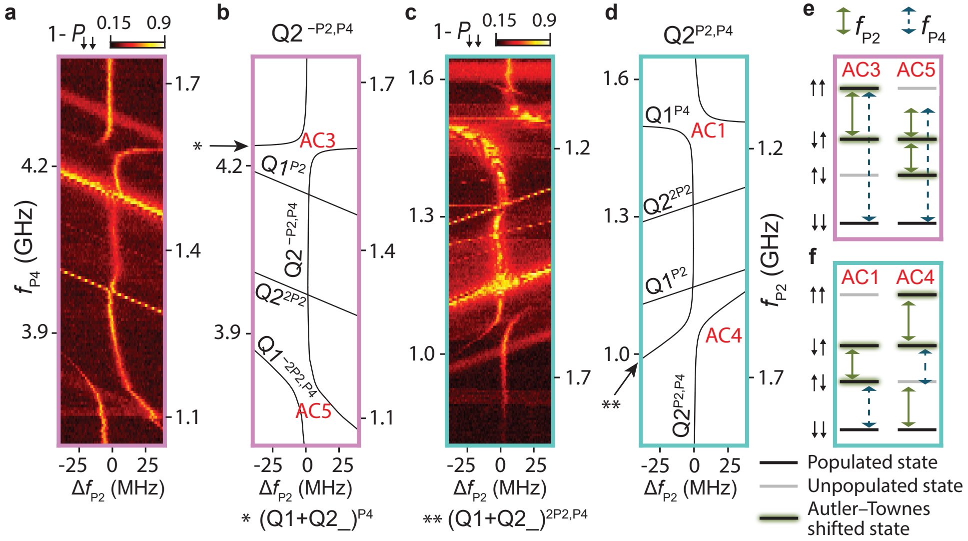

Figure 4.3: **Modelling the frequency anticrossings due to the Autler-Townes effect. a, c** Single-shot probabilities ($1 - P_{\downarrow\downarrow}$) in a frequency range around the bichromatic $Q2^{-P2,P4}$ and $Q2^{P2,P4}$ resonance conditions, respectively. These scans are higher-resolution measurements along the color-coded diagonals enclosed by two dashed lines in Fig.4.2b. Vertical lines of Fig.4.2b appear horizontal, and horizontal lines appear slightly tilted (as can be seen with $Q1^{P2}$ and $Q1^{P4}$ in **d**). The values on the f_{P2} axes are valid at $\Delta f_{P2} = 0$. **b, d** Calculated transitions nearby the $Q2^{-P2,P4}$ and $Q2^{P2,P4}$ resonances. **e, f** Illustration of the driven transitions at the four anticrossings. Strong driving via P2 induces a photon-dressed spin transition.

within the boxed areas indicated in Fig.4.2b. The bichromatic resonance aligns with the expected value of $\Delta f_{\mathrm{P2}} = 0$ for most of the frequency range. However, significant anticrossings occur when the resonance intersects with other qubit transitions. Examples of these anticrossings are observed at specific frequencies, and are labelled as AC5, AC3 (for $\mathrm{Q2}^{-\mathrm{P2,P4}}$), and AC4, AC1 (for $\mathrm{Q2}^{\mathrm{P2,P4}}$).

The appearance of anticrossings in the frequency plane, such as AC3 in Fig. 4.3a, result from resonant driving of monochromatic and bichromatic transitions from the $|\downarrow\downarrow\rangle$ state to higher (1,1) states. As shown in Figs. 4.3e-f, AC3 involves three resonant processes: the bichromatic transition $|\downarrow\downarrow\rangle \leftrightarrow |\downarrow\uparrow\rangle$, the monochromatic P4 drive $|\downarrow\downarrow\rangle \leftrightarrow |\uparrow\uparrow\rangle$, and the monochromatic P2 drive $|\downarrow\uparrow\rangle \leftrightarrow |\uparrow\uparrow\rangle$. Due to the greater driving efficiency of P2 compared to P4 (see projected amplitudes in Fig. 4.1c), the dominant transition is $|\downarrow\uparrow\rangle \leftrightarrow |\uparrow\uparrow\rangle$ (Suppl. Note 8 [23]).

Driving via P2 dresses up the spin states $|\downarrow\uparrow\rangle$ and $|\uparrow\uparrow\rangle$ with microwave photons. In the rotating frame where these states are degenerate in the absence of P2 driving, the eigenstates become dressed in the form $\frac{|\downarrow\uparrow\rangle \pm |\uparrow\uparrow\rangle}{\sqrt{2}}$, and the corresponding eigenvalues exhibit a splitting set by the Rabi frequency. In this context, dressing refers to the coherent interaction between the electromagnetic field and the spin system, resulting in entangled states of spins and photons becoming the eigenstates of the coupled system.

This effect, known as the Autler-Townes effect or ac Stark shift, has been observed in quantum optics and in strongly driven superconducting qubits [26, 27]. It is at the basis of control strategies for highly coherent solid-state qubits [28]. In particular, the continuous driving can decouple the spin from background magnetic field noise and thus extend their coherence [29, 30].

Due to the Autler-Townes effect, the resonance frequencies of the two weaker transitions ($|\downarrow\downarrow\rangle \leftrightarrow |\downarrow\uparrow\rangle$ and $|\downarrow\downarrow\rangle \leftrightarrow |\uparrow\uparrow\rangle$) are shifted by the Rabi frequency of the strongly driven $|\downarrow\uparrow\rangle \leftrightarrow |\uparrow\uparrow\rangle$ transition, resulting in the anticrossing between the resonance lines (AC3 in Figs. 4.3a, b).

We use a two-spin qubit Hamiltonian to model our system and gain a quantitative understanding. The model considers the lowest orbital in each dot, including four states in the (1,1) charge regime, as well as the (0,2) and (2,0) singlet states. Spin-conserving and spin-flip tunneling between the quantum dots are also included, with a coupling strength of t for spin-conserving transitions and Ω for spin-flip transitions (Suppl. Note 8A [23]). Despite neglecting additional electrical g-tensor modulations [3, 31], this minimal model successfully explains electrically driven spin transitions via ac modulation of the detuning voltage using both monochromatic and bichromatic resonance techniques. Here, spin dynamics occur through virtual transitions between the (1,1) spin states and the (0,2) and (2,0) singlet states, mediated by the spin-conserving and spin-flipping terms, as shown in Fig.4.2e.

Our model provides an explanation for the observed resonance crossings and anticrossings in Figs. 4.3a, c. Furthermore, by analyzing the five anticrossings AC1 to AC5 using Floquet theory as discussed in Suppl. Note 8C [23], we estimate the spin-conserving and spin-flip tunneling energies to be on average $t = (18.1 \pm 1.9)\,\mu\mathrm{eV}$ and $\Omega = (14.3 \pm 2.4)\,\mu\mathrm{eV}$ (Suppl. Note 8F [23]).

4.3. DEPENDENCE ON DETUNING ENERGY OF DOUBLE QUANTUM DOT

To verify our theoretical description, we investigate the dependence of the $\mathrm{Q1}^{-\mathrm{P2,P4}}$ resonance anticrossing on the detuning voltage. Experimental data and the expected detuning dependence from the model are shown in Figure 4.4. In the model, we use the average tunneling amplitudes and vary the detuning voltage. Moreover, we utilise an estimated detuning lever arm of $\alpha = 0.0917$ eV/V and quantum dot charging energy of $U = 2.56$ meV (Suppl. Note 8B [23]). Our theoretical model accurately captures the diminishing size of the anticrossing as the detuning approaches $\epsilon_{12} \sim 0$. Both the bichromatic and monochromatic resonance lines fade, indicating a reduced efficiency as detuning approaches zero. This is consistent with our model, since the transitions take

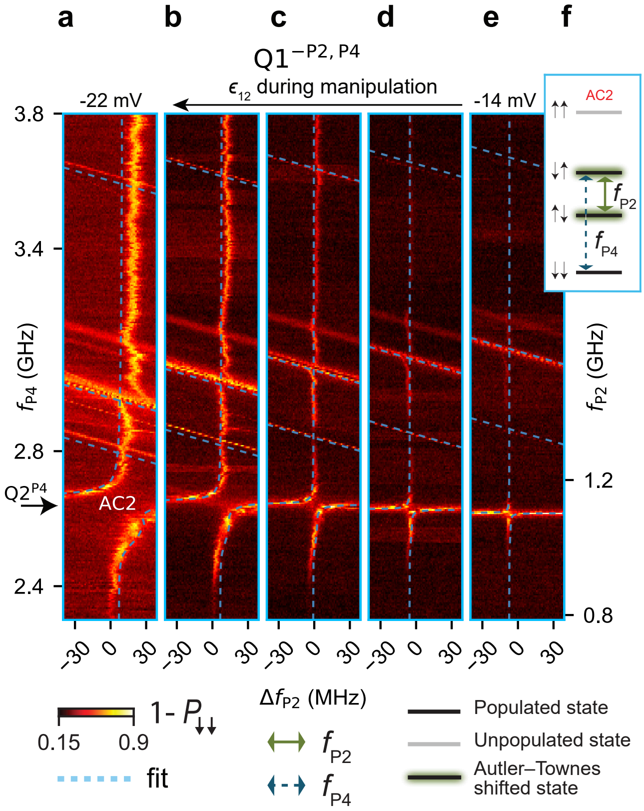

Figure 4.4: **Detuning dependence of the frequency anticrossings. a-e,** Bichromatic spectroscopy around the $f_{\mathrm{Q1}} = f_{\mathrm{P4}} - f_{\mathrm{P2}}$ resonance versus detuning voltage. The anticrossing AC2 originates from strong driving of the $|\uparrow\downarrow\rangle \rightarrow |\downarrow\uparrow\rangle$ transition with P2 via the Autler-Townes shift. The AC2 frequency gap narrows down as a function of detuning voltage due to suppressed virtual transition from the (1, 1) to the (2, 0) charge state. We overlay the transition lines expected from theory. **f,** Driven transitions at AC2, displaying the four lowest states from Fig.4.2c.

place via the S(0,2) and S(2,0) states and in the high detuning limit the transition through S(0,2) dominates the driving. At zero detuning, the two contributions become equal, while the Rabi frequency has a minimum.

The diminished efficiency of bichromatic operations near the charge-symmetry point supports the fundamental role of virtual interdot transitions as the underlying driving mechanism (Section 4.5.2). In Suppl. Note 8D [23], we discuss the limitations of our model and suggest that additional mechanisms, such as EDSR induced by g-tensor modulation, may be necessary to fully interpret all experimental observations [32–34].

4.4. CONCLUSIONS

Electric dipole spin resonance has enabled high-fidelity quantum gates on individual qubits, but a key challenge is the development of advanced operations for scalable control. Here, we have established bichromatic control of spin qubits, and turned challenges in EDSR [15] into an opportunity for addressable qubit control in larger arrays. Moreover, we showed the relevance of interdot motion in obtaining bichromatic and monochromatic driving. Furthermore, as the positions of the observed resonance anticrossings are predictible from the qubits parameters, we envision that, while on the one hand these can be exploited for the operation of dressed semiconductor qubits, on the other hand, these frequencies should be avoided when implementing bichromatic EDSR. Future experiments may focus on the optimization of bichromatic driving, for example by tuning parameters such as the interdot coupling, aiming to achieve high-fidelity control of large qubit arrays.

4.5. Supplementary

4.5.1. Power dependence of anticrossing AC2 $Q1^{-P2,P4}$, $Q2^{P4}$

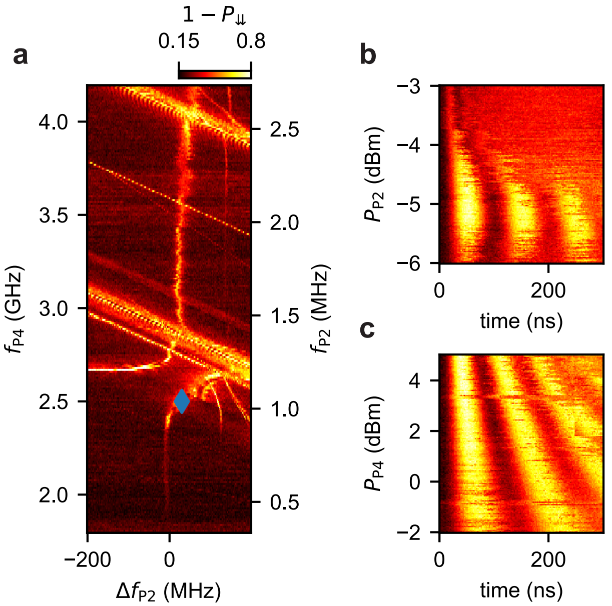

Figure 4.5: **Rabi oscillation of** $Q1^{P4,-P2}$ **as a function of microwave power applied to the two plunger gates at** $\epsilon_{12} = -24$ **mV. a,** EDSR spectroscopy map performed at ac driving power of $(P_{P2}, P_{P4}) = (-5, 3)$ dBm. **b, c** Rabi oscillations as a function of the power on the P2 and P4 driving gates. Here, the strong P2 driving field is resonant with the $\uparrow\downarrow \leftrightarrow \downarrow\uparrow$ transition. This results in a frequency shift of the Lamor frequency of the $\downarrow\downarrow \leftrightarrow \downarrow\uparrow$ transition when sweeping its power. In contrast, the weak P4 probe field does not alter the Lamor frequency, and sweeping its power leads, in fact, only to an increase in the Rabi frequency. This behaviour is consistent with the Autler-Townes splitting of the $\uparrow\downarrow$- and $\downarrow\uparrow$-state. Both plots are performed with $f_{P4} = 2.50$ GHz and $f_{P2} = 1.07$ GHz.

4.5.2. EDSR SPECTROSCOPY MAP AT ZERO DETUNING

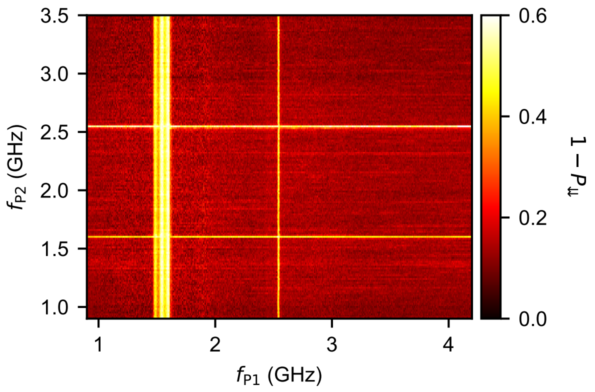

Figure 4.6: **Bichromatic EDSR spectroscopy at zero detuning voltage.** We prepare the double quantum dot system in the $\downarrow\downarrow$-state, apply the bichromatic control sequence, and measure the $1 - P_{\downarrow\downarrow}$ probability. The major difference to Fig. 2 is the preparation of the system at zero detuning. In this configuration, only two vertical and two horizontal lines are observed, the monochromatic transitions Q1 at ~ 1.60 GHz and Q2 at ~ 2.55 GHz. Note that this plot has been taken with f_{P1} and f_{P2}, instead of f_{P2} and f_{P4}. However, we have also observed the absence of the bichromatic signal for f_{P2} and f_{P4} when decreasing the detuning.

4.5.3. EXCHANGE COUPLING AT OPERATION POINT

Here, we determine the exchange coupling at our operation point $\epsilon_{12} = -20$ mV by measuring the resonance frequencies f_{Q1}, $f_{Q1\_}$, f_{Q2}, and $f_{Q2\_}$, defined as:

$$\mathrm{Q1} : \downarrow\downarrow \leftrightarrow \uparrow\downarrow \tag{4.1}$$

$$\mathrm{Q1\_} : \downarrow\uparrow \leftrightarrow \uparrow\uparrow \tag{4.2}$$

$$\mathrm{Q2} : \downarrow\downarrow \leftrightarrow \downarrow\uparrow \tag{4.3}$$

$$\mathrm{Q2\_} : \uparrow\downarrow \leftrightarrow \uparrow\uparrow \tag{4.4}$$

We compare f_{Q1} with $f_{Q1\_}$, and f_{Q2}, $f_{Q2\_}$, obtaining similar values of 55 MHz for f_{Q1} and 57 MHz for f_{Q2}.

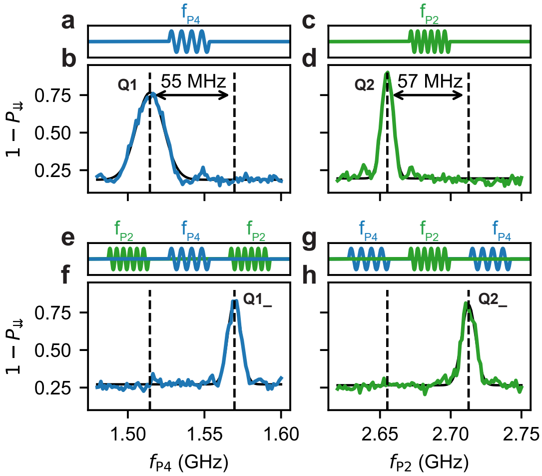

Figure 4.7: **Determination of exchange interaction via conditional EDSR spectroscopy. a, c, e, g,** Pulse sequences to prepare the control qubit in the two basis states and probe the target qubit. The blue (green) pulse is applied on P4 (P2) to control Q1 (Q2). **b, d, f, h** Measurement results from the corresponding pulse sequences to probe Q1, Q1_, Q2, and Q2_ respectively. The difference in resonance frequency concludes an exchange interaction of 56 MHz at a voltage of vP1 = -10 mV, and vP2 = 10 mV.

4.5.4. RESONANCE LINE IDENTIFICATION AND RABI ROTATIONS

To identify all the resonance lines of Figs. 3 and 4, we simulate the position of all the expected lines neglecting the Autler-Townes effect. We can write the considered bichromatic transitions as

$$m \cdot f_{\mathrm{P2}}^{\mathrm{offset}} + f_{\mathrm{P4}} = f_{\mathrm{Q}}, m = \pm 1, \tag{4.5}$$

where f_{Q} represents the qubit frequencies f_{Q1} and f_{Q2}. Our expected resonance lines follow

$$f_{\mathrm{res}} = n_{\mathrm{P2}} \cdot f_{\mathrm{P2}} + n_{\mathrm{P4}} \cdot f_{\mathrm{P4}}, \tag{4.6}$$

where $f_{\mathrm{P2}} = f_{\mathrm{P2}}^{\mathrm{offset}} + \Delta f_{\mathrm{P2}}$. Here, f_{res} can be f_{Q1}, f_{Q2}, or $f_{\mathrm{Q1}} + f_{\mathrm{Q2\_}}$, and n_{P2} and n_{P4} are integers referring to the considered harmonic. By plugging in Eq. (4.5) into Eq. (4.6), we obtain

$$f_{\mathrm{P4}} = \frac{f_{\mathrm{res}}}{m \cdot n_{\mathrm{P2}} + n_{\mathrm{P4}}} + \frac{n_{\mathrm{P2}}}{m \cdot n_{\mathrm{P2}} + n_{\mathrm{P4}}} \cdot (m \cdot f_{\mathrm{Q1}} - \Delta f_{\mathrm{P2}}) \tag{4.7}$$

We use these equations to calculate the expected resonance lines as visible in Fig. 4.8, Fig. 4.9, and Fig. 4.10.

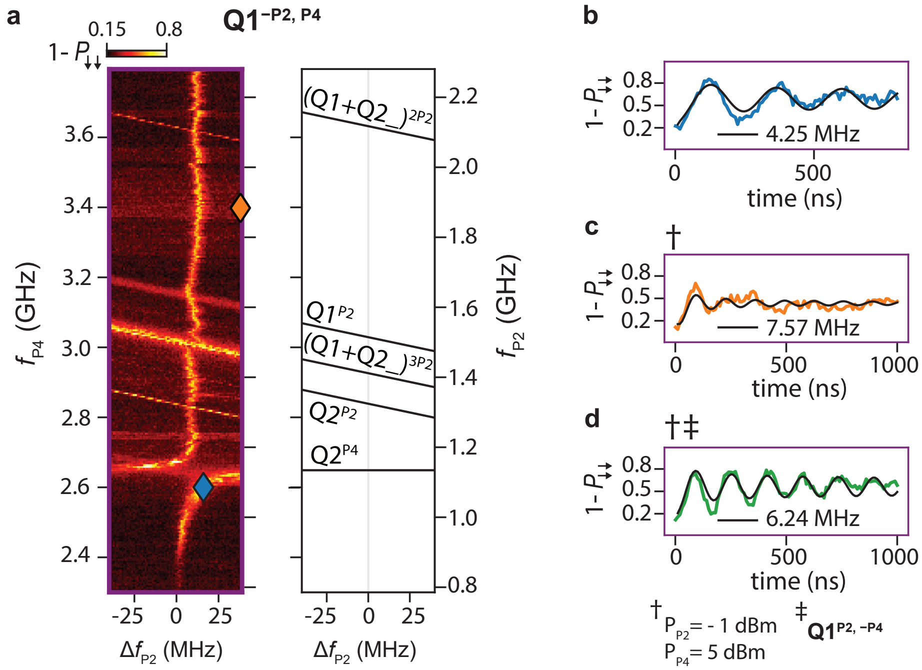

Figure 4.8: **Coherent Rabi control by bichromatic driving. a,** EDSR spectroscopy map of Q1$^{-\mathrm{P2,P4}}$ with two indicated positions, where Rabi oscillations have been performed. **b, c,** Rabi oscillation corresponding to the blue and orange marker in (a). The marker of (c) are shifted 40 MHz away from the bichromatic line because the power on both plungers had to be increased from -5 to -1 dBm for P2 and from 3 to 5 dBm for P4 to see any oscillations. **d,** Rabi oscillations with similar power settings as in (c), but the values of f_{P2} and f_{P4} have been swapped, driving Q1$^{\mathrm{P2,-P4}}$ instead of Q1$^{-\mathrm{P2,P4}}$. This makes the corresponding marker falls outside the depicted regime shown in (a).

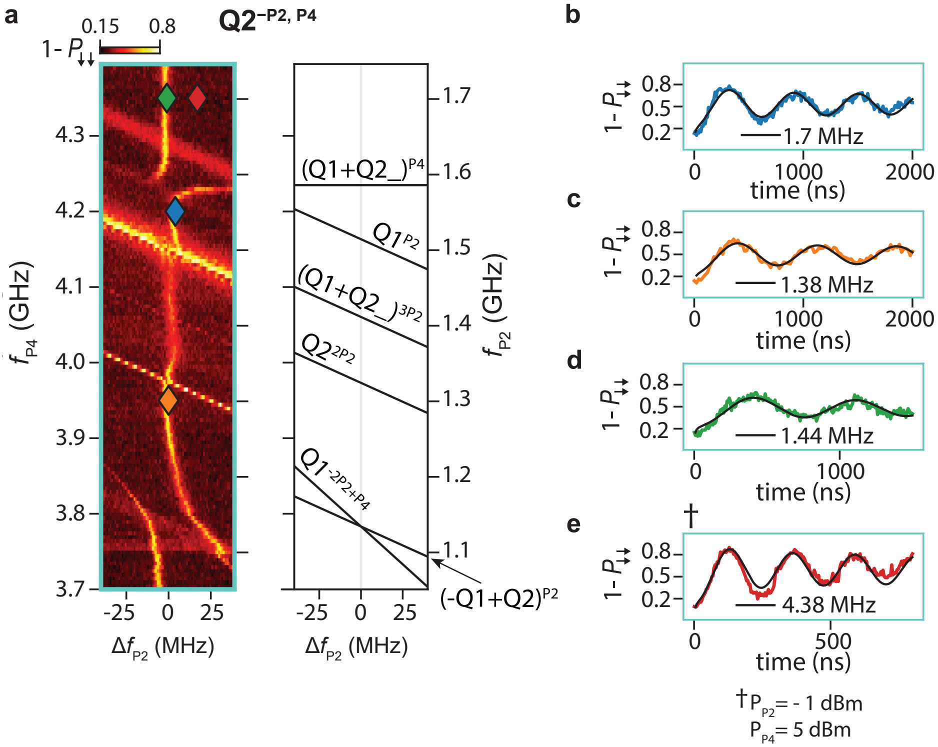

Figure 4.9: **Coherent Rabi control by bichromatic driving. a,** EDSR spectroscopy map of $Q2^{-P2,P4}$ with four indicated positions, where Rabi oscillations have been performed. **b, c, d, e** Rabi oscillation corresponding to the blue, orange, green, and red marker in (a). For the marker of (e) the power on both plungers increased from -5 to -1 dBm for P2 and from 3 to 5 dBm for P4.

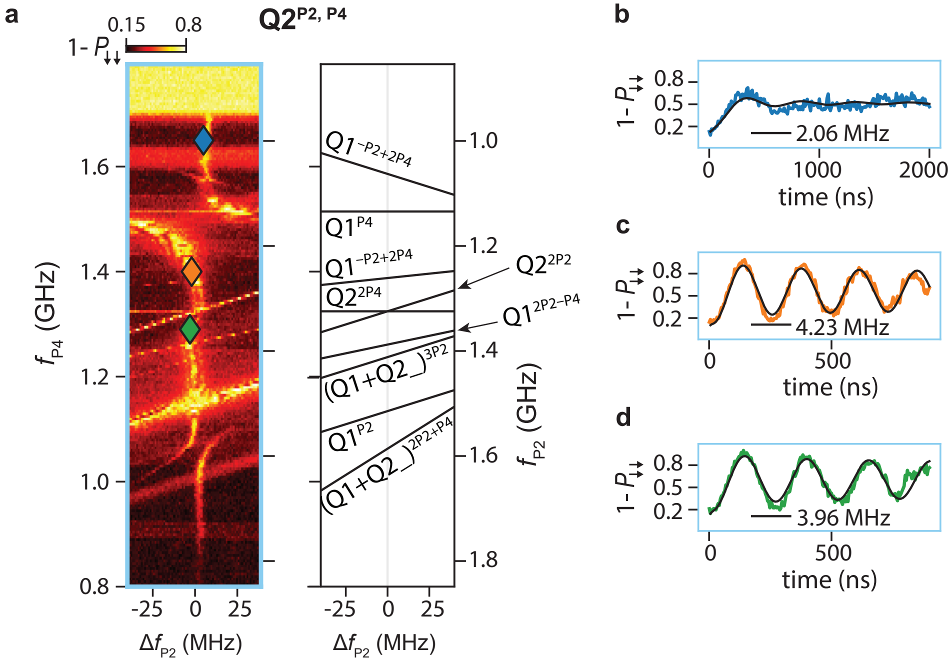

Figure 4.10: **Coherent Rabi control by bichromatic driving. a,** EDSR spectroscopy map of $Q2^{P2,P4}$ with three indicated positions, where Rabi oscillations have been performed. **b, c, d** Rabi oscillation corresponding to the blue, orange, and green marker in (a).

4.5.5. ATTENUATION

We approximate the amplitude arriving at the device by measuring the attenuation of the fridge lines of a comparable setup at cryogenic temperature, and the frequency response of an equivalent diplexer that is used to combine the microwave signal with the baseband pulses from the AWG. The measurement data with the Savitzky-Golay filter can be seen in Fig. 4.11. Since the measurement has only been performed on a similar setup, this constitutes only an approximation, but the general shape of the attenuation is expected to be the same.

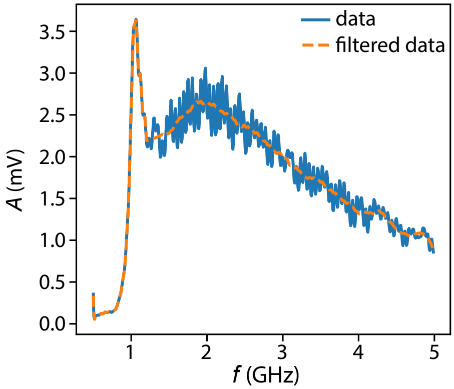

Figure 4.11: **Attenuation caused by diplexer and fridge cables.** Amplitude of the signal arriving at the device level considering $P_{\mathrm{P4}} = 2.5\,\mathrm{dBm}$. The signal of P2 with $P_{\mathrm{P2}} = -6\,\mathrm{dBm}$ is approximately the same since it has 8.5 dB less attenuation on the lines. A Savitzky-Golay filter is applied on the data, the result is shown with orange-dashed line.

4.5.6. MONOCHROMATIC RABI FREQUENCIES

Table 4.1 shows the measured monochromatic Rabi frequencies of the two considered qubits. Notably, $\mathrm{Q1\_}^{\mathrm{P4}}$ differs by a factor of two from $\mathrm{Q1}^{\mathrm{P4}}$. P_{mw} is the microwave power at the output of the signal generator, and corresponds to P_{P2} for Q1 and P_{P2} for Q2.

Table 4.1: Rabi characteristics of selected transitions.

Transition	f_{res} (GHz)	t_{Rabi} (ns)	f_{Rabi} (MHz)	P_{mw} (dBm)	A / mV
$Q1^{\mathrm{P4}}$	1.51	42.5	11.76	2.5	2.3
$Q1\_^{\mathrm{P4}}$	1.57	88.6	5.65	2.5	2.4
$Q2^{\mathrm{P2}}$	2.65	24.2	20.66	−6.0	2.3
$Q2\_^{\mathrm{P2}}$	2.74	22.6	22.10	−5.8	2.2

BIBLIOGRAPHY

[1] S. Tzu. *The Art of War*. Trans. by Lionel Giles. London: Luzac and Company, 1910. URL: `https://classics.mit.edu/Tzu/artwar.html`.

[2] A. Chatterjee et al. "Semiconductor qubits in practice". In: *Nature Reviews Physics* 3.3 (Mar. 2021), pp. 157–177. ISSN: 2522-5820. DOI: `10.1038/s42254-021-00283-9`. URL: `http://www.nature.com/articles/s42254-021-00283-9`.

[3] G. Burkard et al. "Semiconductor spin qubits". In: *Reviews of Modern Physics* 95.2 (June 2023), p. 025003. ISSN: 0034-6861. DOI: `10.1103/RevModPhys.95.025003`. URL: `https://link.aps.org/doi/10.1103/RevModPhys.95.025003`.

[4] L. M. K. Vandersypen et al. "Interfacing spin qubits in quantum dots and donors—hot, dense, and coherent". In: *npj Quantum Information* 3.1 (Dec. 2017), p. 34. ISSN: 2056-6387. DOI: `10.1038/s41534-017-0038-y`. URL: `http://www.nature.com/articles/s41534-017-0038-y`.

[5] D. Franke et al. "Rent's rule and extensibility in quantum computing". In: *Microprocessors and Microsystems* 67 (June 2019), pp. 1–7. ISSN: 01419331. DOI: `10.1016/j.micpro.2019.02.006`. URL: `https://linkinghub.elsevier.com/retrieve/pii/S014193311830293X`.

[6] R. Li et al. "A crossbar network for silicon quantum dot qubits". In: *Science Advances* 4.7 (July 2018), pp. 3960–3966. ISSN: 2375-2548. DOI: `10.1126/sciadv.aar3960`. URL: `https://www.science.org/doi/10.1126/sciadv.aar3960`.

[7] F. Borsoi et al. "Shared control of a 16 semiconductor quantum dot crossbar array". In: *Nature Nanotechnology* 19.1 (Jan. 2024), pp. 21–27. ISSN: 1748-3387. DOI: `10.1038/s41565-023-01491-3`. URL: `https://www.nature.com/articles/s41565-023-01491-3`.

[8] Z. György, A. Pályi, and G. Széchenyi. "Electrically driven spin resonance with bichromatic driving". In: *Physical Review B* 106.15 (Oct. 2022), p. 155412. ISSN: 2469-9950. DOI: `10.1103/PhysRevB.106.155412`. URL: `https://link.aps.org/doi/10.1103/PhysRevB.106.155412`.

[9] W. A. Coish and D. Loss. "Exchange-controlled single-electron-spin rotations in quantum dots". In: *Physical Review B* 75.16 (Apr. 2007), p. 161302. ISSN: 1098-0121. DOI: `10.1103/PhysRevB.75.161302`. URL: `https://link.aps.org/doi/10.1103/PhysRevB.75.161302`.

[10] E. A. Laird et al. "A new mechanism of electric dipole spin resonance: hyperfine coupling in quantum dots". In: *Semiconductor Science and Technology* 24.6 (May 2009), p. 64004. DOI: `10.1088/0268-1242/24/6/064004`. URL: `https://dx.doi.org/10.1088/0268-1242/24/6/064004`.

[11] E. I. Rashba. “Mechanism of half-frequency electric dipole spin resonance in double quantum dots: Effect of nonlinear charge dynamics inside the singlet manifold”. In: *Physical Review B* 84.24 (Dec. 2011), p. 241305. ISSN: 1098-0121. DOI: 10.1103/PhysRevB.84.241305. URL: https://link.aps.org/doi/10.1103/PhysRevB.84.241305.

[12] P. Scarlino et al. “Second-Harmonic Coherent Driving of a Spin Qubit in a Si/SiGe Quantum Dot”. In: *Physical Review Letters* 115.10 (Sept. 2015), p. 106802. ISSN: 0031-9007. DOI: 10.1103/PhysRevLett.115.106802. URL: https://link.aps.org/doi/10.1103/PhysRevLett.115.106802.

[13] J. Romhányi, G. Burkard, and A. Pályi. “Subharmonic transitions and Bloch-Siegert shift in electrically driven spin resonance”. In: *Physical Review B* 92.5 (Aug. 2015), p. 054422. ISSN: 1098-0121. DOI: 10.1103/PhysRevB.92.054422. URL: https://link.aps.org/doi/10.1103/PhysRevB.92.054422.

[14] K. Takeda et al. “Optimized electrical control of a Si/SiGe spin qubit in the presence of an induced frequency shift”. In: *npj Quantum Information* 4.1 (Oct. 2018), p. 54. ISSN: 2056-6387. DOI: 10.1038/s41534-018-0105-z. URL: https://doi.org/10.1038/s41534-018-0105-z.

[15] B. Undseth et al. “Nonlinear Response and Crosstalk of Electrically Driven Silicon Spin Qubits”. In: *Physical Review Applied* 19.4 (Apr. 2023), p. 044078. ISSN: 2331-7019. DOI: 10.1103/PhysRevApplied.19.044078. URL: https://link.aps.org/doi/10.1103/PhysRevApplied.19.044078.

[16] W. Gilbert et al. “On-demand electrical control of spin qubits”. In: *Nature Nanotechnology* 18.2 (Feb. 2023), pp. 131–136. ISSN: 1748-3387. DOI: 10.1038/s41565-022-01280-4. URL: https://www.nature.com/articles/s41565-022-01280-4.

[17] S. Bosco et al. “Phase-Driving Hole Spin Qubits”. In: *Physical Review Letters* 131.19 (Nov. 2023), p. 197001. ISSN: 0031-9007. DOI: 10.1103/PhysRevLett.131.197001.

[18] H. Levine et al. “High-Fidelity Control and Entanglement of Rydberg-Atom Qubits”. In: *Physical Review Letters* 121.12 (Sept. 2018), p. 123603. ISSN: 0031-9007. DOI: 10.1103/PhysRevLett.121.123603. URL: https://link.aps.org/doi/10.1103/PhysRevLett.121.123603.

[19] S. Ebadi et al. “Quantum phases of matter on a 256-atom programmable quantum simulator”. In: *Nature* 595.7866 (July 2021), pp. 227–232. ISSN: 1476-4687. DOI: 10.1038/s41586-021-03582-4. URL: https://doi.org/10.1038/s41586-021-03582-4.

[20] J. A. Valery et al. “Dynamical Sweet Spot Engineering via Two-Tone Flux Modulation of Superconducting Qubits”. In: *PRX Quantum* 3.2 (May 2022), p. 20337. DOI: 10.1103/PRXQuantum.3.020337. URL: https://link.aps.org/doi/10.1103/PRXQuantum.3.020337.

[21] N. W. Hendrickx et al. “A four-qubit germanium quantum processor”. In: *Nature* 591.7851 (Mar. 2021), pp. 580–585. ISSN: 0028-0836. DOI: 10.1038/s41586-021-03332-6. URL: https://www.nature.com/articles/s41586-021-03332-6.

[22] M. Lodari et al. “Low percolation density and charge noise with holes in germanium”. In: *Materials for Quantum Technology* 1.1 (Mar. 2021), p. 011002. ISSN: 2633-4356. DOI: 10.1088/2633-4356/abcd82. URL: https://iopscience.iop.org/article/10.1088/2633-4356/abcd82.

[23] V. John et al. “Bichromatic Rabi Control of Semiconductor Qubits”. In: *Physical Review Letters* 132.6 (Feb. 2024), p. 067001. ISSN: 0031-9007. DOI: 10.1103/PhysRevLett.132.067001.

[24] T. Hensgens et al. “Quantum simulation of a Fermi–Hubbard model using a semiconductor quantum dot array”. In: *Nature* 548.7665 (Aug. 2017), pp. 70–73. ISSN: 1476-4687. DOI: 10.1038/nature23022. URL: https://doi.org/10.1038/nature23022.

[25] W. I. L. Lawrie et al. “Spin Relaxation Benchmarks and Individual Qubit Addressability for Holes in Quantum Dots”. In: *Nano Letters* 20.10 (Oct. 2020), pp. 7237–7242. ISSN: 1530-6984. DOI: 10.1021/acs.nanolett.0c02589. URL: https://pubs.acs.org/doi/10.1021/acs.nanolett.0c02589.

[26] M. Baur et al. “Measurement of Autler-Townes and Mollow Transitions in a Strongly Driven Superconducting Qubit”. In: *Physical Review Letters* 102.24 (June 2009), p. 243602. ISSN: 0031-9007. DOI: 10.1103/PhysRevLett.102.243602. URL: https://link.aps.org/doi/10.1103/PhysRevLett.102.243602.

[27] M. A. Sillanpää et al. “Autler-Townes Effect in a Superconducting Three-Level System”. In: *Physical Review Letters* 103.19 (Nov. 2009), p. 193601. ISSN: 0031-9007. DOI: 10.1103/PhysRevLett.103.193601. URL: https://link.aps.org/doi/10.1103/PhysRevLett.103.193601.

[28] I. Hansen et al. “Implementation of an advanced dressing protocol for global qubit control in silicon”. In: *Applied Physics Reviews* 9.3 (Aug. 2022), p. 31409. ISSN: 1931-9401. DOI: 10.1063/5.0096467. URL: https://doi.org/10.1063/5.0096467.

[29] A. Laucht et al. “A dressed spin qubit in silicon”. In: *Nature Nanotechnology* 12.1 (Jan. 2017), pp. 61–66. ISSN: 1748-3395. DOI: 10.1038/nnano.2016.178. URL: https://doi.org/10.1038/nnano.2016.178.

[30] K. C. Miao et al. “Universal coherence protection in a solid-state spin qubit”. In: *Science* 369.6510 (2020), pp. 1493–1497. DOI: 10.1126/science.abc5186. URL: https://www.science.org/doi/abs/10.1126/science.abc5186.

[31] B. Martinez et al. “Hole spin manipulation in inhomogeneous and nonseparable electric fields”. In: *Physical Review B* 106.23 (Dec. 2022), p. 235426. ISSN: 2469-9950. DOI: 10.1103/PhysRevB.106.235426. URL: https://link.aps.org/doi/10.1103/PhysRevB.106.235426.

[32] M. Russ et al. “High-fidelity quantum gates in Si/SiGe double quantum dots”. In: *Physical Review B* 97.8 (Feb. 2018), p. 085421. ISSN: 2469-9950. DOI: 10.1103/PhysRevB.97.085421. URL: https://link.aps.org/doi/10.1103/PhysRevB.97.085421.

[33] N. W. Hendrickx et al. “Sweet-spot operation of a germanium hole spin qubit with highly anisotropic noise sensitivity”. In: *Nature Materials* 23.7 (July 2024), pp. 920–927. ISSN: 1476-1122. DOI: `10.1038/s41563-024-01857-5`. URL: `https://www.nature.com/articles/s41563-024-01857-5`.

[34] A. Sarkar et al. “Electrical operation of planar Ge hole spin qubits in an in-plane magnetic field”. In: *Physical Review B* 108.24 (Dec. 2023), p. 245301. ISSN: 2469-9950. DOI: `10.1103/PhysRevB.108.245301`. URL: `https://link.aps.org/doi/10.1103/PhysRevB.108.245301`.

5

SHARED CONTROL OF A 16 SEMICONDUCTOR QUANTUM DOT CROSSBAR ARRAY

The number of transistors on a microchip doubles approximately every two years. [1]

Gordon E. Moore

The efficient control of a large number of qubits is one of the most challenging aspects for practical quantum computing. Current approaches in solid-state quantum technology are based on brute-force methods, where each and every qubit requires at least one unique control line, an approach that will become unsustainable when scaling to the required millions of qubits. In this chapter, inspired by random access architectures in classical electronics, we introduce the shared control of semiconductor quantum dots to efficiently operate a two-dimensional crossbar array in planar germanium. We tune the entire array, comprising 16 quantum dots, to the few-hole regime and, to isolate an unpaired spin per dot, we confine an odd number of holes in each site. Moving forward, we demonstrate on a vertical and a horizontal double quantum dot a method for the selective control of the interdot coupling and achieve a tunnel coupling tunability from less than 3 GHz to more than 10 GHz. The operation of a quantum electronic device with fewer control terminals than tunable experimental parameters represents a compelling step forward in the construction of scalable quantum technology.

This chapter has been published as Francesco Borsoi, Nico W. Hendrickx, **Valentin John**, Marcel Meyer, Sayr Motz, Floor van Riggelen, Amir Sammak, Sander L. de Snoo, Giordano Scappucci, and Menno Veldhorst, Shared control of a 16 semiconductor quantum dot crossbar array, *Nat. Nanotechnol.* **19**, 21–27 (2024)

A fault-tolerant quantum computer will require millions of interacting qubits [2–4]. Scaling to such extreme numbers imposes stringent conditions on all the hardware and software components, including their integration [5]. In semiconductor technology, several decades of advancements have led to the integration of billions of transistor components on a single chip. A key enabler has been the ability to control such a large number of components with only a few hundred to a few thousand control lines [6, 7]. In quantum technology, such a game-changing strategy has yet to be embraced owing to the fact that qubits are not sufficiently similar to each other. Nowadays, leading efforts in solid state, such as superconducting and semiconducting qubits, all require that each and every qubit component is connected to at least one unique control line [8]. Clearly, this brute-force approach is not sustainable for attaining practical quantum computation.

The development of spin qubits in semiconductor quantum dots has strongly been inspired by classical semiconductor technology [9–11]. Advanced semiconductor qubit systems are based on CMOS-compatible materials and even foundry-manufactured qubits have been realised [12, 13]. In addition, it is anticipated that the small qubit footprint and compatibility with (cryo-)CMOS electronics will open up avenues to build integrated quantum circuits [14, 15]. To enable the efficient control of large qubit architectures with a sustainable number of control lines, proposals of architectures inspired by classical random access systems have been put forward [16, 17]. However, their practical realisation has been so far prevented by device quality and material uniformity.

In this chapter, we take the first step toward the sustainable control of large quantum processors by operating semiconductor quantum dots in a crossbar architecture. This strategy enables the manipulation of the most extensive semiconductor quantum device with only a few shared-control terminals. This is accomplished by exploiting the high quality and uniformity of strained germanium quantum wells [18], by introducing an elegant gate layout based on diagonal plunger lines and double barrier gates, and by establishing a method that directly maps the transitions lines of charge stability diagrams to the associated quantum dots in the grid. We operate a two-dimensional 16 quantum dot system and demonstrate the tune-up of the full device to the few-hole regime. In this configuration, we also prove the ability to prepare all the quantum dots in the odd charge occupation, as a key step for the confinement of an unpaired spin in each site [19, 20]. We then introduce a random access method for addressing the inter-dot tunnel coupling and find a remarkable agreement in the response of two vertically- and horizontally-coupled quantum dot pairs. We also discuss some critical challenges to efficiently operating future large quantum circuits.

5.1. A TWO-DIMENSIONAL QUANTUM DOT CROSSBAR ARRAY

Our shared-terminals control approach for a two-dimensional quantum dot array with dots Q1, Q2t,...Q7 is based on a multi-layer gate architecture (Figs. 5.1a-d). We use two barrier layers (with gates UBi and LBi with $i \in [1,8]$) to control the interdot tunnel couplings, and exploit a layer of plunger lines (Pi with $i \in [1,7]$) to vary the on-site energies (Fig. 5.1c). In contrast to brute-force implementations, here a single plunger gate is employed to control up to four quantum dots, and an individual barrier up to six nearest-neighbours interactions. In analogy with classical integrated circuits, this strategy en-

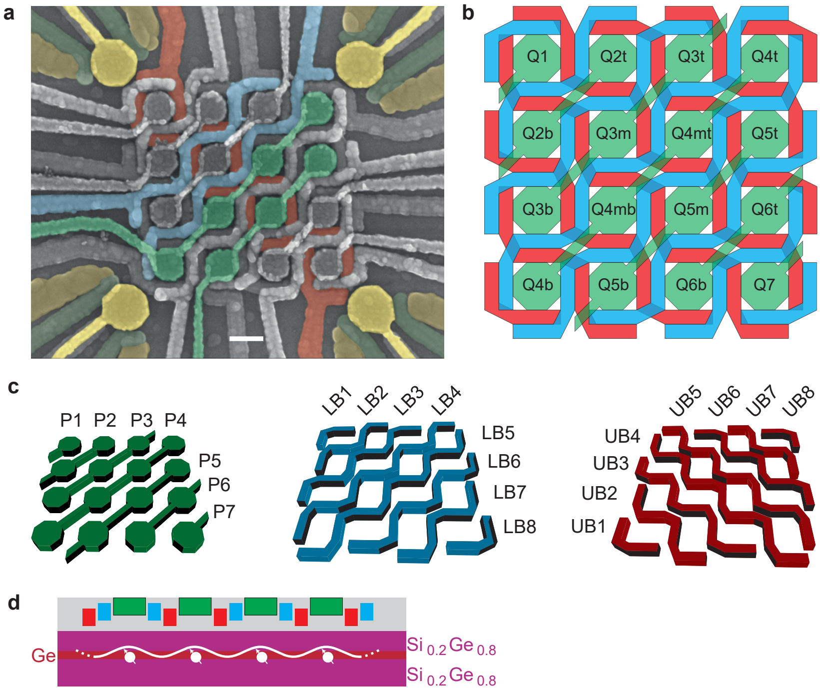

Figure 5.1: **A 16 quantum dot crossbar array. a,** False-colour scanning electron microscopy image of the crossbar array device. The architecture consists of two staircase barrier gate layers (two lines of each layer are shown in red and blue), and one plunger gate layer (two lines are illustrated in green). 16 quantum dots are defined under the plungers, while four charge sensors in the form of single-hole transistors are located at the corners (ohmic contacts in orange, barriers in dark green, and plungers in yellow). The scale bar corresponds to 100 nm, which is also the size of the designed plunger gate diameter. This shared-control approach enables to control a number of quantum dots (g) with a sublinear number of control terminals (T). Here, the scaling is given by $T = 6g^{1/2} - 1$ (Fig. 5.15). **b,** Schematic illustration of the device and labeling of each quantum dot. We choose to label the quantum dots after their positions on their controlling plunger line, e.g., the quantum dot Q6b(t) is located on the bottom (top) site controlled by the plunger line P6. **c,** Shared-control elements: from the top of the gate stack, seven P plunger gates, eight LB barrier gates, and eight UB barrier gates. The overlay of these layers is visible in **(b)**. **d,** Schematic cross-section of the device. Holes are isolated in quantum dots in a 55 nm-deep germanium quantum well in a silicon-germanium heterostructure grown on a silicon wafer.

ables to manage a number of experimental parameters (i.e., dot energies and interdot couplings) with a sub-linear number of control terminals, an approach that may overcome, among other aspects, the wiring interconnect bottleneck of large-scale spin qubit arrays (Fig. 5.15) [7, 8].

To monitor the quantum dot array, we make use of charge sensing techniques [19]. Four single-hole transistors at the corners of the array (named after their cardinal positions: NW as north-west, NE as north-east, SW as south-west and SE as south-east) act as charge sensors as well as hole reservoirs for the array. The simultaneous read-out of their electrical response in combination with fast rastering pulse schemes enables us to continuously measure two-dimensional charge stability diagrams in real-time (i.e., in video-mode technique), while updating the dc gate voltages controlling the array [21, 22].

To bring the device in the 16 quantum dots configuration, we identify an alternative strategy to the tune-up methods established for individually-controlled quantum dot devices [23]. We begin by lowering all gate voltages to starting values based on previous experiments and by defining a set of virtual gates as linear combinations of real gates [23–25]. Such virtual gates are defined to eliminate the crosstalk to the charge sensors and to independently control the on-site energies [24, 25]. Here, we will refer to vPi as the virtual gate associated to the actual gate Pi.

We continue the tuning of the device by adjusting the gates controlling the quantum dots at the corner (i.e., those closest to the charge sensors) until we accumulate the first few holes as signaled by the first addition lines in charge stability diagrams. We then proceed with the tune-up of the adjacent dots and finish with the quantum dots furthest to the sensor. Owing to the homogeneity of our heterostructure [26] and the symmetry of our gate layout, the accumulation of the first few holes in quantum dots controlled by the same plungers occurs at similar gate voltages.

Rather, challenges in tuning up the array are mainly due to elements outside the array. In fact, we observe that small variations of the gate voltages impact the electrostatics of the dense gate fanout area, which in turn affects the charge sensors and the readout quality. Furthermore, specific gate settings cause unintentional quantum dots under the gate fanout, which restrict the operational window. Altogether, these issues are a challenge for the implementation of automated tuning methods [27], but we envision that the integration of a lower layer of “screening" gates or the implementation of the gate fanout in the third dimension [28] can mitigate this issue (section 5.6.2).

FROM MULTI-DOT CHARGE STABILITY DIAGRAMS TO QUANTUM DOT IDENTIFICATION

Moving forward, a direct result of our control approach is the fact that, upon sweeping the voltage of a plunger gate controlling n quantum dots, up to n sets of charge transitions can be observed, each associated with (un)loading an additional hole in one of the n quantum dots. For the case of vP2 and vP3, this results in the charge stability diagram shown in Fig. 5.2 where a number of vertical and horizontal charge addition lines marking well separate charge states are visible. However, because of our control approach, a priori it is unknown to which of the Q3 (Q2) quantum dots these vertical (horizontal)

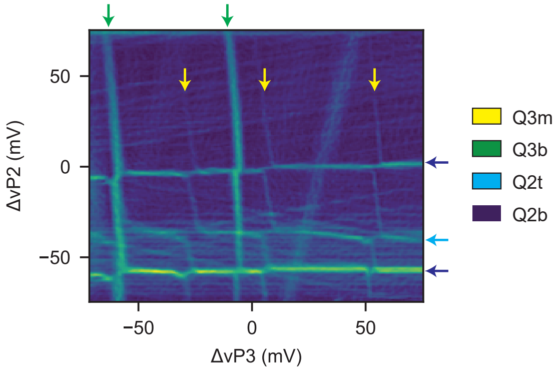

Figure 5.2: **Multi-dot charge stability diagrams** Few-hole charge stability diagram obtained by combining the signal gradients of the SW and NW charge sensors. The labels indicate for each addition line the corresponding quantum dot. At (0,0) the fillings of Q2t, Q2b, Q3t, Q3m, and Q3t are 0, 0, 0, 3, and 0, respectively.

lines are associated.

Here, we solve this problem by establishing a statistical method that maps such transition lines to the respective quantum dot. In our protocol, we first evaluate the shift of the charge transition lines induced by a voltage variation of each barrier gate to estimate the (normalized) capacitive coupling λ between each barrier gate and the associated quantum dot (Figs. 5.3a, b). Because the two barrier layers form a grid of lines and columns, we can use their capacitive couplings to infer the spatial location of the quantum dot in the array. For this purpose, we consider the normalised capacitive couplings of the two orthogonal barrier sets, λ_{vUB} and λ_{vLB}, as two independent probability distributions. We then use λ_{vUB} and λ_{vLB} to calculate the combined probability W on each of the 16 sites (Fig. 5.3c, section 5.5). Finally, our protocol ends assigning the site with the maximum probability to the quantum dot loaded via the specific charge addition lines. In practice, W quantifies how much an electric field generated on each site is perceived by a hole in a specific quantum dot site. Hence, a low (high) W value identifies a location that is weakly (strongly) coupled to the analysed quantum dot.

In Figs. 5.3a-c, we show how this routine is effective for distinguishing and characterising the three Q3 quantum dots, whereas similar results are obtained also for the remaining dots in the grid (Figs. 5.8, 5.9-5.13, 5.14). The demonstrated ability of labelling multi-quantum dot charge stability diagrams makes this method an important tool in the tune-up of large quantum dot devices.

5.2. QUANTUM DOT OCCUPANCIES

Whilst useful in reducing drastically the number of control terminals, a crossbar approach is effective for spin-based quantum computing if it enables to isolate a single or an unpaired spin in the individual quantum dots [9, 17]. Here, we demonstrate the tune-up of the array to an odd-charge occupancy configuration with 11 quantum dots filled with one hole, and five quantum dots filled with three holes.

Our setup allows for fast charge stability maps, albeit of a size that it is often insuf-

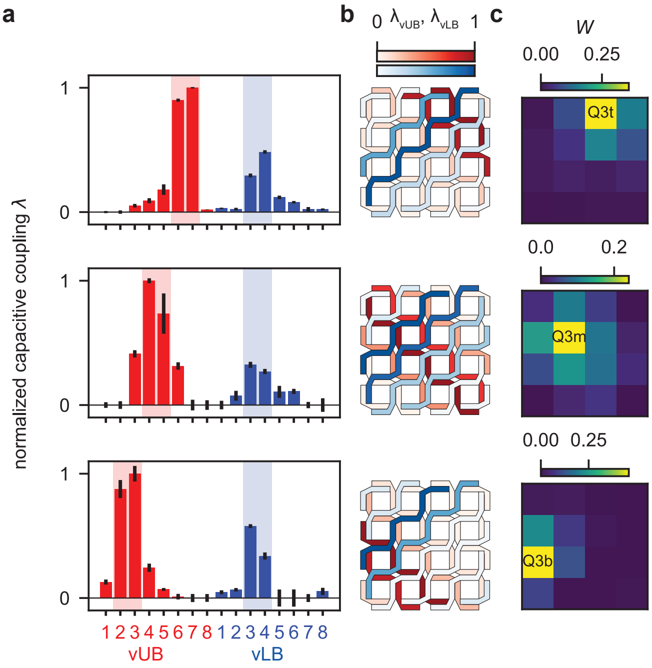

Figure 5.3: **Quantum dot identification. a,** Bar plots of the (normalized) capacitive couplings λ of the barrier gates to the transition lines (in red for the vUB, and in blue for the vLB virtual gates) obtained by analyzing three different sets of transition lines coupled to the virtual plunger vP3. Middle and bottom panels are extracted from the shift of the transition lines at ~ (-20, -63) and (-15, -7) in Fig. 5.2, respectively. The top panel (relative to dot Q3t) is obtained from a measurement shown in Figs. 5.21g,h, where the transition line is more visible. Red and blue backgrounds are added to emphasize the two barriers with the highest couplings. The data points correspond to the peak of the chart bars as well as the centers of the error bars. Each error bar is the standard deviation of the parameter obtained from the linear fit. **b,** Device layout with the capacitive couplings color-coded on the filling of the gate lines. Here, both the vUB and vLB capacitive couplings, λ_{vUB} and λ_{vLB}, are normalized to their maximum values. **c,** Visualisation of the probability (W) calculated from of the shift of the three sets of addition lines (see section 5.5 for details). The comparison of the top, middle, and bottom panels of **a, b, c** clearly distinguishes the three Q3 quantum dots.

ficient to fully visualise the absence of further transition lines in the zero charge state. Therefore, we perform repeated scans of the kind ΔvPx vs ΔvPy, while increasing the dc voltage vPx in discrete steps of 10 mV. We stop the sequence when the quantum dot controlled by vPx, say Qx, is fully depleted. We present these emptying sequences in videos 1-12, which can be found in the supplementary of Ref [29].

In general, multi-dot transition lines, low charge sensitivity, spurious quantum dots and low reservoir-tunnel coupling may complicate the assessment of the occupancy. In fact, quantum dots that are located in the core of the array are loaded/unloaded by means of cotunneling processes via the outer dots [30], leading to latching transition lines and elongated charge interdot transitions when the reservoir-dot tunnelling time approaches the timescale of our scan (~ 0.01 s) [20, 31–33]. We note that adding reservoirs within the array may reduce this effect and simplify the tune-up. However, opti-

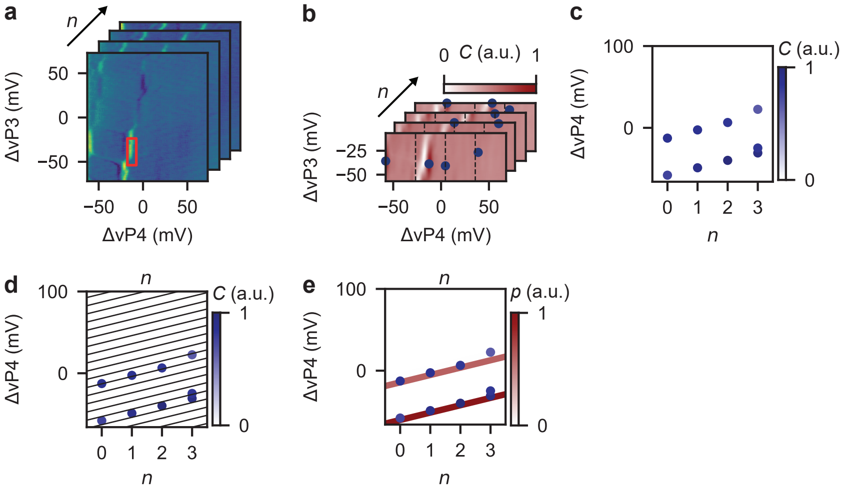

Figure 5.4: **Charge transition detection algorithm. a-e** Illustration of the detection algorithm on the Q4b charge transition lines. From the charge stability diagrams in **(a)**, labeled with the index n, we compute the image correlation (C) maps in **(b)**, with the reference feature in the red box in **(a)** containing a portion of a Q4b charge transition. After splitting the correlation maps in 4 vertical sections (dashed lines in **(b)**) we determine the local maxima in each of them (blue markers in (**b**)). We track the thresholded local maxima across all the scans of the sequence, as displayed in **(c)**. We quantify the occurrence of high-correlation features along potential lines with a fixed expected slope and varying intercept, black lines in **(d)**. In **(d)**, we show only one-fifth of the actual sampling lines for clarity. In **(e)**, we color-code all the potential lines according to their associated p. Emerging peaks in p (i.e., red traces) identify the actual first two Q4b charge transitions.

mal qubit operation and high qubit connectivity may require low tunnel coupling between qubits and reservoirs. Thus, initialising the array without having each quantum dot strongly coupled to a reservoir is highly relevant [7, 11, 34].

To track specific transition lines in complex multi-dot charge stability diagrams, we have defined an algorithm based on image correlation analysis, which may be refined by machine learning methods [27, 35–37]. First, we select a small window from a specific charge stability diagram in the sequence containing a Qx charge addition line. We refer to this as the Qx reference feature as shown in Fig. 5.4a for Q4b. Second, we compute digital image correlation (C) maps of all the charge stability diagrams in the sequence with respect to the previously defined reference feature. Then, we divide the correlation maps into four sections (delimited by the vertical dash lines in Fig. 5.4b), with a size that is smaller than the typical addition voltage. This choice results in a high probability of having, at most, a single occurrence of a Qx charge transition per section. We then select the coordinates of the points with maximum correlation in each section, and threshold them to ensure that only points with high correlation are passed.

Because of the dc voltage step between each map, the same high-correlation feature, if reproducible, is then expected to be found at a ΔvPx value that is 10 mV higher than in the previous charge stability diagram (Fig. 5.4c). Therefore, in a plot of coordinates with high correlation vs scan index (n), we expect these points to follow a line with a well-defined slope of 10 mV/scan. To assess the presence of possible charge transition lines within the clouds of high-correlation coordinates, we consider a series of potential lines with slope 10 mV/scan and varying intercept (Fig. 5.4d). We then define the quantity p that accounts for the density of high-correlation points falling along each line.

Figs. 5.5a-p present the detected coordinates with high correlation of all the 16 quantum dots as a function of scan index and associated stepped voltage, together with all possible transition lines plotted with a colour that is proportional to their respective p. High values of p are rendered as visible lines intercepting several high-correlation features, enabling a rapid visualisation of the charge transition lines of all the quantum dots of the array.

By comparing all the panels, we can resolve a small shared-gate voltage window around the tuning point defined by ΔvPx =0 at the largest n where all the quantum dots are in the odd charge regime.

While the algorithm is successful in detecting the transition lines of every quantum dot, we note that it returns a false-positive line for the case of Q3b. The first visible Q3b transition, labelled with a star in Fig. 5.5i is in reality an outlier due to a detected feature at $n = 0$ and ΔvP3 ~ 55 mV not related to Q3b, but due to an artefact of a charge sensor. While the algorithm is remarkably strong in detecting the transitions, a definite conclusion on the odd occupancy is most likely only achieved by performing coherent operation on each qubit.

5.3. INTERDOT COUPLINGS CONTROL

The ability to selectively tune the interdot coupling in a quantum dot architecture is crucial for generating exchange-based entanglement between semiconductor qubits [9]. Here, inspired by the word and bitlines approach as in dynamic random-access memories [14, 17], we exploit the double barrier design to spatially define and activate unique points in the grid structure. Conceptually, each two-barrier intersection point can be set by the respective voltages in the four configurations: (ON, ON), (ON, OFF), (OFF, ON), (OFF, OFF). For selective two-qubit operations in qubit arrays, the voltage set points should be calibrated such that only when both barriers are in the ON-state a two-qubit interaction is activated, leaving all the other pairs non-interacting (also see Fig. 5.16). Here, we implement a proof-of-principle of this method by demonstrating two-barrier control of the interdot tunnel coupling in a horizontal and a vertical pair of quantum dots. To this end, we investigate the tunnel coupling variations of the horizontal Q6b-Q7 and vertical Q6t-Q7 quantum dot pairs as a function of the two intersecting barriers. Starting from the respective UB4 and LB7 gates, we define the virtual barriers $\mathrm{t}_{6\mathrm{b}7}$ and $\mathrm{j}_{6\mathrm{b}7}$ (section 5.5.2), which separate the quantum dots Q6b and Q7, while keeping their detuning (e67) and on-site (U67) voltages constant at the (3,1)-(2,2) Q6b-Q7 interdot transition (Fig. 5.6a). After obtaining the detuning lever arm $\alpha_{\epsilon_{67}}$ to convert the detuning voltage into an energy scale ($\Delta\epsilon_{67} = \alpha_{\epsilon_{67}} \cdot \Delta\mathrm{e}67$), we evaluate the strength of the interdot couplings by analysing the charge polarisation lines along the detuning axis at ΔU67 = 0 (Figs. 5.6b, c) [38]. By performing this measurement systematically, we demonstrate that the tunnel coupling can be controlled effectively by both barriers (Figs. 5.6d,e). At values of ($\mathrm{t}_{6\mathrm{b}7}$,$\mathrm{j}_{6\mathrm{b}7}$) = (−270, −380) mV, the coupling is virtually OFF, but our method is inherently not accurate for $t_c \leq 3$ GHz, because the thermal energy dominates the broadening of the polarisation line [33, 38]. In contrast, upon activating both barriers at

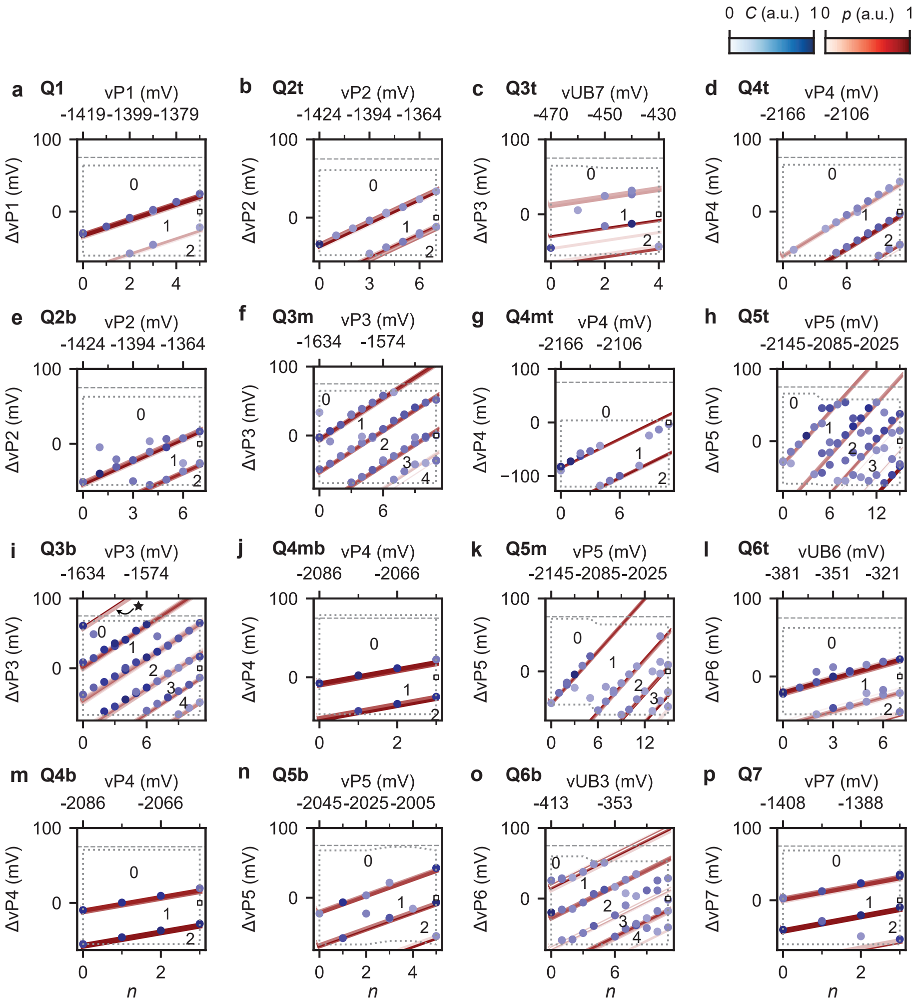

Figure 5.5: **Counting holes in a 16 quantum dot array. a-p,** Same as Fig. 5.2/e for all the 16 quantum dots. The numbers in each plot indicate the quantum dot fillings, according to the algorithm. In 3 cases (Q3t, Q6b, Q6t) out of 16, we step a barrier, rather than a plunger, to better isolate the shift of only one of the dots under the same plunger line. High-correlation features (blue points) are found up to the bounds of the area of the datasets analyzed by the protocol, highlighted by the dotted grey polygon. The horizontal dashed line indicates the actual limit of the dataset. The star in panel **(n)** indicates a false-positive transition line.

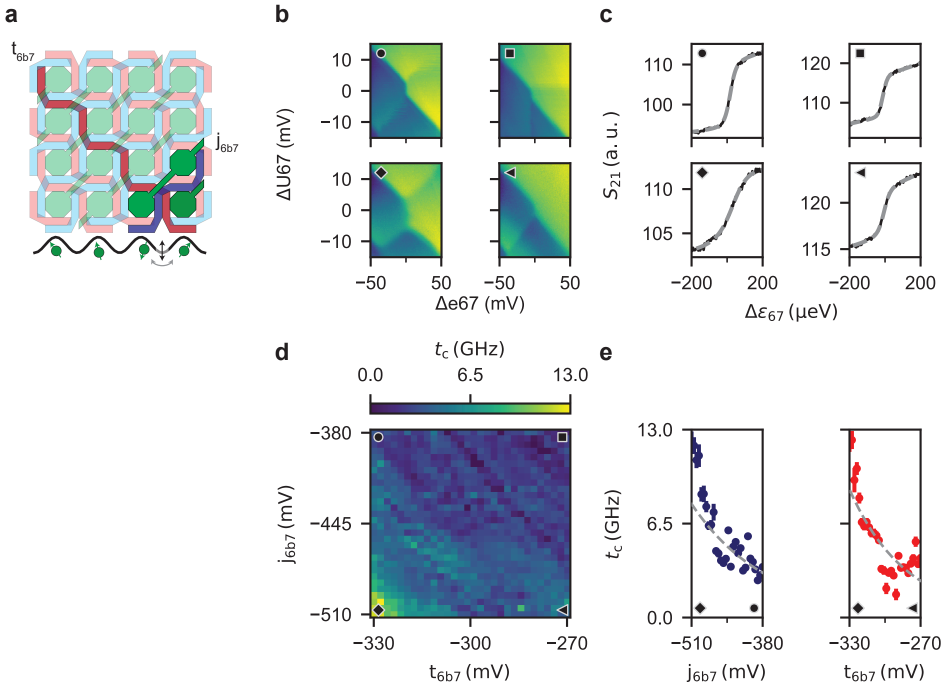

Figure 5.6: **Addressable control of the horizontal interdot tunnel coupling using double barrier gates. a** Schematics of the crossbar indicating the two intersecting barriers (in red and blue) controlling the Q6b-Q7 interdot tunnel coupling. **b** Exemplary charge stability diagrams taken via reflectometry methods showing the (Q6b,Q7) charge states at four different virtual barrier voltage configurations near the (3,1)-(2,2) transition. At the centre of the panels, the vertical interdot transition line is clearly visible. The circle, square, diamond, and triangle markers correlate each map to the voltages, $(t_{6b7}, j_{6b7}) = -(330, 380), (270, 380), (330, 510), (270, 510)$ mV, respectively. **c** Charge polarisation traces (black) relative to panel **(b)**, together with best fit (dashed grey). **d** Colour map of the two-axis controlled tunnel coupling of the systems Q6b-Q7, with markers located at the respective voltages. We note that a variation of a virtual barrier corresponds to the same variation of the real gate. **e** Vertical (left panel) and horizontal (right panel) linecuts of **(d)** at $t_{6b7} = -330$ mV and $j_{6b7} = -510$ mV, respectively. Grey traces are fits with an exponential function of the data, from which we obtain the four effective barrier lever arms (section 5.5).

$(t_{6b7}, j_{6b7}) = (-330, -510)$ mV, the tunnel coupling is turned on following approximately an exponential trend (section 5.5.4). Within the displayed voltage range, we can tune it well above 10 GHz, much higher than in the configuration in which only one barrier is activated. We perform the same experiment on the dots pair Q6t-Q7 by defining the virtual barriers t_{6t7} and j_{6t7} based on the gates UB5 and LB7, respectively (Fig. 5.7a and section 5.5). Using the same barrier voltages window as for Q6b-Q7, we find that the coupling tunability of the pair Q6t-Q7 is comparable to the previous pair, with a virtually OFF state (≤3 GHz) at $(t_{6t7}, j_{6t7}) = (-270, -380)$ mV, and with a ON state reaching 20 GHz at $(t_{6t7}, j_{6t7}) = (-330, -510)$ mV (Figs. 5.7b-e). These results are corroborated by the two-barrier tunability of the interdot capacitive coupling for both double-dot systems (shown in Fig. 5.17) and by the tunability of another dot pair (shown in Fig. 5.18). We envision that for rapid qubits exchange operations at the charge symmetry point, the required

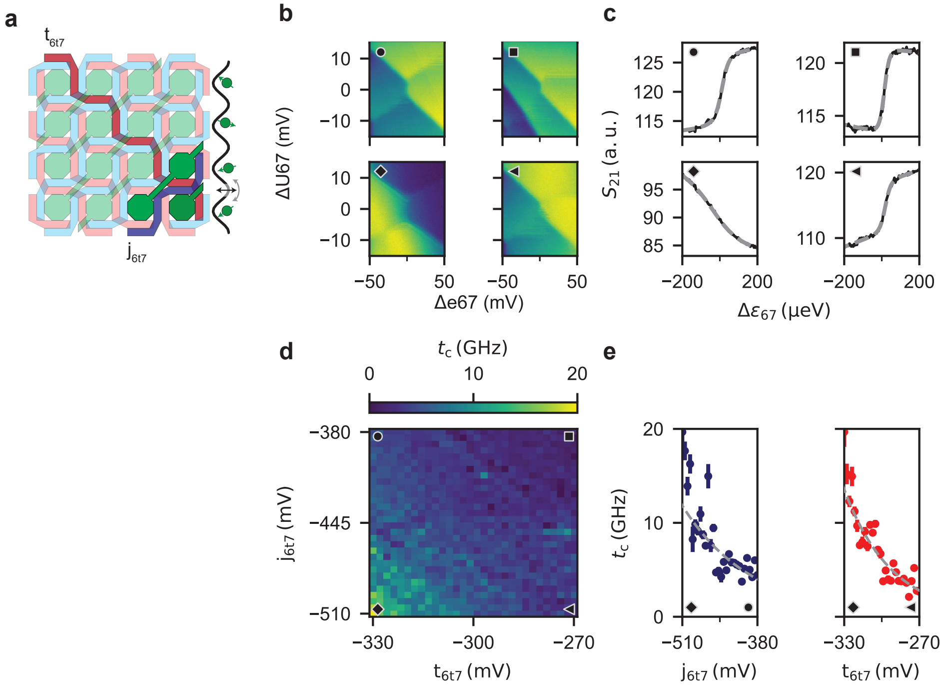

Figure 5.7: **Addressable control of the vertical interdot tunnel coupling using double barrier gates.** Analogous to Fig. 5.6 but for the vertical quantum dot pair Q6t and Q7 and barrier voltages t_{6t7}, j_{6t7}.

barrier voltage window might be different from our measurable window via polarisation lines. Specifically, for state-of-the-art values of ON (OFF) exchange interaction of 50 MHz (10 KHz) and a typical charging energy of 1 mV, the required tunnel coupling is ∼ 2 (0.02) GHz, which can be better calibrated via qubit spectroscopy techniques [21, 39, 40].

5.4. CONCLUSIONS

By implementing a strategy that allows to address a large number of quantum dots with a small number of control lines, we have operated the most extensive two-dimensional quantum dot array so far. With this approach, the number of gate layers is independent of the grid size, which greatly simplifies the nanofabrication of quantum dot arrays. With the introduction of a double barrier paradigm and a statistical method for labelling multi-dot charge stability diagrams, we have demonstrated two critical requirements for quantum logic in shared-control architectures: the tunability of 16 interacting quantum dots into an odd charge state with an unpaired spin and the proof of principle of a method for the selective control of the interdot tunnel coupling, which is crucial for the control of the exchange interaction. We envision that future crossbar arrays may find applications in large and dense two-dimensional quantum processors or as registers that are coupled via long-range quantum links for networked computing.

5.5. METHODS

Each charge sensor is galvanically connected to a NbTiN inductor with an inductance of a few μH forming a resonant tank circuit with resonance frequencies of ~ 100 MHz. In our experiment we have observed only three out of four resonances, likely due to a defect inductor. Moreover, because two resonances overlap significantly, we mostly avoid using reflectometry (unless explicitly stated in the text) and use fast dc measurements with bandwidth up to 50 kHz. Charge stability diagrams here typically consists of a 150x150 pixels scan with a measurement time per pixel of 50 μs. Throughout this article, we refer to Δgi to identify a ramp supplied by an AWG to the gate gi with respect to a fixed dc reference voltage. To enhance the signal-to-noise ratio, we average the same map 5-50 times, obtaining a high-quality map within a minute.

5.5.1. TUNE-UP DETAILS

Throughout the experiment, we have tuned all 16 quantum dots of the device two times. In the first run, the gate voltages were optimised to minimise the number of unintentional quantum dots in order to better visualise and characterise the crossbar quantum dots (Fig. 5.2, 5.3, 5.21 and 5.22). In the second run, the stray dots were neglected to tune the quantum dot array into a global odd-occupation regime (Fig. 5.5). Between the two tune-up cycles, the gate voltages were reset to zero without thermal cycling the device. The protocol followed in the two tuning procedures was the same, but the need for emptying accidental quantum dots in the first session led to some restrictions in the voltage window of certain gates. The starting gate voltage values for the tune-up are -300 mV for the barriers and -600 mV for the plungers. In Fig. 5.23 we display the dc gate voltages relative to the measurements displayed in Fig. 5.5, with the crossbar array tuned in the odd-charge occupation. In this regime, we also study the variability (section 5.6.7) of the first hole voltage onset in each dot obtaining -1660 ± 290 mV (Fig. 5.24). Furthermore, we characterise the variability of the transition lines spacing to be $\sim 10-20\%$ as a metric for the level of homogeneity of the array (Fig. 5.25) [41]. Strategies to further reduce these variations and device design are discussed in section 5.6.2.

The odd charge occupancy is demonstrated by emptying each quantum dot as shown in Suppl. Videos 1-12 [29]. All the datasets underlying Fig. 5.5 and in Suppl. Videos 1-12 are taken at the same gate voltage configuration on the same day. During the experiment, the gate UB8 did not function properly, possibly due to a broken lead. To compensate for this effect and to enable charge loading in the dots P3t and P5t, we set UB7 at a lower voltage compared to the other UB gates. Additionally, LB1 is set at a comparatively higher voltage to mitigate the formation of accidental quantum dots under the fanout of LB1 and P1 at lower voltages. The first addition line of such an accidental quantum dot is visible as a weakly interacting horizontal line in Fig. 5.4a.

5.5.2. VIRTUAL MATRIX

The matrix M defined by $\vec{G} = M \cdot v\vec{G}$, with virtual gates $v\vec{G}$ and actual gates $\vec{G}$ is shown as a colour map in the supplemental material of Ref. [29]. For the tunnel coupling experiments presented in Fig. 5.6 and 5.7, we employ additional virtual gate systems for achieving independent control of the detuning voltage e67 and U67, and of the interdot interactions via virtual barriers t_{6b7}, j_{6b7}, t_{6t7} and j_{6t7}. With SE_P the SE plunger gate, we write:

$$\begin{pmatrix} \mathrm{P5} \\ \mathrm{P6} \\ \mathrm{P7} \\ \mathrm{SE\_P} \end{pmatrix} = \begin{pmatrix} 0.04 & -1.2 \\ -0.5 & 0.9 \\ 0.492 & 0.9 \\ -0.08 & -0.26 \end{pmatrix} \begin{pmatrix} \mathrm{e67} \\ \mathrm{U67} \end{pmatrix}$$

$$\begin{pmatrix} \mathrm{P6} \\ \mathrm{P7} \\ \mathrm{UB5} \\ \mathrm{LB7} \\ \mathrm{SE\_P} \end{pmatrix} = \begin{pmatrix} -1.28 & -0.33 \\ -1.18 & -0.72 \\ 1 & 0 \\ 0 & 1 \\ 0.15 & -0.01 \end{pmatrix} \begin{pmatrix} \mathrm{t_{6t7}} \\ \mathrm{j_{6t7}} \end{pmatrix}$$

$$\begin{pmatrix} \mathrm{P6} \\ \mathrm{P7} \\ \mathrm{UB4} \\ \mathrm{LB7} \\ \mathrm{SE\_P} \end{pmatrix} = \begin{pmatrix} -2.05 & -0.97 \\ -1.18 & -0.41 \\ 1 & 0 \\ 0 & 1 \\ -0.19 & -0.01 \end{pmatrix} \begin{pmatrix} \mathrm{t_{6b7}} \\ \mathrm{j_{6b7}} \end{pmatrix}$$

5.5.3. QUANTUM DOT IDENTIFICATION

To obtain the capacitive coupling of all the barrier gates to a set of transition lines (as shown in Fig. 5.3a and Fig. 5.9- 5.13.), we acquire and analyse sets of 112 charge stability diagrams. The same charge stability diagram is taken after stepping each barrier gate around its current voltage in steps of 1 mV in the range of -3 to 3 mV (i.e., 7 scans x 16 barriers). Figure 5.8 depicts one such example. The number of charge stability diagrams required to identify all quantum dots scales linearly with their total number. The number of maps results from the product of the number of plunger and barrier gates, which both scale as its square root. We emphasise that an array with individual control would also require a linear number of charge stability diagrams to infer each dot. In the analysis, we first subtract a slowly varying background to the data (with ndimage.gaussian.filter of the open-source scipy package) and then calculate the gradient of the map (with ndimage.gaussian_gradient_magnitude). For a given line cut of such two-dimensional maps, we extract the peaks position using a Gaussian fit function. Due to cross capacitance, the transition line positions manifest a linear dependence on each of the 16 barriers, which we quantify by extracting the linear slope (Fig. 5.8). After normalisation to the maximum value, these parameters are named capacitive couplings (λ), and, because of the grid structure of the two barrier layers, provide a first information of where the hole is added/removed to/from. To extract the quantum dot positions, we consider the capacitive couplings to the vUB (λ_{vUB}) and vBL (λ_{vLB}) gates as two independent probability distributions. With this approach, the integral of the λ_{vUB} (λ_{vLB}) between vUBi (vLBk) and vUBj (vLBl) returns a "probability" $p_{U,(i,j)}$ ($p_{L,(k,l)}$) to find the dot in-between these control lines. As a result, the combined probability in the site confined by these four barriers is given by the product of these elements: $w_{(i,j),(k,l)} = p_{U,(i,j)} \cdot p_{L,(k,l)}$. We note that the sum of the 16 probabilities returns 1. As already observed in ref. [42], the gates cross-coupling to a specific quantum dot defined in a germanium quantum well manifest a slow falloff in space (i.e., gates with a distance to the dot of > 100 nm still have a considerable cross-coupling to the dot). This can be attributed to the rather large vertical distance between the gates and the quantum dots (> 60 nm), and is in contrast with experiments in SiMOS devices where the falloff is rather immediate due to the tight charge confinement. This aspect explains why our probability W at the identified quantum dot reaches at a max of 0.25 – 0.5.

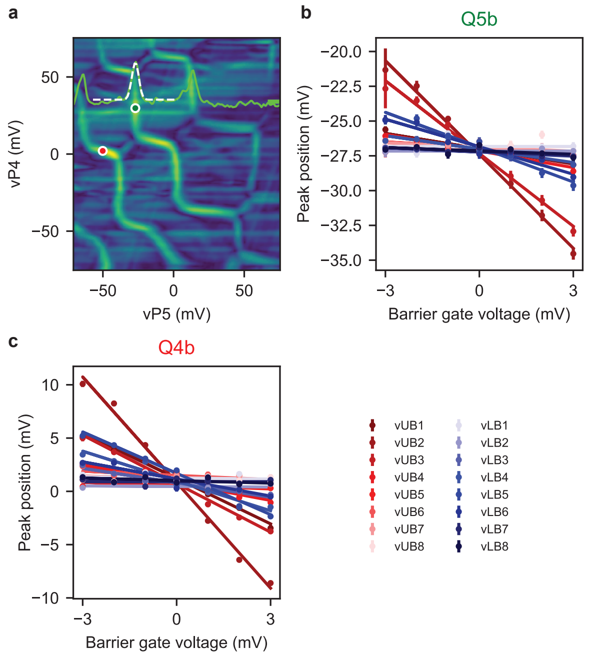

Figure 5.8: **Detecting the shift of the transition lines: an exemplary case. a,** Charge stability diagram (gradient of the SW sensor signal) showcasing a set of vertical and horizontal charge transition lines. The green trace shows the derivative of the data at the vP4 value identified by the horizontal green tick. The white dashed line is a fit of the linecut with a Gaussian function, and the green marker identifies the fitted centre of the peak. The red marker labels the fitted coordinate of a vertical transition line (not shown). **b, c,** Scatter points are the fitted positions of the green and red markers, respectively, as a function of the voltage applied at all barriers. Error bars on the points display the standard deviation of the fitted centre of the Gaussian. Dashed lines are the best linear fit to the data. The normalised absolute values of the slope parameter are taken as capacitive couplings of each gate to the specific transition line. The error bar on the capacitive coupling is taken as one standard deviation of the fitted slope parameter. The horizontal (vertical) transition line in **(a)** is attributed to the quantum dot Q4b (Q5b).

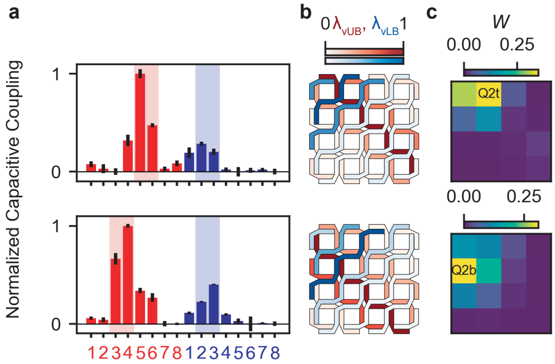

Figure 5.9: **Quantum dot identification of the Q2 quantum dots. a,** Bar plots of the (normalised) capacitive couplings (in red for the vUB, and in blue for the vLB gates) obtained by the analysis of transition lines attributed to different quantum dots as shown in Fig. 5.8. Red and blue backgrounds are added to emphasise the two barriers that surround the labeled quantum dot. **b,** Device layout with the capacitive couplings colour-coded on the filling of the gate lines. The vUB (vLB) capacitive couplings are normalised to their maximum values. Intuitively, the quantum dot associated with the analysed transition lines is located at the intersection of the two intensely coloured red and blue lines. **c,** Extracted probabilities (W) of each set of addition lines (calculated as discussed in section 5.5). The comparison of the top and bottom panels of **a, b, c** clearly distinguishes the two Q2 quantum dots. In **a** the data points correspond to the peak of the chart bars as well as the centers of the error bars. Each error bar is the standard deviation of the parameter obtained from the linear fit.

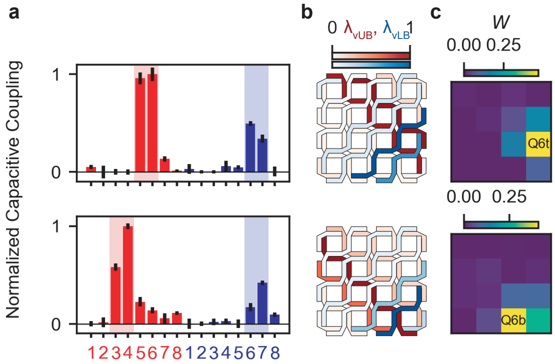

Figure 5.10: **Quantum dot identification of the Q6 quantum dots** Same as in Fig. 5.9 but applied to the Q6 quantum dots. TThe comparison of the top and bottom panels of **a, b, c** clearly distinguishes the two Q6 quantum dots.

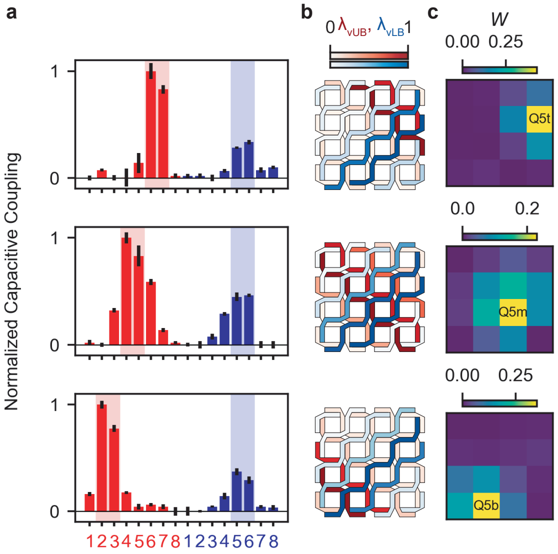

Figure 5.11: **Quantum dot identification of the Q6 quantum dots** Same as in Fig. 5.9 but applied to the Q5 quantum dots. The three different rows of panels **a, b, c** enable to label the Q5 quantum dots.

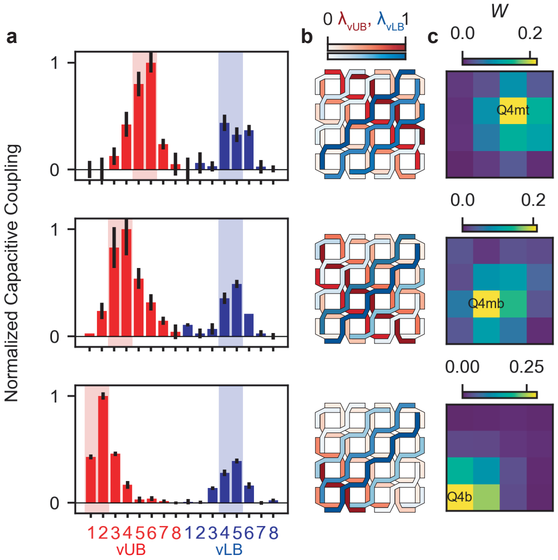

Figure 5.12: **Quantum dot identification of the Q6 quantum dots** Same as in Fig. 5.9 but applied to the Q4 quantum dots. The three different rows of panels **a, b, c** enable to label the Q4 quantum dots. The dot Q4t could not be systematically analysed because, in this gating regime, we observe a slow loading mechanism via the defective barrier UB8 with respect to the timescale of our scan (~ ms). However, because such transition lines are controlled by vP4 (labelled in Fig. 5.21), do strongly respond to vUB7 and vLB5, we can still map them to the site Q4t, in a qualitative way.

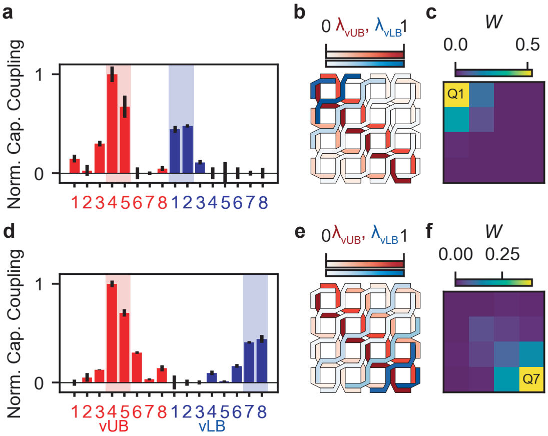

Figure 5.13: **Quantum dot identification applied to the Q1 and Q7 quantum dot** The method in Fig. 5.9 is applied to the two quantum dots controlled by independent plunger lines Q1 and Q7 in panels **a, b, c** and **d, e, f**, respectively.

SPURIOUS QUANTUM DOT IDENTIFICATION: AN EXAMPLE

We make use of the method presented above to also map the position of accidental quantum dots that arise outside the crossbar array. In Fig. 5.14a, we display the capacitive coupling of the barrier gates to a spurious quantum dot. The addition lines of such a quantum dot are mainly controlled by vP2 and are visible as quasi-vertical lines in the charge stability diagrams of the type ΔvP2 vs ΔvP3 in the Supplementary Videos. In particular, from these maps, it is possible to observe a negligible mutual capacitance between this specific accidental dot and the crossbar quantum dots Q1, and Q3b. However, we emphasise that the presence of such spurious quantum dot complicates the tuning efficiency of our device, and strategies to mitigate their presence need to be in place in the near future, as already discussed in the main text. In Fig. 5.14b, we present the device layout with the capacitive couplings colour-coded on the filling of the gate lines. Here, both the vUB and vLB capacitive couplings, λ_{vUB} and λ_{vLB}, are normalised to their maximum values. Following this analysis, we can conclude that such spurious quantum dot is approximately located under the fanout of the gates UB1, LB3 and UB3. This is furthermore corroborated by the fact that this dot is well sensed by the SW charge sensor.

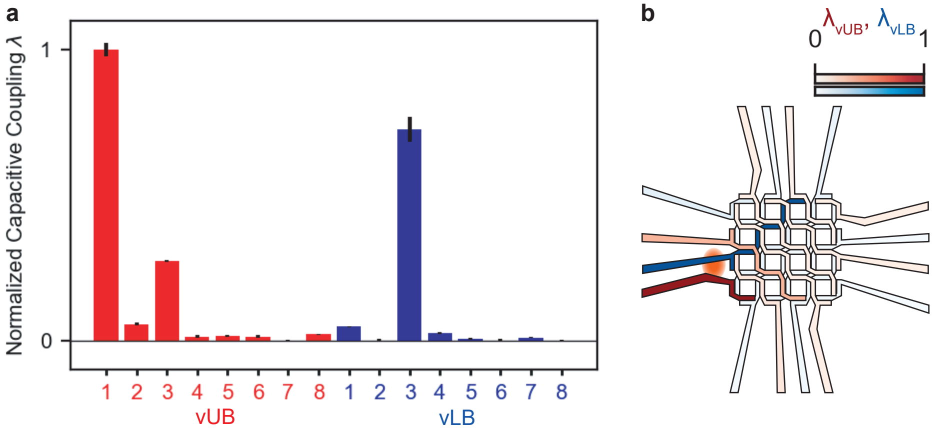

Figure 5.14: **Spurious quantum dot identification. a,** Bar plots of the (normalised) capacitive couplings (in red for the vUB, and in blue for the vLB gates) obtained from the analysis of transition lines attributed to a spurious quantum dot located under the gates fanout. The data points correspond to the peak of the chart bars as well as the centers of the error bars. Each error bar is the standard deviation of the parameter obtained from the linear fit. **b,** Device layout with the capacitive couplings colour-coded on the filling of the gate lines. The vUB (vLB) capacitive couplings are normalised to their maximum values. The orange oval in **(b)** indicates the approximate position of the quantum dot associated with the analysed transition lines (under the fanout of the barriers UB1 and LB3).

5.5.4. TUNNEL COUPLING EVALUATION

For the estimation of the tunnel coupling results presented in Fig. 5.6 and 5.7, we established an automated measurement procedure that follows this sequence: 1) we step the virtual barriers across the two-dimensional map (t, j); 2) at each barrier configuration, we take a two-dimensional (e67, U67) charge stability map (Figs. 5.6b and 5.7b); 3) we identify the accurate position of charge interdot via a fitting procedure of the map (Fig. 5.17) [43]; 4) we perform small adjustments at the e67, U67 virtual gates to centre the interdot at the (0,0) dc-offset; 5) measure the polarisation line by using ~0.1 kHz AWG ramps (Figs. 5.6c and 5.7c). For an accurate analysis, each polarisation line is the result of an average of 150 traces, using a measurement integration time of 50 μs per pixel. With this method, the full 30x30 maps are taken in a few hours. We fit the traces considering an electron temperature of 138 mK and a detuning lever arm of $\alpha_{\epsilon_{67}} = 0.012(4)$ eV/V, extracted from a thermally broadened polarisation line (Fig. 5.20). We observe that the extracted tunnel coupling follows approximately an exponential trend as a function of the barrier gates. We fit the data presented in Figs. 5.6e and 5.7e with the function $A{\cdot}e^{-BV_g}$, with A a prefactor, B the effective barrier lever arm and V_g the gate axis. We find that the effective barrier lever arms of $j_{6\mathrm{b}7}$ and $t_{6\mathrm{b}7}$ are $0.007{\pm}0.002$ and $0.021 \pm 0.003\,\mathrm{mV}^{-1}$, respectively. Similarly, we find for $j_{6\mathrm{t}7}$ and $t_{6\mathrm{t}7}$ values of 0.008 ± 0.001 and $0.026 \pm 0.003\,\mathrm{mV}^{-1}$, respectively. This indicates that the real barrier LB7 controls the vertical and horizontal coupling in a similar manner. Altogether these results indicate that the lower barrier layer of UB gates is ~ 3 times more effective than the upper barrier layer of LB gates. This is consistent with what is found in Fig. 5.3a and Fig. 5.10. We note that for qubit operations in such crossbar array, it is actually necessary to fully characterise and calibrate the two-barrier tunability of all the 24 nearest-neighbours. Performing this task requires improving further our hardware implementation and is beyond the scope of this work.

5.6. SUPPLEMENTARY

5.6.1. RENT'S RULE AND GATE COUNT

Scalable architectures impose stringent requirements at all layers of the quantum computing stack [5]. If we focus on the lowest layers of the computing stack, state-of-the-art solid-state quantum processors do not meet these prerequisites yet [8]. In fact, current processors still make use of a few control terminals per qubit, an approach that will lead to arduous interconnectivity and control challenges in the route toward millions qubits [44, 45]. To quantify the level of optimisation and interconnectivity of a quantum processor, we borrow the concept of Rent's rule from classical electronics [46]. In quantum dot devices, the Rent's rule can be used to correlate the number of control terminals T (i.e., gates, ohmic leads,...) and the number of active components g (i.e., quantum dots or qubits):

$$T = tg^{p} \tag{5.1}$$

where t is the average number of control terminals per qubit and p is the Rent exponent that lies in the range $(0,1]$. Without any quantum hardware optimisation, the number of terminals will keep increasing linearly with the number of qubits, creating major interconnect problems in the quantum computing stack [8].

An analogous challenge emerged in the 1950s in classical electronics when every electrical component needed to be soldered to several others [47]. The turning point was the

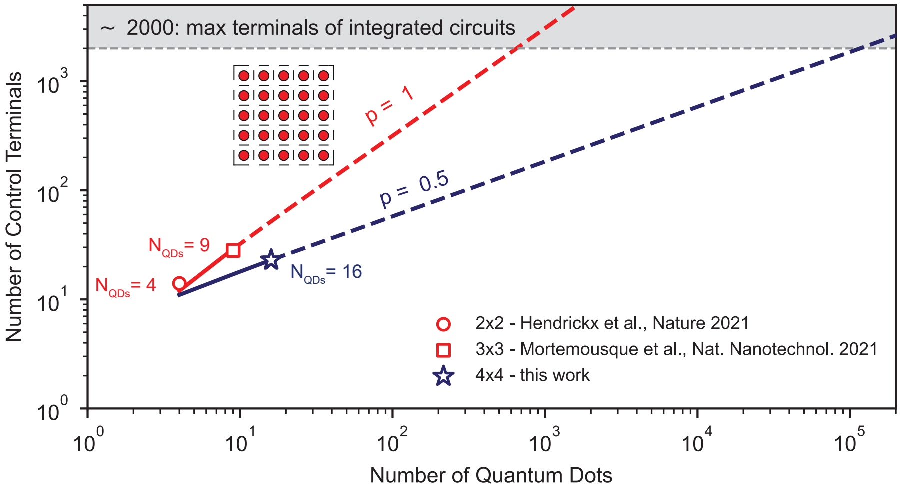

Figure 5.15: **Rent's rule in two-dimensional quantum dot architectectures and gates count.** Number of control terminals (gates) versus the number of quantum dots for a two-dimensional array. The blue trace indicates the scaling of our shared-control gate architecture. The red trace shows the scaling for an architecture with individual control (inset) of interdot couplings and quantum dot energies. Scatter points represent the gates counts of a 2x2 [39], 3x3 [34] and 4x4 quantum dot array (this chapter). We draw a horizontal line at 2000 control terminals, which currently identify the current maximum number of input/output terminals of classical integrated circuits. Assuming this as a practical limit for the control terminals of a quantum processor without on-chip control logic [7], the individual control strategy is limited to control up to a few hundred quantum dots. In contrast, the shared control approach may be able to control few hundreds of thousands.

invention of the integrated circuit, which led to the realisation of the first microprocessor - the Intel 4004 - with 2300 transistors and only 16 external pins. Nowadays, integrated circuits are at the heart of our technology and, with a Rent exponent of about 0.5 and a maximum number of input/output lines of $T \sim 2 \cdot 10^3$, present a ratio of transistor to input/output pins g/T of $\sim 10^6$ [7, 48]. On the contrary, in infant quantum chips, the g/T ratio is below 1 [8], and therefore, significant efforts have to be made to downscale the quantum Rent exponent.

In our work, we have moved from electrostatic gating strategies with individual control of every unit to crossbar architectures with shared control of quantum dots energies and interdot couplings [17]. This advance is crucial for scalability because it may enable to use $O(N^{1/2})$ terminals for $O(N)$ qubits (i.e., $p = 0.5$). The impact of this strategy can be visualised in Fig. 5.15, where we compare the different scalings of control terminals for a two-dimensional quantum dot array controlled with a shared- and with an individual-control approach. For the shared-control architecture presented in this chapter, the gates count as a function of quantum dots g is given by:

$$T = 6g^{1/2} - 1 \propto 6g^{1/2} \tag{5.2}$$

while for an architecture with individual control of all the on-site dot energies and interdot couplings (see inset of Fig. 5.15), we obtain:

$$T = 3g + 2g^{1/2} - 4 \propto 3g \tag{5.3}$$

These equations hold for square arrays with a minimum 2x2 size, i.e., $g \geq 4$.

Scaling the crossbar architecture to a 6x6 crossbar array would already result in a device with fewer gates than total number of quantum dots. In particular, a 6x6 crossbar array with 36 quantum dots requires only 35 gates. We note that while this may seem a marginal improvement, comparing the required number of gates to quantum dot devices with individual connectivity shows already a remarkable difference: a 4x4 (6x6) quantum dot device requires 23 vs 52 (35 vs 116), for the respective systems.

We emphasise that in these considerations we do not account for the terminals controlling the read-out charge sensors. In the future, a strategy for integrating charge sensors within quantum dot crossbar arrays needs to be fully worked out to establish and operate scalable modules of semiconductor qubit arrays with a Rent exponent of 0.5. We note that germanium can make ohmic contacts to metals, thus facilitating a very small footprint for charge sensors, and providing a route toward the integration of charge sensors in the quantum dot array.

5.6.2. PRACTICAL DEVICE IMPROVEMENTS

Here, we present a series of practical ideas to mitigate challenges observed (and not) throughout the experiment.

1. The tune-up of the current implementation is complicated by the emergence of a few (~ 5) unwanted stray dots outside the array, located under the dense gates fanout. These decrease the read-out sensitivity to the designed quantum dots and, in general, complicate the system tune-up.
   Near-term solutions can be: the addition of a lower “screening” gate layer (kept

at a more positive voltage), or an upper "depleting" gate layer that prevents any charge puddles from forming in between different gate lines. A more sophisticated solution consists of the implementation of vertical interconnect access through the oxide layer that enables to fan out the gate lines at a much higher level in the stack [28]. We also envision that, in the future, boundary effects of large qubit arrays need to be accounted for (e.g., dots at the perimeter of the array experience a smaller electric field than the ones in the middle). Hence, another possibility is to neglect the dots at the perimeter completely.

2. A faster device tune-up can be achieved by using radio frequency reflectometry, which, in our experiment, worked out only partially.

3. A higher level of homogeneity and functionality than is presented here will be needed for practical quantum computation with quantum dots. Leaving aside the development on the material stack itself (Ge/SiGe) and on the device nanofabrication, there appears to still be space for improvements on the gate layout. Similarly to the behaviour of the turn-on voltages in transistors [49], a higher quantum dot homogeneity may be achieved by increasing their size. This will also have the beneficial effect of increasing the plunger gates lever arm, which will be less screened by the lower layers. Clearly, an excessively large quantum dot can lead to (Pauli spin-blockade) read-out problems if the energy of the first excited state is too low. Therefore a search for an optimal size needs to be performed.

4. In the current device, we observed that the ratio of the two barrier layers lever arms is approximately 2-3. Due to imperfections in the nanofabrication and an oxide layer in between them, the top layer partially overlaps the bottom one. As a consequence, its electric field is screened. To enhance the coupling of the top layer, one can design the top layer to have a slightly larger width, or add a gap of a few nm in between the two lines.

5.6.3. ADDRESSABLE EXCHANGE OPERATIONS WITH A DOUBLE BARRIER DESIGN

The ability to control the tunnel coupling with two barriers opens the opportunity to design addressable exchange-based two-qubit gates in architectures with shared control. We envision an operation strategy in which a two-qubit gate can be activated only when both barriers are in the ON state. For a fast CPHASE gate with a duration of 5 ns, we require to activate an exchange interaction of $J_{\mathrm{ON}}/h = 100$ MHz. In all other cases (i.e., when the barriers are in the configurations (ON, OFF), (OFF, ON), (OFF, OFF)), we demand a sufficiently low exchange to minimise errors. State-of-the-art values of OFF exchange interaction are in the order of $J_{\mathrm{OFF}}/h \sim 10$ KHz [40].

Fig. 5.16 illustrates the required barrier voltage points to obtain such exchange interactions considering symmetric lever arms, a quantum dot charging energy of U = 1 meV and operations at the charge symmetry point (i.e., at zero detuning). In Fig. 5.16, we have approximated the dependence of the tunnel coupling energy t_{C} with respect to the two barrier voltages B_x and B_y with [9, 21, 50]:

$$t_{\mathrm{C}} = \frac{\sqrt{JU}}{2} = c_1 \cdot e^{-c_2\alpha(B_x - B_{x,ON})} \cdot e^{-c_2\alpha(B_y - B_{y,ON})} \tag{5.4}$$

with $B_{x,ON}$ and $B_{y,ON}$ the ON set-points of the two barriers.
In this example, we have set the prefactor c_1 to $5 \cdot h$ GHz with h the Plank constant, and the effective barrier lever arms $c_2 \cdot \alpha$ to 0.04 V^{-1}.

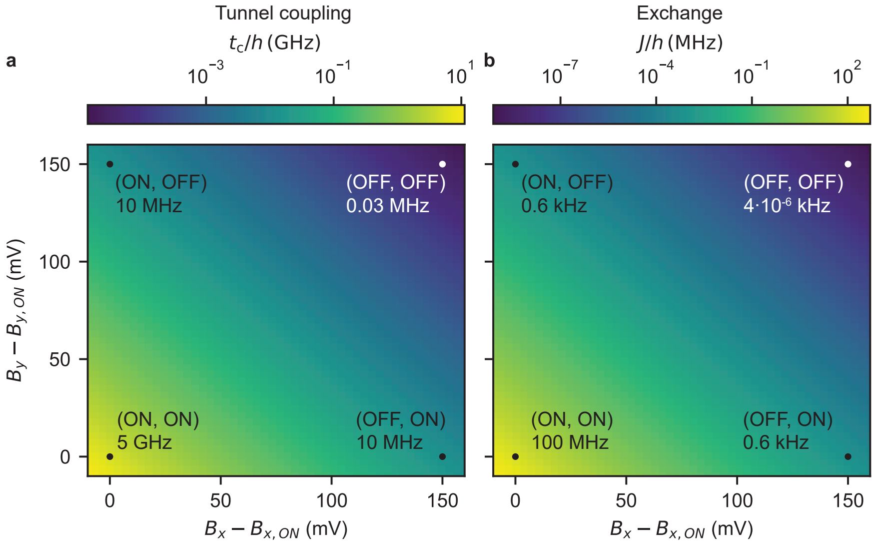

Figure 5.16: **Addressable exchange operation with a double barrier design. a, b** Target tunnel coupling and exchange required for fast two-qubit gates with interaction ON (bottom left corner), and OFF (top left, top right, bottom left corners in the map). The exchange interaction of qubit pairs at (ON, OFF) crossing points remains four orders of magnitude smaller than in the (ON, ON) cases. The parameters displayed are calculated at the coordinates (0, 0), (0, 150), (150, 0), (150, 150) mV. In reference to the experimental results of Fig. 5.6 and 5.7, the measurable tunnel coupling range (> 1 GHz) via polarisation lines is the bottom left corner of panel **(a)** extending up to +24 mV on both axes.

TWO-AXIS CONTROL OF THE INTERDOT TRANSITION LINE

By fitting the two-dimensional (e67, U67) charge stability maps (examples in Figs. 5.17a, b), we obtain an estimate of the (3,1)-(2,2) charge interdot size L for the double dot systems Q6b-Q7 and Q6t-Q7. The size of the interdot line is indicative of the capacitive coupling between the adjacent quantum dots. Consistent with the two-axis tunability of the tunnel coupling, the interdot size is varied as the effective distance between the dots and is modified by the action of the two tunnel barriers (Figs. 5.17c-f).

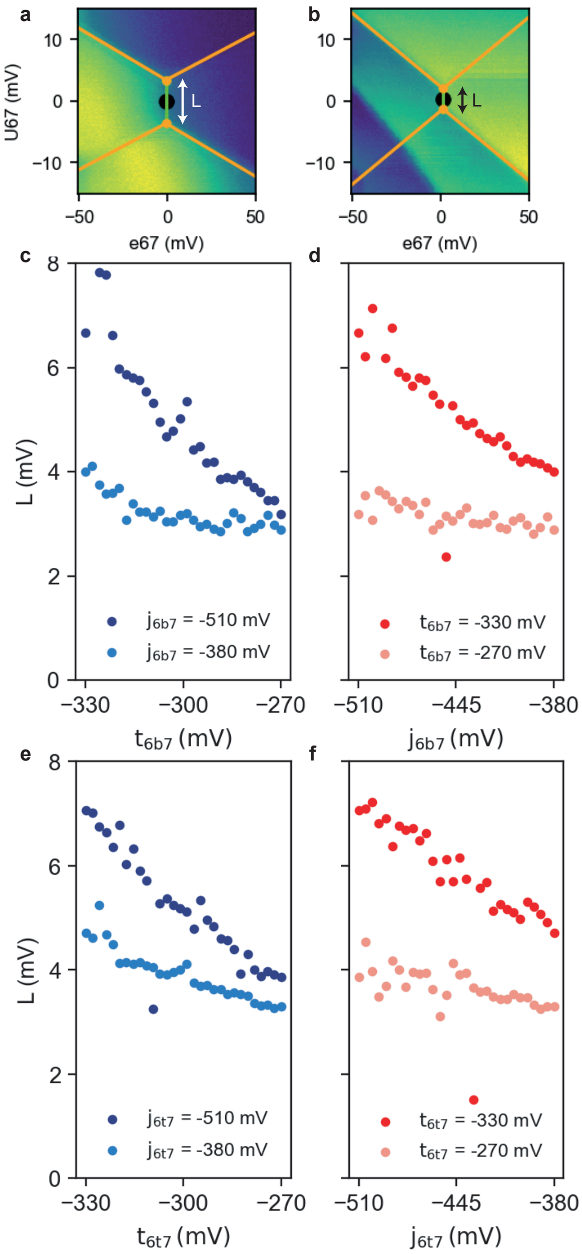

Figure 5.17: **Two-axis control of the quantum dot interdot transition line. a, b,** Exemplary charge stability diagrams taken at the Q6t-Q7 (3,1)-(2,2) charge interdot line. The two maps are taken at the diagonally opposite points of the two-dimensional barrier scan, at t_{6t7}, j_{6t7} = (-330, -510) and (-270, -380) mV, respectively. Orange lines represent a fit to the map following the procedure shown in ref. [43]. A black circle identifies the fitted centre of the interdot, and the arrow illustrates the size in voltage of the interdot line. **c, d,** Size of the Q6b-Q7 (3,1)-(2,2) charge interdot line as a function of the two virtual barriers. **e, f,** Same for the Q6t-Q7 (3,1)-(2,2) charge interdot line. Outliers in the plot are due to non-accurate fits of the image.

TWO-AXIS CONTROL OF THE Q6B-Q5M INTERACTION

We repeat the tunnel coupling experiments considering the double-dot pair Q6b and Q5m by defining the virtual barriers t_{6b5} and j_{6b5} starting from the relative UB4 and LB6 barriers (Fig. 5.18):

$$\begin{pmatrix} \mathrm{P5} \\ \mathrm{P6} \\ \mathrm{UB4} \\ \mathrm{LB6} \\ \mathrm{SE\_P} \end{pmatrix} = \begin{pmatrix} -1.63 & -0.58 \\ -1.61 & -0.48 \\ 1 & 0 \\ 0 & 1 \\ -0.43 & -0.02 \end{pmatrix} \begin{pmatrix} \mathrm{t}_{6b5} \\ \mathrm{j}_{6b5} \end{pmatrix}$$

We observe that the limited sensitivity at the interdot hinders a quantitative tunnel coupling analysis. However, at a qualitative level, we still observe the expected pattern with the size of the interdot tunable by both barriers.

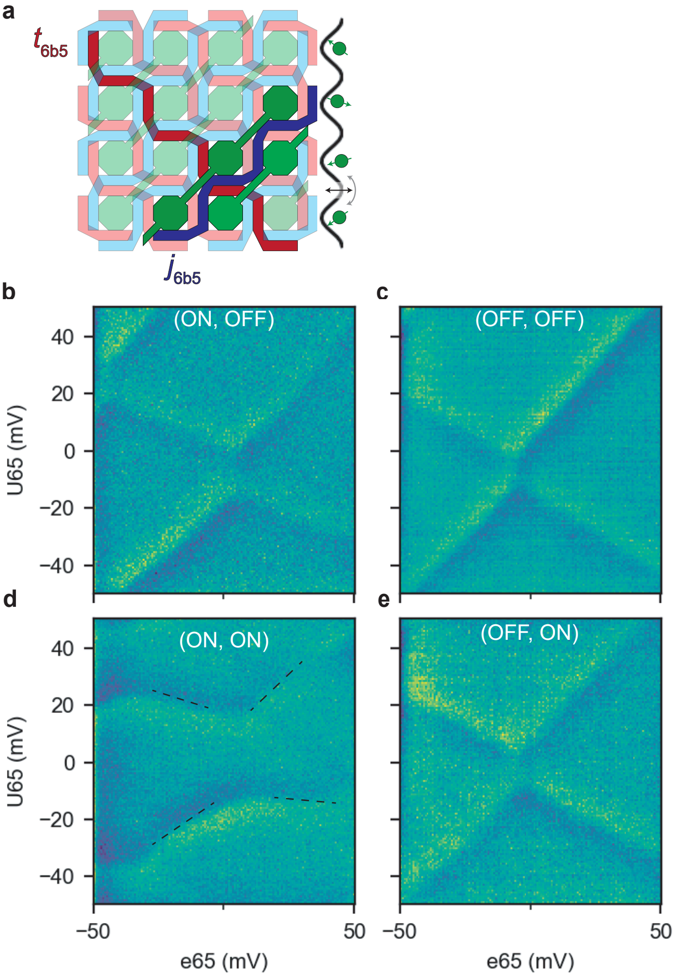

Figure 5.18: **Two-axis control of the Q6b-Q5m interdot coupling.** **a** Schematic of the crossbar indicating the two intersecting virtual barriers (in red and blue) controlling the Q6b-Q5m interaction. **b-e** Charge stability diagrams at different barrier voltages: **(b)** (t_{6b5}, j_{6b5}) = (-330, -380) mV, **(c)** (-270, -380) mV, **(d)** (-270, -510) mV, **(e)** (-330, -510) mV. In **(d)**, in the high interdot coupling regime, we add dashed lines as guide for the eyes on weakly visible transition lines. Here, we display the signal from the SE charge sensor after subtraction of a background.

5.6.4. ELECTRON TEMPERATURE EXTRACTION

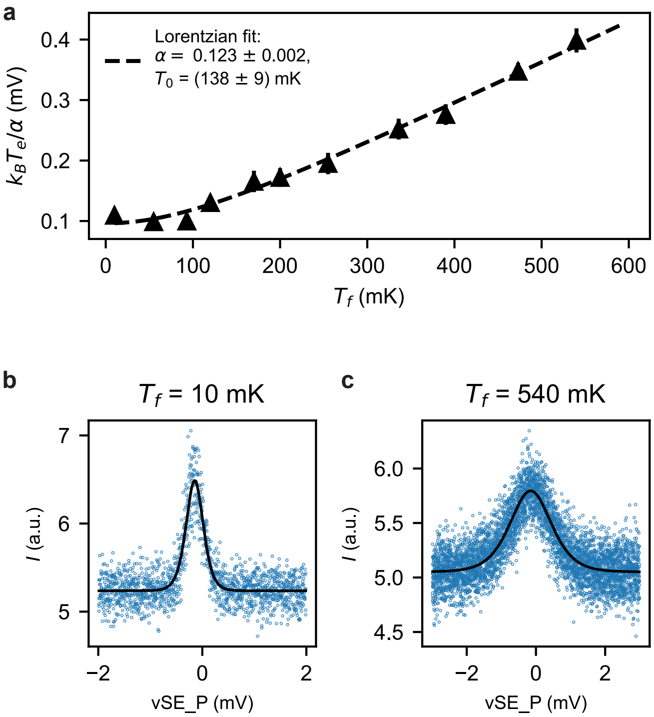

Figure 5.19: **Electron temperature extraction. a** Coulomb peak width as a function of fridge temperature. **b, c.** Exemplary data (scatter points) and best fits (black lines) collected at $T_f = 10$ mK and $T_f = 540$ mK, respectively. For every temperature, we perform five plunger sweeps across the Coulomb peak (each averaged 500 times) and, by fitting the curves, we obtain five different estimates for the Coulomb peak width. In **(a)**, we show the average width. The depicted standard deviation is determined by considering the standard deviation from the single fit itself or the standard deviation between the five different fitting estimates, depending on which is dominant.

We estimate the electron temperature of our setup by fitting a temperature broadened Coulomb peak of the SE charge sensor. We choose a source-drain voltage V_{SD} and coupling energy to the leads $h\Gamma$ such that $h\Gamma, eV_{\mathrm{SD}} \ll k_BT_e$, with h and k_B the Planck and Boltzmann constants, respectively and Γ the lead-dot tunnel rate. The current I at the Coulomb peak is fitted with the Lorentzian distribution

$$I_{model} = a \cdot \cosh^{-2}\left(\frac{\alpha_{sensor} \cdot \epsilon}{2k_BT_e}\right) + c, \tag{5.5}$$

where a is an amplitude prefactor, α_{sensor} is the lever arm of the sensor plunger gate, ϵ is the plunger gate voltage and c an offset. The full width half maximum (FWHM) of the peak is therefore given by

$$\mathrm{FWHM} = \frac{k_BT_e}{\alpha_{sensor}} = \frac{k_B\sqrt{T_0^2 + T_f^2}}{\alpha_{sensor}}, \tag{5.6}$$

where T_f is the nominal fridge temperature and T_0 the base electron temperature [51]. We use the FWHM dependence on the nominal fridge temperature to extract both T_0 and α_{sensor}. The result can be seen in Fig. 5.19 with two exemplary fits for 10 and 540 mK. The fit with Equation 5.6 results in $T_0 = 138 \pm 9$ mK and $\alpha_{sensor} = 0.123 \pm 0.002$ eV/V, which is consistent with an independent lever arm extraction from Coulomb diamonds.

5.6.5. DETUNING LEVER ARM EXTRACTION

For an accurate estimation of the interdot tunnel coupling, we evaluate the quantum dot detuning lever arm by fitting the sensor signal S_{21} with a thermally limited polarisation line (Fig. 5.20) as described in [38]:

$$S_{model} = S_0 \pm \delta S \frac{\epsilon}{\Omega} \cdot \tanh\left(\frac{\Omega}{2k_B T_e}\right) + \frac{\partial S}{\partial \epsilon}\epsilon \tag{5.7}$$

with S_0 the background signal of the charge sensor, δS the signal amplitude, ϵ the detuning energy, Ω the energy difference between the two levels and the term $\frac{\partial S}{\partial \epsilon}\epsilon$ a linear slope due to cross-talk to the charge sensor. In the low-tunnelling regime, we can approximate $\Omega = \sqrt{\epsilon^2 + 4t^2} \approx \epsilon$, which reduces Equation 5.7 to

$$S_{\text{model}} = S_0 \pm \delta S \cdot \tanh\left(\frac{\alpha_{QD} \cdot \epsilon}{2k_B T_e}\right) + \frac{\partial S}{\partial \epsilon}\epsilon. \tag{5.8}$$

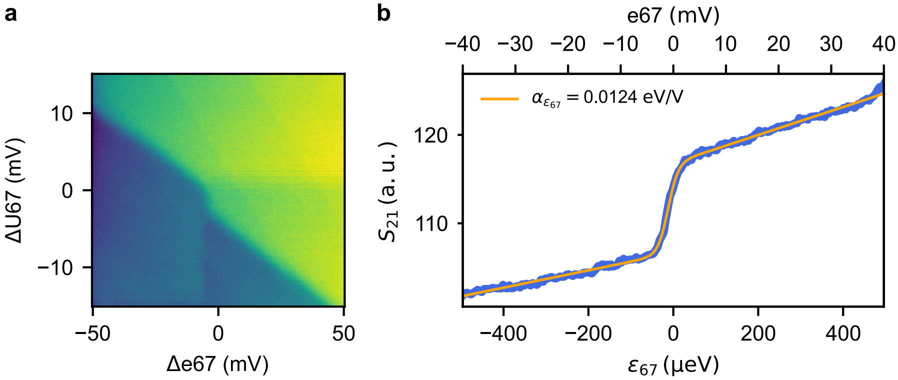

Figure 5.20: **Temperature limited polarisation line. a,** Charge stability diagram of the uncoupled Q6b-Q7 at the (3,1)-(2,2) charge interdot. In this configuration, the tunnel time in Q6b is small with respect to the ramp time of the detuning axis, therefore the interdot is extended and the Q6b addition line is not clearly visible in the map. **b,** Thermally limited polarisation line (blue trace) taken at the centre of the interdot shown in **(a)**. From the best fit (orange line), we obtain the detuning lever arm $\alpha_{\epsilon_{67}} = 0.012(4)$ eV/V.

5.6.6. CHARGE STABILITY DIAGRAMS AND APPLIED GATE VOLTAGES

In Fig. 5.21, we display the charge stability diagrams obtained for the first tune-up of the device with the quantum dots in the few-holes regime. These maps are part of the data sets that are used for the analysis presented in Fig. 5.9-5.13. The applied voltages at this phase of the experiment are shown in Fig. 5.22.

The gate voltages of the crossbar in the odd-charge regime during the second tune up are shown in Fig. 5.23.

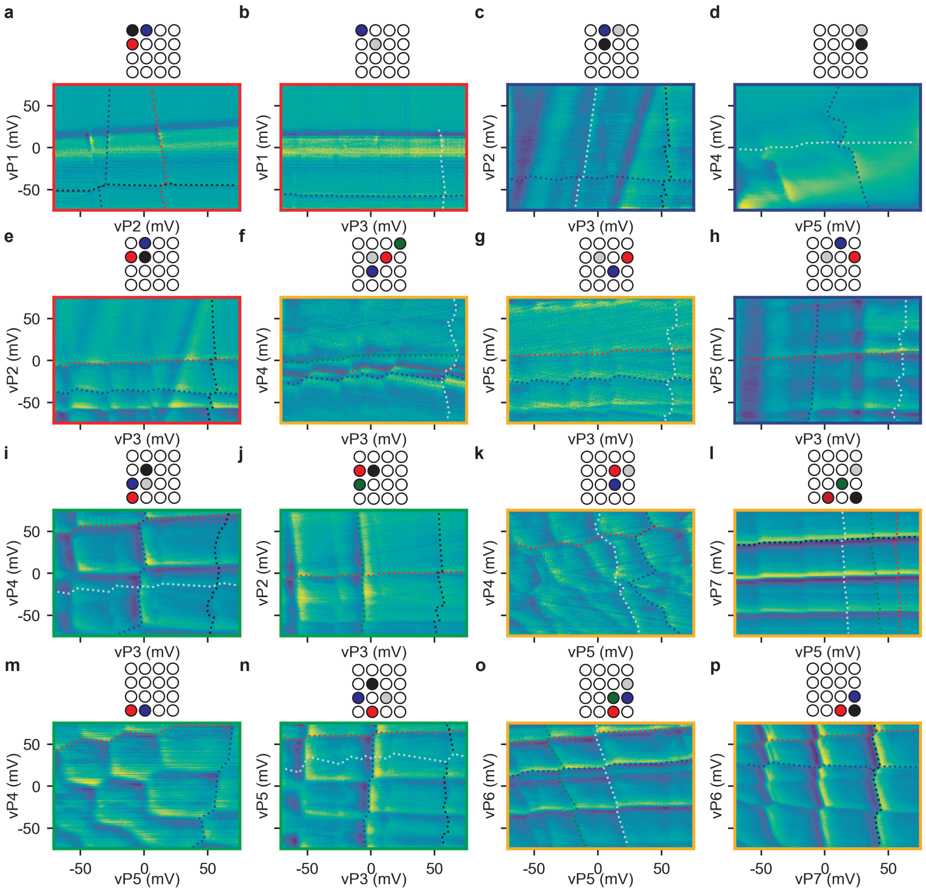

Figure 5.21: **Tune-up of the crossbar array in the few-holes regime. a-p,** Charge stability diagrams (raw sensor signal after subtraction of a background) showcasing the 16 quantum dot system in the few-hole regime. These measurements are taken in the first tune-up of the crossbar array. In each map, the first visible transition lines from the right or the top are labelled and assigned to the relative quantum dot by dashed lines with colours defined in the schematic at the top. The identification is performed via the results of Fig. 5.9-5.13. The colour of the panel frame identifies the sensor used: NW in red, NE in blue, SW in green, and SE in ochre.

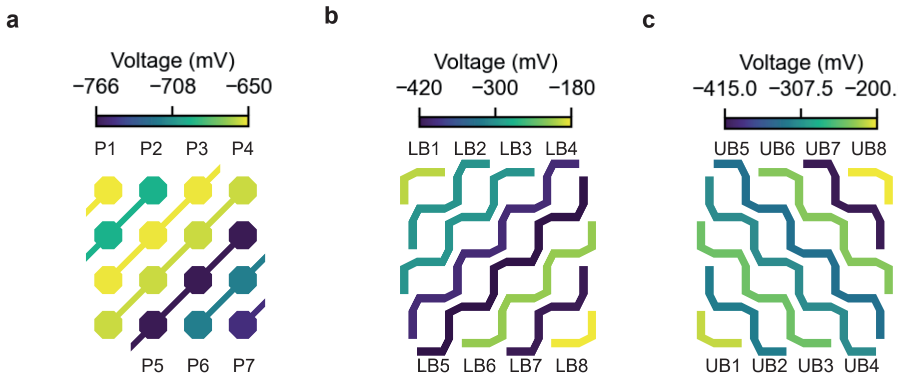

Figure 5.22: **Tune-up of the crossbar array in the few-holes regime. a-c,** Schematics of the voltage applied at all crossbar gates at the phase of the experiment shown in Fig. 5.21. The voltages are here optimised to circumvent stray dots.

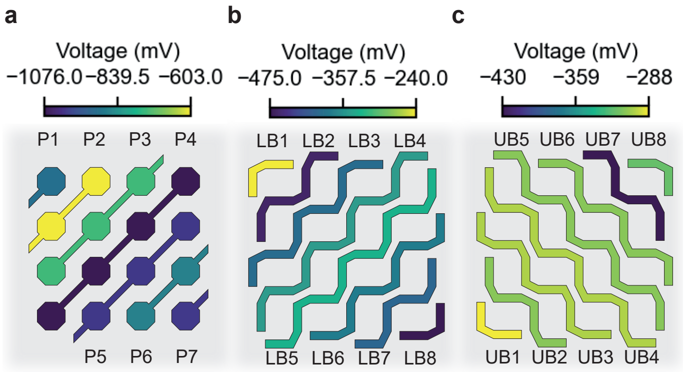

Figure 5.23: **Crossbar gate voltages. a-c,** Voltages applied at the real P, LB and UB gates, respectively, when the system is tuned in the odd charge occupation regime.

5.6.7. CHARACTERISATION OF THE VARIABILITY OF THE QUANTUM DOT ARRAY

We have characterised the level of homogeneity in the array considering two different metrics.

First, we consider the onset voltage of the first hole in each quantum dot, as displayed in Figs. 5.24a, b. We obtain an average first-hole voltage of -1660 ± 290 mV, that indicates a rather high variability across the quantum dot array. We also observe that a more negative voltage is required to accumulate the first hole when going toward the center of the array (e.g. under P4 and P5). This trend is anticorrelated with the voltages set to the LB barrier gates, that run in parallel to the plunger gates (Fig, 5.24c). The higher values of LB4 and LB5 lead to more negative values of the plunger gates within the array, due to cross capacitance. We note that the need to set LB4 and LB5 to a more positive voltage comes from the demand to maintain the charge sensors well separated by the array. In practice, we have observed that the needs to preserve the quality of the charge sensors and to set the interdot tunnel barriers seem conflicting. Therefore, we suggest in future designs to dedicate to one gate the function to isolate the sensor to the dots and to another gate to determine the interdot barriers.

A second metric to asses the variability in size and in dot lever arm relies on evaluating the homogeneity in quantum dot addition voltages, i.e. the spacing between two consecutive charge transition lines [41]. We extract the charge addition voltages of all the quantum dots from the corresponding stability diagrams (Fig. 5.25), and extract the averaged spacing of the first and second hole to be 51 ± 6 mV and 50 ± 9, respectively, indicating a $\sim 10-20\%$ variability of the quantum dot confinement properties across the array.

Overall, this demonstrates that, while quantum dots are accumulated at rather different voltages under each plunger gate, their size and plunger gate coupling are similar, owing to the grid structure of our design.

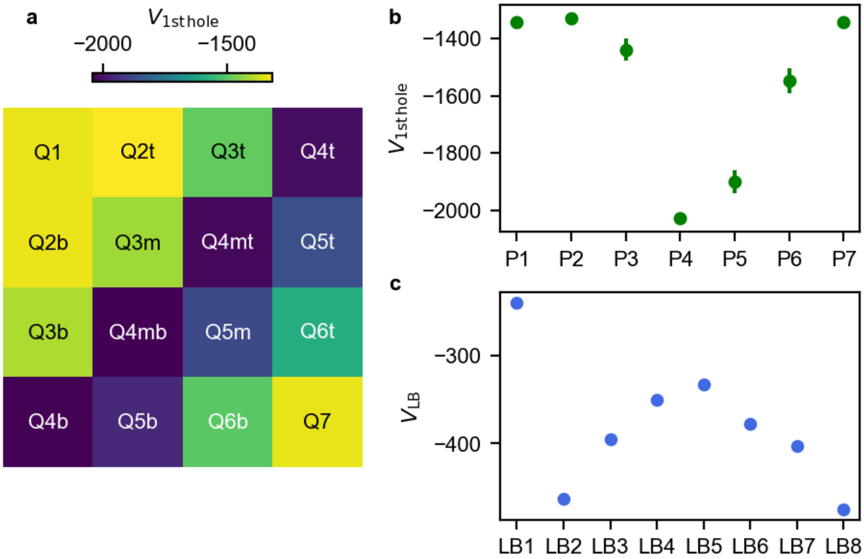

Figure 5.24: **Onset voltages for the first hole. a,** Colormap of the virtual plunger voltages required to accumulate the first hole in each quantum dot. **b,** Averages first hole virtual plunger voltages. The error bars represent the standard deviations around the mean. We note that, while the variability of dot voltages for the same plunger is rather low, the overall variability of 290 mV remains high. **c,** Voltages of the LB gates in the odd charge regime.

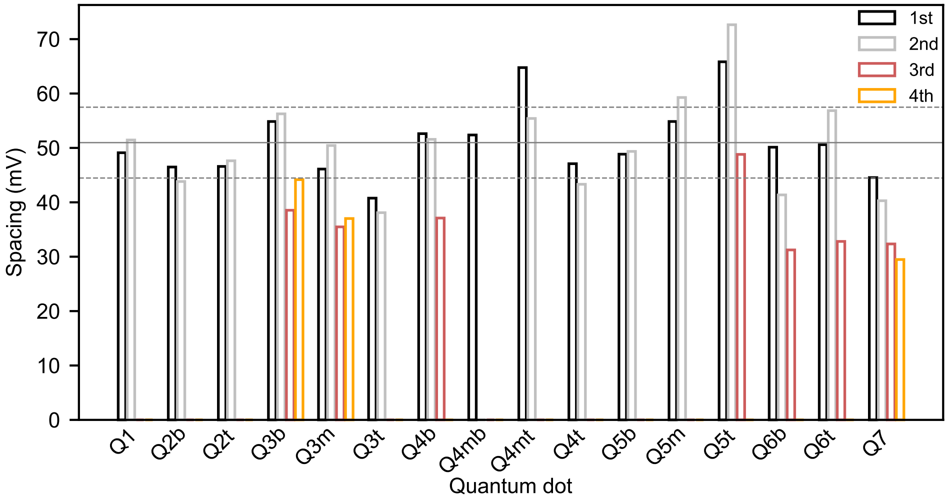

Figure 5.25: **Charge Addition voltages of all the quantum dots.** Bar plot of the addition voltages of each quantum dot considering the first spacings, when detectable in the already existing datasets. The three horizontal lines identify the spread of the first hole addition voltage of 51 ± 6 mV.

BIBLIOGRAPHY

[1] Intel. *Moore's law*. Sept. 2023. URL: https://newsroom.intel.com/press-kit/moores-law.

[2] A. G. Fowler et al. "Surface codes: Towards practical large-scale quantum computation". In: *Physical Review A* 86.3 (Sept. 2012), p. 032324. ISSN: 1050-2947. DOI: 10.1103/PhysRevA.86.032324. URL: https://link.aps.org/doi/10.1103/PhysRevA.86.032324.

[3] D. Wecker et al. "Gate-count estimates for performing quantum chemistry on small quantum computers". In: *Physical Review A* 90.2 (Aug. 2014), p. 022305. ISSN: 1050-2947. DOI: 10.1103/PhysRevA.90.022305. URL: https://link.aps.org/doi/10.1103/PhysRevA.90.022305.

[4] B. M. Terhal. "Quantum error correction for quantum memories". In: *Reviews of Modern Physics* 87.2 (Apr. 2015), pp. 307–346. ISSN: 0034-6861. DOI: 10.1103/RevModPhys.87.307. URL: https://link.aps.org/doi/10.1103/RevModPhys.87.307.

[5] R. Van Meter and D. Horsman. "A blueprint for building a quantum computer". In: *Communications of the ACM* 56.10 (Oct. 2013), pp. 84–93. ISSN: 0001-0782. DOI: 10.1145/2494568. URL: https://dl.acm.org/doi/10.1145/2494568.

[6] B. Landman and R. Russo. "On a Pin Versus Block Relationship For Partitions of Logic Graphs". In: *IEEE Transactions on Computers* C-20.12 (Dec. 1971), pp. 1469–1479. ISSN: 0018-9340. DOI: 10.1109/T-C.1971.223159. URL: https://ieeexplore.ieee.org/document/1671752/.

[7] L. M. K. Vandersypen et al. "Interfacing spin qubits in quantum dots and donors—hot, dense, and coherent". In: *npj Quantum Information* 3.1 (Dec. 2017), p. 34. ISSN: 2056-6387. DOI: 10.1038/s41534-017-0038-y. URL: http://www.nature.com/articles/s41534-017-0038-y.

[8] D. Franke et al. "Rent's rule and extensibility in quantum computing". In: *Microprocessors and Microsystems* 67 (June 2019), pp. 1–7. ISSN: 01419331. DOI: 10.1016/j.micpro.2019.02.006. URL: https://linkinghub.elsevier.com/retrieve/pii/S014193311830293X.

[9] D. Loss and D. P. DiVincenzo. "Quantum computation with quantum dots". In: *Physical Review A* 57.1 (Jan. 1998), pp. 120–126. ISSN: 1050-2947. DOI: 10.1103/PhysRevA.57.120. URL: https://link.aps.org/doi/10.1103/PhysRevA.57.120.

[10] F. A. Zwanenburg et al. "Silicon quantum electronics". In: *Reviews of Modern Physics* 85.3 (July 2013), pp. 961–1019. ISSN: 0034-6861. DOI: 10.1103/RevModPhys.85.961. URL: https://link.aps.org/doi/10.1103/RevModPhys.85.961.

[11] A. Chatterjee et al. "Semiconductor qubits in practice". In: *Nature Reviews Physics* 3.3 (Mar. 2021), pp. 157–177. ISSN: 2522-5820. DOI: `10.1038/s42254-021-00283-9`. URL: `http://www.nature.com/articles/s42254-021-00283-9`.

[12] R. Maurand et al. "A CMOS silicon spin qubit". In: *Nature Communications* 7 (Nov. 2016). ISSN: 20411723. DOI: `10.1038/ncomms13575`.

[13] A. M. J. Zwerver et al. "Qubits made by advanced semiconductor manufacturing". In: *Nature Electronics* 5.3 (Mar. 2022), pp. 184–190. ISSN: 2520-1131. DOI: `10.1038/s41928-022-00727-9`. URL: `https://www.nature.com/articles/s41928-022-00727-9`.

[14] M. Veldhorst et al. "Silicon CMOS architecture for a spin-based quantum computer". In: *Nature Communications* 8.1 (Dec. 2017), p. 1766. ISSN: 2041-1723. DOI: `10.1038/s41467-017-01905-6`. URL: `http://www.nature.com/articles/s41467-017-01905-6`.

[15] X. Xue et al. "CMOS-based cryogenic control of silicon quantum circuits". In: *Nature* 593.7858 (May 2021), pp. 205–210. ISSN: 0028-0836. DOI: `10.1038/s41586-021-03469-4`. URL: `https://www.nature.com/articles/s41586-021-03469-4`.

[16] C. D. Hill et al. "Quantum Computing: A surface code quantum computer in silicon". In: *Science Advances* 1.9 (Oct. 2015). ISSN: 23752548. DOI: `10.1126/SCIADV.1500707`. URL: `https://www.science.org`.

[17] R. Li et al. "A crossbar network for silicon quantum dot qubits". In: *Science Advances* 4.7 (July 2018), pp. 3960–3966. ISSN: 2375-2548. DOI: `10.1126/sciadv.aar3960`. URL: `https://www.science.org/doi/10.1126/sciadv.aar3960`.

[18] G. Scappucci et al. "Crystalline materials for quantum computing: Semiconductor heterostructures and topological insulators exemplars". In: *MRS Bulletin* 46.7 (July 2021), pp. 596–606. ISSN: 0883-7694. DOI: `10.1557/s43577-021-00147-8`. URL: `https://link.springer.com/10.1557/s43577-021-00147-8`.

[19] R. Hanson et al. "Spins in few-electron quantum dots". In: *Reviews of Modern Physics* 79.4 (Oct. 2007), pp. 1217–1265. ISSN: 0034-6861. DOI: `10.1103/RevModPhys.79.1217`. URL: `https://link.aps.org/doi/10.1103/RevModPhys.79.1217`.

[20] W. I. L. Lawrie et al. "Spin Relaxation Benchmarks and Individual Qubit Addressability for Holes in Quantum Dots". In: *Nano Letters* 20.10 (Oct. 2020), pp. 7237–7242. ISSN: 1530-6984. DOI: `10.1021/acs.nanolett.0c02589`. URL: `https://pubs.acs.org/doi/10.1021/acs.nanolett.0c02589`.

[21] N. W. Hendrickx et al. "Fast two-qubit logic with holes in germanium". In: *Nature* 577.7791 (Jan. 2020), pp. 487–491. ISSN: 0028-0836. DOI: `10.1038/s41586-019-1919-3`. URL: `https://www.nature.com/articles/s41586-019-1919-3`.

[22] F. Vigneau et al. "Probing quantum devices with radio-frequency reflectometry". In: *Applied Physics Reviews* 10.2 (June 2023), p. 21305. ISSN: 1931-9401. DOI: `10.1063/5.0088229`. URL: `https://pubs.aip.org/apr/article/10/2/021305/2885320/Probing-quantum-devices-with-radio-frequency`.

[23] C. Volk et al. “Loading a quantum-dot based “Qubyte” register”. In: *npj Quantum Information* 5.1 (Dec. 2019), p. 29. ISSN: 2056-6387. DOI: 10.1038/s41534-019-0146-y. URL: http://www.nature.com/articles/s41534-019-0146-y.

[24] T. Hensgens et al. “Quantum simulation of a Fermi–Hubbard model using a semiconductor quantum dot array”. In: *Nature* 548.7665 (Aug. 2017), pp. 70–73. ISSN: 1476-4687. DOI: 10.1038/nature23022. URL: https://doi.org/10.1038/nature23022.

[25] A. R. Mills et al. “Shuttling a single charge across a one-dimensional array of silicon quantum dots”. In: *Nature Communications* 10.1 (Dec. 2019). ISSN: 20411723. DOI: 10.1038/S41467-019-08970-Z.

[26] M. Lodari et al. “Low percolation density and charge noise with holes in germanium”. In: *Materials for Quantum Technology* 1.1 (Mar. 2021), p. 011002. ISSN: 2633-4356. DOI: 10.1088/2633-4356/abcd82. URL: https://iopscience.iop.org/article/10.1088/2633-4356/abcd82.

[27] A. Dawid et al. “Modern applications of machine learning in quantum sciences”. In: *Alba Cervera-Lierta* 15 (Apr. 2022). URL: https://arxiv.org/abs/2204.04198v4.

[28] W. Ha et al. “A Flexible Design Platform for Si/SiGe Exchange-Only Qubits with Low Disorder”. In: *Nano Letters* 22.3 (Feb. 2022), pp. 1443–1448. ISSN: 1530-6984. DOI: 10.1021/acs.nanolett.1c03026. URL: https://doi.org/10.1021/acs.nanolett.1c03026.

[29] F. Borsoi et al. “Shared control of a 16 semiconductor quantum dot crossbar array”. In: *Nature Nanotechnology* 19.1 (Jan. 2024), pp. 21–27. ISSN: 1748-3387. DOI: 10.1038/s41565-023-01491-3. URL: https://www.nature.com/articles/s41565-023-01491-3.

[30] S. De Franceschi et al. “Electron Cotunneling in a Semiconductor Quantum Dot”. In: *Physical Review Letters* 86.5 (Jan. 2001), pp. 878–881. ISSN: 0031-9007. DOI: 10.1103/PhysRevLett.86.878.

[31] C. H. Yang et al. “Charge state hysteresis in semiconductor quantum dots”. In: *Applied Physics Letters* 105.18 (Nov. 2014). ISSN: 0003-6951. DOI: 10.1063/1.4901218.

[32] P. Harvey-Collard et al. “High-Fidelity Single-Shot Readout for a Spin Qubit via an Enhanced Latching Mechanism”. In: *Physical Review X* 8.2 (May 2018), p. 021046. ISSN: 2160-3308. DOI: 10.1103/PhysRevX.8.021046. URL: https://link.aps.org/doi/10.1103/PhysRevX.8.021046.

[33] H. G. J. Eenink et al. “Tunable Coupling and Isolation of Single Electrons in Silicon Metal-Oxide-Semiconductor Quantum Dots”. In: *Nano Letters* 19.12 (Dec. 2019), pp. 8653–8657. ISSN: 1530-6984. DOI: 10.1021/acs.nanolett.9b03254. URL: https://pubs.acs.org/doi/10.1021/acs.nanolett.9b03254.

[34] P.-A. Mortemousque et al. “Enhanced Spin Coherence while Displacing Electron in a Two-Dimensional Array of Quantum Dots”. In: *PRX Quantum* 2.3 (Aug. 2021), p. 030331. DOI: 10.1103/PRXQuantum.2.030331. URL: https://journals.aps.org/prxquantum/abstract/10.1103/PRXQuantum.2.030331.

[35] H. Moon et al. “Machine learning enables completely automatic tuning of a quantum device faster than human experts”. In: *Nature Communications* 11.1 (Aug. 2020), p. 4161. ISSN: 2041-1723. DOI: 10.1038/s41467-020-17835-9.

[36] J. P. Zwolak et al. “Ray-Based Framework for State Identification in Quantum Dot Devices”. In: *PRX Quantum* 2.2 (June 2021), p. 020335. ISSN: 2691-3399. DOI: 10.1103/PRXQuantum.2.020335. URL: https://link.aps.org/doi/10.1103/PRXQuantum.2.020335.

[37] J. Ziegler et al. “Toward Robust Autotuning of Noisy Quantum dot Devices”. In: *Physical Review Applied* 17.2 (Feb. 2022), p. 024069. ISSN: 2331-7019. DOI: 10.1103/PhysRevApplied.17.024069. URL: https://link.aps.org/doi/10.1103/PhysRevApplied.17.024069.

[38] L. DiCarlo et al. “Differential Charge Sensing and Charge Delocalization in a Tunable Double Quantum Dot”. In: *Physical Review Letters* 92.22 (June 2004), p. 226801. ISSN: 0031-9007. DOI: 10.1103/PhysRevLett.92.226801. URL: https://link.aps.org/doi/10.1103/PhysRevLett.92.226801.

[39] N. W. Hendrickx et al. “A four-qubit germanium quantum processor”. In: *Nature* 591.7851 (Mar. 2021), pp. 580–585. ISSN: 0028-0836. DOI: 10.1038/s41586-021-03332-6. URL: https://www.nature.com/articles/s41586-021-03332-6.

[40] X. Xue et al. “Quantum logic with spin qubits crossing the surface code threshold”. In: *Nature* 601.7893 (Jan. 2022), pp. 343–347. ISSN: 0028-0836. DOI: 10.1038/s41586-021-04273-w. URL: https://www.nature.com/articles/s41586-021-04273-w.

[41] D. M. Zajac et al. “Scalable Gate Architecture for a One-Dimensional Array of Semiconductor Spin Qubits”. In: *Physical Review Applied* 6.5 (Nov. 2016), p. 054013. ISSN: 2331-7019. DOI: 10.1103/PhysRevApplied.6.054013.

[42] W. I. Lawrie et al. *Quantum dot arrays in silicon and germanium*. Feb. 2020. DOI: 10.1063/5.0002013.

[43] C. J. van Diepen et al. “Automated tuning of inter-dot tunnel coupling in double quantum dots”. In: *Applied Physics Letters* 113.3 (July 2018), p. 33101. ISSN: 0003-6951. DOI: 10.1063/1.5031034. URL: https://pubs.aip.org/apl/article/113/3/033101/37032/Automated-tuning-of-inter-dot-tunnel-coupling-in.

[44] F. Arute et al. “Quantum supremacy using a programmable superconducting processor”. In: *Nature* 574.7779 (Oct. 2019), pp. 505–510. ISSN: 0028-0836. DOI: 10.1038/s41586-019-1666-5. URL: https://www.nature.com/articles/s41586-019-1666-5.

[45] S. G. J. Philips et al. "Universal control of a six-qubit quantum processor in silicon". In: *Nature* 609.7929 (Sept. 2022), pp. 919–924. ISSN: 0028-0836. DOI: 10.1038/s41586-022-05117-x. URL: https://www.nature.com/articles/s41586-022-05117-x.

[46] M. Y. Lanzerotti, G. Fiorenza, and R. A. Rand. "Microminiature packaging and integrated circuitry: The work of E. F. Rent, with an application to on-chip interconnection requirements". In: *IBM Journal of Research and Development* 49.4.5 (July 2005), pp. 777–803. ISSN: 0018-8646. DOI: 10.1147/rd.494.0777.

[47] J. Morton and W. Pietenpol. "The Technological Impact of Transistors". In: *Proceedings of the IRE* 46.6 (June 1958), pp. 955–959. ISSN: 0096-8390. DOI: 10.1109/JRPROC.1958.286834.

[48] P. Christie and D. Stroobandt. "The interpretation and application of Rent's rule". In: *IEEE Transactions on Very Large Scale Integration (VLSI) Systems* 8.6 (Dec. 2000), pp. 639–648. ISSN: 1063-8210. DOI: 10.1109/92.902258.

[49] P. L. Bavdaz et al. "A quantum dot crossbar with sublinear scaling of interconnects at cryogenic temperature". In: *npj Quantum Information* 8.1 (July 2022), p. 86. ISSN: 2056-6387. DOI: 10.1038/s41534-022-00597-1. URL: https://www.nature.com/articles/s41534-022-00597-1.

[50] M. Russ et al. "High-fidelity quantum gates in Si/SiGe double quantum dots". In: *Physical Review B* 97.8 (Feb. 2018), p. 085421. ISSN: 2469-9950. DOI: 10.1103/PhysRevB.97.085421. URL: https://link.aps.org/doi/10.1103/PhysRevB.97.085421.

[51] L. Petit et al. "Spin Lifetime and Charge Noise in Hot Silicon Quantum Dot Qubits". In: *Physical Review Letters* 121.7 (Aug. 2018), p. 076801. ISSN: 0031-9007. DOI: 10.1103/PhysRevLett.121.076801. URL: https://link.aps.org/doi/10.1103/PhysRevLett.121.076801.

6

OPERATING SEMICONDUCTOR QUANTUM PROCESSORS WITH HOPPING SPINS

> *I would say that balance (while walking) was not difficult; however, I did some fairly high jumps and found that there was a tendency to tip over backwards on a high jump.* [1]
>
> Neil Armstrong

Qubits that can be efficiently controlled are essential for the development of scalable quantum hardware. Although resonant control is used to execute high-fidelity quantum gates, the scalability is challenged by the integration of high-frequency oscillating signals, qubit crosstalk and heating. Here, we show that by engineering the hopping of spins between quantum dots with a site-dependent spin quantization axis, quantum control can be established with discrete signals. We demonstrate hopping-based quantum logic and obtain single-qubit gate fidelities of 99.97%, coherent shuttling fidelities of 99.992% per hop, and a two-qubit gate fidelity of 99.3%, corresponding to error rates that have been predicted to allow for quantum error correction. We also show that hopping spins constitute a tuning method by statistically mapping the coherence of a 10-quantum dot system. Our results show that dense quantum dot arrays with sparse occupation could be developed for efficient and high-connectivity qubit registers.

Parts of this chapter have been published in Chien-An Wang, **Valentin John**, Hanifa Tidjani, Cécile X. Yu , Alexander S. Ivlev, Corentin Déprez, Floor van Riggelen-Doelman, Benjamin D. Woods, Nico W. Hendrickx, William I. L. Lawrie, Lucas E. A. Stehouwer, Stefan D. Oosterhout, Amir Sammak, Mark Friesen, Giordano Scappucci, Sander L. de Snoo, Maximilian Rimbach-Russ, Francesco Borsoi, and Menno Veldhorst, Operating semiconductor quantum processors with hopping spins, *Science* **385**, 447-452 (2024).

Loss and DiVincenzo proposed hopping of electrons between two quantum dots as an efficient method for coherent spin control [2]. By applying discrete pulses to the quantum dot gates, a single spin can be transferred between qubit sites with differently oriented spin quantization axes, thereby enabling two-axis control of the qubit. Universal quantum logic is then achieved through a tunable exchange interaction between spins residing in different quantum dots. That work initiated the field of semiconductor spin qubits and inspired more than two decades of extensive research, but a successful implementation of Loss and DiVincenzo's initial proposal has remained elusive because of experimental challenges [3].

Alternative methods for coherent single-spin control have emerged, including electron spin resonance [4, 5] and electric dipole spin resonance using either micromagnets [6, 7] or spin-orbit interaction [8–11] to enable a coupling between the electric field and the spin degree of freedom. However, all of these methods rely on resonant Rabi driving and require high-power, high-frequency analog control signals that already limit qubit performance in small quantum processors [12–14]. The development of local, efficient, low-power control mechanisms of semiconductor spins is now a key driver [15–17]. To this end, qubits encoded in multiple spins and in multiple quantum dots, such as singlet-triplet, hybrid, and exchange-only qubits, have been investigated as possible platforms [3]. Although these qubit encodings have enabled digital single-qubit control, they also come with new challenges in coherence, control, and creation of quantum links. For example, the exchange-only qubits are susceptible to leakage outside of their computational subspace and require four exchange pulses to execute an arbitrary single-qubit gate and ≥ 12 exchange pulses for a single two-qubit gate [18–20].

Here, we demonstrate that single-spin qubits can be operated using baseband control signals, as envisaged in the original proposal for quantum computation with quantum dots [2]. We used hole spins in germanium quantum dots, in which the strong spin-orbit interaction gives rise to an anisotropic g-tensor that is strongly dependent on the electrostatic and strain environment [21]. We harnessed the resulting differences in the spin quantization axis between quantum dots [22, 23] to achieve high-fidelity single-qubit control using discrete pulses by shuttling the spin between quantum dot sites. A key advantage in such a hopping-based operation is that the spin rotation frequency is given by the Larmor precession. The latter remains sizeable even at small magnetic fields where quantum coherence is substantially improved [24, 25]. This enabled us to perform universal quantum control with error rates exceeding the thresholds predicted for practical quantum error correction[26] while also operating with low-frequency baseband signals. We then exploited the differences in quantization axes to map the spin dephasing times and g-factor distributions of an extended 10-quantum dot array, thereby efficiently gathering statistics on relevant metrics in large spin qubit systems.

6.1. HIGH-FIDELITY SINGLE-QUBIT OPERATIONS AND LONG QUBIT COHERENCE TIMES AT LOW MAGNETIC FIELD

A large difference in the orientation of the spin quantization axes between quantum dots is essential for hopping-based qubit operations. Holes in planar germanium heterostructures manifest a pronounced anisotropic g-tensor, with an out-of-plane g-

factor $g_\perp$ that can be two orders of magnitude larger than the in-plane component, $g_\parallel$ [21, 25, 27, 28]. Consequently, a small tilt of the applied magnetic field from the in-plane g-tensor will lead to a strong reorientation of the spin quantization axis in the out-of-plane direction. Subsequently, when an in-plane magnetic field is applied, the orientation of the spin quantization axis is highly sensitive to the local g-tensor, and thus to confinement, strain, and electric fields, thus becoming a site-dependent property [22, 25, 29, 30]. Here, we exploited this aspect to establish hopping-based quantum operations in two different devices: a four-quantum dot array [31] arranged in a 2×2 configuration and a 10-quantum dot system arranged in a 3-4-3 configuration.

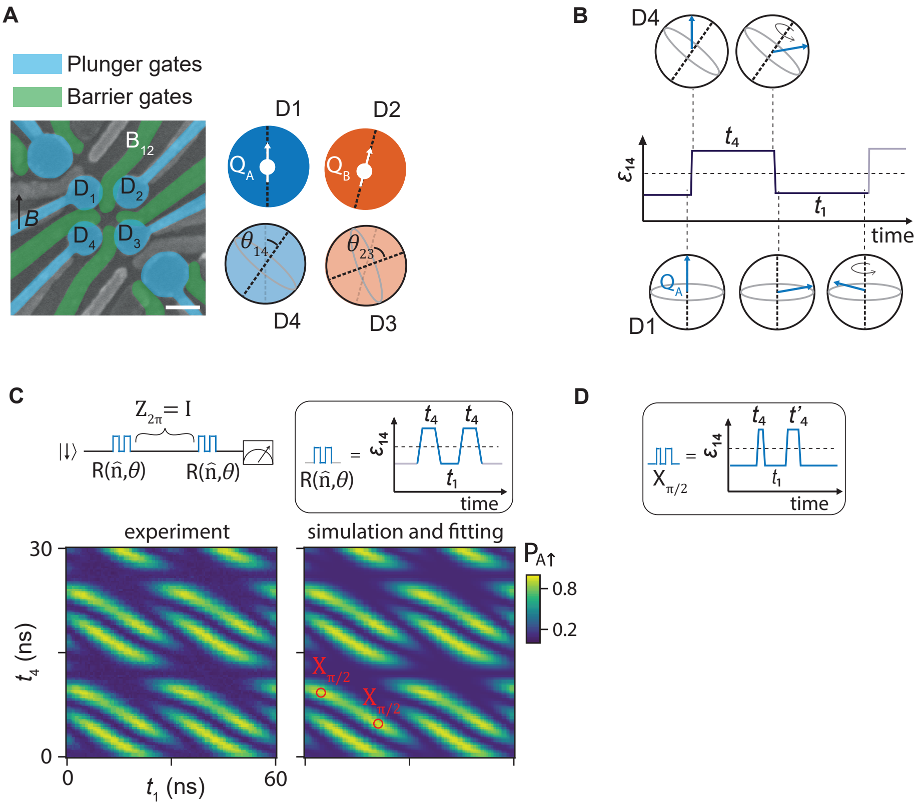

Figure 6.1: **Hopping-based single-qubit operations - schematics and tune-up.** **(A)** Left: scanning electron microscopy image of the 2×2 quantum dot array device [31], including gate-defined charge sensors at two corners. Scale bar, 100 nm. Right: schematic of the two spin qubits, Q_A and Q_B. The black dashed lines mark the relative quantization axis direction in the quantum dot pair D1-D4 (D2-D3), with the angle θ_{14} (θ_{23}). **(B)** Example of a baseband pulse $\epsilon_{14}(t)$ used to manipulate qubit Q_A, by shuttling the spin back and forth between quantum dots D1 and D4 and allowing the spin to precess in the individual quantum dots for the time t_4 and t_1. **(C)** Tune-up procedure of a four-shuttle pulse for the $X_{\pi/2}$ gate of Q_A at 20 mT. Top: pulse sequence of the experiment. Bottom left: measured spin-up probability $P_{A\uparrow}(t_1, t_4)$. Bottom right: simulation results. The red markers identify the timings for implementing an $X_{\pi/2,A}$ gate and corresponds to the maximal spin-up probability. The markers are periodic in t_1 and t_4, but for clarity we only plot a few of them. **(D)** Calibrated pulse for $X_{\pi/2,A}$ gate with unequal wait time t_4 and t'_4.

We populated the four-quantum dot array with quantum dots Dm with $m \in [[1, 4]]$ with two hole spins Q_A and Q_B which can be shuttled between quantum dots by electrical pulses on the gate electrodes (Fig. 6.1A). A magnetic field up to 40 mT was applied to split the spin states and positioned in-plane up to sample-alignment accuracy (see Section 6.4). The relatively small magnetic fields ensured that the maximum qubit frequency (140 MHz) and its corresponding precession period (7 ns) were within the bandwidth of the arbitrary waveform generators used. In combination with engineered voltage pulses with sub-nanosecond resolution [22] (Section 6.5.4), we were able to shuttle a spin qubit to an empty quantum dot and thereby accurately change the qubit precession direction several times within one precession period. Altogether, this enables efficient single-qubit control through discrete voltage pulses (Fig. 6.1B).

The net effect of a multiple-shuttle protocol is a rotation $R(\hat{n},\theta)$ of the spin state around an axis $\hat{n}$ and with an angle θ. To implement a specific rotation such as the quantum gate $X_{\pi/2}$, the number of required shuttling steps depends on the angle between the two quantization axes. Because of the large angle between the axes of D1 and D4, $\theta_{14} > 90°/4 = 22.5°$, a pulse consisting of four shuttling steps is sufficient to realize a precise quantum gate $X_{\pi/2,A}$. As outlined on the top right panel of Fig. 6.1C, such a four-shuttle pulse moves the spin between D1 and D4 four times with waiting periods t_1 and t_4, respectively. By measuring the spin-flip probability of Q_A, $P_{A\uparrow}$, after two consecutive rotations $R(\hat{n},\theta)^2$, we could determine the values of t_1 and t_4 where $P_{A\uparrow}$ is maximal, which occurs when $R(\hat{n},\theta) = X_{\pi/2,A}$.

Although this method allows calibration of the pulse timing to compose an $X_{\pi/2,A}$ gate, it is not necessarily the optimal trajectory. Different choices of (t_1, t_4) are possible (Fig. 6.1C), including a composition of four-shuttle pulses with different waiting times in D4. The latter implementation allows for the construction of gates with a rotation angle θ less sensitive to Larmor frequency fluctuations in D4. We constructed such a gate by fitting the data in Fig. 6.1C to an effective model and determined the quantization axes angle θ_{14} between the quantum dots D1 and D4, the individual Larmor frequencies, and the effective precession time during the ramp. Through simulation of the qubit dynamics, we designed a more noise-resilient $X_{\pi/2,A}$ gate based on four shuttling steps with unequal wait times t_4 and t_4' in D4 (Fig. 6.1D). Following the same approach, we design an $X_{\pi/2,B}$ gate for Q_B that only requires a two-shuttle protocol because the angle of the difference in quantization axes of D2 and D3, θ_{23}, is very close to 45°.

We further calibrated the pulse timing using repetition sequences, as shown in Fig. 6.2C, and in AllXY sequences [32]. The $Y_{\pi/2}$ gate in the AllXY sequences was realized by $Y_{\pi/2} = Z_{\pi/2}X_{\pi/2}Z_{3\pi/2}$ and the $Z_{\pi/2}$ gate was implemented by idling the qubit for the time defined by its precession in the lab frame. The calibrated $X_{\pi/2}$ gates had a total gate time of 98 (35) ns for Q_A (Q_B), corresponding to effective qubit rotation frequencies of 2.6 (7.1) MHz, considerable compared with the Larmor frequencies $f_{A(B)} = 42.6$ (89.5) MHz at the in-plane magnetic field of 25 mT.

The high ratio between qubit rotation and Larmor frequency results in low power dissipation, which is a critical aspect for scaling up quantum processors [33]. To compare the power consumption of the hopping-based single-qubit control with the electric dipole spin resonance technique, we defined the required number of voltage oscillations to flip a qubit, N_{cycles}, and the derived energy efficiency, $\eta = 1/N_{\text{cycles}}$, which

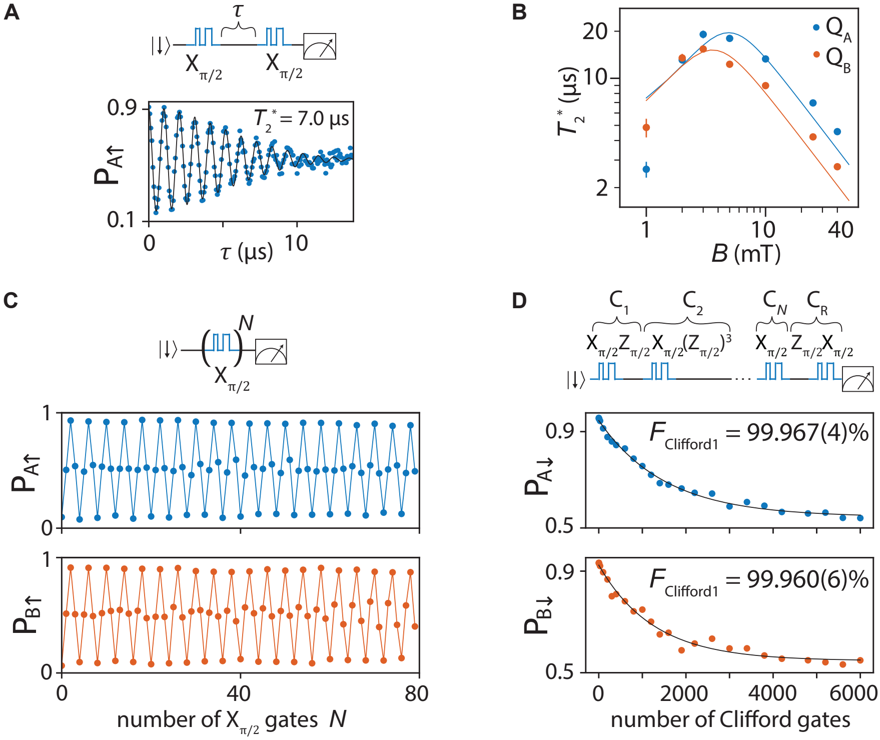

Figure 6.2: **Hopping-based single-qubit operations - gate fidelity and coherence times at low magnetic field.** **(A)** Free induction decay obtained from Ramsey experiments at 25 mT. **(B)** T_2^* as a function of magnetic field. The data points are fitted with an effective model including electric noise and nuclear noise. **(C)** Spin-up probability after applying a varying number of $X_{\pi/2}$ gates on each qubit. **(D)** Example of a pulse sequence in Q_A single-qubit randomized benchmarking and the measurement results of both qubits. The uncertainties are obtained from bootstrapping with 95% confidence intervals.

we found largely determines the power dissipation under the assumption that dielectric losses are dominant over other dissipation mechanisms (Section 6.5.1). For our system, we estimate an efficiency of $\eta = 25(50)\%$ for $Q_A(Q_B)$. By comparison, previous demonstrations of high-fidelity universal qubit logic in silicon exhibited η in the range of 0.04 to 0.07% [12, 13, 16]. Moreover, despite applying sizeable amplitudes to move the spins between localized orbitals of adjacent quantum dots, we still obtained a factor of 20 reduction in power dissipation with respect to the electric dipole spin resonance technique (Section 6.5.1). Engineering lower required pulse amplitudes and increasing the orthogonality of the spin quantization axes will enable a further reduction of the dissipated power. Furthermore, the hopping-based approach can simplify the signal delivery and required control electronics and thus alleviate the detrimental heating effects.

Having established universal single-qubit control, we used the set of gates $\{X_{\pi/2}, Y_{\pi/2}\}$ to investigate the qubit coherence times at low magnetic fields. By using a Ramsey sequence (Fig. 6.2A), we obtained a dephasing time T_2^* of 7.0 (4.5) μs at 25 mT for $Q_A(Q_B)$, an order of magnitude larger than that measured at 1 T in the same sample [24, 31]. We were able to further extend the coherence times using Hahn and Carr-Purcell-Meiboom-Gill (CMPG) techniques, obtaining $T_2^{\mathrm{H}} = (32 \pm 24)\,\mu$s and $T_2^{\mathrm{CPMG-512}} = 1.9(1.7)$ ms, respectively. The dependence of the dephasing times as a function of magnetic field (Fig. 6.2B) indicates that charge noise remains the main cause for decoherence for magnetic fields as low as 5 mT (Suppl. Section 5 of Ref. [34]).

We characterize the single-qubit gate fidelity using randomized benchmarking (RB) and gate set tomography (GST) [35–37] (Suppl. Section 6 and 7 of Ref. [34]). The results of RB with average Clifford fidelity (Fig. 6.2D) set the lower bounds of the $\mathrm{X}_{\pi/2}$ average gate fidelity at $F_{\mathrm{X}_{\pi/2},\mathrm{A}} \geq 99.967(4)\%$ and $F_{\mathrm{X}_{\pi/2},\mathrm{B}} \geq 99.960(6)\%$. Using GST we benchmarked the $\mathrm{X}_{\pi/2}$ and $\mathrm{Y}_{\pi/2}$ gates, obtaining an average gate fidelity $\gtrsim 99.9\%$. From the GST analysis, we infer that dephasing is the dominant contribution to the average gate infidelity. Taking into account the multiple shuttling steps to execute a single gate, we estimate a coherent shuttling fidelity per hop as high as $F_{\mathrm{shuttle}} = 99.992\%$ (Suppl. Section 9 of Ref. [34]).

6.1.1. HIGH-FIDELITY TWO-QUBIT EXCHANGE GATE

We now focus on assessing the single-qubit and two-qubit gate performance in the two-qubit space. We implemented a two-qubit state preparation and measurement (SPAM) protocol (Figs. 6.3A,B). For the state preparation, we adiabatically converted the two-spin singlet in D2 to the triplet $|\mathrm{Q_A Q_B}\rangle = |{\downarrow\downarrow}\rangle$. For the state measurement, we performed sequential Pauli spin blockade (PSB) readouts on $\mathrm{Q_A}$ and $\mathrm{Q_B}$ by loading ancillary spins from the reservoir and adiabatic conversion to the state $|{\downarrow\downarrow}\rangle$ in quantum dots D3 and D4. The difference in the effective g-factor between the quantum dots D1 and D2 allows for the construction of a controlled-Z (CZ) gate even at low magnetic fields. We did so by pulsing the virtual barrier gate voltage vB_{12}, which controls the exchange coupling J between $\mathrm{Q_A}$ and $\mathrm{Q_B}$ from 10 kHz to 40 MHz (Fig. 6.4C) (Suppl. Section 10 and 11 of Ref. [34]). Because the maximum exchange coupling strength is non-negligible compared with the Zeeman energy difference ΔE_{Z} and the qubit frequency f_{A}, pulse shaping is essential to mitigate coherent errors [13, 38]. We implemented exchange pulses with a Hamming window and performed the CZ gate calibration (Fig. 6.4D) (Suppl. Section 12 of Ref. [34]).

We now advance to benchmarking a two-qubit gate in germanium, by executing two-qubit randomized benchmarking. Individual Clifford gates were implemented by sequentially applying one or more of the gates CZ, $\mathrm{X}_{\pi/2}^{\mathrm{A(B)}}$, $\mathrm{Z}_{\pi/2}^{\mathrm{A(B)}}$, and I. From the fit of the decay constants of the reference and interleaved sequence in Fig. 6.4E, we determined the average Clifford gate fidelity as $F_{\mathrm{Clifford2}} = 98.60(6)\%$ and the average CZ gate fidelity as $F_{\mathrm{CZ}} = 99.33(10)\%$. For the single-qubit gate performance in the two-qubit space, we estimate the lower bound of fidelity, averaged between both qubits, as $\frac{1}{2}(F_{\mathrm{X}_{\pi/2},\mathrm{A}} + F_{\mathrm{X}_{\pi/2},\mathrm{B}}) \geq 99.90(5)\%$. We believe that these high fidelities to result from the high driving efficiency and relatively long $T_2^\star$ at low magnetic field.

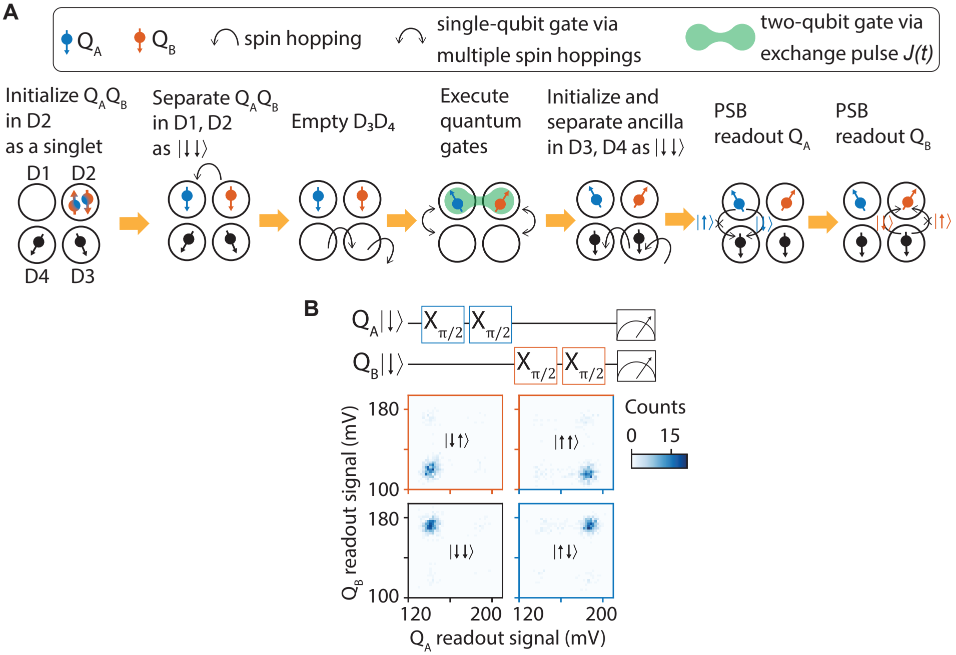

Figure 6.3: **High-fidelity two-qubit gate in germanium - schematics.** **(A)** Schematics of two-qubit initialization, manipulation and individual readout. $|Q_A Q_B\rangle$ was initialized by relaxing to the singlet ground state in D2 and then adiabatically moving one spin to D1. Quantum circuits consisting of single-qubit gates (spin hoppings) and two-qubit gates (exchange pulse $J(t)$) were performed. The final quantum state was read out by preparing ancillary spins and then performing two PSB readouts. In each readout, the chemical potentials of the quantum dots were pulsed such that the spin can either move to the neighboring dot (indicated by arrows) or stay in the original dot (indicated by arrows with × markers) with probabilities depending on the spin state $|Q_{A(B)}\rangle$. **(B)** Two dimensional histograms of the sensor signals formed by 500 single-shot measurements for four different two-qubit states, which are prepared by applying $X_{\pi/2,A(B)}$ gates.

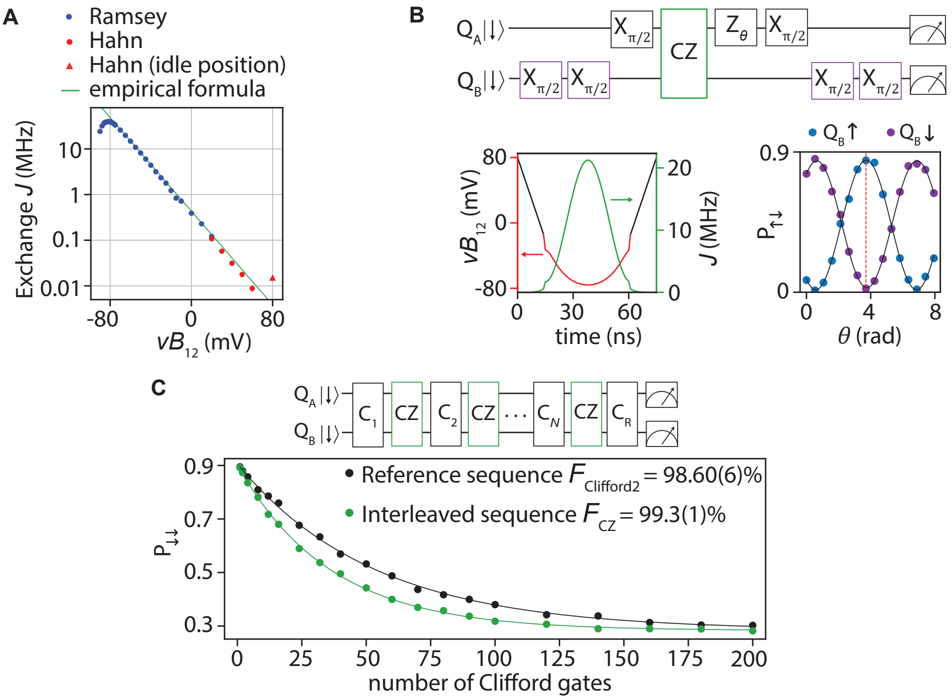

Figure 6.4: **High-fidelity two-qubit gate in germanium - measurement results.** **(A)** Exchange coupling as a function of virtual barrier gate vB_{12}, measured by Ramsey (Hahn echo) experiments in the large (small) coupling regime. The idle position corresponds to the barrier voltage where single qubit gates were performed, but at slightly different plunger gate voltage. The empirical formula for mapping vB_{12} and J is detailed in Suppl. Section 12 of Ref. [39]. The bending on the left side of the plot results from the energy level anti-crossing when $J \sim f_A$. **(B)** The voltage pulse of the CZ gate was shaped to have exchange $J(t)$ in the form of a Hamming window, as illustrated on the bottom left. The CZ gate calibration circuit for single-qubit phases is on the top, with the measurement outcome plotted on the bottom right. The target qubit (Q_A) phase depends on the control qubit Q_B being in the state $|\downarrow\rangle$ in blue ($|\uparrow\rangle$ in purple). The red dashed line marks the required single-qubit phase of Q_A for the CZ gate. **(C)** Gate sequence and measurement result of two-qubit interleaved RB.

6.2. HOPPING SPINS TO BENCHMARK LARGE AND HIGH-CONNECTIVITY QUANTUM DOT ARCHITECTURES

The presented sparse occupation of a quantum dot array allows the construction of high-fidelity hopping-based quantum logic, but it may also facilitate the implementation of quantum circuits with high-connectivity. Although two-dimensional quantum circuits with nearest neighbor connectivity can already tolerate high error rates [26, 40, 41], an increased connectivity may substantially lower the physical qubit overhead and lower the logical qubit error rate [42]. We therefore envision a qubit architecture with sparse occupation (Fig. 6.5A) to be a potential platform. Here, qubits may be shuttled to remote sites for distant two-qubit logic, and single-qubit logic can be executed during this

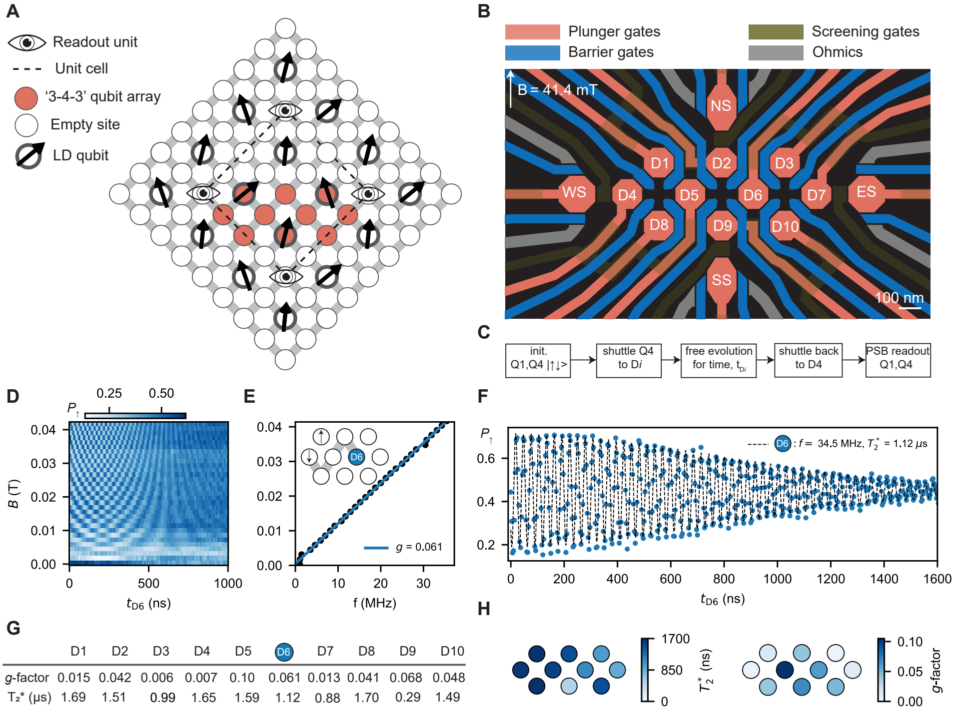

	D1	D2	D3	D4	D5	D6	D7	D8	D9	D10
g-factor	0.015	0.042	0.006	0.007	0.10	0.061	0.013	0.041	0.068	0.048
T_2^* (μs)	1.69	1.51	0.99	1.65	1.59	1.12	0.88	1.70	0.29	1.49

Figure 6.5: **Hopping spins to benchmark large and high-connectivity quantum dot architectures.** **(A)** Our vision of a semiconductor quantum computing architecture comprising hopping Loss-DiVincenzo (LD) spin qubits (black arrows), readout units (eyes), and empty quantum dot sites for shuttling operations. **(B)** Layout of the 10 quantum dot array, with gate-defined charge sensors labelled in analogy to the four cardinal points (NS, ES, WS, and SS). **(C)** Control sequence used to characterize the array. A spin originally in D4 was shuttled across the whole array, allowed to evolve at a certain quantum dot, and read out. **(D)** Qubit rotations induced by the difference in quantization axes as a function of idling time in quantum dot D6 and magnetic field. **(E)** D6 Larmor frequency, extracted from the Fourier analysis of (D) versus magnetic field. Linear fit yields an estimated g-factor of 0.062. Inset shows the shuttling trajectory of the spin qubit from D4 to D6. **(F)** Extended time evolution in D6 at B = 41.4 mT, yielding a qubit frequency of 34.51 MHz and a dephasing time of T_2^* =1.12 μs. The experimental trace was fitted (dashed lines) as described in Section 6.5.6. **(G and H)** Table and visualization of the extracted parameters: g-factors and T_2^*, respectively.

trajectory.

As a first step toward such architectures, we developed and characterized an extended system comprising 10 quantum dots. The system (Fig. 6.5B) consists of a multilayer gate architecture with quantum dots, Dn with $n \in [[1, 10]]$, and peripheral charge sensors, which may be integrated within the array through development of vertical interconnects such as in [43]. By exploiting dedicated (virtual) barrier and plunger gate voltages, we prepared the quantum dots D1 and D4 in the single-hole regime, leaving the others empty (see Section 14 of the supplementary material, and Section 6.5.5).

The hopping-based qubit gates were used to rapidly characterize the different quantum dot g-factors and coherence times. After initializing the associated qubit pair Q1,Q4 into its $|\uparrow\downarrow\rangle$ eigenstate, we diabatically shuttled the Q4 spin to another quantum dot site, Dn. We let it precess for a time $t_{\mathrm{D}n}$, after which the spin was shuttled back and read out. The misalignment between the spin quantization axes gives rise to spin rotations with the Larmor frequency $f_{\mathrm{D}n}$ [22]. The resulting oscillations are shown as a function of waiting time in D6, t_{D6}, and magnetic field (Fig. 6.5D). From the linear scaling of the D6 Larmor frequency with the magnetic field, we extracted an effective g-factor of 0.062 (Fig. 6.5E) and from the decay of the oscillations a dephasing time of $T_2^* = 1.12\,\mu$s (Fig. 6.5F). Repeating this protocol to reach all the quantum dots, we extracted the Larmor frequency and dephasing time at each site, as displayed in Figs. 6.5G, H. For the case of Q1 (Q4), we shuttled the spin to D5 (D8) back and forth twice, interleaved by a varying precession time in D1, t_{Q1} (in D4, t_{Q4}), which we explain in detail in subsection 6.5.3. Our experiments showed an average T_2^* of $1.3 \pm 0.4\,\mu$s at a magnetic field of 41.4 mT (Section 6.5.6), and we attribute the fast dephasing of D9 ($T_2^* = 290$ ns) to charge noise originating from a fluctuator nearby. Furthermore, we obtained an average g-factor of 0.04 ± 0.03. The observed variability in this distribution is likely a result of multiple factors: the heterogeneity inherent in the shapes of the quantum dots (dot-to-dot variability), the presence of strain gradients in the quantum well arising from the gates above or the SiGe strained relaxed buffer below, and the impact of interface charges. The average g-factor that we obtained was considerably lower than what has been observed in the literature [11, 25, 31, 44]. We suggest that this reduction is primarily due to two phenomena: a precise in-plane magnetic field configuration and an appreciable renormalization of the gyromagnetic ratio from the pure heavy-hole value of ~ 0.18 [10, 29, 45]. Such renormalization is driven by substantial inter-band mixing between the heavy-hole and the light-hole band, which we attribute to asymmetries in the strain. Furthermore, these simulations indicate that such a low average effective g-factor only occurs when the misalignment of the magnetic field is smaller than 0.1° with respect to the plane of the g-tensors, emphasizing the importance of accurately controlling the magnetic field orientation when operating with germanium qubits.

6.3. CONCLUSION

We have shown that hopping spin qubits between quantum dots with site-dependent g-tensors allows for coherent shuttling with fidelities up to 99.992%, single-qubit gate fidelities up to 99.97%, and two-qubit gate fidelities up to 99.3%. This method allows for efficient control with baseband pulses only and fast execution of quantum gates even at low magnetic fields where the coherence is high. Using this approach for the control of dense quantum dot arrays with sparse qubit occupation can alleviate challenges in crosstalk and heating, while providing high connectivity. Recent theoretical developments predict that increased connectivity can substantially improve logical qubit performance and reduce the required overhead on physical qubits [42]. Sparse spin qubit arrays could be particularly suited for error correction schemes requiring either a larger number of nearest neighbors or coupling beyond nearest neighbors. A substantial challenge remains in addressing the qubit-to-qubit variation. This was already highlighted in the original work by Loss and DiVincenzo [2]. We envision that the characterization of larger qubit arrays and statistical analysis will become pivotal, with the presented 10-quantum dot array already providing a first indication that design considerations can determine relevant qubit parameters. Site-dependent quantization axes can be realized by g-tensor engineering such as in elongated quantum dots [46], by using nanomagnets, or by applying currents through nanowires above the qubit plane [47]. The developed control methods for high timing accuracy can also advance exchange-only qubits that are operated using baseband pulses [20] and affect platforms such as superconducting qubits [48]. We envision establishing high-fidelity quantum operation through low-power control in uniform and large-scale systems to be a critical step in realizing fault-tolerant quantum computing.

6.4. METHODS

We estimate a possible misalignment angle between the device plane and the magnetic field axis of ±2°. We also note that due to an offset in the height position of the 10 quantum dots chip on the cold finger of the cryostat with respect to the center of the field, the effective magnetic field is 69% of the applied field. We have determined this factor using the Ge-73 gyromagnetic ratio, measured via CPMG sequences on a different device mounted in the same position in a different cool-down. This factor also agrees well to what estimated using simulations of the coil field.

6.5. SUPPLEMENTARY

6.5.1. POWER DISSIPATION AND SCALING ADVANTAGES OF SHUTTLING-BASED CONTROL

To execute the shuttling operations, trapezoidal voltage pulses are applied on the gates. To achieve high-fidelity single qubit control a handful of such shuttling pulses are required, each with ramp times of a few nanoseconds between two discrete voltage levels. This stands in stark contrast with state-of-the-art electron dipole spin resonance (EDSR) control where typically high frequency, sinusoidal pulses are applied, and many oscillations of the driving signal are needed to achieve the desired gate fidelity [12, 13]. This gives an advantage to a shuttling-based architecture considering energy dissipation, crosstalk and complexity of the required control electronics.

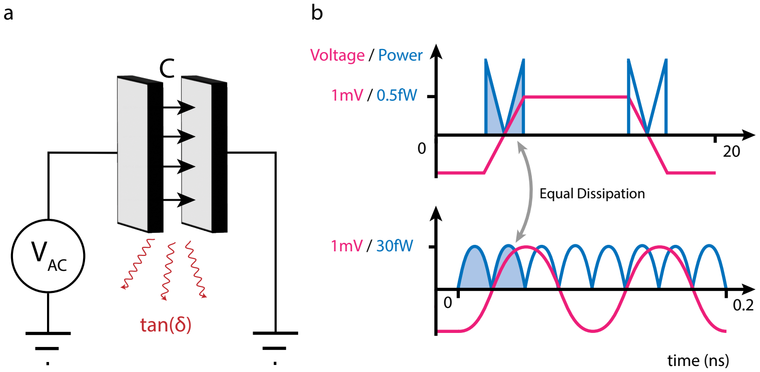

Figure 6.6: **Heat dissipation. a,** Schematic of the model of the heat dissipation, due to some capacitor C with loss tangent $\tan(\delta)$. **b,** For equal pulse amplitude and DC-offset, the heat dissipated per cycle is the same independent of the pulse shape. $C \cdot \tan(\delta) = 10 \times 10^{-18}$ F was assumed in this example.

Already at the current system sizes, EDSR-based devices experience a drift in qubit frequency that is linked to heat dissipation of the signal [17]. When resistive losses are limited, this heat-dissipation is believed to result from a dielectric loss of energy stored in the electric field around the signal-line. Effectively the system is a capacitor with some loss tangent $\tan(\delta)$, defined as $\tan(\delta) = \epsilon''/\epsilon'$ in a non-conductive system, with ϵ'' and ϵ' the imaginary and real part of the electric permittivity [49]. During each charging cycle, a fraction proportional to $\tan(\delta)$ of the stored electric energy is lost as depicted in Fig. 6.6. With a DC bias around zero the total capacitive energy stored and discharged by the signal line is proportional to CV_{AC}^2, where C is the capacitance and V_{AC} the EDSR amplitude, with which the capacitor is charged. The total energy lost is proportional to $E_{\mathrm{Loss}} = N_{\mathrm{cycles}} \tan(\delta) C V_{\mathrm{AC}}^2$, where N_{cycles} gives the number of oscillations required to perform a qubit operation. In a simplified model, we can take the electric permittivity and with it the loss tangent of silicon and germanium to be largely independent of frequency in the relevant frequency range [50, 51]. In this model, for an identical geometry and driving amplitude, the energy dissipation is assumed to solely depends on the number of cycles of the operation and not on the pulse-shape, as indicated in Fig. 6.6. Hence

$1/N_{\text{cycles}}$ is a measure of the efficiency of the operation.

For an EDSR-based X_π-gate the number of cycles is given by $N_{\text{cycles,EDSR}} = \frac{f_{\text{Larmor}}}{2f_{\text{Rabi}}}$, which is exactly the inverse of the efficiency η as defined in the main text. The driving efficiency is inherently limited by the relatively small Rabi frequency $f_{\text{Rabi}} \ll f_{\text{Larmor}}$ when operating in the weak-driving (adiabatic) regime, in which the rotating-wave approximation holds. We note that while faster driving is possible, it requires complex amplitude and phase modulation for high-fidelity implementations [38, 52] which also dissipate additional heat. An experimental demonstration of high-fidelity qubit logic is given by Xue et al. operated with Rabi (Larmor) frequencies of $f_{\text{Rabi}} = 2\,\text{MHz}$ ($f_{\text{Larmor}} = 12\,\text{GHz}$) [13, 16]. This corresponds to an efficiency of $\eta = 2f_{\text{Rabi}}/f_{\text{Larmor}} \approx 1/3000$. Similarly Noiri et al. demonstrated $\eta \approx 1/1500$ [12]. For the prior device, an EDSR amplitude of $V_{\text{AC}} \approx 5\,\text{mV}$ is reported at the bond pads of the chip [16]. This corresponds to an energy dissipation of $E_{\text{Loss}} \approx 0.075\tan(\delta)C\,\text{V}^2$ per X_π-gate for high-fidelity EDSR control.

Shuttling based gates do not face a similar inherit efficiency limitation, instead being limited by the relative tilt in quantization axis. In the main part of the paper we demonstrate that to perform an X_π-gate using shuttling, the hole is shuttled two to four times back and forth depending on the angle between the quantization axes of the quantum dot pairs. With periodic pulse timings and negligible ramp times this corresponds to $N_{\text{cycles}} = 1/\eta$. This is done with a typical amplitude $V_{\text{AC}} = 20\,\text{mV}$. Using the $N_{\text{cycles}} = 4$ figure, this corresponds to a heat-dissipation corresponding to $E_{\text{Loss}} = 2\cdot 0.0016\tan(\delta)C\,\text{V}^2 = 0.0032\tan(\delta)C\,\text{V}^2$, where the additional factor of two accounts for the two plunger gates on which the voltage is applied.

Crosstalk, like heat dissipation, is a problem observed in the current spin-qubit devices and is expected to become more significant as the number and density of qubits increase [14]. This crosstalk can originate from close spacing of signal lines, both on and off the qubit chip. As the density of the quantum dots increases, the capacitance between the gates is expected to grow accordingly, increasing the crosstalk further. Since the admittance between signal lines is directly proportional to the signal frequency, the capacitive crosstalk will be less for low-frequency shuttling-based pulses, compared to high-frequency EDSR experiments which face challenges similar to conventional high-frequency integrated circuits [53]. In integrated circuits design, a rule of thumb is to keep the distance between traces to three times the trace width [53]. This might pose a significant limitation for qubit routing, especially for larger 2D arrays. An architecture based on the demonstrated high-fidelity shuttling gates is thus expected to be less sensitive to crosstalk, which will be advantageous in scaling to large qubit counts.

In large spin systems consisting of many hundreds or thousands of qubits, the scalability of control electronics is a major consideration. The electronic hardware required to generate the IQ modulated sinusoidal EDSR pulses need high analog voltage resolution, which is significantly more involved than the shuttling pulses consisting of two voltage levels. The lower required voltage accuracy and precision of the shuttling based control allows scaling the qubit count while limiting the electronic overhead, cost and energy consumption. The required timing resolution of shuttling based control should be below 90 ps for a 40 MHz Larmor frequency (Section 6.5.4), higher than the sampling resolution of the IQ modulated EDSR driving. However, EDSR signals need to control the qubit phase with a similar precision as the shuttling pulses, thus requiring a similarly high resolution.

6.5.2. CHARGE TUNING AND VIRTUAL GATE CONTROL OF THE 10 QUANTUM DOT ARRAY

We prepare the 10 quantum dot system shown in Fig. 6.7 in the charge configuration with D1 and D4 in the single-hole regime, and the others in the empty charge regime. Figs. 6.8a-k display the charge stability diagrams acquired via charge sensing as a function of virtual plunger gates. At first, a virtual gate framework, with virtual matrix shown in Fig. 6.9, is defined in software to:

- compensate the cross-capacitance of each gate with fast (ac) control to the four charge sensors;
- achieve independent control of the quantum dots chemical potentials via virtual plunger gates vP1-vP10.

A second matrix, shown in Fig. 6.10, is used for the definition of virtual barriers J1-J12, as a linear combinations of vB1-vB12 and vP1-vP10. J1-J12 serve to independently control the interdot tunnel couplings, without changing the quantum dots chemical potentials.

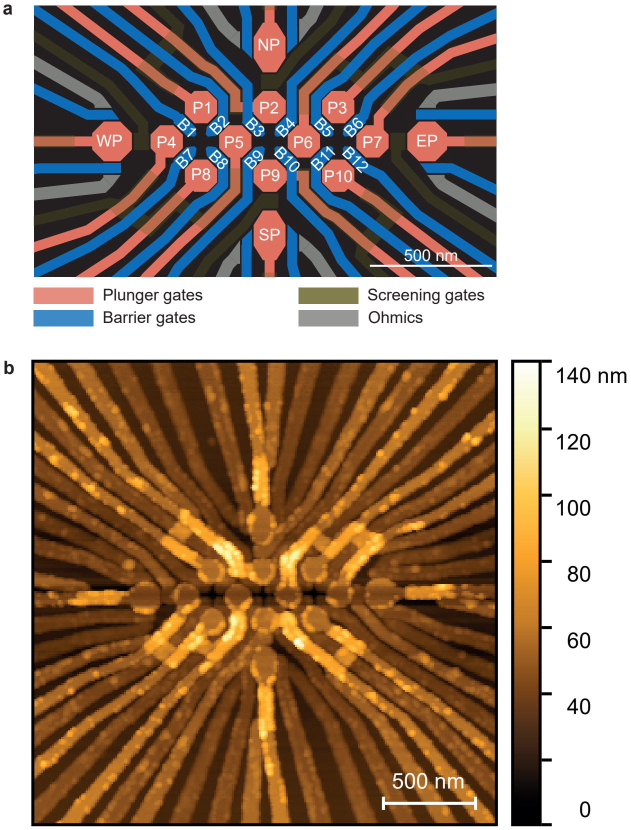

Figure 6.7: **The 10 quantum dot array device. a,** Layout of the device indicating the names of the relevant gates. Plungers and barriers are labelled with P and B, respectively. In analogy to the cardinal coordinates, the sensors plunger gates are labelled as NP (north), EP (east), SP (south), and WP (west). **b,** Atomic force microscopy image of the device.

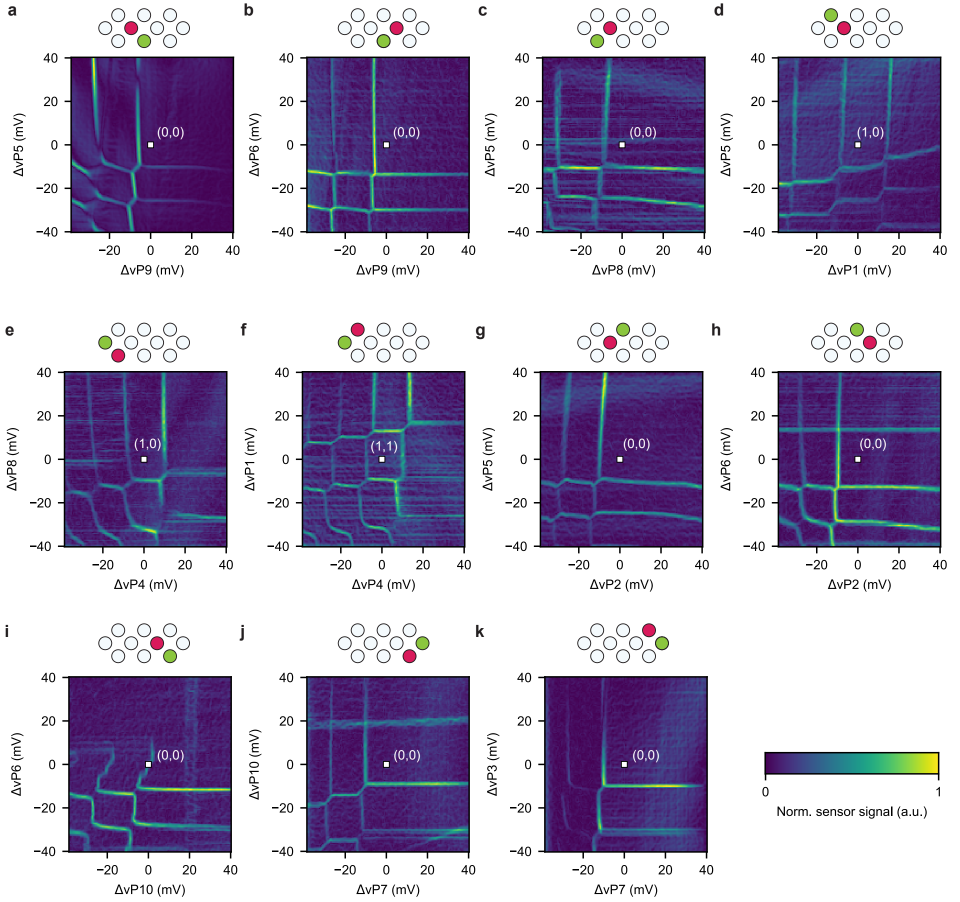

Figure 6.8: **Charge tune-up in the 10 quantum dot array. a-k,** Charge stability diagrams of the 10 quantum dot system showcasing the transition lines of each quantum dot. At the centre of each map (white square), quantum dots D1 and D4 are prepared in the single-hole regime, while all the other quantum dots are in an empty state. In the schematic above each map, the green quantum dot is tuned by the gate swept on the x axis, and the red dot by the gate swept on the y axis. The horizontal lines at ΔvP6 ~ 15 mV in panel **h** and at ΔvP10 ~ 20 mV are spurious quantum dots transition lines, while the deformation of the vertical transition lines in **i** is due to charge latching effects. ΔvPi indicates a relative voltage swing with respect to the dc voltage point.

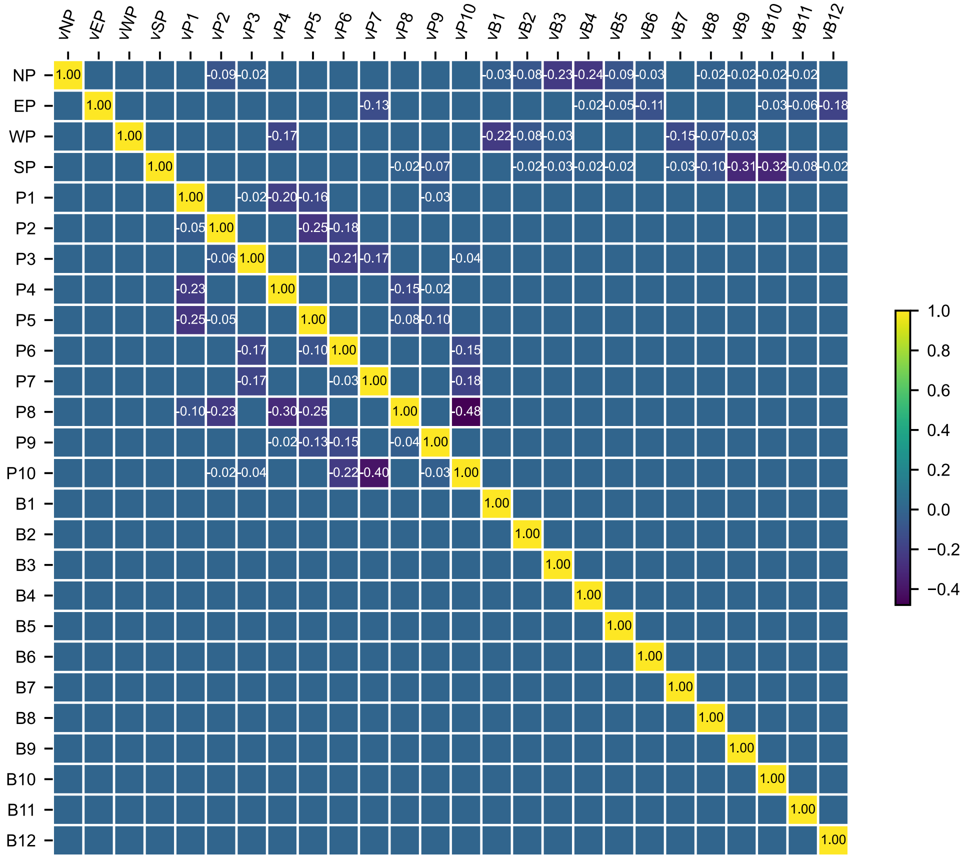

	vNP	vEP	vWP	vSP	vP1	vP2	vP3	vP4	vP5	vP6	vP7	vP8	vP9	vP10	vB1	vB2	vB3	vB4	vB5	vB6	vB7	vB8	vB9	vB10	vB11	vB12
NP	1.00					-0.09	-0.02								-0.03	-0.08	-0.23	-0.24	-0.09	-0.03		-0.02	-0.02	-0.02	-0.02	
EP		1.00									-0.13							-0.02	-0.05	-0.11				-0.03	-0.06	-0.18
WP			1.00					-0.17							-0.22	-0.08	-0.03				-0.15	-0.07	-0.03			
SP				1.00								-0.02	-0.07			-0.02	-0.03	-0.02	-0.02		-0.03	-0.10	-0.31	-0.32	-0.08	-0.02
P1					1.00		-0.02	-0.20	-0.16				-0.03													
P2					-0.05	1.00			-0.25	-0.18																
P3						-0.06	1.00			-0.21	-0.17			-0.04												
P4					-0.23			1.00				-0.15	-0.02													
P5					-0.25	-0.05			1.00			-0.08	-0.10													
P6							-0.17		-0.10	1.00				-0.15												
P7							-0.17			-0.03	1.00			-0.18												
P8					-0.10	-0.23		-0.30	-0.25			1.00		-0.48												
P9								-0.02	-0.13	-0.15		-0.04	1.00													
P10						-0.02	-0.04			-0.22	-0.40		-0.03	1.00												
B1															1.00											
B2																1.00										
B3																	1.00									
B4																		1.00								
B5																			1.00							
B6																				1.00						
B7																					1.00					
B8																						1.00				
B9																							1.00			
B10																								1.00		
B11																									1.00	
B12																										1.00

Figure 6.9: **Virtual gate matrix.** Virtual gates are defined to compensate the crosstalk to the charge sensors and to obtain independent control of the chemical potential of each quantum dot via virtual plungers (vP1-vP10).

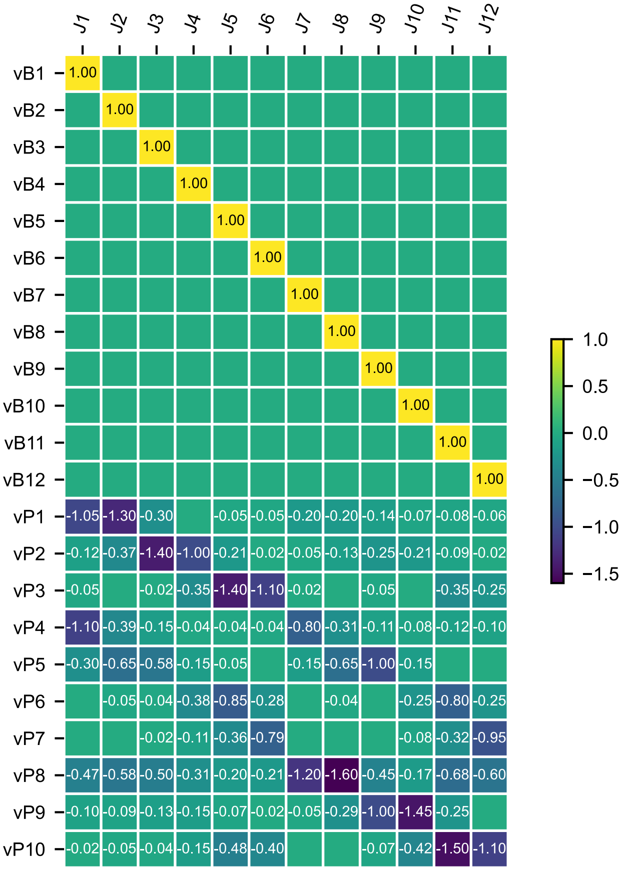

	J1	J2	J3	J4	J5	J6	J7	J8	J9	J10	J11	J12
vB1	1.00											
vB2		1.00										
vB3			1.00									
vB4				1.00								
vB5					1.00							
vB6						1.00						
vB7							1.00					
vB8								1.00				
vB9									1.00			
vB10										1.00		
vB11											1.00	
vB12												1.00
vP1	-1.05	-1.30	-0.30		-0.05	-0.05	-0.20	-0.20	-0.14	-0.07	-0.08	-0.06
vP2	-0.12	-0.37	-1.40	-1.00	-0.21	-0.02	-0.05	-0.13	-0.25	-0.21	-0.09	-0.02
vP3	-0.05		-0.02	-0.35	-1.40	-1.10	-0.02		-0.05		-0.35	-0.25
vP4	-1.10	-0.39	-0.15	-0.04	-0.04	-0.04	-0.80	-0.31	-0.11	-0.08	-0.12	-0.10
vP5	-0.30	-0.65	-0.58	-0.15	-0.05		-0.15	-0.65	-1.00	-0.15		
vP6		-0.05	-0.04	-0.38	-0.85	-0.28		-0.04		-0.25	-0.80	-0.25
vP7			-0.02	-0.11	-0.36	-0.79				-0.08	-0.32	-0.95
vP8	-0.47	-0.58	-0.50	-0.31	-0.20	-0.21	-1.20	-1.60	-0.45	-0.17	-0.68	-0.60
vP9	-0.10	-0.09	-0.13	-0.15	-0.07	-0.02	-0.05	-0.29	-1.00	-1.45	-0.25	
vP10	-0.02	-0.05	-0.04	-0.15	-0.48	-0.40			-0.07	-0.42	-1.50	-1.10

Figure 6.10: **Virtual barriers matrix.** J barriers are built as control parameters defined as linear combinations of the virtual barriers and virtual plungers. They are defined to obtain independent control over the interdot couplings, while leaving the quantum dots chemical potentials unaffected.

6.5.3. HOPPING-INDUCED OSCILLATIONS IN OCCUPIED QUANTUM DOTS

Obtaining shuttling-induced oscillation in occupied quantum dots (as for the case of the filled quantum dots D1 and D4 of the main text) requires shuttling the spin back and forth between the corresponding quantum dot and an empty neighboring dot. In this section we motivate our procedure and explain why shuttling two times is required.

We assume to have two quantum dots D1 and D2 with a spin qubit Q1 in D1, and D2 empty. For simplicity, both sites have a g-factor of 0.05 and have a quantisation angle difference of 0.3π. If we want to obtain shuttling-induced oscillations of Q1 in D1, it is not sufficient to shuttle Q1 using the sequence D1 → D2 → D1, since the rotation in D1 needs to be projected onto another quantisation axis. Hence, we require shuttling the spin Q1 using this sequence: D1 → D2 → D1 → D2 → D1, as displayed in Fig. 6.11a. Here, we vary the second time in D1 and wait 10 ns between all shuttle events. This protocol enables to convert the free evolution in D1 around the z axis to a rotation around a different axis of the D1 Bloch sphere. The resulting oscillation is shown in Fig. 6.11b. The corresponding state evolution in the Bloch sphere for the points labelled as i-viii in Fig. 6.11b, are shown in Fig. 6.11c.

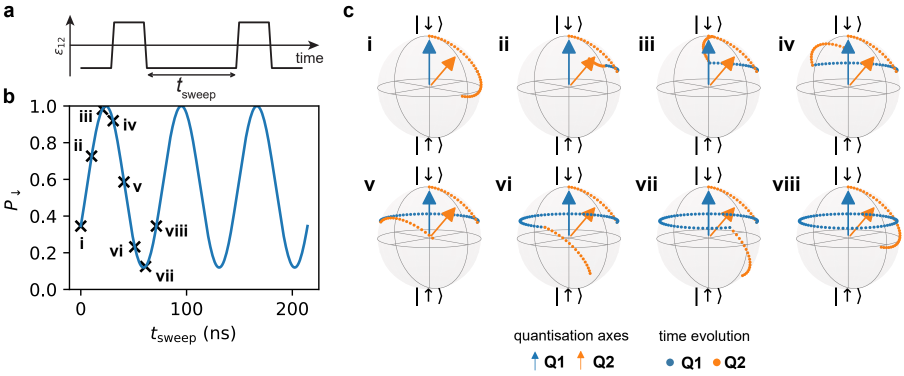

Figure 6.11: **Hopping-induced oscillations in occupied dots. a,** Shuttling sequence that moves Q1 from D1 to D2 and back to D1, twice. In the experiment, we vary the time in Q1, indicated as t_{sweep} **b,** Calculated spin down probability as a function of sweep time in D1. The visibility is dependent on the waiting times in D2 and the difference in quantization axis. **c,** State evolution during the shuttling sequence for different waiting times in D1, as indicated in **b**. The final time evolution around the z-axis is not displayed for clarity.

6.5.4. TIMING PRECISION OF SHUTTLING PULSES

High fidelity hopping-based gates require a precise timing of shuttling pulses. A qubit fidelity above 99.99% can be achieved when the rotation has an incoherent error of less than 1.3 degrees. In a simplified example where two quantum dots having quantization axes which are perpendicular, the timing error of ramps for an $X_{\pi/2}$ shuttling gate on a qubit with a Larmor frequency of 40 MHz should be less than 90 ps. This timing precision is far below the sample rate of 1 GSa/s of the used AWG. Ramps can be timed with precision higher than the sample rate, because the voltage resolution of the AWG can be used to shift the ramp in time as shown in Fig. 6.12a. The time resolution Δt_{res} of a ramp with a duration long enough to be not affected by the transients at the start and end of the ramp can be approximated by $\Delta t_{\text{res}} = t_{\text{ramp}} \Delta V / A$, where t_{ramp} the duration of the ramp, ΔV the voltage resolution of the AWG and A the amplitude of the ramp. This approximation assumes that the low-pass filter has a cut-off frequency just below the Nyquist frequency. Surprisingly, the sample rate has no direct effect on the time resolution of the ramp. A higher sample rate combined with a higher cut-off frequency allows the generation of shorter ramps and shorter ramps have a higher time resolution. The voltage resolution and thus the time resolution effectively decrease when oversampling is used, i.e. when the cut-off frequency is significantly lower than the Nyquist frequency.

We have used AWGs with a voltage resolution of 0.37 mV and pulses with an amplitude on the order of 200 mV at the AWG outputs (this translates to 25.2 mV on the device due to the attenuation on the line) and a ramp time of 2 ns. This setting gives a time resolution of 3.7 ps, which meets the requirement for high-fidelity gates. However, the ramps for the shuttling pulses are short with respect to the transient response of the low-pass filter. The filter of the AWG adds small wiggles to the short ramps making the timing less precise. This effect is shown in Fig. 6.12d, where the time deviation for the ramps with different time shift t_{shift} are plotted. From these calculated ramps we have derived

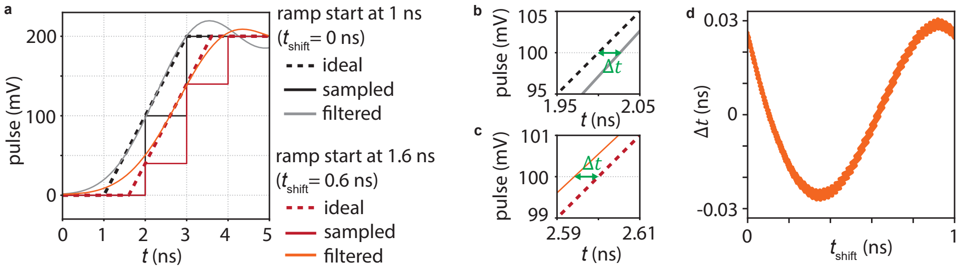

Figure 6.12: **Pulse timing. a,** Digital inputs and analogue outputs of the AWG for two pulses with time shifts $t_{\text{shift}} = 0$ and 0.6 ns. The dotted lines are the ideal linear ramps with 0.6 ns time shift that we are aiming for. The solid lines are the digital inputs, represented by the discrete sampling with 1 ns resolution. To produce a time shift of 0.6 ns, a 60 mV decrement of the digital input is made on the rising ramp. The low-pass filtering of the AWG results in the smoothened output voltages represented by the solid curves, as well as the oscillations (ringing) after the ramp. **b, c,** Zoom-in of the pulses around the middle of the ideal ramps. The deviation in time between the ideal ramps and the analogue outputs at half of the voltage amplitude is denoted as Δt. **d,** The deviation Δt as a function of time shift t_{shift}. The data set is generated with equally distributed time shifts from 0 to 0.999 ns. The mean of the distribution corresponds to $\Delta t = 0$. The analogue outputs in all the plots are calculated using the measured step response of the AWG.

a maximum deviation of 30.4 ps from the average and a standard deviation of 19.4 ps, satisfying the basic requirements for 99.99% fidelity.

6.5.5. SHUTTLING ACROSS MULTIPLE QUANTUM DOTS: DETUNING AND BARRIER VOLTAGE DEPENDENCE

We probe the oscillations induced by differences in quantization axes as a function of detuning and barrier voltages. In practice, to shuttle from D4 to D8, we follow this protocol:

1. initialize the D1, D4 double quantum dot system in the $|\uparrow\downarrow\rangle$;
2. ramp the gate voltages from the set point defined as (1,0) to the (0,1), passing through the (1,0)-(0,1) charge anticrossing (AC). Here, the first number defines the filling of D4, and the second of D8. Ramp times in between these points are of ~ 10 ns;
3. wait in the (0,1) point for a varying free-precession time;
4. pulse back to the AC, and to the (1,0) setpoint;
5. readout the spin via Pauli spin blockade.

To probe the dependence of the D8 Larmor frequency, we sweep the detuning of the (0,1) set point. The results of this measurement are shown in Fig. 6.13a. Oscillations starts to arise when the gate voltage overcomes the charge anticrossing, that is found at $\epsilon_{4,8} = 10$ mV. For lower detuning voltages, the spin remains in D4, and therefore oscillations are not present. The Fast Fourier Transform of the data shows well the dependence of the Larmor frequency in the detuning voltage window. Similar measurements are shown for the case of a spin transfer from D8 to D5 (Fig. 6.13b), from D6 to D10 (Fig. 6.13c) and from D3 to D7 (Fig. 6.13d). We observe that, except for the region around the charge anticrossing, the qubit frequencies are not strongly affected by the detuning voltages. Rather, barrier gates do have a much stronger effect on the qubit frequencies, which mostly shift linearly, as illustrated in Fig. 6.14. Interestingly, the D7 Larmor frequency crosses zero as a function of J6, suggesting a change of sign in the g-factor of the qubit.

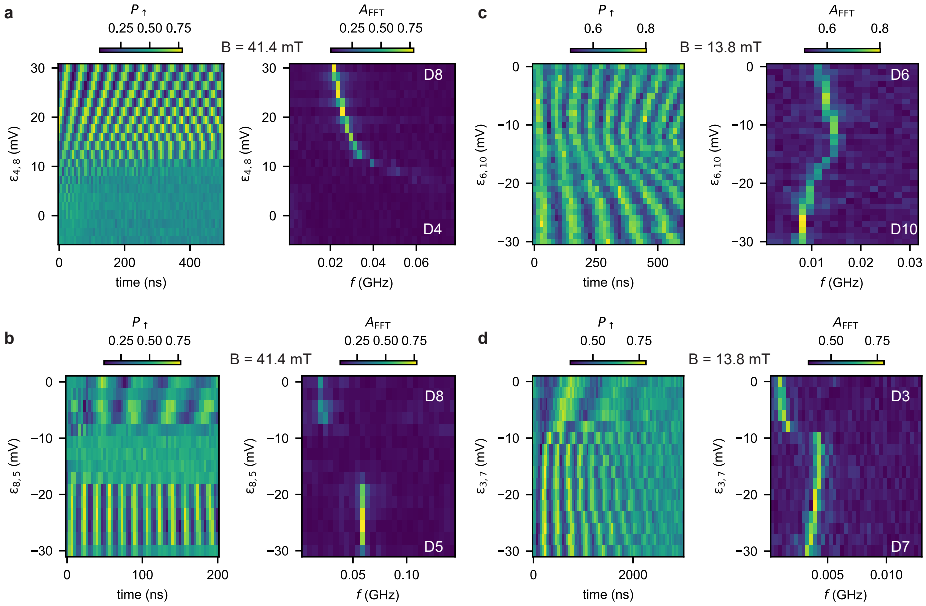

Figure 6.13: **Detuning dependence of the hopping-induced spin oscillations. a,** We vary the detuning gate voltage of the (0, 1) set point, corresponding to the shuttling sequence that moves the single spin from D4 to D8, i.e., from the (1,0) to the (0,1) charge state, across the charge interdot. Similarly to ref. [22], oscillations arise when the spin is transferred from one dot to the other. We observe that the onset of the oscillations corresponds to the charge interdot point. The panel on the right shown the FFT of the data. In **b, c, d,**, we illustrate similar measurements taken for spin shuttling from D8 to D5, from D6 to D10, from D3 to D7, respectively.

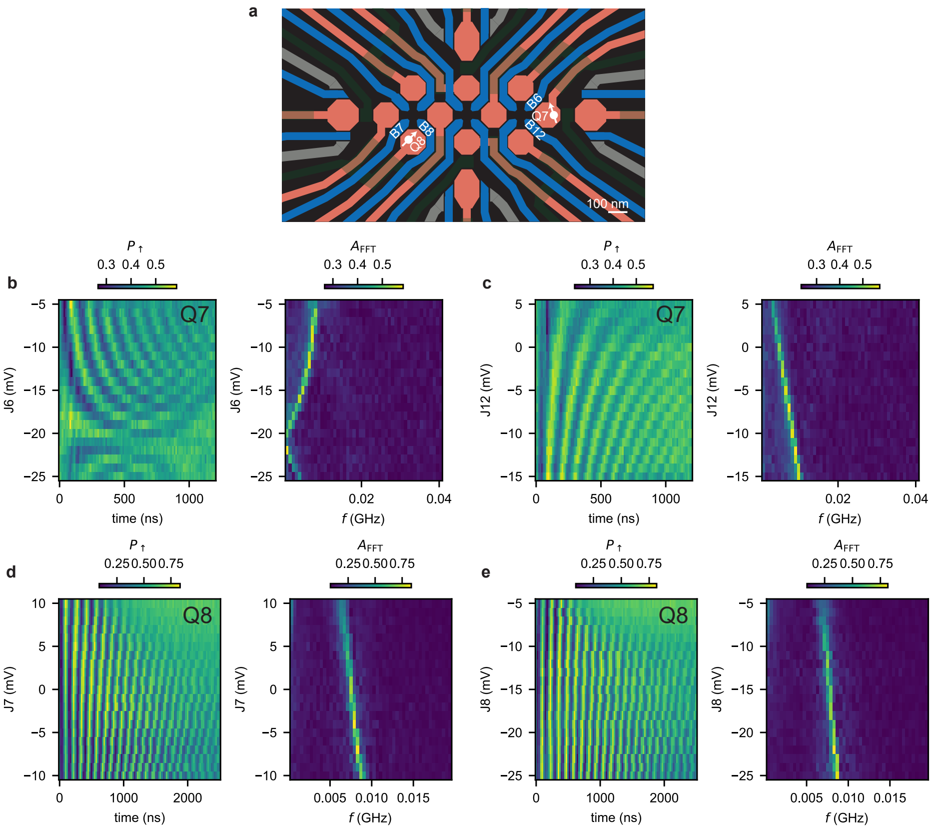

Figure 6.14: **Barrier gate dependence of the hopping-induced spin oscillations. a,** Device layout indicating the two quantum dots D8 and D7, together with the surrounding barrier gates. **b, c** D7 Larmor frequency evolution while sweeping the J6 and J12 voltages, respectively. **d, e** D8 Larmor frequency evolution as a function of J7 and J8. Small changes in the barrier voltages induce a linear shift of the D8 frequency.

6.5.6. DEPHASING TIMES AND LARMOR FREQUENCIES IN THE 10 QUANTUM DOT ARRAY

We study the dephasing times (T_2^*) of the 10 quantum dots by shuttling a spin diabatically from the double quantum dot system D1, D4 to each of the quantum dots, and let it evolve for a varying idle time. We measure the decay of the oscillations as a function of the time spent in each site by fitting the data shown in Fig. 6.15 and Fig. 6.5F using the equation: $A \cdot \sin(2\pi f t + \phi) \exp\left(-(t/T_2^*)^2\right) + C$. Here, $2 \cdot A$ is the visibility, f the Larmor frequency, t the free precession time, ϕ the starting phase, and C the oscillations offset. The Larmor frequency of an isolated Loss-diVincenzo spin qubit satisfies the relation: $f = \frac{g\mu_\mathrm{B}B}{h}$, with g the g-factor, μ_B the Bohr magneton, B the applied magnetic field and h the Planck constant. From the measurements of the oscillations as a function of magnetic field, we extract the g-factor for all the 10 quantum dots (Fig. 6.16). We find that except for the tunnel coupled Q1, Q4 qubits, f shows a linear dependence to the magnetic field. The deviation from the linear trend can be explained from the coexistence of finite exchange coupling and non-parallel quantization axes.

In general, the lower-than-unity and varying visibilities of the hopping-induced oscillations (Figs. S21, S22, S24, S25) are caused by both SPAM errors and by the non-orthogonality of the quantization axes of adjacent quantum dots. As the estimated SPAM fidelities are typically in the range of 80-95% (Suppl. Section 6 and 7 of Ref. [34]), we speculate that the origin of oscillation amplitudes below ~ 0.8 and their variability are mainly due to unfavourable spin alignment. In the current approach, we adopted a simple and sequential tuning approach, which can result in reduced rotations in the Bloch sphere. However, we could envision more involved tuning protocols that would lead to a higher contrast if desired, such as further optimization of the time spent in each dot and possibly additional shuttling steps to ensure that a phase rotation in a dot leads to a full amplitude rotation.

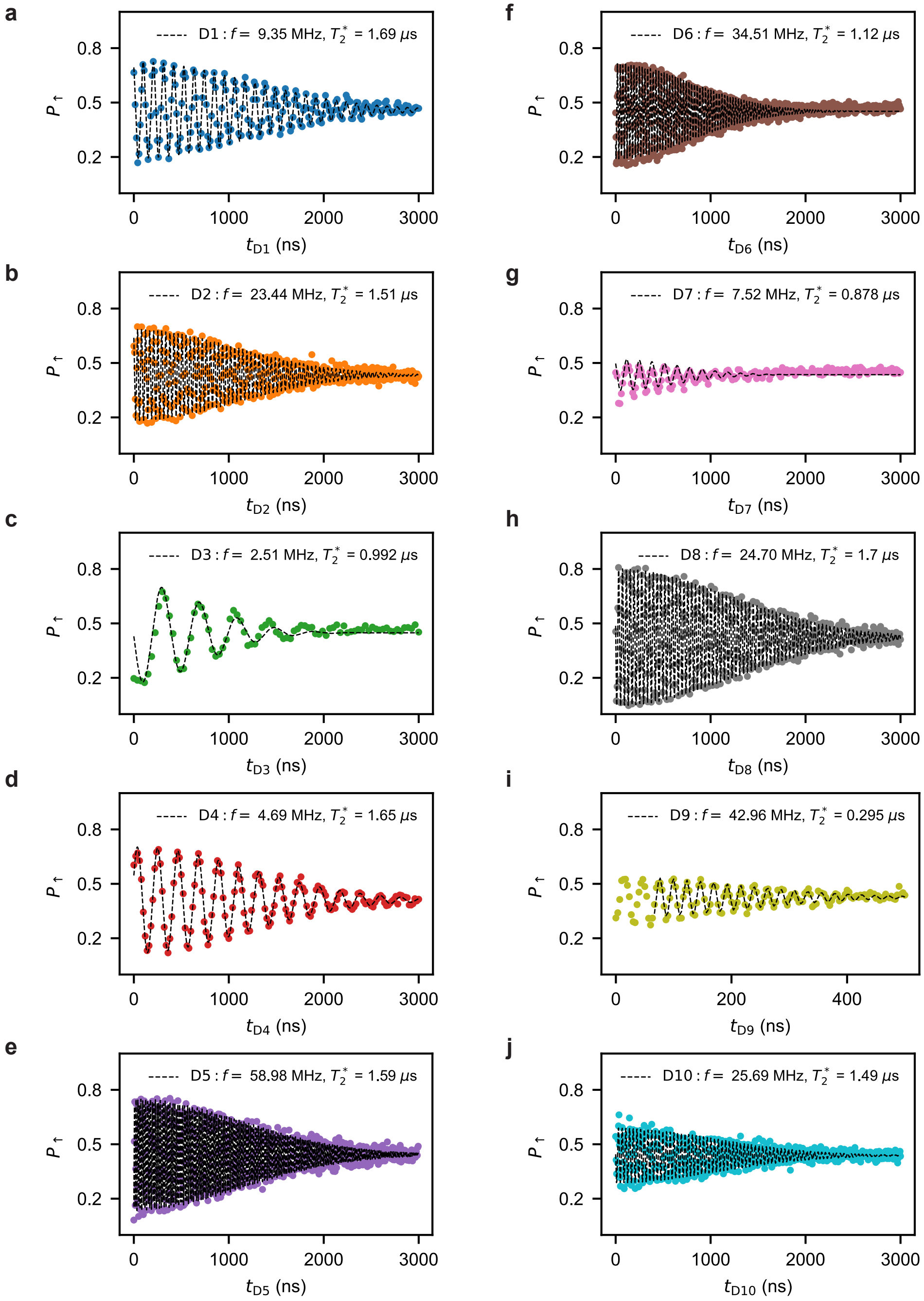

Figure 6.15: T_2^* **of the 10 quantum dot array at 41.4 mT. a-j,** Each panel is measured using the same method as presented in Fig. 6.5. We fit the dataset of D9 from 68 ns onward as we observe a frequency shift in the first ~ 100 ns possibly due to a delay in the electrical response.

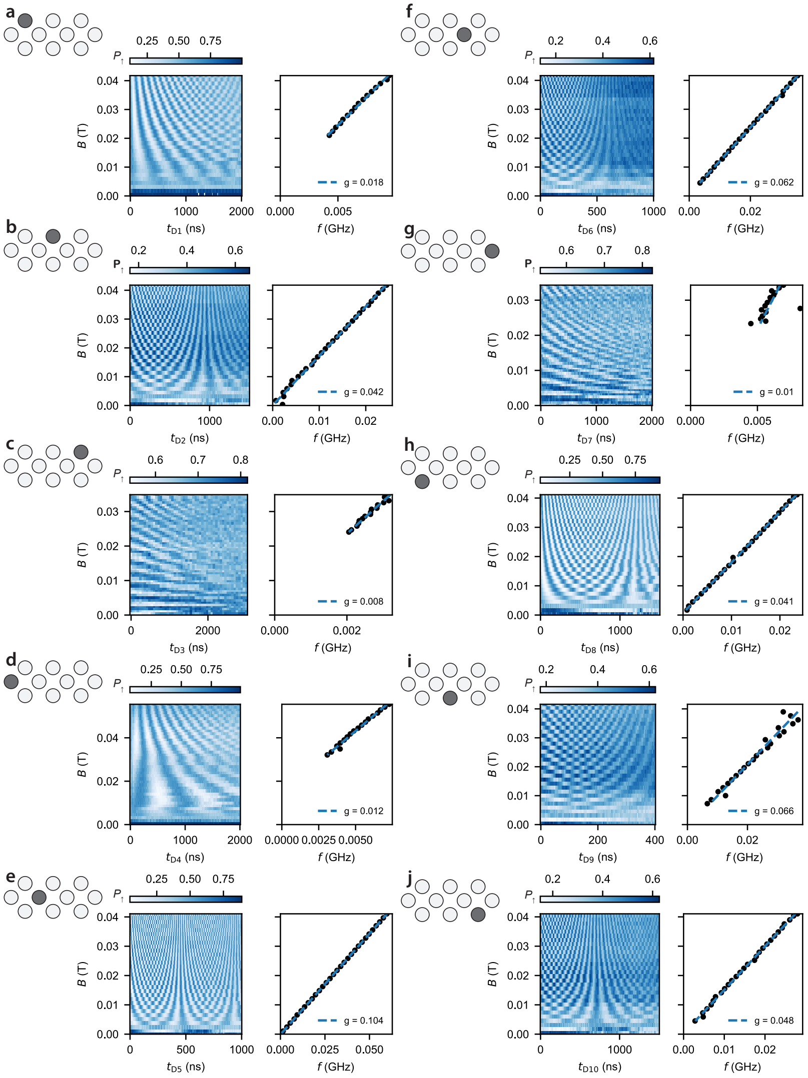

Figure 6.16: **Single-qubit rotations as a function of in-plane magnetic field for the 10 quantum dots. a-j,** We repeat the experiments shown in Fig. 6.5 and Fig. 6.15 as a function of magnetic field to obtain a more accurate estimate of the g-factors. We linearly fit the oscillation frequencies as a function of the magnetic field. We observe that all qubits but Q1 and Q4 display a Larmor frequency that intersects zero at zero magnetic field.

BIBLIOGRAPHY

[1] *Apollo 11 Technical Crew Debriefing*. Tech. rep. Houston: National Aeronautics and Space Administration, July 1969. URL: https://sma.nasa.gov/SignificantIncidents/assets/a11_tcdb.pdf.

[2] D. Loss and D. P. DiVincenzo. "Quantum computation with quantum dots". In: *Physical Review A* 57.1 (Jan. 1998), pp. 120–126. ISSN: 1050-2947. DOI: 10.1103/PhysRevA.57.120. URL: https://link.aps.org/doi/10.1103/PhysRevA.57.120.

[3] G. Burkard et al. "Semiconductor spin qubits". In: *Reviews of Modern Physics* 95.2 (June 2023), p. 025003. ISSN: 0034-6861. DOI: 10.1103/RevModPhys.95.025003. URL: https://link.aps.org/doi/10.1103/RevModPhys.95.025003.

[4] F. H. L. Koppens et al. "Driven coherent oscillations of a single electron spin in a quantum dot". In: *Nature* 442.7104 (Aug. 2006), pp. 766–771. ISSN: 0028-0836. DOI: 10.1038/nature05065. URL: https://www.nature.com/articles/nature05065.

[5] M. Veldhorst et al. "An addressable quantum dot qubit with fault-tolerant control-fidelity". In: *Nature Nanotechnology* 9.12 (Dec. 2014), pp. 981–985. ISSN: 1748-3387. DOI: 10.1038/nnano.2014.216. URL: https://www.nature.com/articles/nnano.2014.216.

[6] M. Pioro-Ladrière et al. "Micromagnets for coherent control of spin-charge qubit in lateral quantum dots". In: *Applied Physics Letters* 90.2 (Jan. 2007), p. 24105. ISSN: 0003-6951. DOI: 10.1063/1.2430906. URL: https://pubs.aip.org/apl/article/90/2/024105/333158/Micromagnets-for-coherent-control-of-spin-charge.

[7] J. Yoneda et al. "A quantum-dot spin qubit with coherence limited by charge noise and fidelity higher than 99.9%". In: *Nature Nanotechnology* 13.2 (Feb. 2018), pp. 102–106. ISSN: 1748-3387. DOI: 10.1038/s41565-017-0014-x. URL: https://www.nature.com/articles/s41565-017-0014-x.

[8] D. V. Bulaev and D. Loss. "Electric Dipole Spin Resonance for Heavy Holes in Quantum Dots". In: *Physical Review Letters* 98.9 (Feb. 2007), p. 097202. ISSN: 0031-9007. DOI: 10.1103/PhysRevLett.98.097202. URL: https://link.aps.org/doi/10.1103/PhysRevLett.98.097202.

[9] S. Nadj-Perge et al. "Spin–orbit qubit in a semiconductor nanowire". In: *Nature* 468.7327 (Dec. 2010), pp. 1084–1087. ISSN: 0028-0836. DOI: 10.1038/nature09682. URL: https://www.nature.com/articles/nature09682.

[10] K. Wang et al. “Ultrafast coherent control of a hole spin qubit in a germanium quantum dot”. In: *Nature Communications* 13.1 (Jan. 2022), p. 206. ISSN: 2041-1723. DOI: 10.1038/s41467-021-27880-7. URL: https://www.nature.com/articles/s41467-021-27880-7.

[11] N. W. Hendrickx et al. “Fast two-qubit logic with holes in germanium”. In: *Nature* 577.7791 (Jan. 2020), pp. 487–491. ISSN: 0028-0836. DOI: 10.1038/s41586-019-1919-3. URL: https://www.nature.com/articles/s41586-019-1919-3.

[12] A. Noiri et al. “Fast universal quantum gate above the fault-tolerance threshold in silicon”. In: *Nature* 601.7893 (Jan. 2022), pp. 338–342. ISSN: 0028-0836. DOI: 10.1038/s41586-021-04182-y. URL: https://www.nature.com/articles/s41586-021-04182-y.

[13] X. Xue et al. “Quantum logic with spin qubits crossing the surface code threshold”. In: *Nature* 601.7893 (Jan. 2022), pp. 343–347. ISSN: 0028-0836. DOI: 10.1038/s41586-021-04273-w. URL: https://www.nature.com/articles/s41586-021-04273-w.

[14] S. G. J. Philips et al. “Universal control of a six-qubit quantum processor in silicon”. In: *Nature* 609.7929 (Sept. 2022), pp. 919–924. ISSN: 0028-0836. DOI: 10.1038/s41586-022-05117-x. URL: https://www.nature.com/articles/s41586-022-05117-x.

[15] K. Takeda et al. “Optimized electrical control of a Si/SiGe spin qubit in the presence of an induced frequency shift”. In: *npj Quantum Information* 4.1 (Oct. 2018), p. 54. ISSN: 2056-6387. DOI: 10.1038/s41534-018-0105-z. URL: https://doi.org/10.1038/s41534-018-0105-z.

[16] B. Undseth et al. “Nonlinear Response and Crosstalk of Electrically Driven Silicon Spin Qubits”. In: *Physical Review Applied* 19.4 (Apr. 2023), p. 044078. ISSN: 2331-7019. DOI: 10.1103/PhysRevApplied.19.044078. URL: https://link.aps.org/doi/10.1103/PhysRevApplied.19.044078.

[17] B. Undseth et al. “Hotter is Easier: Unexpected Temperature Dependence of Spin Qubit Frequencies”. In: *Physical Review X* 13.4 (Oct. 2023), p. 041015. ISSN: 2160-3308. DOI: 10.1103/PhysRevX.13.041015.

[18] M. Russ and G. Burkard. “Three-electron spin qubits”. In: *Journal of Physics: Condensed Matter* 29.39 (Oct. 2017), p. 393001. ISSN: 0953-8984. DOI: 10.1088/1361-648X/aa761f.

[19] R. W. Andrews et al. “Quantifying error and leakage in an encoded Si/SiGe triple-dot qubit”. In: *Nature Nanotechnology* 14.8 (Aug. 2019), pp. 747–750. ISSN: 1748-3387. DOI: 10.1038/s41565-019-0500-4.

[20] A. J. Weinstein et al. “Universal logic with encoded spin qubits in silicon”. In: *Nature* 615.7954 (Mar. 2023), pp. 817–822. ISSN: 0028-0836. DOI: 10.1038/s41586-023-05777-3. URL: https://www.nature.com/articles/s41586-023-05777-3.

[21] G. Scappucci et al. “The germanium quantum information route”. In: *Nature Reviews Materials* 6.10 (Dec. 2020), pp. 926–943. ISSN: 2058-8437. DOI: 10.1038/s41578-020-00262-z. URL: https://www.nature.com/articles/s41578-020-00262-z.

[22] F. van Riggelen-Doelman et al. “Coherent spin qubit shuttling through germanium quantum dots”. In: *Nature Communications* 15.1 (July 2024), p. 5716. ISSN: 2041-1723. DOI: 10.1038/s41467-024-49358-y. URL: https://www.nature.com/articles/s41467-024-49358-y.

[23] B. Jadot et al. “Distant spin entanglement via fast and coherent electron shuttling”. In: *Nature Nanotechnology* 16.5 (May 2021), pp. 570–575. ISSN: 1748-3387. DOI: 10.1038/s41565-021-00846-y. URL: https://www.nature.com/articles/s41565-021-00846-y.

[24] W. I. L. Lawrie et al. “Simultaneous single-qubit driving of semiconductor spin qubits at the fault-tolerant threshold”. In: *Nature Communications* 14.1 (June 2023), p. 3617. ISSN: 2041-1723. DOI: 10.1038/s41467-023-39334-3. URL: https://www.nature.com/articles/s41467-023-39334-3.

[25] N. W. Hendrickx et al. “Sweet-spot operation of a germanium hole spin qubit with highly anisotropic noise sensitivity”. In: *Nature Materials* 23.7 (July 2024), pp. 920–927. ISSN: 1476-1122. DOI: 10.1038/s41563-024-01857-5. URL: https://www.nature.com/articles/s41563-024-01857-5.

[26] A. G. Fowler et al. “Surface codes: Towards practical large-scale quantum computation”. In: *Physical Review A* 86.3 (Sept. 2012), p. 032324. ISSN: 1050-2947. DOI: 10.1103/PhysRevA.86.032324. URL: https://link.aps.org/doi/10.1103/PhysRevA.86.032324.

[27] D. Jirovec et al. “Dynamics of Hole Singlet-Triplet Qubits with Large g-Factor Differences”. In: *Physical Review Letters* 128.12 (Mar. 2022), p. 126803. ISSN: 0031-9007. DOI: 10.1103/PhysRevLett.128.126803. URL: https://link.aps.org/doi/10.1103/PhysRevLett.128.126803.

[28] C.-A. Wang et al. “Modeling of planar germanium hole qubits in electric and magnetic fields”. In: *npj Quantum Information* 10.1 (Oct. 2024), p. 102. ISSN: 2056-6387. DOI: 10.1038/s41534-024-00897-8.

[29] J. C. Abadillo-Uriel et al. “Hole-Spin Driving by Strain-Induced Spin-Orbit Interactions”. In: *Physical Review Letters* 131.9 (Sept. 2023), p. 097002. ISSN: 0031-9007. DOI: 10.1103/PhysRevLett.131.097002. URL: https://link.aps.org/doi/10.1103/PhysRevLett.131.097002.

[30] C. Corley-Wiciak et al. “Nanoscale Mapping of the 3D Strain Tensor in a Germanium Quantum Well Hosting a Functional Spin Qubit Device”. In: *ACS Applied Materials & Interfaces* 15.2 (Jan. 2023), pp. 3119–3130. ISSN: 1944-8244. DOI: 10.1021/acsami.2c17395.

[31] N. W. Hendrickx et al. “A four-qubit germanium quantum processor”. In: *Nature* 591.7851 (Mar. 2021), pp. 580–585. ISSN: 0028-0836. DOI: 10.1038/s41586-021-03332-6. URL: https://www.nature.com/articles/s41586-021-03332-6.

[32] M. D. Reed. "Entanglement and Quantum Error Correction with Superconducting Qubits". PhD thesis. Yale University, 2013.

[33] L. M. K. Vandersypen et al. "Interfacing spin qubits in quantum dots and donors—hot, dense, and coherent". In: *npj Quantum Information* 3.1 (Dec. 2017), p. 34. ISSN: 2056-6387. DOI: 10.1038/s41534-017-0038-y. URL: http://www.nature.com/articles/s41534-017-0038-y.

[34] C.-A. Wang et al. "Operating semiconductor quantum processors with hopping spins". In: *Science* 385.6707 (July 2024), pp. 447–452. ISSN: 0036-8075. DOI: 10.1126/science.ado5915. URL: https://www.science.org/doi/10.1126/science.ado5915.

[35] E. Nielsen et al. "Gate Set Tomography". In: *Quantum* 5 (Oct. 2021), p. 557. ISSN: 2521-327X. DOI: 10.22331/q-2021-10-05-557. URL: https://quantum-journal.org/papers/q-2021-10-05-557/.

[36] R. Blume-Kohout et al. "Demonstration of qubit operations below a rigorous fault tolerance threshold with gate set tomography". In: *Nature Communications* 8.1 (Feb. 2017), p. 14485. ISSN: 2041-1723. DOI: 10.1038/ncomms14485.

[37] J. P. Dehollain et al. "Optimization of a solid-state electron spin qubit using gate set tomography". In: *New Journal of Physics* 18.10 (Oct. 2016), p. 103018. ISSN: 1367-2630. DOI: 10.1088/1367-2630/18/10/103018.

[38] M. Rimbach-Russ et al. "Simple framework for systematic high-fidelity gate operations". In: *Quantum Science and Technology* 8.4 (Oct. 2023), p. 045025. ISSN: 2058-9565. DOI: 10.1088/2058-9565/acf786. URL: https://iopscience.iop.org/article/10.1088/2058-9565/acf786.

[39] C.-A. Wang. "Interacting and hopping spin qubits in germanium". PhD thesis. Delft University of Technology, Feb. 2025.

[40] D. S. Wang, A. G. Fowler, and L. C. L. Hollenberg. "Surface code quantum computing with error rates over 1%". In: *Physical Review A* 83.2 (Feb. 2011), p. 020302. ISSN: 1050-2947. DOI: 10.1103/PhysRevA.83.020302. URL: https://link.aps.org/doi/10.1103/PhysRevA.83.020302.

[41] B. Hetényi and J. R. Wootton. "Creating Entangled Logical Qubits in the Heavy-Hex Lattice with Topological Codes". In: *PRX Quantum* 5.4 (Dec. 2024), p. 040334. ISSN: 2691-3399. DOI: 10.1103/PRXQuantum.5.040334.

[42] S. Bravyi et al. "High-threshold and low-overhead fault-tolerant quantum memory". In: *Nature* 627.8005 (Mar. 2024), pp. 778–782. ISSN: 0028-0836. DOI: 10.1038/s41586-024-07107-7.

[43] W. Ha et al. "A Flexible Design Platform for Si/SiGe Exchange-Only Qubits with Low Disorder". In: *Nano Letters* 22.3 (Feb. 2022), pp. 1443–1448. ISSN: 1530-6984. DOI: 10.1021/acs.nanolett.1c03026. URL: https://doi.org/10.1021/acs.nanolett.1c03026.

[44] D. Jirovec et al. "A singlet-triplet hole spin qubit in planar Ge". In: *Nature Materials* 20.8 (Aug. 2021), pp. 1106–1112. ISSN: 1476-1122. DOI: 10.1038/s41563-021-01022-2. URL: https://www.nature.com/articles/s41563-021-01022-2.

[45] B. Martinez et al. "Hole spin manipulation in inhomogeneous and nonseparable electric fields". In: *Physical Review B* 106.23 (Dec. 2022), p. 235426. ISSN: 2469-9950. DOI: 10.1103/PhysRevB.106.235426. URL: https://link.aps.org/doi/10.1103/PhysRevB.106.235426.

[46] S. Bosco et al. "Squeezed hole spin qubits in Ge quantum dots with ultrafast gates at low power". In: *Physical Review B* 104.11 (Sept. 2021), p. 115425. ISSN: 2469-9950. DOI: 10.1103/PhysRevB.104.115425. URL: https://link.aps.org/doi/10.1103/PhysRevB.104.115425.

[47] R. Li et al. "A crossbar network for silicon quantum dot qubits". In: *Science Advances* 4.7 (July 2018), pp. 3960–3966. ISSN: 2375-2548. DOI: 10.1126/sciadv.aar3960. URL: https://www.science.org/doi/10.1126/sciadv.aar3960.

[48] D. L. Campbell et al. "Universal Nonadiabatic Control of Small-Gap Superconducting Qubits". In: *Physical Review X* 10.4 (Dec. 2020), p. 041051. ISSN: 2160-3308. DOI: 10.1103/PhysRevX.10.041051.

[49] D. M. Pozar. *Microwave engineering*. Wiley, 2012, p. 756. ISBN: 9781118213636.

[50] A. C. Baynham, A. F. Gibson, and J. W. Granville. "On the Dielectric Constant of Germanium at Microwave Frequencies". In: *Proceedings of the Physical Society* 75.2 (Feb. 1960), pp. 306–309. ISSN: 0370-1328. DOI: 10.1088/0370-1328/75/2/418.

[51] J. Krupka et al. "Dielectric properties of semi-insulating silicon at microwave frequencies". In: *Applied Physics Letters* 107.8 (Aug. 2015). ISSN: 0003-6951. DOI: 10.1063/1.4929503.

[52] L. S. Theis et al. "Counteracting systems of diabaticities using DRAG controls: The status after 10 years ^(a)". In: *EPL (Europhysics Letters)* 123.6 (Oct. 2018), p. 60001. ISSN: 1286-4854. DOI: 10.1209/0295-5075/123/60001. URL: https://iopscience.iop.org/article/10.1209/0295-5075/123/60001.

[53] F. Mbairi, W. Siebert, and H. Hesselbom. "High-Frequency Transmission Lines Crosstalk Reduction Using Spacing Rules". In: *IEEE Transactions on Components and Packaging Technologies* 31.3 (Sept. 2008), pp. 601–610. ISSN: 1521-3331. DOI: 10.1109/TCAPT.2008.2001163.

7

ROBUST AND LOCALISED CONTROL OF A 10-SPIN QUBIT ARRAY IN GERMANIUM

> ***Ten cubits*** *away stood those of royal blood;* ***ten cubits*** *further back were the intimates of Shapur; the king of kings [...]* ***ten cubits*** *still further away could be found the king's entertainers, [...]. Behind them the musicians and singers of the second rank took their places, then* ***ten cubits*** *further back the mass of lute, zand or mandolin player. [1]*
>
> From *The Garden of Life* by Armin Malouf

Quantum computers require the systematic operation of qubits with high fidelity. For holes in germanium, the spin-orbit interaction allows for electric, fast and high-fidelity qubit gates. However, the strong g-tensor anisotropy of holes in germanium and their sensitivity to the operational and environmental conditions challenge the operation of large qubit arrays. Here, we investigate a two-dimensional 10-spin qubit array with single-qubit gate fidelities above 99%, and obtain surprisingly uniform qubit properties. By tuning the hole occupation, we demonstrate control over the spin susceptibility, enabling fast plunger gate driving with Rabi frequencies consistently above $1.45\,\mathrm{MHz}/(\mathrm{mV}\cdot\mathrm{T})$. *Moreover, we probe the locality of electric dipole spin resonance and find that the configuration with three-hole occupancy driven by the associated quantum dot plunger gate reduces crosstalk, lowering it by an average factor of 2.5 to nearest neighbours, compared to single-hole plunger driving. Theoretical modelling points towards the pronounced anisotropy of p-like orbitals as the main mechanism with significant contributions through Coulomb interactions, giving directions for reproducible control of large qubit arrays.*

Parts of this chapter have been published in **Valentin John**, Cécile X. Yu, Barnaby van Straaten, Esteban A. Rodríguez-Mena, Mauricio Rodríguez, Stefan D. Oosterhout, Lucas E. A. Stehouwer, Giordano Scappucci, Maximilian Rimbach-Russ, Stefano Bosco, Francesco Borsoi, Yann-Michel Niquet, Menno Veldhorst, **Robust and localised control of a 10-spin qubit array in germanium**, Nat Commun 16, 10560 (2025)

SEMICONDUCTOR spin qubits have seen significant progress over the last few years, with four-qubit and six-qubit quantum processors demonstrated across different platforms and encodings [2–5]. In pursuit of scaling beyond these systems, larger quantum dot (QD) arrays have been explored showcasing charge tune-up in a 4×4 QD array using a crossbar architecture [6], qubit characterisation of a two-dimensional 10-QD array by coherent single spin shuttling [7], and demonstration of a linear array comprising 12 qubits [8].

Hole spin qubits in planar strained Ge/SiGe heterostructures emerged as a compelling platform that can offer all-electrical control, fast Rabi driving, long coherence times, and absence of valley degree of freedom [9–11]. However, the strong anisotropy of the g-tensor opens a narrow window around the in-plane magnetic field direction, containing sweet but also weak operation spots for electric dipole spin resonance (EDSR) and coherence times [12–15]. The magnetic field directions of these optimal and weak spots are hard to predict and sensitive to electrostatic and strain fluctuations [16, 17], which differ across quantum dots due to device-specific and cooldown-dependent potential landscapes. Beyond optimising global qubit parameters, such as material growth properties or magnetic field orientation, qubit performance can also be tuned by adjusting local control parameters, such as dot occupation or drive gate. For holes in silicon, it was observed that the hole occupancy can have little effect on the g-tensor [18, 19]. For electrons in silicon operated with a micromagnet, it was shown that higher charge occupancies can increase the Rabi driving [20]. This was speculated to result from an increased mobility of the qubit charge in the magnetic field gradient, though more recent theoretical work also considered the effect of spin-orbit interaction via the quadrupolar contribution [21]. This raises the question whether the hole occupancy can be used to improve EDSR driving, in particular in systems with strong spin-orbit interaction, and whether further optimization is possible by choosing the gate drive.

In this work, we investigate a two-dimensional 10-QD device hosting 10 hole-spin qubits, with two central qubits each connected to four different neighbours. We systematically evaluate the EDSR drive efficiency of each qubit for QDs occupied with one, three, and five holes, to assess how charge configuration influences driving mechanisms. We apply a magnetic field slightly out-of-plane just outside the narrow window containing sweet and weak spots. This analysis is extended across all 22 available gates in the device for each qubit, which gives us insights about the locality and crosstalk of EDSR driving. Additionally, to probe the variation in noise sensitivity in each configuration, we perform longitudinal spin-electric susceptibility (LSES) measurements by analysing the changes in resonance frequency as a function of gate voltages under different charge configurations, which is closely related to the qubit coherence. Crucially, we find that it is possible to have systematic efficient driving with limited crosstalk when operating with three-hole occupancy using the plunger gate.

7.1. THE TWO-DIMENSIONAL 10-SPIN QUBIT ARRAY

Figure 7.1a displays our device, comprising 10 QDs arranged in a 3-4-3 configuration, and four charge sensors located at the cardinal points of the array, identical to the device layout described in Ref. [22]. In this work, the quantum device is fabricated on a Ge/SiGe heterostructure grown on a germanium wafer [23], exhibiting a high mobility

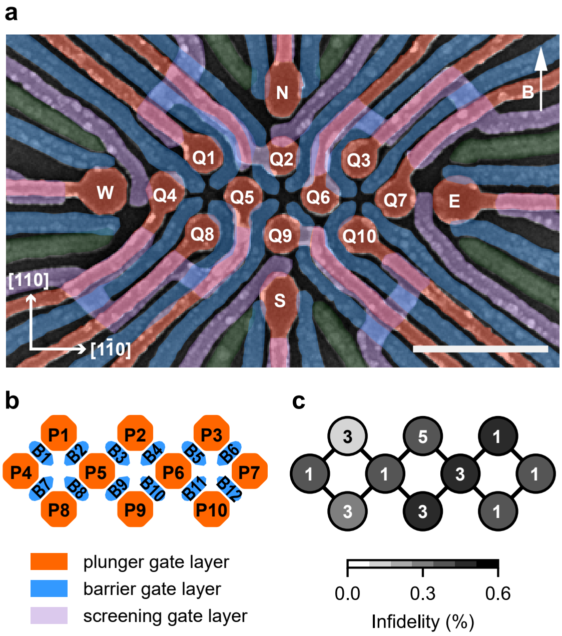

Figure 7.1: **A high-fidelity 10-spin-qubit array in germanium. a,** A false-coloured scanning electron microscope image of a nominally identical device, with the 10 quantum dot plunger gates highlighted in orange, the twelve barrier gates shown in blue, and the screening gates that screen the fanout of the plunger gates to avoid accumulation outside the quantum dot array in purple. Four single hole transistors labelled as N, E, W and S are located at the edge of the array. The 10 qubits are labelled as Q1-Q10. The applied magnetic field is 41.4 mT. The scale bar on the bottom right represents 500 nm. **b,** Simplified gate layout of the quantum dot array where the plunger gates are labelled as P1-P10 and the barrier gates as B1-B12. **c,** Randomised benchmarking single-qubit gate infidelities with the corresponding charge occupation of the 10 quantum dots annotated.

of $3.4(1) \times 10^{6}$ cm^{2}/Vs, indicating a uniform and low-noise potential landscape for QD arrays [22]. The QDs are defined and operated using plunger and barrier gates, as illustrated in Figure 7.1b. A magnetic field of 41.4 mT is applied by a uniaxial solenoid magnet, tilted approximately 2-3 degrees from the in-plane orientation [22].

The 10-QD array is tuned to a dense charge configuration, with an odd number of holes at each QD site, defining 10 qubits labelled Q1–Q10. Each qubit is initialised and readout pairwise using Pauli spin blockade with a nearby charge sensor [24, 25]. Figure 7.1c shows the occupation of each QD in the initial tune-up, along with the corresponding single-qubit gate infidelity, all below 0.6%, obtained through randomized benchmarking [26] (see subsection 7.6.3). All qubit properties in this initial tune-up including the drive gate of each qubit used for randomised benchmarking are indicated in subsection 7.6.4. An in-depth noise analysis detailed in Ref. [22] indicates that the qubit performance is bounded by a hyperfine-limited T_2^* of approximately 2 μs arising from the out-of-plane component of the magnetic field, which could be alleviated by using purified germanium [27, 28]. We also demonstrate tunable exchange interactions between neighbouring qubit pairs (see subsection 7.6.5), making this spin qubit array representative for future quantum processors based on densely occupied QD arrays.

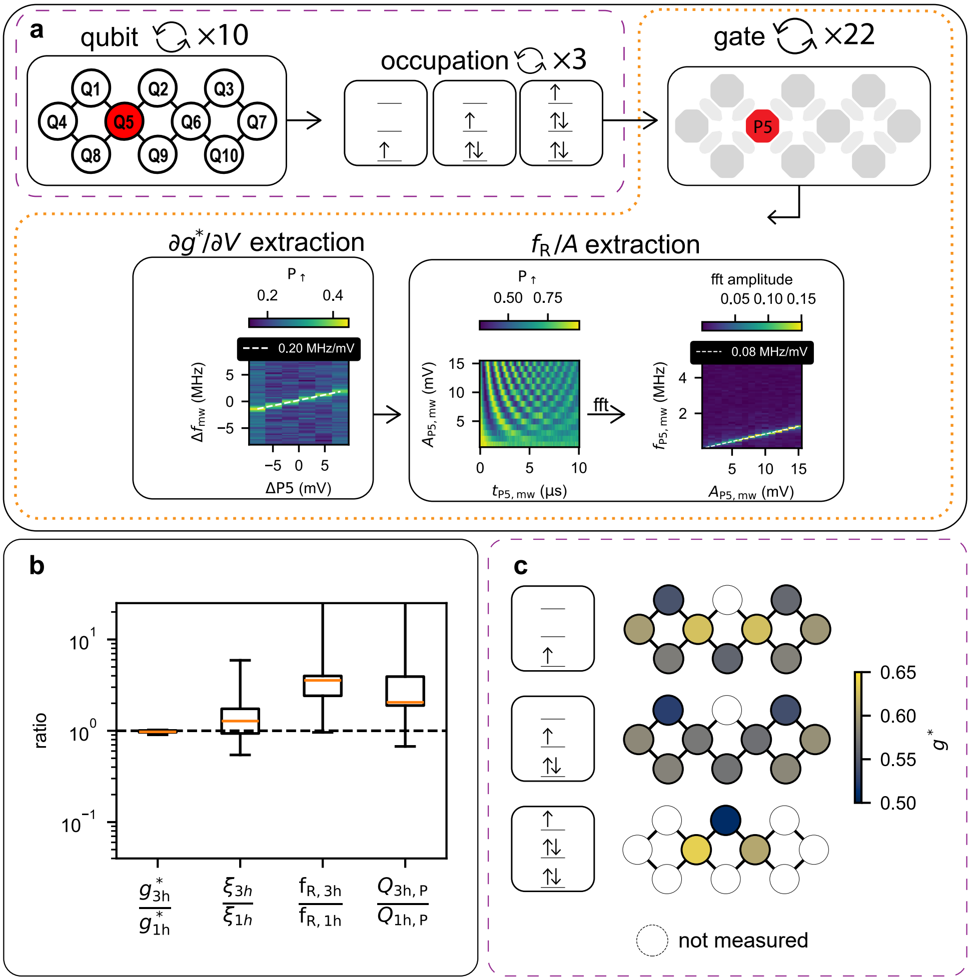

Figure 7.2: **Statistical analysis of the 10-spin qubit arrray. a,** Flow diagram of g^*-tunability and driving efficiency extraction. After selecting one of the qubits, Q1-Q10, and looping over the one-, three-, and five-hole occupation, the g^*-tunability and drive efficiencies are extracted sequentially for each of the 10 plunger and 12 barrier gates. For the g^*-tunability each of the gates is scanned in the range of ±8mV while sweeping the microwave frequency across the corresponding qubit frequency on a dedicated fixed gate. By fitting the peak in the recorded signal, the frequency slope can be determined in MHz/mV, which can be converted into a g-factor slope in 1/mV. For the driving efficiency the amplitude is swept from 1 to 15 mV, while applying a microwave pulse on each of the gates. By performing a fast-Fourier transform and fitting the dominant frequency contribution with a linear fit, the driving slope in MHz/mV can be extracted. **b,** Boxplots in Spear style containing the ratios of g^*, LSES, driving efficiency, and quality factor in the three- and one-hole occupation for plunger drive. Each boxplot contains 9 data points with all 10 qubits except Q2. The orange line denotes the median value and the whiskers are from the first quartile to third quartile. **c,** g^* of all 10 qubits in the one-, three-, and five-hole occupation.

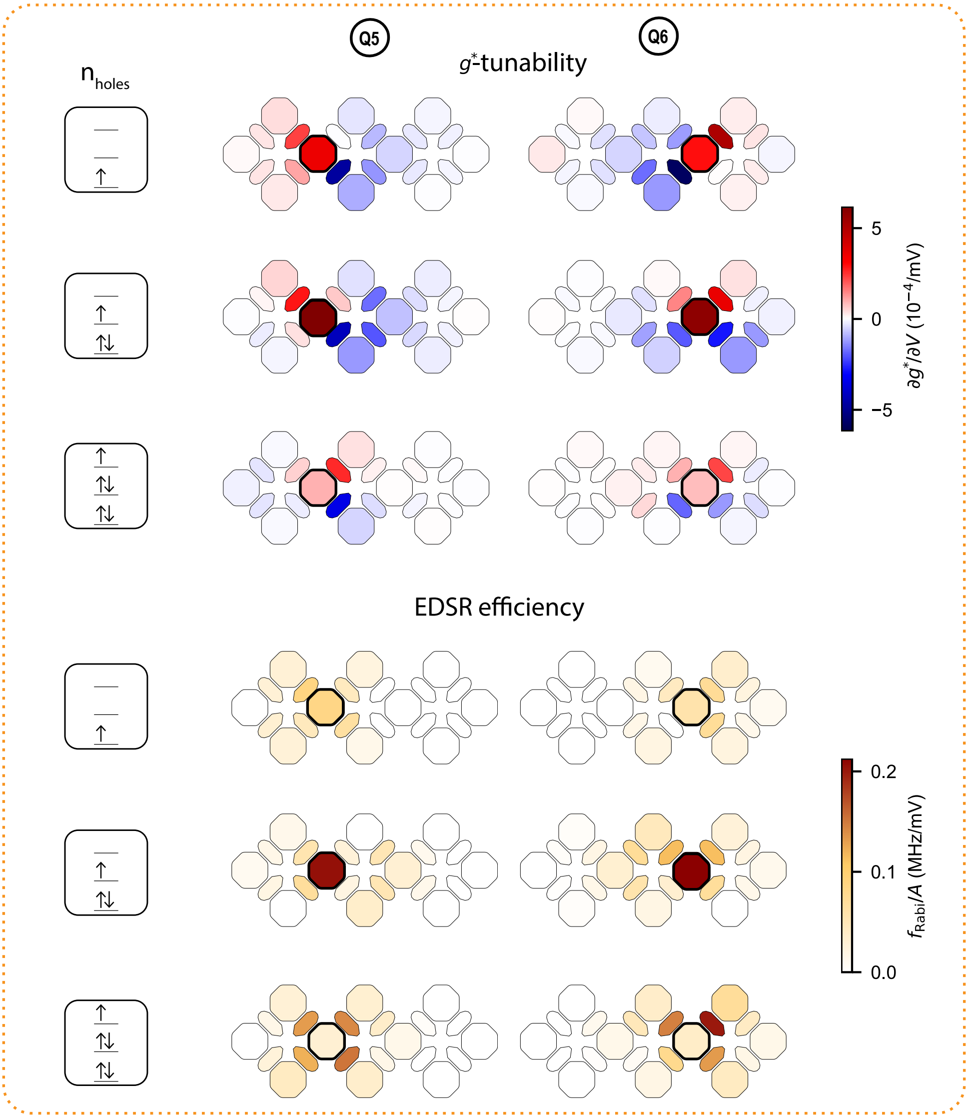

Figure 7.3: **Statistical analysis of the 10-spin qubit arrray.** g^*-tunability and driving efficiency for qubit Q5 and Q6 as a function of all 10 plunger and 12 barrier gates. Each row corresponds to a different hole occupation of one, three, and five respectively.

7.2. QUBIT DRIVE EFFICIENCY AND TUNABILITY

This two-dimensional 10-qubit array provides a sufficiently large and robust platform to gather a comprehensive dataset on the effects of varying qubit sites and hole occupancies while avoiding device-to-device variability. By systematically performing the measurement protocol shown in Figure 7.2a, we characterise the LSES and driving efficiency f_R/A, with f_R the Rabi frequency and A the applied drive amplitude on the device level, across all qubits with one-, three-, and five-hole occupancy.

These driving properties are intimately linked to the sensitivity of the g-tensor to the electrostatics and its environment [29, 30]. Indeed, Rabi oscillations are governed by modulation of the transverse component of the g-tensor through AC gate voltages, while the LSES measures the gate ability to tune the longitudinal component, which influences qubit coherence in the charge-noise-limited regime via $T_2^* \propto 1/\xi$ with $\xi = \sqrt{\sum_{\text{gate}}(\partial g^*/\partial V_{\text{gate}})^2}$ [13, 31]. Here, the effective g-factor for a given magnetic field is expressed as $g^* = |\mathbf{g}\vec{b}|$, with $\mathbf{g}$ representing the g-tensor and $\vec{b} = \vec{B}/|\vec{B}|$ the normalised magnetic field direction. The total longitudinal susceptibility, ξ, encompasses all the gates of the device and assumes uncorrelated noise contributions between them. The interplay between driving efficiency and longitudinal susceptibility can be captured by a qubit quality factor, defined as $Q = f_R/\xi \propto f_R \cdot T_2^*$ [32]. The quality factor Q enables identification of operational sweet spots and their dependence on hole configurations.

Figure 7.2b summarises qubit statistics collected across the 10 qubits for single- and three-hole occupations, visualising their ratios in a boxplot. We refer to plunger drive when the qubit is driven with a plunger gate, and barrier drive when a barrier gate is used. For the drive efficiency, we only focus on the plunger drive for each qubit. As the hole occupancy increases from one to three, both g^* and ξ show minimal variation, while the plunger drive efficiency improves by a median factor of 3.6. With a modest median increase of 1.3 in ξ, the quality factor improves by a median factor of 2.0[0]. Notably, the whisker representing the Rabi frequency and quality factor ratio for single- and three-hole occupancies extends towards infinity, as no measurable driving of Q3 using the plunger gate P3 was observed in the single-hole occupancy within the applied voltage amplitude range, which confirms the importance of investigating the gate and hole occupation dependence of EDSR in large qubit arrays.

The underlying data of the g-factor variability is visualised in Figure 7.2c across different hole occupancies and qubit sites. Despite holes in germanium having a large g-tensor anisotropy, we find a small relative variation in g-factors across 10 qubits within a single device and different hole configurations, with an average g-factor of 0.58±0.03. We believe that this small variability results from the large contribution of the perpendicular component of the g-tensor when the magnetic field is oriented out-of-plane.

Exemplary data for the central qubits, Q5 and Q6, which are measured across one-, three- and five-hole occupancies, are shown in Figure 7.3. The data show a distinct increase in qubit plunger drive as the hole occupation increases from one to three, while the efficiency of the barriers remain approximately unchanged. However, increasing the hole occupation to five reverses this pattern, with the qubit plunger drive becoming sig-

---

[0] Here, we refer to the median values, as the average is skewed by Q3, which is barely driven by the plunger gate in the single-hole occupation regime.

nificantly weaker while the barrier drives become stronger. The observed g^*-tunability patterns include barriers exhibiting both negative and positive $\partial g^*/\partial V_{\mathrm{gate}}$, but the relative positions of these barriers do not reveal clear trends across the full array, making it challenging to identify their origin. Generally, barriers along the diagonal often have approximately opposite values, e.g., for Q5 barrier gates B2 and B9 have similar magnitude but opposite sign for the single and three-hole occupation, while B3 and B8 are both weak. The $\partial g^*/\partial V_{\mathrm{gate}}$ value associated with the qubit plunger gate is always positive, but its magnitude is comparable to that of the associated barriers. These patterns are supported and further explained by numerical simulations in Supplementary Note 6 in Ref. [33]. The trend of increased top plunger driving efficiency from one to three holes is observed in eight of the nine measured qubits (Q2 has only been measured in the five-hole regime). The exception is qubit Q4, which exhibits a constant plunger drive efficiency from one- to three-hole occupation. The complete dataset for g^*-tunability and driving efficiency across all qubits and gates is provided in Supplementary Note 7 and 8 in Ref. [33]. Overall, the three-hole regime is a more favourable regime for operation, as the driving mechanisms are more robust, with importantly no instances of zero driving, unlike in the single-hole regime.

7.3. MODELLING OF SINGLE- AND MULTI-HOLE QUANTUM DOTS

The improvement of driving efficiency in the three-hole regime is captured by simulations of a realistic geometry using a four-band Luttinger-Kohn Hamiltonian and full configuration interaction for the Coulomb correlations. These simulations help understanding the trends of the LSES and Rabi frequency shown in Figure 7.2 and Figure 7.3 (see also Supplementary Note 6 in Ref. [33]).

Our analytical and numerical modelling suggests that the enhancement of the driving efficiency of the plunger gate in the three-hole regime results from the interplay between symmetry breakings and Coulomb interactions. In the single-hole regime, the ground state is a spin doublet with a quasi-circular *s*-like envelope. When driven by the plunger gate, the radius of the envelope oscillates, but its shape remains circular resulting in an isotropic response of the in-plane g-factors. This modulates the longitudinal (LSES) component much stronger than the transverse (Rabi) component of the Larmor vector $\mathbf{g}\cdot\vec{b}$. This could be the reason why Q3 could not be driven by the plunger in the single-hole occupation.

In the non-interacting three-hole regime, the ground state doublet is an elongated *p*-like orbital $p_{\mathbf{u}}$ whose in-plane axis $\mathbf{u}$ is oriented along the direction of weakest confinement. It is energetically split from an orthogonal $p_{\mathbf{v}}$ orbital by bias and disorder-induced asymmetries, giving rise to a well-defined qubit. This $p_{\mathbf{u}}$ orbital as well as its response to the plunger gate are much more anisotropic, enabling stronger transverse coupling and thus faster Rabi oscillations. The same argument could also explain a decrease in Rabi frequency of the plunger gate in the five-hole regime. The next spin doublet now occupies the $p_{\mathbf{v}}$ orbital, which is however less responsive to the plunger gate because its axis is oriented along a stronger confinement direction. The shape of the spin wave-function is less relevant for the barrier gates, whose highly anisotropic potentials can couple states

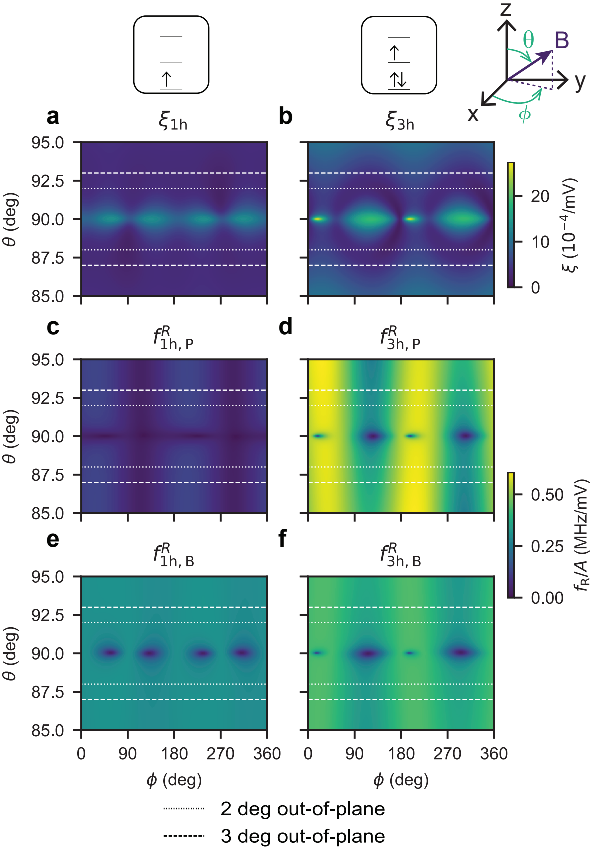

Figure 7.4: **Simulated ξ and Rabi frequency f_R as a function of magnetic field angle at 41 mT in single- and three-hole occupancies.** Data has been obtained through full configuration interaction simulations. **a,** ξ in the single-hole occupation, **b,** ξ in the triple-hole occupation, **c,** f_R in the single-hole occupation when driving with the top plunger, **d,** f_R in the triple-hole occupation when driving with the top plunger, **e,** f_R in the single-hole occupation when driving with the most efficient barrier, **f,** f_R in the triple-hole occupation when driving with the most efficient barrier. The dashed and dotted lines indicate the estimated operation field angle of the experiments.

with any symmetry.

The above considerations, drawn in the non-interacting limit, can be extended to the interacting case. The Rabi frequency can generally be split into single-particle (SP) and many-body (MB) contributions: $f_\mathrm{R} = \left|\vec{f}_R^{SP} + \vec{f}_R^{MB}\right|$. The latter depends on the strength of the Coulomb interactions and the gap between the single-particle orbitals. By mixing orbital configurations together, the Coulomb interactions reshape the hole density and the response of the ground state doublet to the drive fields. Interestingly, the MB contributions can be mapped to a disordered Hubbard spin model, where the sites correspond to the orbital states,. Consequently, the Rabi driving could be enhanced similar to flopping-mode qubits [34] (see Supplementary Note 6C in Ref. [33]). In general, we find that our full configuration interaction simulations still match the trends of the non-interacting model but reveal that the Coulomb interactions have a significant quantitative impact on the Rabi frequencies, especially for barrier gates.

Maps of simulated ξ and Rabi frequencies for the plunger gate and one of the barrier gates are shown in Figure 7.4 as a function of the magnetic field orientation. They highlight the increase of the efficiency of the plunger gate in the three-hole regime, and the strong dependence of all quantities on the azimuthal angle ϕ when the magnetic field goes in-plane ($\theta = 90°$). In particular, the driving efficiency approaches zero while ξ is large (hence T_2^* small) at specific angles ϕ. The device-to-device variability of these angles resulting from bias conditions is a considerable challenge for the tuning and calibration of large-scale systems. We envision that imprinting an initial anisotropy, strain or potential, can help in reducing these variations.

The simulations thus clearly show the benefits of avoiding the region around $\theta = 90°$ and setting the magnetic field slightly out-of-plane in the region indicated by the dashed lines. The Rabi frequency of the plunger gate is sufficiently strong and more uniform in ϕ in the three-hole regime, while the charge susceptibility is much improved (smaller ξ). Consequently, driving three-hole qubits with the plunger gate and magnetic field slightly out-of-plane may provide a reliable and uniform operation mode for scaling up to large arrays in nuclear spin-free purified germanium [27, 28].

7.4. DRIVING LOCALITY IN EXTENDED QUBIT ARRAYS

EDSR is commonly expected to be a local driving mechanism due to the localized nature of the electric field [9, 35, 36]. However the locality of EDSR may be altered by electric crosstalk, which can arise from capacitive coupling between gates or electric field propagating in the heterostructure. Here we aim to assess the extent of this locality. To do so, we analyse the acquired data by focusing on the driving efficiency of each gate to each qubit. Specifically, we evaluate the driving locality when applying a microwave pulse to any of the 22 available plunger and barrier gates. In this analysis, we consider four distinct cases involving either barrier or plunger drive and either one- or three-hole occupation. The five-hole occupation is excluded in this study due to insufficient data across the array. For each driving gate, the corresponding target qubit is defined as the qubit closest to the driving gate. We note that the plunger gates are patterned after the barrier gates and they are separated by a 10 nm thick oxide layer.

In Figure 7.5, driving efficiency is categorised by the physical distance of each gate to each qubit. Independent of direction, we then define nearest neighbours based on this physical proximity. Driving efficiency is quantified by the averaged results for all n-th nearest qubits over all driving gates. Figure 7.5a–d present the Rabi driving efficiencies as boxplots up to the sixth nearest neighbour for both barrier and plunger drive, with a corresponding maximum physical distance of 550 nm in the device plane (all distances of the n-th nearest qubits and their ranks are listed in subsection 7.6.8). To evaluate drive locality, we express our data in terms of the normalized driving efficiency f_R/f_R^{target}, obtained by normalizing the Rabi driving efficiency relative to that of the target qubit. Lower normalized driving efficiencies for distant qubits indicate less cross-talk and more localized driving. For qubits located beyond the sixth nearest neighbour, driv-

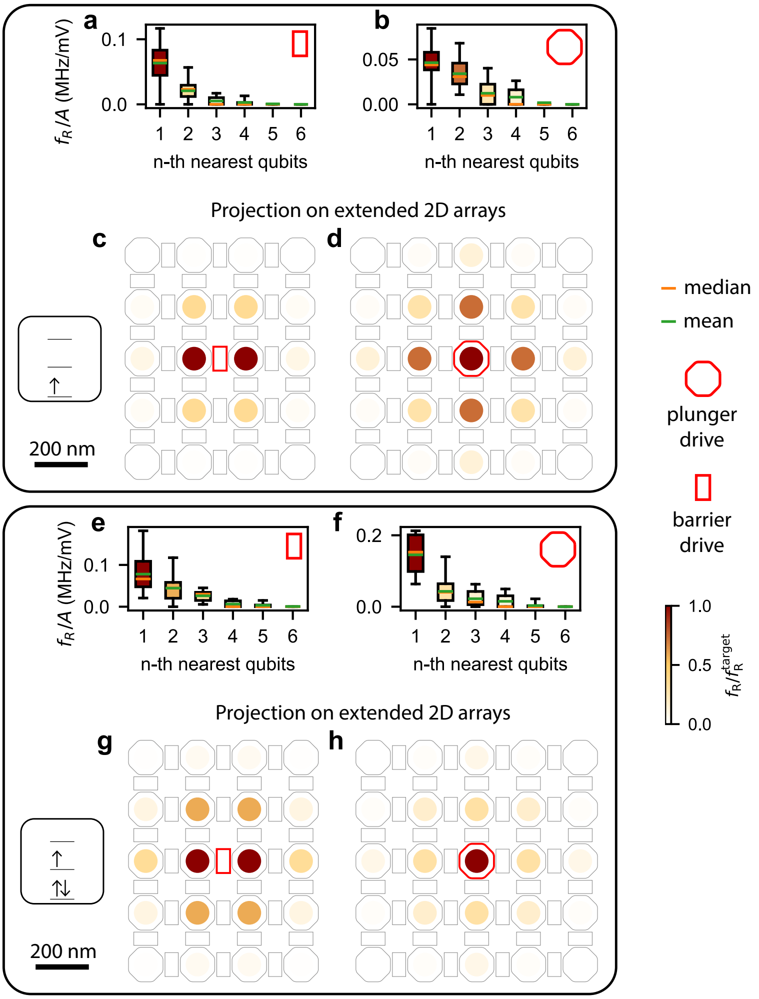

Figure 7.5: **Rabi driving locality a–d,** Boxplots in Spear style depicting the Rabi driving efficiency for all gates up to the sixth nearest qubit with indicated mean (green line) and median value (orange line). Data are shown for (**a**) barrier drive in the single-hole occupation, (**b**) plunger drive in the single-hole occupation, (**c**) barrier drive in the three-hole occupation, and (**d**) plunger drive in the three-hole occupation. The colour of each boxplot represents the Rabi frequency normalized to that of the target qubit. **e–h,** Projection of the normalized Rabi frequency onto an extended, densely populated two-dimensional spin qubit array. Data are shown for barrier drive in the single-hole occupation (**e**), plunger drive in the single-hole occupation (**f**), barrier drive in the three-hole occupation (**g**), and plunger drive in the three-hole occupation (**h**).

ing efficiency falls below 0.01 MHz/mV, which is below the sensitivity of the measurement within the range of applied drive amplitudes. We generally observe a decrease in driving efficiency for larger distances in both one- and three-hole cases, for both plunger and barrier drives. The drop in mean driving efficiency from the first to the second nearest qubit is largest for the three-hole plunger drive and single-hole barrier drive. These results are compatible with the expected electric field decay as further discussed in subsection 7.6.9.

To illustrate the impact of cross-talk, we project the measured results onto an extended densely populated two-dimensional spin qubit array. When driving a target qubit with a specific gate, the *n*-th nearest qubits are colour-coded according to the mean of the normalized Rabi efficiency measured experimentally and presented in the boxplots of Figure 7.5a–d. This visualization highlights how much each qubit would be affected when driven using a plunger or barrier gate under single- and three-hole occupations.

Figure 7.5e and g depict the projected cross-talk for barrier driving. By design, barrier gates drive the two nearest qubits equally, leading to pronounced cross-talk between them. Beyond the first nearest qubits, the single-hole occupation exhibits significantly reduced cross-talk. Figure 7.5f and h illustrate the projected cross-talk for plunger driving. In the three-hole regime, cross-talk is small. In contrast, in the single-hole regime, plunger driving can result in negligible or even vanishing driving efficiencies, requiring large drive amplitudes and consequently inducing substantial cross-talk.

Comparing the different regimes, the most localized driving is observed for plunger driving in the three-hole regime and barrier driving in the single-hole regime. Among these, the former achieves minimal cross-talk while maintaining the highest driving efficiencies, making it here the most favourable driving scheme in terms of efficiency and cross-talk mitigation in a two-dimensional array with dense occupation. In subsection 7.6.10, we further estimate that this operational regime enables the control of extended 2D arrays by engineering repeating tiles that require only eight unique Larmor frequencies across the entire array.

7.5. CONCLUSIONS

Our results demonstrate that despite the strong sensitivity of the highly anisotropic germanium g-tensor, remarkably uniform qubit characteristics can be obtained in a 10-qubit array. We have observed an enhanced and highly localized drive when manipulating qubits in the three-hole occupation regime using the plunger gate, consistent across the entire array. Numerical and analytical simulations reinforce these findings, highlighting the impact of *p*-like orbital anisotropy and intra-dot Coulomb interactions in the multi-hole regime. For future quantum processors based on spin qubits in strained Ge/SiGe quantum wells, we envision that an effective approach may be to orient the magnetic field slightly out of plane to avoid weak spots and ensure robust, localized control, as demonstrated here. Our work also highlights the importance of including parameters such as the hole occupation and drive gate into the design considerations of large qubit arrays.

7.6. SUPPLEMENTARY

7.6.1. RAW SEM IMAGE

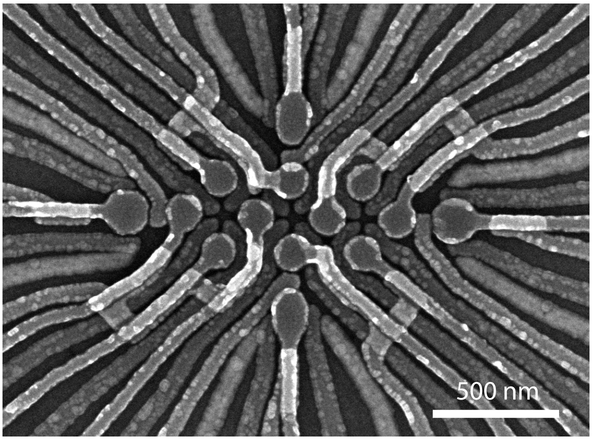

Figure 7.6: Scanning electron microscope image of a device nominally identical to the one utilised in the experiments without any false colouring.

7.6.2. READ-OUT VISIBILITIES

Since the system has been re-tuned for various charge configurations, visibilities and integration times do vary. Exemplary values for each qubit during randomised benchmarking are given in the following table:

Table 7.1: Read-out visibilities and integration times of Q1-Q5

	Q1	**Q2**	**Q3**	**Q4**	**Q5**
PSB pair	Q1,Q4	Q2,Q6	Q3,Q7	Q1,Q4	Q5,Q9
Sensor	S_{West}	S_{North}	S_{East}	S_{West}	S_{South}
Visibility	0.44	0.66	0.68	0.49	0.66
t_{measure} (µs)	12	6	5	15	8
t_{settle} (µs)	0.5	0.5	0.5	0.5	3

Table 7.2: Read-out visibilities and integration times Q6-Q10.

	Q6	**Q7**	**Q8**	**Q9**	**Q10**
PSB pair	Q2,Q6	Q3,Q7	Q4,Q8	Q5,Q9	Q7,Q10
Sensor	S_{North}	S_{East}	S_{West}	S_{South}	S_{East}
Visibility	0.62	0.85	0.68	0.58	0.50
t_{measure} (µs)	6	5	8	12	3
t_{settle} (µs)	0.5	0.5	0.5	0.5	0.5

While the readout visibility is currently limited, this is due to the lack of readout parameter optimization, which can decrease SPAM errors significantly. Improved visibility could be achieved by refining ramp times, and initialisation sequences such as larger exchange coupling during initialisation.

7.6.3. Single-qubit gate randomised benchmark

We perform randomised benchmarking (RB) to measure the single-qubit gate fidelity of the 10 qubits in the initial hole configuration, outlined in Table 7.6 and 7.7, using the set of Clifford gates defined in Table 7.3. Details about this Clifford group can be found in Ref. [37].

Table 7.3: Single-qubit Clifford sequence and their composition. $X_{\pi/2}$ and $Z_{\pi/2}$ are referring to $\pi/2$ rotation around the x-axis and the z-axis, respectively, of the Bloch sphere of a single-qubit. The average number of elementary gates per Clifford composition is 2 as the Z rotation is generated by a change of qubit's reference frame in software, which makes it error-free.

Clifford	Composition
C_1	$X_{\pi/2}X_{-\pi/2}$
C_2	$X_{\pi/2}X_{\pi/2}$
C_3	$Z_{-\pi/2}X_{\pi/2}X_{\pi/2}Z_{\pi/2}$
C_4	$X_{\pi/2}Z_{\pi/2}Z_{\pi/2}X_{\pi/2}$
C_5	$X_{\pi/2}Z_{-\pi/2}X_{\pi/2}Z_{\pi/2}$
C_6	$X_{\pi/2}Z_{\pi/2}X_{\pi/2}Z_{\pi/2}$
C_7	$X_{-\pi/2}Z_{-\pi/2}X_{\pi/2}Z_{\pi/2}$
C_8	$X_{-\pi/2}Z_{\pi/2}X_{\pi/2}Z_{-\pi/2}$
C_9	$Z_{-\pi/2}X_{\pi/2}Z_{\pi/2}X_{\pi/2}$
C_{10}	$Z_{-\pi/2}X_{\pi/2}Z_{\pi/2}X_{-\pi/2}$
C_{11}	$Z_{\pi/2}X_{\pi/2}Z_{-\pi/2}X_{\pi/2}$
C_{12}	$Z_{\pi/2}X_{\pi/2}Z_{-\pi/2}X_{-\pi/2}$
C_{13}	$Z_{-\pi/2}X_{\pi/2}Z_{\pi/2}X_{\pi/2}Z_{-\pi/2}$
C_{14}	$Z_{\pi/2}X_{-\pi/2}Z_{-\pi/2}X_{-\pi/2}Z_{\pi/2}$
C_{15}	$X_{\pi/2}Z_{\pi/2}X_{-\pi/2}$
C_{16}	$X_{\pi/2}Z_{-\pi/2}X_{-\pi/2}$
C_{17}	$X_{-\pi/2}Z_{\pi/2}Z_{\pi/2}X_{-\pi/2}Z_{-\pi/2}$
C_{18}	$X_{-\pi/2}Z_{-\pi/2}Z_{-\pi/2}X_{-\pi/2}Z_{\pi/2}$
C_{19}	$X_{\pi/2}Z_{-\pi/2}X_{\pi/2}$
C_{20}	$X_{\pi/2}Z_{\pi/2}X_{\pi/2}$
C_{21}	$Z_{-\pi/2}X_{\pi/2}Z_{\pi/2}X_{\pi/2}Z_{\pi/2}$
C_{22}	$Z_{-\pi/2}X_{\pi/2}Z_{\pi/2}X_{-\pi/2}Z_{-\pi/2}$
C_{23}	$X_{\pi/2}X_{\pi/2}Z_{\pi/2}$
C_{24}	$X_{-\pi/2}X_{-\pi/2}Z_{-\pi/2}$

The randomised benchmarking data for all 10 qubits are shown in Figure 7.7. We assume an exponential decay of the form $P_{\text{even}} = aF^n + b$ where F is the circuit level fidelity, n is the number of Clifford operations, a and b are fitting parameters depending on the state preparation and measurement. The Clifford fidelity is then given by

$$F_{\mathrm{C}} = 1 - (1-F)/2, \tag{7.1}$$

and the native gate fidelity is

$$F_{\text{gate}} = 1 - (1-F_{\mathrm{C}})/(2N_{\text{avg}}), \tag{7.2}$$

where N_{avg} is the average gate number per Clifford, which for our chosen Clifford set is 2 [37]. For each of these datasets we have probed up to either 100, 200, or 400 numbers of Clifford gates in either 100 or 199 steps. We use for each Clifford gate number 10 randomisations. The gate fidelity and its corresponding standard deviation are calculated using maximum likelihood estimation (MLE). The standard deviation here captures the statistical error of the fit following MLE, and does not take into account systematic errors. To capture these coming e.g. from drifts over time or gate-dependent depolarising noise one would need to perform more elaborated measurements such as blind RB or gate set tomography [38, 39]. We estimate the systematic error to be of the order of 0.1%, i.e. the systematic error is likely dominant over the small statistical error. Hence, the gate fidelities given in Figure 1c of the main manuscript are represented in discrete steps of 0.1%, while the fits in Figure 7.7 are shown with the statistical error.

Table 7.4 and 7.5 show the expected (obtained from Rabi oscillations just before the RB measurement) and measured offset and amplitude for the RB decay. The fits are close to the expected fitting parameters. Particularly, the fits for Q1, Q2, and Q8, which all do not reach saturation have very good agreement between the expected and measured amplitude and offset. We also plot the decay curve for a gate fidelity of 99% and 99.9% using the same amplitude and offset as obtained from the maximum likelihood estimation. The data shows that all single qubit gate fidelities of the ten qubits are clearly above 99%.

Table 7.4: Offset and amplitude of measured Rabi oscillations.

	Q1	**Q2**	**Q3**	**Q4**	**Q5**	**Q6**	**Q7**	**Q8**	**Q9**	**Q10**
A	0.22	0.33	0.34	0.24	0.33	0.31	0.42	0.34	0.29	0.25
B	0.41	0.39	0.57	0.47	0.44	0.40	0.47	0.40	0.37	0.44

Table 7.5: Fitting parameters of the RB datasets.

	Q1	**Q2**	**Q3**	**Q4**	**Q5**	**Q6**	**Q7**	**Q8**	**Q9**	**Q10**
A	0.197	0.323	0.353	0.203	0.336	0.371	0.407	0.357	0.366	0.305
B	0.436	0.385	0.529	0.382	0.504	0.444	0.465	0.424	0.474	0.488

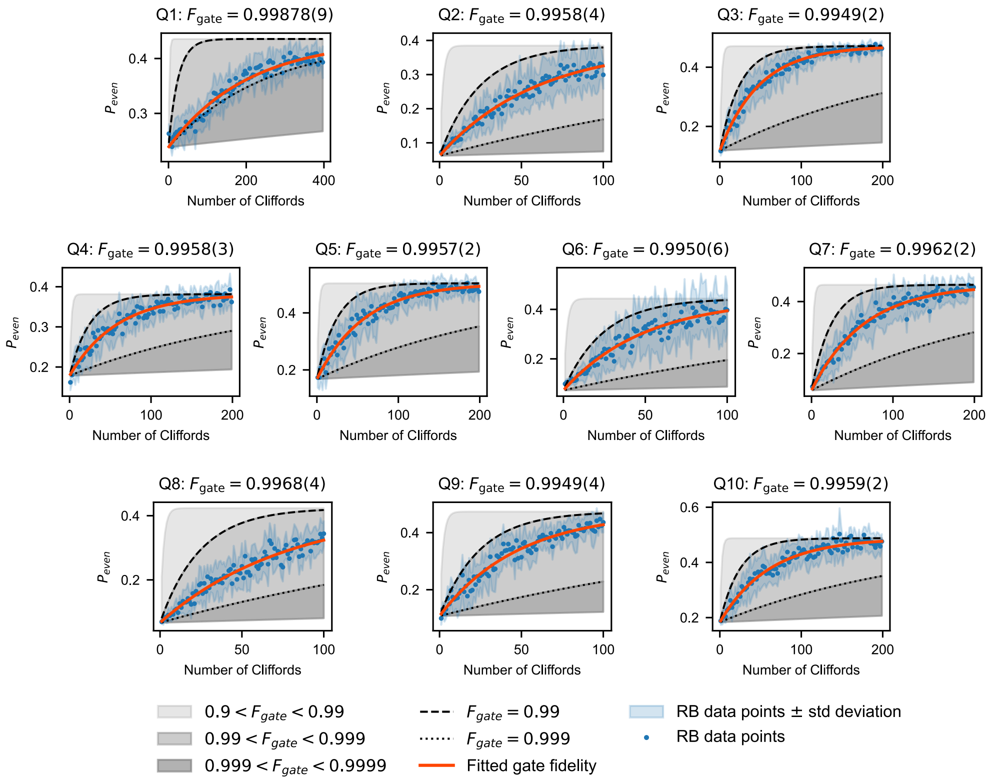

Figure 7.7: Single-qubit gate benchmarking on the 10 qubits. The black dots correspond to the averaged randomised benchmarking data over 10 randomisations, the red line is the exponential fit to extract the gate fidelity F_{gate} and the grey area covers the standard deviation of the data. The error bar denotes the statistical error of the fit obtained through maximum likelihood estimation. The systematic error is expected to be on the order of ~ 0.1%. We note that while sequence lengths of 100 Cliffords are sufficient to reach saturation for fidelities below 99%, longer sequences may be required to accurately resolve the fidelities of higher-performing qubits.

7.6.4. QUBIT PROPERTIES IN THE INITIAL HOLE CONFIGURATION

Table 7.6: Q1-Q5 properties in the original charge configuration at 41.4 mT.

label	**Q1**	**Q2**	**Q3**	**Q4**	**Q5**
Charge occupation	3	5	1	1	1
Larmor frequency (MHz)	302	293	319	347	361
g-factor	0.52	0.51	0.55	0.60	0.62
coherence time T_2^* (ns)	2381	2252	1710	2238	2041
Drive gate	P1	P2	B5	B7	P5
Maximum driving strength (MHz/mV)	0.15	0.19	0.05	0.06	0.08
Single-qubit fidelity (%)	99.9	99.6	99.5	99.6	99.6
RB Rabi frequency (MHz)	2.00	2.00	1.25	1.25	1.25

Table 7.7: Q6-Q10 properties in the original charge configuration at 41.4 mT.

label	**Q6**	**Q7**	**Q8**	**Q9**	**Q10**
Charge occupation	3	1	3	3	1
Larmor frequency (MHz)	321	355	335	327	331
g-factor	0.55	0.61	0.58	0.56	0.57
coherence time T_2^* (ns)	2134	2319	2207	2018	1975
Drive gate	P6	B12	P8	P9	B12
Maximum driving strength (MHz/mV)	0.21	0.13	0.15	0.09	0.11
Single-qubit fidelity (%)	99.8	99.6	99.7	99.5	99.6
RB Rabi frequency (MHz)	2.00	2.00	2.00	1.00	2.00

7.6.5. EXCHANGE INTERACTION IN THE 10-QUBIT ARRAY

Here we show the exchange interaction spectroscopy measurements for all ten qubits where we observe the exchange splitting between each qubit and one neighbouring qubit, see Figure 7.8. Figure 7.9 shows qubit pairs, where we measured exchange interaction splitting for both qubits demonstrating the connectivity of the qubit array. The exchange interaction is probed as a function of virtual barrier gates that are defined in section 3.4.

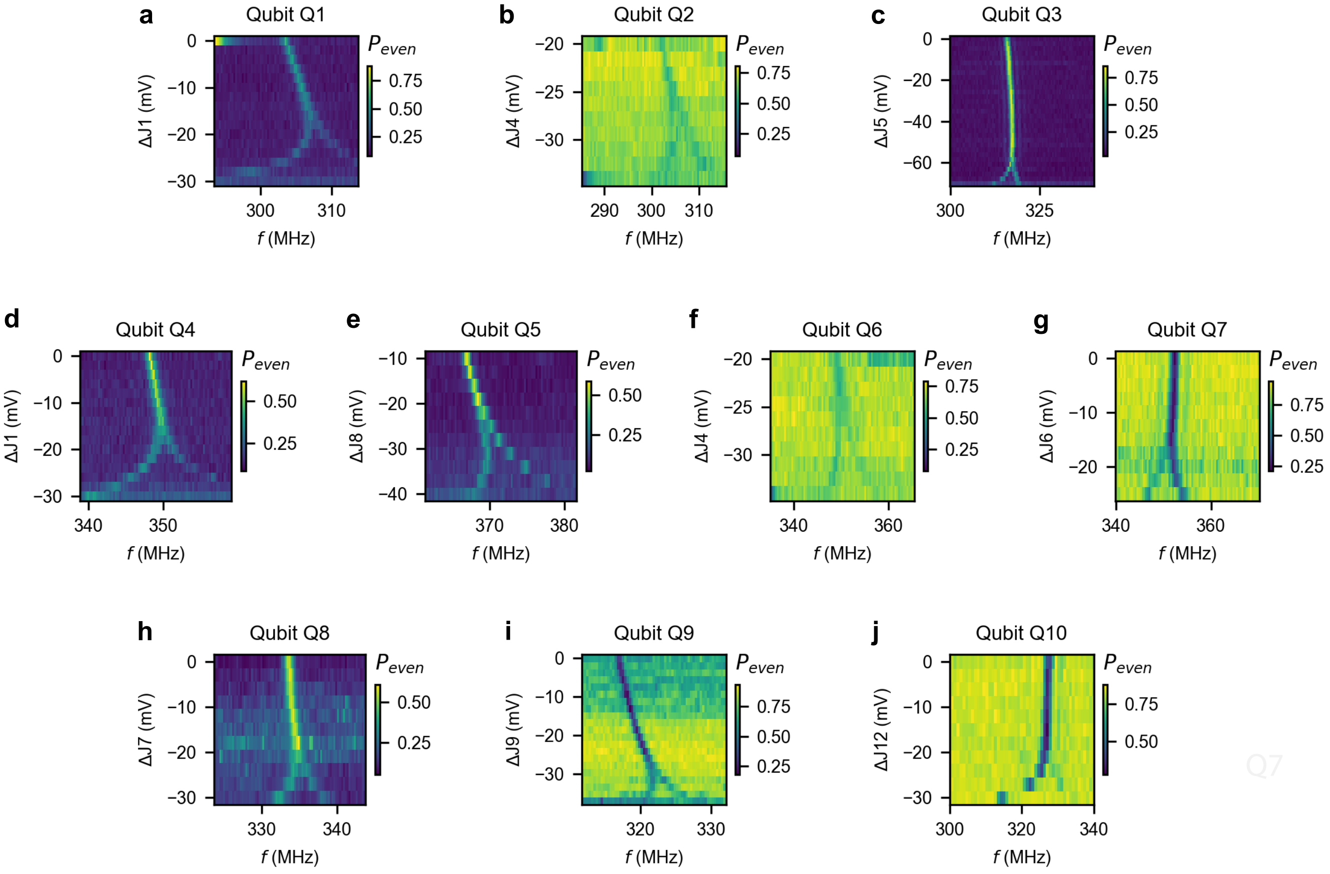

Figure 7.8: **a-j. Exchange splitting for all ten qubits.** The observed splitting of the qubit resonance frequency as a function of virtual barrier voltage is directly proportional to the exchange coupling between qubits.

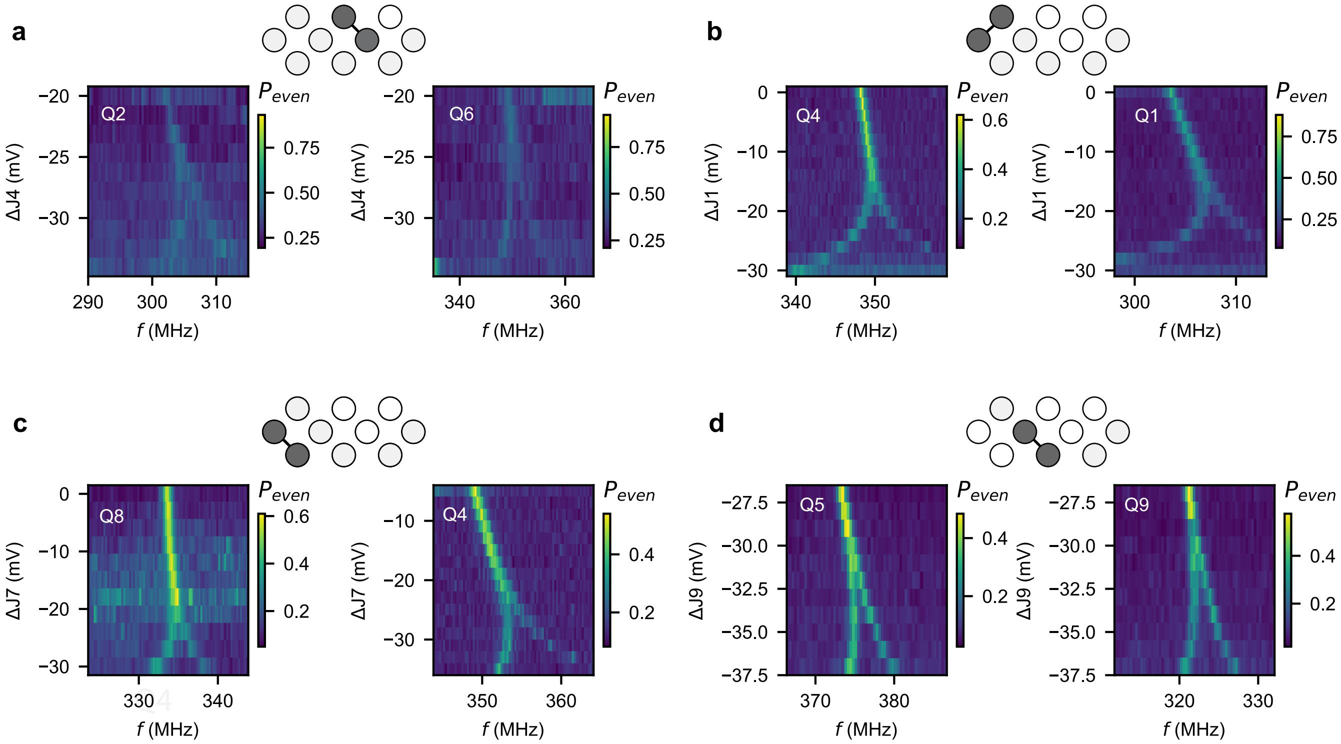

Figure 7.9: a-d. Examplary data of exchange interaction between qubit pairs.

7.6.6. LSES EXTRACTION

To extract the g-factor susceptibility of a qubit to each gate, microwave frequency sweeps around the Larmor frequency have been performed, while changing the applied voltage on each gate one after the other. In this experiment, we used a chirp signal to probe the resonance frequency of each qubit. After, the resonance frequency for each configuration is determined and fitted with a linear fit. The corresponding slope indicates the gate susceptibility $\partial f_{\mathrm{Rabi}}/\partial V_{\mathrm{gate}}$. In Figure 7.10 and 7.11 examples of the data and the corresponding linear fits are plotted.

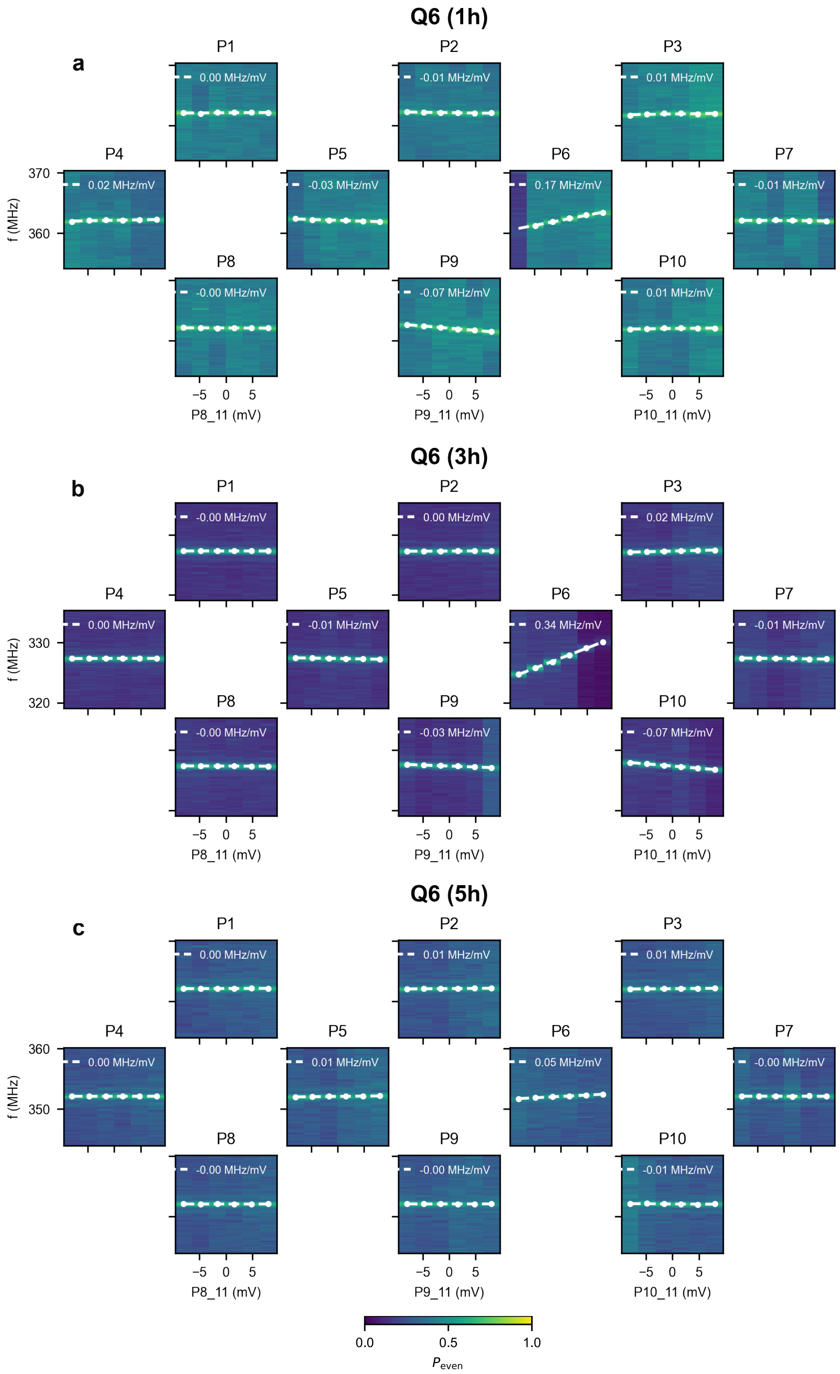

Figure 7.10: **LSES contribution of plungers for Q6 with 1, 3, and 5 hole occupation.**

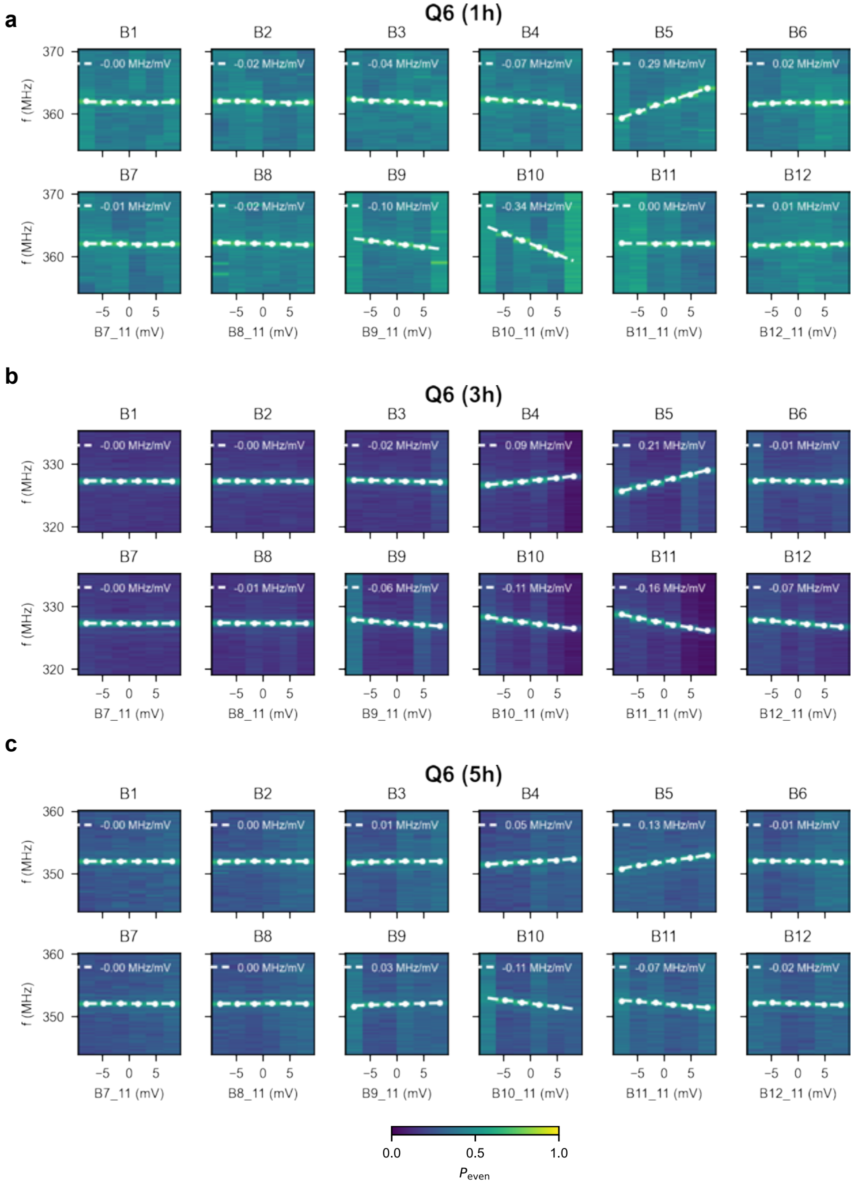

Figure 7.11: **LSES contribution of barriers for Q6 with 1, 3, and 5 hole occupation.**

7.6.7. DRIVING EFFICIENCY EXTRACTION

To extract the EDSR driving efficiency, Rabi measurements are performed as a function of drive amplitude. Next a fast-Fourier transform is applied to the raw data, and then fitted. In Suppl. Figs. 7.12-7.15 examples of the data and the corresponding linear fits are plotted. The slope determines the driving efficiency.

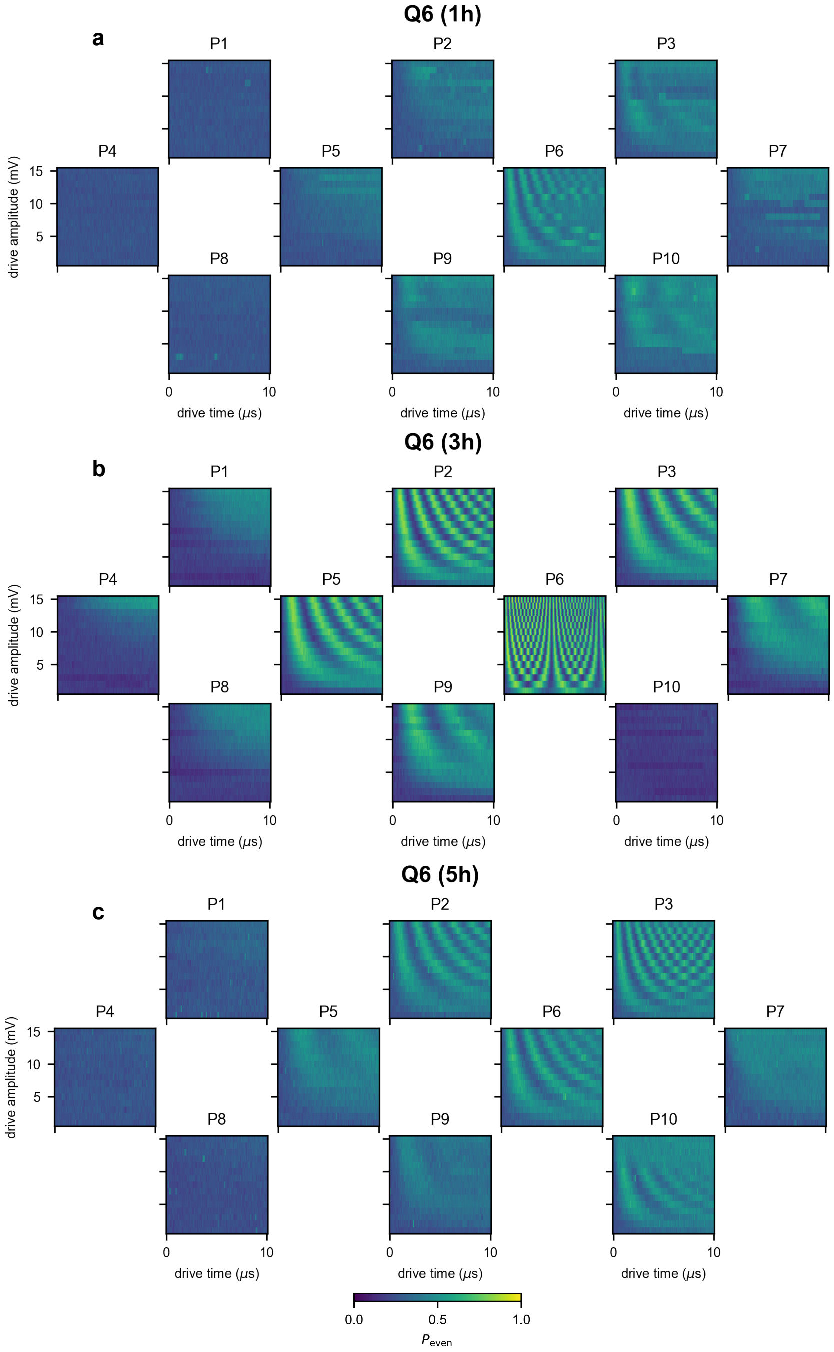

Figure 7.12: **EDSR driving of plungers for Q6 with 1, 3, and 5 hole occupation.**

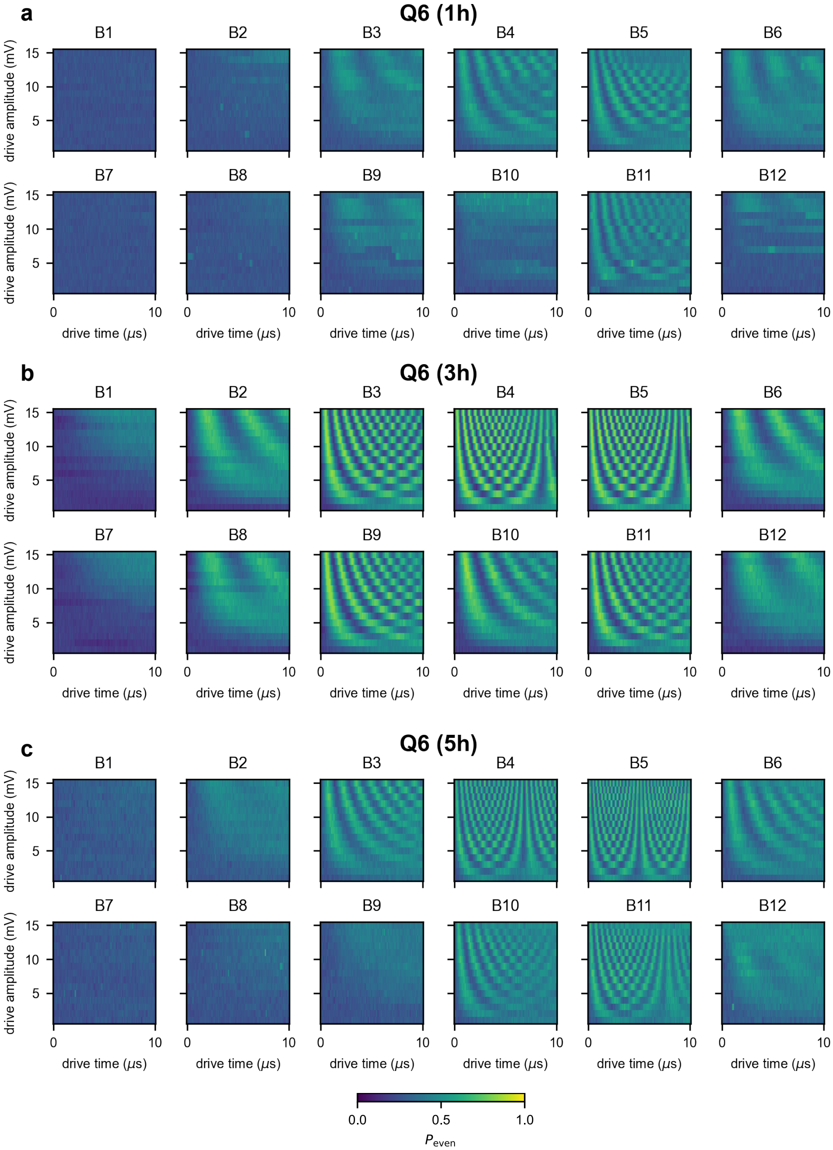

Figure 7.13: **EDSR driving of barriers for Q6 with 1, 3, and 5 hole occupation.**

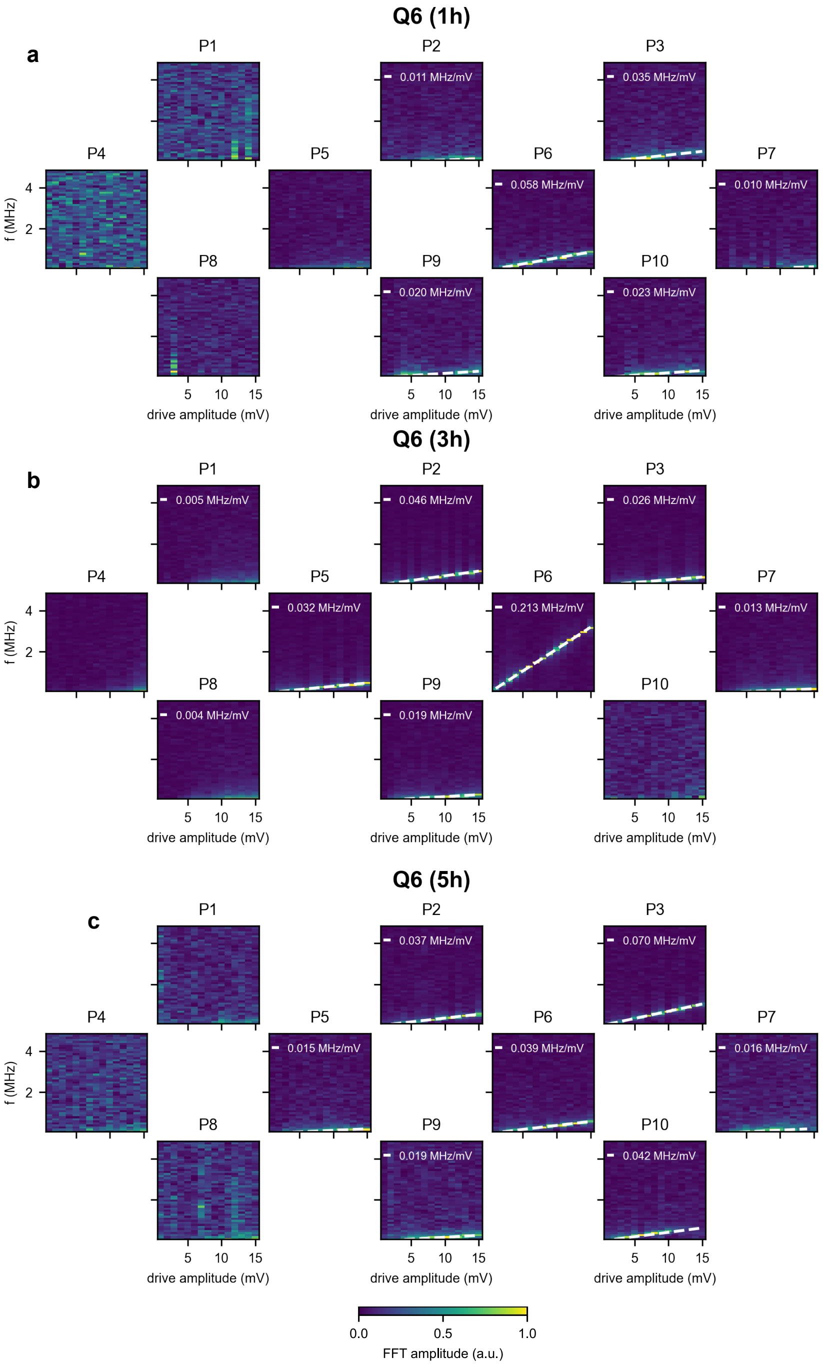

Figure 7.14: **FFT and linear fit of EDSR driving of plungers for Q6 with 1, 3, and 5 hole occupation.**

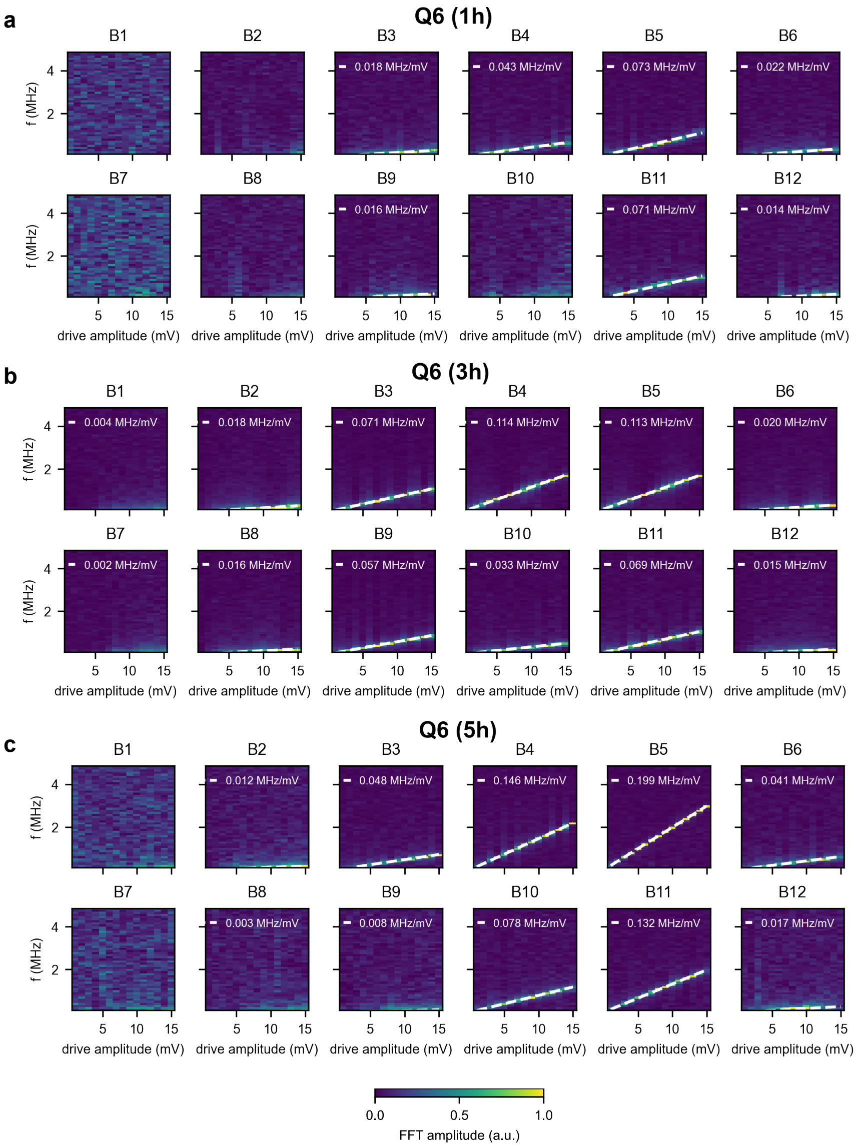

Figure 7.15: **FFT and linear fit of EDSR driving of barriers for Q6 with 1, 3, and 5 hole occupation.**

7.6.8. PHYSICAL DISTANCE FROM GATES TO QUBITS

To categorise the driving efficiency of all gates to all qubits, we calculate the physical distance in the device plane from the expected qubit position at the centre of its top plunger, to any of the 22 gates. Afterwards, we rank each physical distance for plunger and barrier gates independent from each other, and assign it an integer number n corresponding to the *n*-th nearest qubit-to-gate distance. We use these assigned ranks to calculate an average value for the *n*-th nearest qubit for a plunger and barrier gate drive as shown in Figure 4 of the main text.

Table 7.8: Physical distance from each gate to each qubit in μm

	Q1	**Q2**	**Q3**	**Q4**	**Q5**	**Q6**	**Q7**	**Q8**	**Q9**	**Q10**
P1	0.00	0.28	0.55	0.20	0.20	0.44	0.70	0.28	0.39	0.62
P2	0.28	0.00	0.28	0.44	0.20	0.20	0.44	0.39	0.28	0.39
P3	0.55	0.28	0.00	0.70	0.44	0.20	0.20	0.62	0.39	0.28
P4	0.20	0.44	0.70	0.00	0.28	0.55	0.83	0.20	0.44	0.70
P5	0.20	0.20	0.44	0.28	0.00	0.28	0.55	0.20	0.20	0.44
P6	0.44	0.20	0.20	0.55	0.28	0.00	0.28	0.44	0.20	0.20
P7	0.70	0.44	0.20	0.83	0.55	0.28	0.00	0.70	0.44	0.20
P8	0.28	0.39	0.62	0.20	0.20	0.44	0.70	0.00	0.28	0.55
P9	0.39	0.28	0.39	0.44	0.20	0.20	0.44	0.28	0.00	0.28
P10	0.62	0.39	0.28	0.70	0.44	0.20	0.20	0.55	0.28	0.00
B1	0.10	0.35	0.62	0.10	0.22	0.49	0.76	0.22	0.40	0.65
B2	0.10	0.22	0.49	0.22	0.10	0.35	0.62	0.22	0.29	0.53
B3	0.22	0.10	0.35	0.35	0.10	0.22	0.49	0.29	0.22	0.40
B4	0.35	0.10	0.22	0.49	0.22	0.10	0.35	0.40	0.22	0.29
B5	0.49	0.22	0.10	0.62	0.35	0.10	0.22	0.53	0.29	0.22
B6	0.62	0.35	0.10	0.76	0.49	0.22	0.10	0.65	0.40	0.22
B7	0.22	0.40	0.65	0.10	0.22	0.49	0.76	0.10	0.35	0.62
B8	0.22	0.29	0.53	0.22	0.10	0.35	0.62	0.10	0.22	0.49
B9	0.29	0.22	0.40	0.35	0.10	0.22	0.49	0.22	0.10	0.35
B10	0.40	0.22	0.29	0.49	0.22	0.10	0.35	0.35	0.10	0.22
B11	0.53	0.29	0.22	0.62	0.35	0.10	0.22	0.49	0.22	0.10
B12	0.65	0.40	0.22	0.76	0.49	0.22	0.10	0.62	0.35	0.10

Table 7.9: Ranked physical distance determining the n-th nearest neighbours

	Q1	**Q2**	**Q3**	**Q4**	**Q5**	**Q6**	**Q7**	**Q8**	**Q9**	**Q10**
P1	1	3	6	2	2	5	8	3	4	7
P2	3	1	3	5	2	2	5	4	3	4
P3	6	3	1	8	5	2	2	7	4	3
P4	2	5	8	1	3	6	9	2	5	8
P5	2	2	5	3	1	3	6	2	2	5
P6	5	2	2	6	3	1	3	5	2	2
P7	8	5	2	9	6	3	1	8	5	2
P8	3	4	7	2	2	5	8	1	3	6
P9	4	3	4	5	2	2	5	3	1	3
P10	7	4	3	8	5	2	2	6	3	1
B1	1	4	8	1	2	6	10	2	5	9
B2	1	2	6	2	1	4	8	2	3	7
B3	2	1	4	4	1	2	6	3	2	5
B4	4	1	2	6	2	1	4	5	2	3
B5	6	2	1	8	4	1	2	7	3	2
B6	8	4	1	10	6	2	1	9	5	2
B7	2	5	9	1	2	6	10	1	4	8
B8	2	3	7	2	1	4	8	1	2	6
B9	3	2	5	4	1	2	6	2	1	4
B10	5	2	3	6	2	1	4	4	1	2
B11	7	3	2	8	4	1	2	6	2	1
B12	9	5	2	10	6	2	1	8	4	1

7.6.9. SPATIAL LOCALITY OF THE ELECTRIC FIELD AND QUBIT DRIVE

We can make a basic electrostatic estimation of the electric field coming from a plunger gate by approximating it as a charged circular disk. The value of the charge density is not important here, since we are only interested in the relative change of the electric field as a function of the vertical distance z and the radial distance r. We assume electric field propagation in vacuum and evaluate the electric field along r and z by integrating the contribution of each point of the charged disk using Coulomb law. We also assume the qubit site to be a single point in space. In Figure 7.16a one can see the total electric field at each point for z ranging from -20 nm to -150 nm and r ranging from -800 nm to $+800$ nm, normalised to the maximum of the total electric field $E_{\mathrm{qw}}^{\mathrm{max}}$ at $z = -72$ nm. The positions of qubit sites relative to the plunger gate positions are indicated by the black dots. In Figure 7.16b a linecut of the total electric field E_{qw} has been taken at $z = -72$ nm, which corresponds to the distance of the plunger gate layer to the quantum well. Hence, we denote the linecut with the subscript qw. The dashed vertical lines indicate qubit sites relative to the plunger gate. In Figure 7.16c and d we separate the electric field contribution into a radial (E_r) and horizontal (E_z) part. We can see that E_z falls of substantially even towards the nearest neighbour. In contrast the radial electric field starts to dominate for all qubit sites of the nearest neighbour and beyond.

To connect the electric field decay with the observed locality of the qubit drive, we assume that we can fully separate the qubit drive coming from E_r and E_z. We note that in a more accurate picture, the electric field of the qubit is non-separable [40]. Since the vertical and horizontal driving mechanism differ, we can assign relative weights to these driving mechanisms (denoted w_r^{1h}, w_z^{1h}, w_r^{3h}, and w_z^{3h}), such that the experimentally observed decay in driving efficiency matches

$$\frac{f_{\mathrm{Rabi}}}{A} \propto \sqrt{|(w_r E_r)^2 + (w_z E_z e^{i\phi})^2|} \tag{7.3}$$

where ϕ is the phase difference between the radial and horizontal drive. Such an assignment of the weights is shown in Figure 7.16e, where $w_z^{3h} = 1$ and all other weights are relative to that. The result from assigning these weights can be seen in Figure 7.16e, where the proportionality is compared with the measurement data of $f_{1h,P}^{R}$ and $f_{3h,P}^{R}$, which is also displayed in Fig. 4b and d of the main manuscript. It shows very good agreement with the experimental data. Interestingly, the assigned phase difference does not make a big difference since heavy constructive and deconstructive interference is only happening before the electric field hits the first neighbouring qubit site. The assigned weights also align well with the the FCI simulations. We know from Figure 7.4 that barrier drive, which has a significant E_r component, does not change as much between 1-hole and 3-hole occupation. This is in contrast to the plunger drive, which has exclusively an E_z component. These observations are reflected in the weights, where w_r^{1h} and w_r^{3h} are similar but w_z^{1h} and w_z^{3h} change significantly.

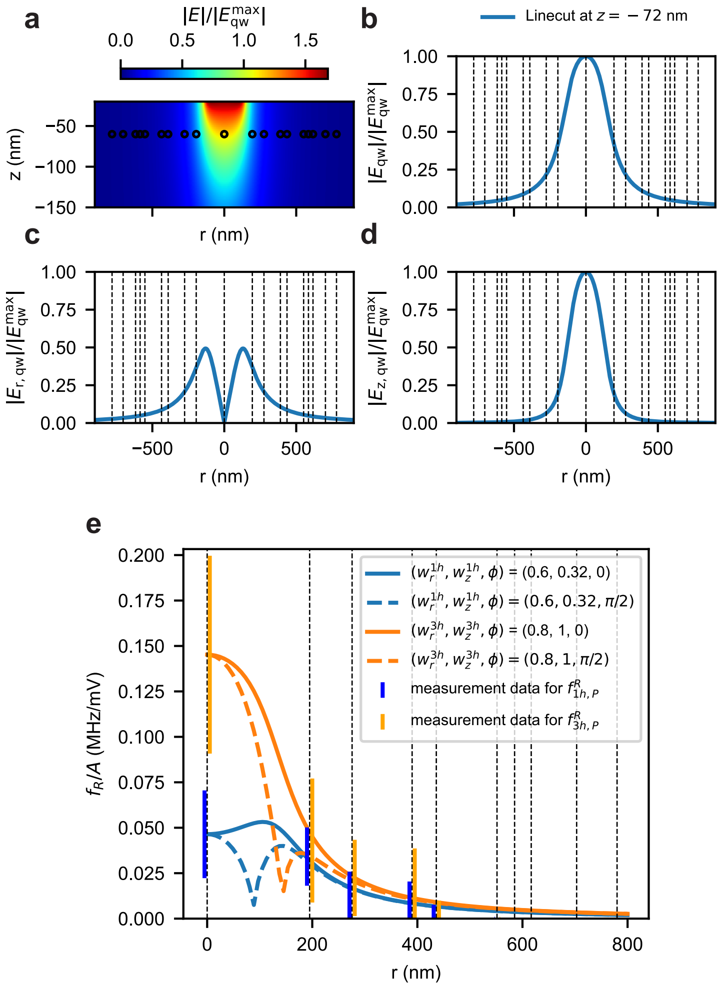

Figure 7.16: **a.** Electric field of a circular disk with diameter 130 nm assuming electric field propagation in vacuum. The black dots indicate the positions of qubits. **b-c.** normalised electric field taken along $z = -72$ nm for E, E_r, and E_z respectively. The dashed vertical lines indicate qubit positions. The red dashed line is a fit of the electric field simulation data to extract a decay exponent of the electric field. **e.** Rabi drive efficiency as a function of spatial distance. The displayed data including the represented standard deviation is the same as in Fig. 4b and d of the main manuscript. The continuous and dashed lines indicate weighted drive contribution estimates of electric field with constructive and deconstructive interference of the r-drive and the z-drive respectively.

7.6.10. FREQUENCY CROSS-TALK

The cross-talk analysis in the main text is focused on achieving locality in qubit driving independent of frequency detuning between neighbouring qubits. Specifically, we analysed crosstalk under the worst-case scenario where all qubits share the same resonance frequency. This sets the minimum distance at which no two qubits should operate at the same frequency.

If assuming that we can reliably target Larmor frequencies, it becomes possible to operate a quasi-periodic two-dimensional qubit array composed of repeating tiles QX, each requiring only eight distinct Larmor frequencies. We note that due to its electrical tunability these frequencies can be tuned around the given target value. An example of such a frequency mapping is shown in Fig. 7.17, where Larmor frequencies between 200 and 400 MHz have been assigned across the array. The nearest-neighbour resonance frequency differences range from 62.4 MHz between QX6 and QX7 to 200 MHz between QX11 and QX12.

To estimate the local qubit-to-qubit crosstalk $\chi_{i,j}^{\mathrm{local}}$, we combine the measured spatial decay of drive strength (i.e. its dependence on nearest-neighbour distance) with a frequency-dependent suppression factor coming from the magnitude-squared of the complex valued spectral density of the pulse shape. Specifically, we approximate the global crosstalk contribution between two qubits using the following expression, which constitutes the worst-case scenario assuming a square pulse envelope:

$$\chi_{i,j}^{\mathrm{global}} = \frac{f_{\mathrm{rabi}}^2}{f_{\mathrm{rabi}}^2 + (f_{Qi} - f_{Qj})^2} \tag{7.4}$$

where f_{rabi} is the Rabi frequency of the driven qubit. The full local crosstalk $\chi_{i,j}^{\mathrm{local}}$ is then obtained by weighting this frequency response with the spatially dependent drive strength extracted from the nearest-neighbour dataset (Figure 7.5f):

$$\chi_{i,j}^{local} = A(d_{i,j}) \cdot \chi_{i,j}^{global} \tag{7.5}$$

where $A(d_{i,j})$ is the experimentally determined rotation of the residual drive at the location of qubit j when driving qubit i, as a function of their distance $d_{i,j}$. This approach incorporates both spatial and spectral selectivity, and provides a quantitative estimate of crosstalk for arbitrary frequency allocations. Table 7.10 summarises both the maximum $\max\left(\chi_{i,j}^{local}\right)$ and the total $\sum \chi_{i,j}^{local}$ crosstalk per qubit. The maximum values range from 10^{-5} to 10^{-4}, and the total crosstalk from 10^{-4} to 10^{-3}. Pulse shaping can further suppress these values by many orders of magnitude [41–44].

Usually it is beneficial to have a Δg between neighbouring qubits as large as possible, as long as the Larmor frequencies remain large enough to avoid triggering multi-photon resonances [45, 46] and breaking the rotating wave approximation [47]. However, commonly one has to adapt to other operation and design constraints that only allow Larmor frequencies within a certain window, e.g. 200 - 400 MHz to be able to drive them with state-of-the-art arbitrary waveform generators (considering convenience and economics).

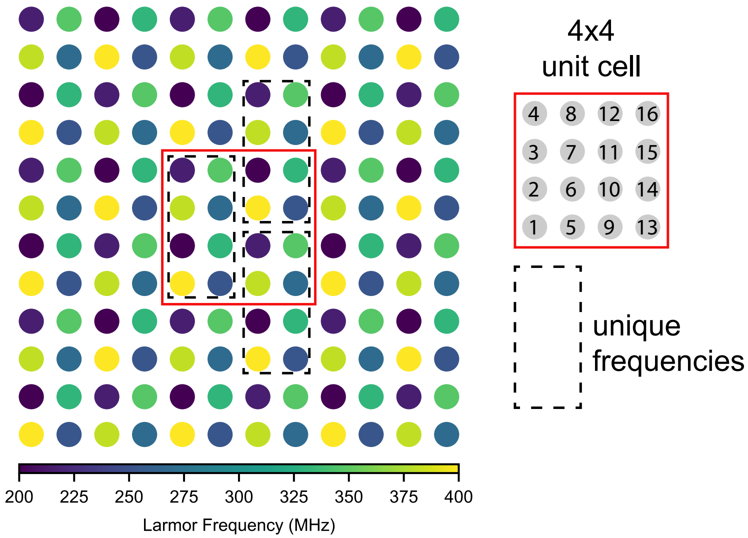

Figure 7.17: Eight unique frequencies that can make up an infinite dense qubit array. The frequencies are selected within a 4x4 unit cell.

7

Table 7.10: Assigned Larmor frequencies and experienced crosstalk.

Subnumber i	f_{Larmor} (MHz)	$\max_j\left(\chi_{i,j}^{\text{local}}\right)$ (10^{-3})	$\sum_j \chi_{i,j}^{\text{local}}$ (10^{-3})
1	400.00	0.07	0.45
2	200.00	0.08	0.52
3	381.04	0.10	0.63
4	216.91	0.08	0.66
5	253.21	0.10	0.78
6	331.23	0.09	0.70
7	268.83	0.10	0.72
8	347.48	0.10	0.77
9	381.04	0.10	0.63
10	216.91	0.08	0.66
11	400.00	0.07	0.45
12	200.00	0.08	0.52
13	268.83	0.10	0.72
14	347.48	0.10	0.77
15	253.21	0.10	0.78
16	331.23	0.09	0.70

BIBLIOGRAPHY

[1] A. Maalouf. *The gardens of light : a novel.* English. Time Warner Books, Sept. 1997, p. 136. ISBN: 9780349108711.

[2] N. W. Hendrickx et al. “A four-qubit germanium quantum processor”. In: *Nature* 591.7851 (Mar. 2021), pp. 580–585. ISSN: 0028-0836. DOI: 10.1038/s41586-021-03332-6. URL: https://www.nature.com/articles/s41586-021-03332-6.

[3] S. G. J. Philips et al. “Universal control of a six-qubit quantum processor in silicon”. In: *Nature* 609.7929 (Sept. 2022), pp. 919–924. ISSN: 0028-0836. DOI: 10.1038/s41586-022-05117-x. URL: https://www.nature.com/articles/s41586-022-05117-x.

[4] X. Zhang et al. “Universal control of four singlet–triplet qubits”. In: *Nature Nanotechnology* (Oct. 2024). ISSN: 1748-3387. DOI: 10.1038/s41565-024-01817-9. URL: https://www.nature.com/articles/s41565-024-01817-9.

[5] I. Thorvaldson et al. “Grover’s algorithm in a four-qubit silicon processor above the fault-tolerant threshold”. In: *Nature Nanotechnology* 20.4 (Apr. 2025), pp. 472–477. ISSN: 1748-3387. DOI: 10.1038/s41565-024-01853-5. URL: https://www.nature.com/articles/s41565-024-01853-5.

[6] F. Borsoi et al. “Shared control of a 16 semiconductor quantum dot crossbar array”. In: *Nature Nanotechnology* 19.1 (Jan. 2024), pp. 21–27. ISSN: 1748-3387. DOI: 10.1038/s41565-023-01491-3. URL: https://www.nature.com/articles/s41565-023-01491-3.

[7] C.-A. Wang et al. “Operating semiconductor quantum processors with hopping spins”. In: *Science* 385.6707 (July 2024), pp. 447–452. ISSN: 0036-8075. DOI: 10.1126/science.ado5915. URL: https://www.science.org/doi/10.1126/science.ado5915.

[8] H. C. George et al. “12-Spin-Qubit Arrays Fabricated on a 300 mm Semiconductor Manufacturing Line”. In: *Nano Letters* 25.2 (Jan. 2025), pp. 793–799. ISSN: 1530-6984. DOI: 10.1021/acs.nanolett.4c05205. URL: https://pubs.acs.org/doi/10.1021/acs.nanolett.4c05205.

[9] D. V. Bulaev and D. Loss. “Spin Relaxation and Decoherence of Holes in Quantum Dots”. In: *Physical Review Letters* 95.7 (Aug. 2005), p. 076805. ISSN: 0031-9007. DOI: 10.1103/PhysRevLett.95.076805. URL: https://link.aps.org/doi/10.1103/PhysRevLett.95.076805.

[10] D. V. Bulaev and D. Loss. “Electric Dipole Spin Resonance for Heavy Holes in Quantum Dots”. In: *Physical Review Letters* 98.9 (Feb. 2007), p. 097202. ISSN: 0031-9007. DOI: 10.1103/PhysRevLett.98.097202. URL: https://link.aps.org/doi/10.1103/PhysRevLett.98.097202.

[11] G. Scappucci et al. “The germanium quantum information route”. In: *Nature Reviews Materials* 6.10 (Dec. 2020), pp. 926–943. ISSN: 2058-8437. DOI: `10.1038/s41578-020-00262-z`. URL: `https://www.nature.com/articles/s41578-020-00262-z`.

[12] Z. Wang et al. “Optimal operation points for ultrafast, highly coherent Ge hole spin-orbit qubits”. In: *npj Quantum Information* 7.1 (Apr. 2021), p. 54. ISSN: 2056-6387. DOI: `10.1038/s41534-021-00386-2`. URL: `https://www.nature.com/articles/s41534-021-00386-2`.

[13] N. W. Hendrickx et al. “Sweet-spot operation of a germanium hole spin qubit with highly anisotropic noise sensitivity”. In: *Nature Materials* 23.7 (July 2024), pp. 920–927. ISSN: 1476-1122. DOI: `10.1038/s41563-024-01857-5`. URL: `https://www.nature.com/articles/s41563-024-01857-5`.

[14] M. J. Carballido et al. “Compromise-free scaling of qubit speed and coherence”. In: *Nature Communications* 16.1 (Aug. 2025), p. 7616. ISSN: 2041-1723. DOI: `10.1038/s41467-025-62614-z`. URL: `https://www.nature.com/articles/s41467-025-62614-z`.

[15] M. Bassi et al. “Optimal operation of hole spin qubits”. In: *arXiv* (Dec. 2024). URL: `http://arxiv.org/abs/2412.13069`.

[16] J. C. Abadillo-Uriel et al. “Hole-Spin Driving by Strain-Induced Spin-Orbit Interactions”. In: *Physical Review Letters* 131.9 (Sept. 2023), p. 097002. ISSN: 0031-9007. DOI: `10.1103/PhysRevLett.131.097002`. URL: `https://link.aps.org/doi/10.1103/PhysRevLett.131.097002`.

[17] L. Mauro et al. “Geometry of the dephasing sweet spots of spin-orbit qubits”. In: *Physical Review B* 109.15 (Apr. 2024), p. 155406. ISSN: 2469-9950. DOI: `10.1103/PhysRevB.109.155406`. URL: `https://link.aps.org/doi/10.1103/PhysRevB.109.155406`.

[18] S. D. Liles et al. “Spin and orbital structure of the first six holes in a silicon metal-oxide-semiconductor quantum dot”. In: *Nature Communications* 9.1 (Aug. 2018), p. 3255. ISSN: 2041-1723. DOI: `10.1038/s41467-018-05700-9`. URL: `https://www.nature.com/articles/s41467-018-05700-9`.

[19] I. K. Jin et al. “Probing g-tensor reproducibility and spin-orbit effects in planar silicon hole quantum dots”. In: *arXiv* (Nov. 2024). URL: `http://arxiv.org/abs/2411.06016`.

[20] R. C. C. Leon et al. “Coherent spin control of s-, p-, d- and f-electrons in a silicon quantum dot”. In: *Nature Communications* 11.1 (Feb. 2020), p. 797. ISSN: 2041-1723. DOI: `10.1038/s41467-019-14053-w`. URL: `https://www.nature.com/articles/s41467-019-14053-w`.

[21] P. Y. Mai et al. “Enhancement of Electric Drive in Silicon Quantum Dots with Electric Quadrupole Spin Resonance”. In: *arXiv* (Feb. 2025). URL: `http://arxiv.org/abs/2502.01040`.

[22] L. E. A. Stehouwer et al. “Exploiting strained epitaxial germanium for scaling low-noise spin qubits at the micrometre scale”. In: *Nature Materials* 24.12 (Dec. 2025), pp. 1906–1912. ISSN: 1476-1122. DOI: 10.1038/s41563-025-02276-w. URL: https://www.nature.com/articles/s41563-025-02276-w.

[23] L. E. A. Stehouwer et al. “Germanium wafers for strained quantum wells with low disorder”. In: *Applied Physics Letters* 123.9 (Aug. 2023), p. 92101. ISSN: 0003-6951. DOI: 10.1063/5.0158262. URL: https://doi.org/10.1063/5.0158262.

[24] K. Ono et al. “Current Rectification by Pauli Exclusion in a Weakly Coupled Double Quantum Dot System”. In: *Science* 297.5585 (Aug. 2002), pp. 1313–1317. ISSN: 0036-8075. DOI: 10.1126/science.1070958. URL: https://www.science.org/doi/10.1126/science.1070958.

[25] J. Fransson and M. Råsander. “Pauli spin blockade in weakly coupled double quantum dots”. In: *Physical Review B* 73.20 (May 2006), p. 205333. ISSN: 1098-0121. DOI: 10.1103/PhysRevB.73.205333.

[26] E. Knill et al. “Randomized benchmarking of quantum gates”. In: *Physical Review A* 77.1 (Jan. 2008), p. 012307. ISSN: 1050-2947. DOI: 10.1103/PhysRevA.77.012307. URL: https://link.aps.org/doi/10.1103/PhysRevA.77.012307.

[27] A. J. Sigillito et al. “Electron Spin Coherence of Shallow Donors in Natural and Isotopically Enriched Germanium”. In: *Physical Review Letters* 115.24 (Dec. 2015), p. 247601. ISSN: 0031-9007. DOI: 10.1103/PhysRevLett.115.247601. URL: https://link.aps.org/doi/10.1103/PhysRevLett.115.247601.

[28] O. Moutanabbir et al. “Nuclear Spin-Depleted, Isotopically Enriched 70Ge/28Si70Ge Quantum Wells”. In: *Advanced Materials* 36.8 (Feb. 2024), p. 2305703. ISSN: 0935-9648. DOI: 10.1002/adma.202305703. URL: https://onlinelibrary.wiley.com/doi/10.1002/adma.202305703.

[29] A. Crippa et al. “Electrical spin driving by g-matrix modulation in spin-orbit qubits”. In: *Physical Review Letters* 120.13 (Oct. 2017). DOI: 10.1103/PhysRevLett.120.137702. URL: http://dx.doi.org/10.1103/PhysRevLett.120.137702.

[30] V. P. Michal, B. Venitucci, and Y.-M. Niquet. “Longitudinal and transverse electric field manipulation of hole spin-orbit qubits in one-dimensional channels”. In: *Physical Review B* 103.4 (Jan. 2021), p. 045305. ISSN: 2469-9950. DOI: 10.1103/PhysRevB.103.045305. URL: https://link.aps.org/doi/10.1103/PhysRevB.103.045305.

[31] N. Piot et al. “A single hole spin with enhanced coherence in natural silicon”. In: *Nature Nanotechnology* 17.10 (Oct. 2022), pp. 1072–1077. ISSN: 1748-3387. DOI: 10.1038/s41565-022-01196-z. URL: https://www.nature.com/articles/s41565-022-01196-z.

[32] P. Stano and D. Loss. “Review of performance metrics of spin qubits in gated semiconducting nanostructures”. In: *Nature Reviews Physics* 4.10 (Aug. 2022), pp. 672–688. ISSN: 2522-5820. DOI: 10.1038/s42254-022-00484-w. URL: https://www.nature.com/articles/s42254-022-00484-w.

[33] V. John et al. “Robust and localised control of a 10-spin qubit array in germanium”. In: *Nature Communications* 16.1 (Nov. 2025), p. 10560. ISSN: 2041-1723. DOI: 10.1038/s41467-025-65577-3. URL: https://www.nature.com/articles/s41467-025-65577-3.

[34] M. Benito et al. “Electric-field control and noise protection of the flopping-mode spin qubit”. In: *Physical Review B* 100.12 (Sept. 2019), p. 125430. ISSN: 2469-9950. DOI: 10.1103/PhysRevB.100.125430. URL: https://link.aps.org/doi/10.1103/PhysRevB.100.125430.

[35] V. N. Golovach, M. Borhani, and D. Loss. “Electric-dipole-induced spin resonance in quantum dots”. In: *Physical Review B* 74.16 (Oct. 2006), p. 165319. ISSN: 1098-0121. DOI: 10.1103/PhysRevB.74.165319.

[36] K. C. Nowack et al. “Coherent Control of a Single Electron Spin with Electric Fields”. In: *Science* 318.5855 (Nov. 2007), pp. 1430–1433. ISSN: 0036-8075. DOI: 10.1126/science.1148092.

[37] X. Xue et al. “Benchmarking Gate Fidelities in a Si/SiGe Two-Qubit Device”. In: *Physical Review X* 9.2 (Apr. 2019), p. 021011. ISSN: 2160-3308. DOI: 10.1103/PhysRevX.9.021011. URL: https://link.aps.org/doi/10.1103/PhysRevX.9.021011.

[38] J. J. Wallman, M. Barnhill, and J. Emerson. “Robust characterization of leakage errors”. In: *New Journal of Physics* 18.4 (Apr. 2016), p. 043021. ISSN: 1367-2630. DOI: 10.1088/1367-2630/18/4/043021.

[39] E. Nielsen et al. “Gate Set Tomography”. In: *Quantum* 5 (Oct. 2021), p. 557. ISSN: 2521-327X. DOI: 10.22331/q-2021-10-05-557. URL: https://quantum-journal.org/papers/q-2021-10-05-557/.

[40] B. Martinez et al. “Hole spin manipulation in inhomogeneous and nonseparable electric fields”. In: *Physical Review B* 106.23 (Dec. 2022), p. 235426. ISSN: 2469-9950. DOI: 10.1103/PhysRevB.106.235426. URL: https://link.aps.org/doi/10.1103/PhysRevB.106.235426.

[41] L. S. Theis et al. “Counteracting systems of diabaticities using DRAG controls: The status after 10 years ^(a)”. In: *EPL (Europhysics Letters)* 123.6 (Oct. 2018), p. 60001. ISSN: 1286-4854. DOI: 10.1209/0295-5075/123/60001. URL: https://iopscience.iop.org/article/10.1209/0295-5075/123/60001.

[42] I. Heinz and G. Burkard. “Crosstalk analysis for single-qubit and two-qubit gates in spin qubit arrays”. In: *Physical Review B* 104.4 (July 2021), p. 045420. ISSN: 2469-9950. DOI: 10.1103/PhysRevB.104.045420. URL: https://link.aps.org/doi/10.1103/PhysRevB.104.045420.

[43] M. Rimbach-Russ et al. “Simple framework for systematic high-fidelity gate operations”. In: *Quantum Science and Technology* 8.4 (Oct. 2023), p. 045025. ISSN: 2058-9565. DOI: 10.1088/2058-9565/acf786. URL: https://iopscience.iop.org/article/10.1088/2058-9565/acf786.

[44] Y.-H. Wu et al. “Simultaneous High-Fidelity Single-Qubit Gates in a Spin Qubit Array”. In: *arXiv* (July 2025). URL: http://arxiv.org/abs/2507.11918.

[45] V. John et al. “Bichromatic Rabi Control of Semiconductor Qubits”. In: *Physical Review Letters* 132.6 (Feb. 2024), p. 067001. ISSN: 0031-9007. DOI: `10.1103/PhysRevLett.132.067001`.

[46] Z. György, A. Pályi, and G. Széchenyi. “Electrically driven spin resonance with bichromatic driving”. In: *Physical Review B* 106.15 (Oct. 2022), p. 155412. ISSN: 2469-9950. DOI: `10.1103/PhysRevB.106.155412`. URL: `https://link.aps.org/doi/10.1103/PhysRevB.106.155412`.

[47] D. A. Rower et al. “Suppressing Counter-Rotating Errors for Fast Single-Qubit Gates with Fluxonium”. In: *PRX Quantum* 5.4 (Dec. 2024), p. 040342. ISSN: 2691-3399. DOI: `10.1103/PRXQuantum.5.040342`. URL: `https://link.aps.org/doi/10.1103/PRXQuantum.5.040342`.

8

GE HOLE SPIN QUBITS WITH A ROOM-TEMPERATURE MAGNET

For my ally is the Force, and a powerful ally it is. [1]

Yoda

Germanium spin qubits exhibit strong spin-orbit interaction, which allow for high-fidelity qubit control, but also provide a strong dependence on the magnetic field. Superconducting vector magnets are often used to minimize dephasing due to hyperfine interactions and to maximize spin control, but these compromise the sample space and thus challenge scalability. Here, we explore whether a permanent magnet outside the cryostat can be used as an alternative. Operating in a hybrid mode with an internal and external magnet, we find that we can fine-tune the magnetic field to an in-plane orientation. We obtain a qubit dephasing time $T_2^* = 13\,\mu\text{s}$*, Hahn-echo times* $T_2^{\text{H}} = 88\,\mu\text{s}$*, and an average single-qubit Clifford gate fidelity above 99.9%. Then we demonstrate that it is possible to operate qubits with the internal superconducting magnet switched off, so the magnetic field is produced only by the external magnet. In this regime we find long coherence times for holes with* $T_2^* = 31\,\mu\text{s}$ *and Hahn-echo* $T_2^{\text{H}} = 252\,\mu\text{s}$*, while using natural germanium. These results show that room temperature magnets allow for high qubit performance. Our approach may be used to scale semiconductor qubits and use the increased sample space for the integration of cryogenic control circuitry and wiring to advance to large-scale quantum processors.*

This chapter has been published as Cécile X. Yu, Barnaby van Straaten, Alexander S. Ivlev, **Valentin John**, Damien R. Crielaard, Stefan D. Oosterhout, Lucas E. A. Stehouwer, Francesco Borsoi, Giordano Scappucci, Menno Veldhorst, Optimising germanium hole spin qubits with a room-temperature magnet, *arXiv:2507.03390* (2025)

SPIN qubits in semiconductor quantum dots are an attractive platform for quantum computing, as they offer long coherence times, allow for high-fidelity quantum gates, and have high compatibility with industrial semiconductor fabrication [2]. Germanium has emerged as a promising material for hosting hole-based spin qubits, offering strong spin-orbit interaction and all-electrical control [3–6]. Despite these advantages, achieving precise control over the qubit properties requires accurate alignment of the external magnetic field to the substrate plane to optimise coherence and fidelity due to the strong g-tensor anisotropy [7–10].

Even if the g-tensor plane is aligned with the sample crystallographic axes, achieving sub-degree accuracy in magnetic field alignment is challenging due to factors such as sample mounting variability and the differential thermal contraction of materials within the cryostat. While vector magnets can compensate for these misalignments to minimise hyperfine-induced dephasing and enhance the efficiency of electric dipole spin resonance (EDSR) operations [7, 11], their implementation requires considerable space and thermal load within the cryostat, and limit the available sample space [12].

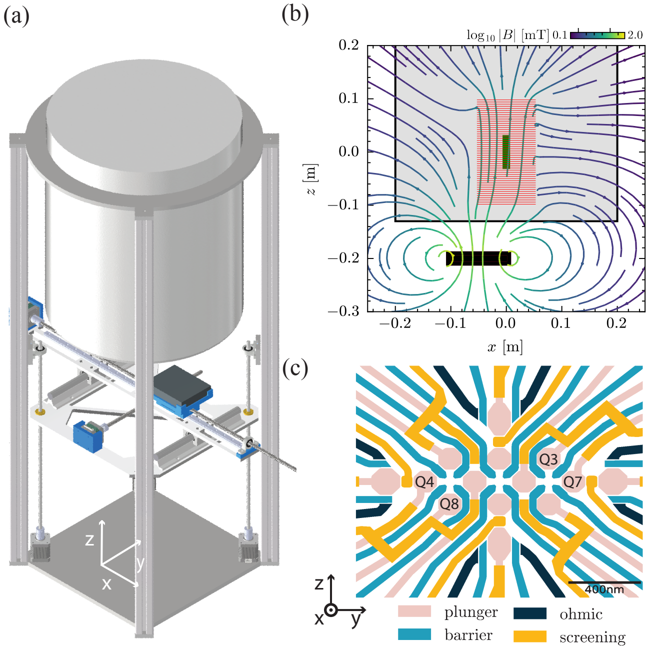

Figure 8.1: **Experimental set-up.** **a**, Diagram showing the XYZ stage used to position the permanent magnet (grey block). The stage is attached to the vacuum can of the fridge. **b,** Diagram showing a simulation of the magnetic field lines produced by the superconducting solenoid magnet (red) and the permanent magnet (black).The sample board is shown in green mounted in the centre of the solenoid magnet. **c,** Device layout indicating the qubits investigated in the experiments. The scale bar corresponds to 400 nm.

This work explores an alternative approach using a movable permanent magnet outside the dilution refrigerator to fine-tune the magnetic field at the qubit location in addition to the uniaxial superconducting magnet in the cryostat. This internal magnet provides a primary magnetic field of a few tens of millitesla, chosen to be small enough that any misalignment can be effectively corrected using the external magnet.

To characterise the feasibility of this approach, we perform EDSR drive on the qubit to evaluate its resonance frequency as a function of the uniaxial superconducting magnetic field strength, as well as the position of the external magnet relative to the sample. This study is further extended by characterising the qubit performance through Ramsey and Hahn echo experiments, along with single-qubit gate randomized benchmarking and gate set tomography. Our findings demonstrate that a qubit fine-tuned by an external magnet can achieve high quality qubit control, with fidelities exceeding 99.9%. We then switch off the uniaxial superconducting magnet to demonstrate that qubit operation is possible with the field produced by the permanent magnet only. We characterise the qubit properties under this field, finding long coherence times.

8.1. EXPERIMENTAL SET-UP

In this experiment, we use a standard cryogen-free dilution refrigerator equipped with a uniaxial superconducting magnet. To fine-tune the magnetic field, we move an NdFeB N45 block magnet of dimensions 110.6 × 89 × 19.5 mm, in three dimensions beneath the fridge (see Figure 8.1a). The motion of the external magnet is accomplished by suspending a Cartesian gantry system from the vacuum can of the dilution refrigerator, with motion along the x, y, and z axes controlled remotely by linear actuators and an Arduino board. A complete description of the system is provided in subsection 8.7.1.

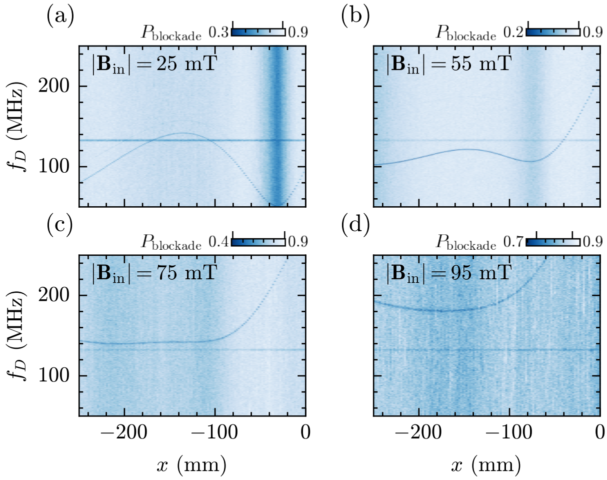

Figure 8.2: **Effect of the internal magnetic field magnitude.** Microwave spectroscopy of the qubit frequency as a function of permanent magnet position in x, with $y = 0$ and $z = -200$ mm at different internal magnetic field magnitude. P_{blockade} defines the probability of the even spin state being blockaded and f_{D} is the microwave drive tone frequency. The resonance around 130 MHz corresponds to the resonance frequency of the readout resonator.

For our coordinate system, we take the z axis as parallel to the vertical axis of the dilution refrigerator. If the sample were mounted perfectly, fields applied in this direction correspond to the [110] crystallographic direction and therefore are in-plane. In previous work on this device [13], we estimate there is a 2-3 degree misalignment, meaning that the magnetic field of the internal superconducting solenoid has a small out-of-plane component. We define the x axis close to parallel to the heterostructures [001] growth direction; therefore, fields applied in this direction are out of plane. The permanent magnet was oriented with its magnetisation axis along the z-axis, so that at $x, y = 0$ its field is parallel to that of the solenoid, see Figure 8.1b for a Magpylib simulation of the field lines [14]. By moving the magnet in the x direction, we expect to be able to compensate and cancel out the orthogonal field component, provided the external magnetic field is sufficiently strong.

We perform our qubit experiments on a 10-quantum dot device on a Ge/SiGe heterostructure as detailed in Ref. [10, 13] and investigate the effect of the magnetic field. We focus on qubits Q8 and Q3, which are initialised and read out using ancilla qubits Q4 and Q7, respectively, see Figure 8.1c. The coordinate system is defined relative to the sample, meaning that $(x, y, z) = (0, 0, 0)$ corresponds to the sample. We will refer to the magnetic field applied by the superconducting uniaxial solenoid inside the fridge as $\mathbf{B}_{\text{in}}$, and $\mathbf{B}_{\text{ext}}$ as the magnetic field generated by the external magnet.

8.2. QUBIT FREQUENCY TUNABILITY

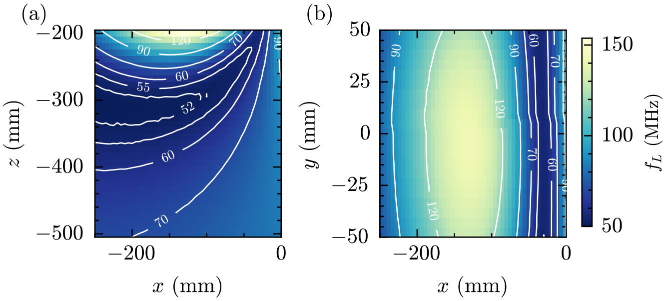

Figure 8.3: **Experimentally measured Larmor frequencies of the qubit as a function of magnet position at $|\mathbf{B}_{\text{in}}| = 25$ mT. a,** Larmor frequency in the xz-plane of the permanent magnet at $y = 0$ mm. **b,** Larmor frequency in the xy-plane of the permanent magnet at $z = -200$ mm. The contour lines are defined by connecting the corresponding experimental data points.

We begin by assessing the effect of the external magnet on the total magnetic field sensed by the spin qubit. The total field sensed by the qubit is $\mathbf{B}_T = \mathbf{B}_{\text{ext}} + \mathbf{B}_{\text{in}}$, which gives rise to a qubit Larmor frequency of $hf_L = \mu_B |g\mathbf{B}_T|$, where g is the germanium hole-spin g-tensor [7]. Relative to gyromagnetic axes of the spins, we anticipate this g-tensor to take the form $g = \text{diag}(g_x, g_y, g_z)$ with significant anisotropy such that $g_z \gg g_x, g_y$. We expect the axis corresponding to g_z to be aligned to within a few degrees with the crystallographic [001] axis and therefore also to within a few degrees of the x-axis. We will label this axis $\hat{\mathbf{g}}_z$.

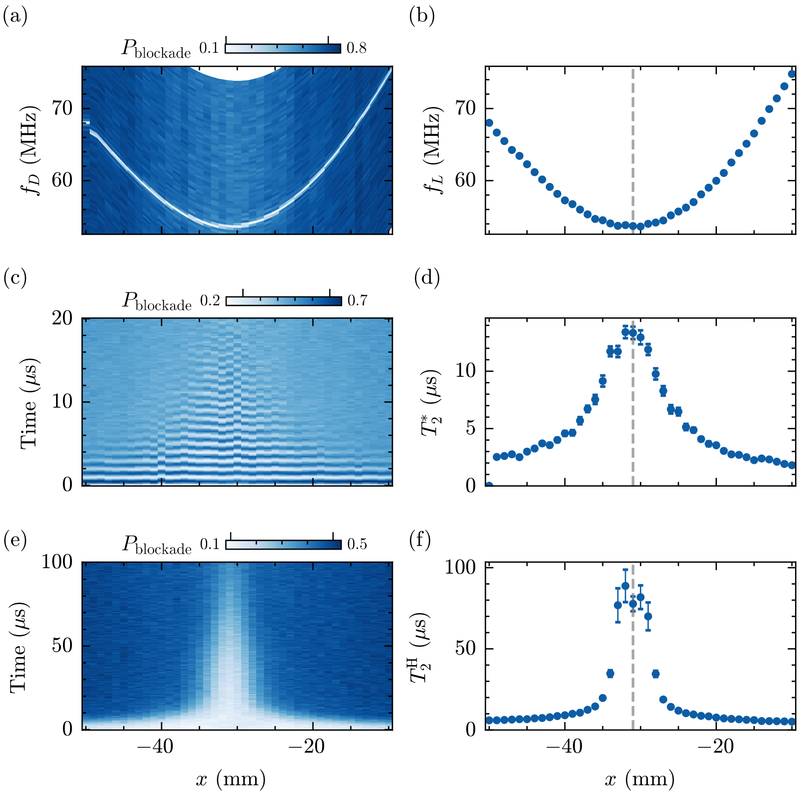

Figure 8.4: **Qubit coherence times at the magnetic field sweet-spot. a, b,** Larmor frequency f_{L} as a function of the x-position of the permanent magnet extracted from the microwave spectroscopy. **c, d,** Dephasing times T_2^* as a function of the magnet position in x measured with a Ramsey sequence. **e, f,** T_2^{H} measured with a Hahn echo sequence. The dashed grey lines indicate the optimal field spot at the minimum of the Larmor frequency where the magnetic field points in-plane. The error bars represent the precision of the fit.

To probe the effect of $\mathbf{B}_{\mathrm{ext}}$, we perform EDSR on qubit Q8 while varying the external magnet position along the x-axis from 0 to −250 mm, with the magnet held at $(y,z) = (0,-200)$ mm. For each position, we map the qubit Larmor frequency at different amplitudes of the internal field $\mathbf{B}_{\mathrm{in}}$. As the external magnet is displaced, both B_x^{ext} and B_z^{ext} vary, leading to a change in the orientation of the total field $\mathbf{B}_T$ relative to $\hat{\mathbf{g}}_z$. Because of the large anisotropy in g, even small components of $\mathbf{B}_T$ parallel to $\hat{\mathbf{g}}_z$ strongly affect the enhance g-factor and hence the Larmor frequency.

At low $|\mathbf{B}_{\mathrm{in}}|$ (see Figure 8.2a-b), the resonance frequency exhibits both a minimum and a local maximum as a function of magnet position. The minimum corresponds to the point where B_z^{ext} cancels the out-of-plane contribution parallel to $\hat{\mathbf{g}}_z$ of $\mathbf{B}_{\mathrm{in}}$ and thereby minimizing the effective g-factor. Moving the magnet further off-axis, B_z^{ext} begins to overcompensate the internal field while the magnitude of $\mathbf{B}_{\mathrm{ext}}$ at the qubit decreases with distance. This competition produces a local maximum in the Larmor frequency before it falls off again.

At larger $|\mathbf{B}_{\mathrm{in}}|$ (see Figure 8.2c-d), the external field is no longer strong enough to fully cancel the out-of-plane component of $\mathbf{B}_{\mathrm{in}}$, and the resonance frequency evolves smoothly with a parabolic dependence on the magnet position. Finally, we note that in the low-field regime of Figure 8.2a–b, the qubit initialization and readout fidelity decreases as the total field rotates from out-of-plane to in-plane. We attribute this to reduced initialization of the $|\uparrow\downarrow\rangle$ state: in-plane fields enhance the quantization-axis mismatch between the two qubits, which increases the probability of preparing the $|T_-\rangle = |\downarrow\downarrow\rangle$ state [15].

Now we set $|\mathbf{B}_{\mathrm{in}}| = 25\,\mathrm{mT}$ and fully characterise the tunability of the Larmor frequency in the xz- and xy-planes as shown in Figure 8.3. The Larmor frequency, f_{L}, varies from 50 MHz to 150 MHz, with the x-axis playing the dominant role by determining the out-of-plane component of the total magnetic field, and thus causing the strongest tunability on the qubit frequency. In the xz-plane, the qubit resonance frequency exhibits a minimum corresponding to the optimal field orientation where the external magnet compensates the internal magnetic field, resulting in a fully in-plane configuration. In contrast, in the xy-plane, variations in magnet position primarily tune the in-plane magnetic field orientation.

8.3. QUBIT COHERENCE TIMES

We now focus on the qubit performance at the magnetic field sweet spot to enhance the qubit dephasing times. We fix the z-position to $-200\,\mathrm{mm}$ and the y-position to zero, while the x-position is varied around the point corresponding to the minimum Larmor frequency. At this position, the magnetic field is expected to be aligned within the plane of the sample, where dephasing noise is minimized due to the hyperfine interactions with nuclear spins being minimal [7, 16]. Thus, to enhance the qubit dephasing times, the magnetic field has to be aligned perpendicular to the growth direction, where the anisotropic hyperfine interaction between heavy hole states and nuclear spins is expected to be negligible [16].

We measure the coherence times of Q8 by means of Ramsey and Hahn echo experiments to probe the impact of field tuning on spin coherence as shown in Figure 8.4. We find that when the Larmor frequency reaches its minimum value, T_2^* and T_2^{H} are simultaneously maximised, indicating an in-plane magnetic field orientation. By orienting the magnetic field fully in-plane at the hyperfine noise sweet spot, the dephasing time of the qubit reaches $T_2^* = (13.41 \pm 0.53)\,\mu\mathrm{s}$ while the echo time $T_2^{\mathrm{H}} = (88.77 \pm 9.99)\,\mu\mathrm{s}$. This is comparable with coherence times measured at the magnetic field sweet spot in a vector magnet [7]. Qubit Q3 also exhibits the same trend as a function of the external magnet position along the x direction, see subsection 8.7.2. For comparison, without the external magnet, the Ramsey and Hahn echo experiments on Q8 (subsection 8.7.3) indicate coherence times of $T_2^* = (1.70 \pm 0.12)\,\mu\mathrm{s}$ and $T_2^{\mathrm{H}} = (4.23 \pm 0.11)\,\mu\mathrm{s}$, respectively, revealing a hyperfine noise limited regime [13]. In subsection 8.7.4, we also show the Rabi drive efficiency of Q8 as a function of the magnet x-position. It reveals a peak in drive efficiency that coincides with the maximum coherence time, indicating that, for this qubit, an in-plane magnetic field is beneficial for both long coherence times and fast driving [7, 8].

We furthermore evaluate the single-qubit gate fidelity using both randomized benchmarking (RB) and gate set tomography (GST). We perform RB using the Clifford set detailed in subsection 8.7.5, giving us an average Clifford fidelity of $F_C = (99.936 \pm 0.005)$ %. Detailed methods and results for the GST are provided in Supplementary Note 5 of Ref. [17]. By dividing the average gate fidelity by the number of native gate per Clifford operation, we obtain a single-qubit gate fidelity of (99.980 ± 0.002) %, comparable to the highest reported values for qubits and measured using vector magnets [7, 18]. GST, which is more sensitive to systematic errors, reports average fidelities of $99.95 \pm 0.02\%$ for the $X90$ gate and $99.88 \pm 0.02\%$ for the $Y90$ gate. The lower fidelities reported by GST are expected to come from dynamical decoupling effects present in the RB sequence [19]. subsection 8.7.6 displays additional qubit coherence and fidelity data as a function of the magnet position with the device in a different electrostatic configuration.

8.4. ZERO INTERNAL FIELD OPERATION

A key challenge in scaling towards large-scale quantum processors is represented by the limited space available at the base temperature in a cryostat [20]. By removing the superconducting magnet inside the cryostat, the available sample space can be increased substantially, allowing for more control lines and improved prospects of scalability.

Here, we simulate this scenario by switching off the internal magnetic field, such that the qubit only senses the magnetic field of the permanent magnet. In this configuration, we measure the Larmor frequency as a function of the external magnet's position along the x-axis. By tuning the magnet position to the point where the qubit Larmor frequency reaches its minimum, approximately 9.5 MHz, we identify the optimal operating field. This process was slightly complicated by a small hysteretic effect in the magnet position, discussed in subsection 8.7.7. At this working point, we re-optimise the initialisation and readout pulse sequence using an optimiser based on Ref. [21]. We then observe long coherence times of $T_2^* = 31.4\,\mu\text{s}$ and $T_2^{\text{H}} = 252.0\,\mu\text{s}$ for hole-spin qubits in germanium. We attribute these long coherence times to the suppression of charge noise at low magnetic fields, as well as to the reduced hyperfine interactions achieved by aligning the magnetic field in the plane.

However, operating at low magnetic fields also reduces the achievable Rabi frequency. Under these conditions, we obtain a Rabi frequency of $f_R = 52\,\text{kHz}$ using a drive amplitude of $A = 8.4\,\text{mV}$ at the sample. Consistent with the slow Rabi frequency, we measure single-qubit Clifford gate fidelities of 99.7% using EDSR, confirmed through randomized benchmarking, see subsection 8.7.8.

By contrast, hopping-based gates are expected to operate at rates orders of magnitude faster than EDSR, with characteristic frequencies that reach a substantial fraction of the qubit Larmor frequency [5]. Incorporating such hopping gates could therefore dramatically accelerate qubit control in the low-field regime, enabling fast, high-fidelity spin manipulation without requiring large magnetic fields. Should EDSR be required, higher magnetic fields at the device level up to 1 T could be achieved by using a block magnet placed inside the cryostat near the qubit chip [22, 23]. This can be combined with a room-temperature permanent magnet to fine-tune the magnetic field orientation for optimal qubit operations.

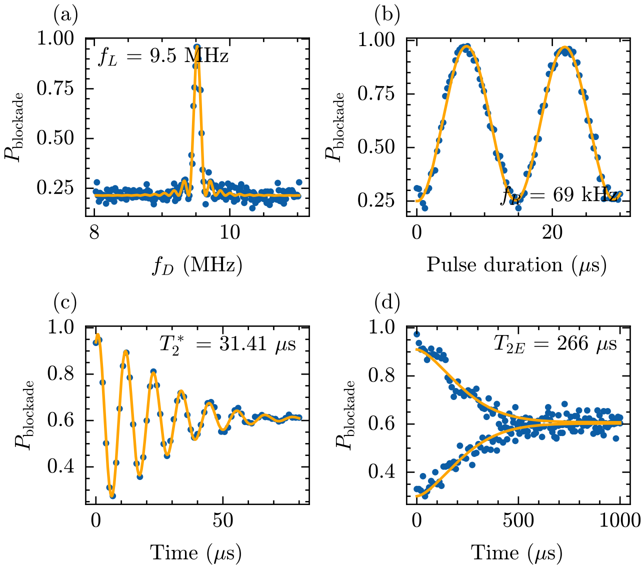

Figure 8.5: **Zero internal field qubit Larmor, Rabi, Ramsey and Hahn echo** measured with the external magnet at (x, y, z) = (-7, 0, -200) mm **a,** Qubit Larmor resonance along with the fit to extract the qubit Larmor frequency. **b,** Qubit Rabi oscillations along with the fit to extract the qubit Rabi frequency. **c,** Ramsey oscillations along with the fit to extract T_2^*, with an integration time of 30 minutes. **d,** Hahn echo with the qubit initialised in both the up and down states, along with the fit to extract T_2^{H}.

8.5. CONCLUSION

Superconducting magnets inside dilution refrigerators require considerable space, and can introduce current noise or ground loops into the qubit system. We demonstrate that a room-temperature permanent magnet offers an effective alternative to fine-tune the magnetic field experienced by germanium spin qubits. Our versatile room-temperature magnet setup enables in-plane magnetic field alignment, allowing natural germanium devices to operate in regimes less affected by hyperfine noise, thereby enhancing qubit coherence and gate fidelity. Even qubits hosted in isotopically purified materials [24, 25] will need to be tuned to optimal operating conditions [10], which can similarly done with the external magnet approach presented here. The cryostat space may then be used to integrate control wiring and cryo electronics for the construction of large-scale quantum hardware.

8.6. METHODS

The spin qubit device and general setup is the same as in chapter 7. The NdFeB N45 block magnet is commercially available under article ID Q-111-89-20-E, its dimensions are 110.6 × 89 × 19.5 mm and it has an adhesive force of 200 kg. Its magnetic field strength is probed using 3D magnetic Hall sensors integrated on a printed circuit board (ref. TLE493D-P3XX-MS2GO).

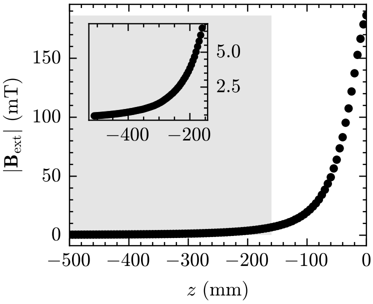

Figure 8.6: Measured magnetic field amplitude of the permanent magnet as a function of distance. The grey shaded area denotes the z-range used in the experiments and the inner plot shows the field strength in this z-range.

In the experiments, we initialise the qubit by pulsing from the (0,2) singlet state to the center of the (1,1) state adiabatically to prepare a $|\uparrow,\downarrow\rangle$ state. We then perform qubit manipulation via EDSR before reading out the spin state using Pauli spin blockade readout.

8.7. SUPPLEMENTARY

8.7.1. EXTERNAL MAGNET ASSEMBLY

The external magnet is a neodymium-iron-boron (NdFeB) magnet with a grade of N45, corresponding to a maximal energy product of ≈ 44 mega gauss-oersted and a demagnetisation temperature above 80°C. The dimensions of the magnet are 110.6 mm × 89 mm × 19.5 mm, magnetised along the short axis, resulting in a specified total holding force of 1960 N.

This magnet is mounted onto a gantry system (see Figure 8.1a) which provides linear movement in three dimensions, along the x, y and z-axis. The magnetisation direction of the magnet is aligned along the z-axis. Linear movement is enabled by a total of 4 NEMA17 stepper motors, two of which are used for the vertical z-direction and one for each horizontal direction. The two motors for the z-direction have a specified holding torque of 0.55 Nm, sufficient to move the system up and down, and a specified resolution of 1.8° per step. The horizontal direction is powered by motors with a higher resolution of 0.9°, but a lower holding torque of 0.21 Nm. All motors axels are attached to a 2mm pitched lead screw using a flexible coupler. Given the step-resolution of the motors and the lead screw pitch, the system achieves a theoretical resolution of 50 µm in the horizontal direction, and 100 µm in the vertical direction. In practise this resolution will be limited by mechanical tolerances in the assembly which have not been quantified directly, as they were deemed small enough to not limit the resolution on the qubit drive frequency.

8.7.2. ADDITIONAL QUBIT DATA

Here we plot the coherence times as a function of the magnet position along x direction for qubit Q3 that is located on the east side of the device, see Figure-1c in the main text. This qubit demonstrates the same trend in Larmor frequency and coherence times as a function of the magnet x-position. Note that we cannot compare the sweet spot position in x-direction between Q3 and Q8 investigated in the main text due to hysteresis effect of the magnet movement (see subsection 8.7.7). For these measurements we positioned the permanent magnet at $y = 0$, $z = -200$ and $|\mathbf{B}_{\text{in}}| = 25$ mT.

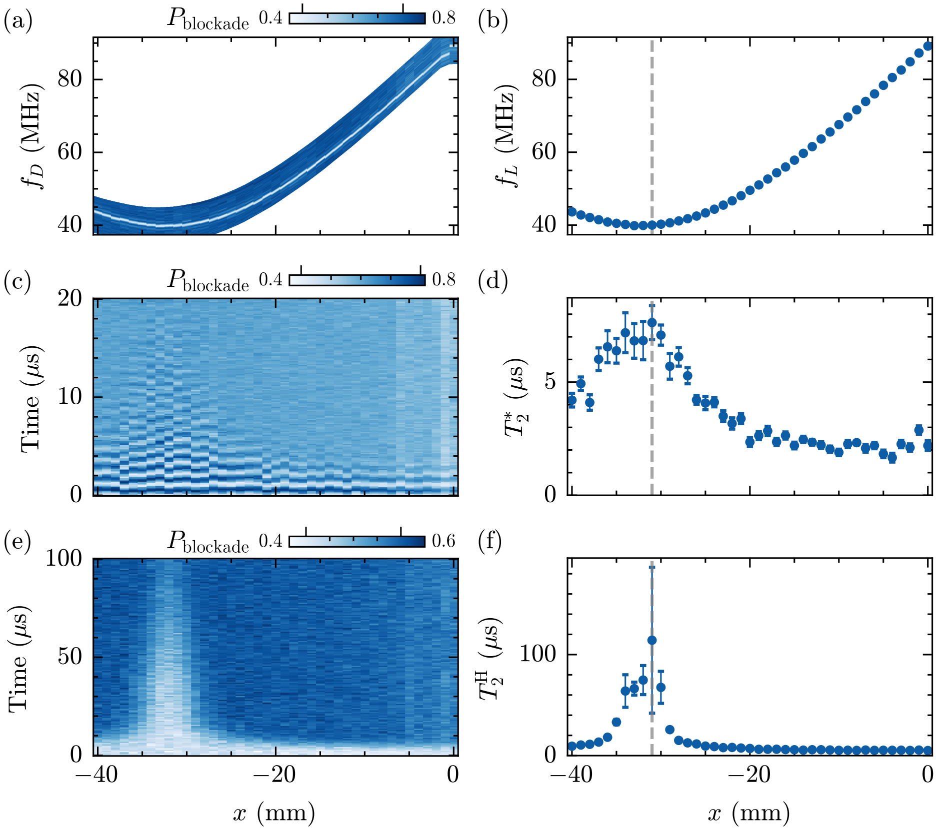

Figure 8.7: **a, b,** Larmor frequency f_{L} as a function of the x-position of the permanent magnet extracted from the microwave spectroscopy. **c,d,** Dephasing times T_2^* as a function of the magnet position in x measured with a Ramsey sequence. **e, f,** T_2^{H} measured with a Hahn echo sequence. For both Ramsey and Hahn echo sequences, t_{wait} denotes the total free evolution time. The dashed grey lines indicate the optimal field spot at the minimum of the Larmor frequency where the magnetic field points in-plane. The error bars represent the precision of the fit.

8.7.3. QUBIT COHERENCE TIMES WITHOUT THE EXTERNAL MAGNET

In Figure 8.8, we measure the coherence times of qubit Q8 by operating with the internal magnet set to 25 mT while the external magnet is 700 mm away from the sample such that we assume it has no effect on the total magnetic field. We estimate that here the magnetic field points 2-3 degrees out-of-plane and the qubit coherence times are expected to be hyperfine limited [10, 13].

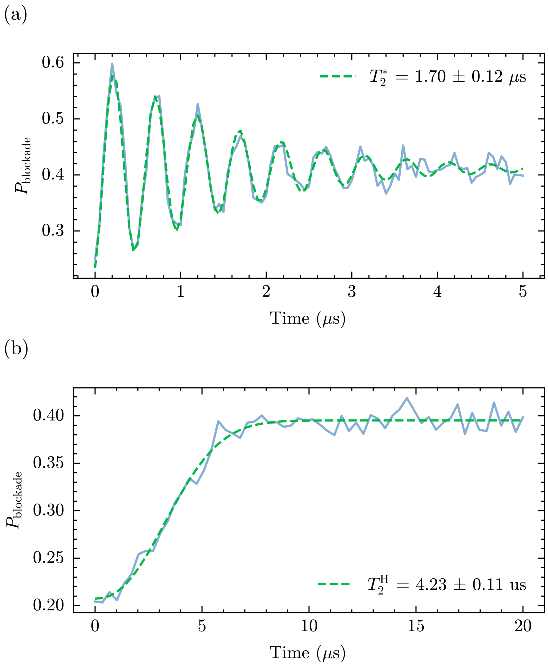

Figure 8.8: Coherence times of qubit Q8 without the external magnet. The blue curves represent the measurement data, and the green dashed lines show the fits for a Ramsey sequence (**a**) and a Hahn-echo sequence (**b**).

8.7.4. DRIVING EFFICIENCY

In Figure 8.9 we plot the Rabi drive efficiency and the dephasing time T_2^* of Q8 as a function of the external magnet position in the x direction.

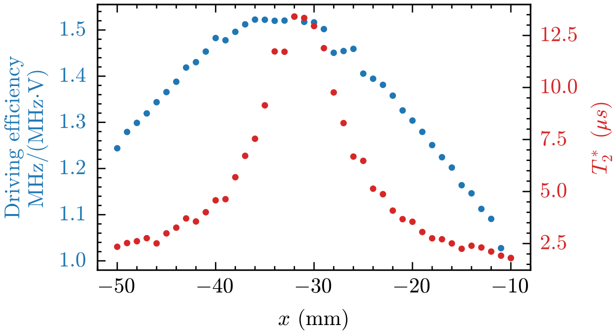

Figure 8.9: We define the driving efficiency as $f_{\mathrm{Rabi}}/(f_{\mathrm{L}} \cdot A)$, with f_{Rabi} being the Rabi frequency, f_{L} the Larmor frequency and A the drive amplitude at the qubit level.

8.7.5. RANDOMISED BENCHMARKING

In this work we perform single qubit RB in an identical fashion to that described in [18]. In particular, we randomly sample Clifford gates, composed from the native X90 and Y90 gates according to Table 8.1. We then append a recovery gate, taken to be the Clifford gate which is the inverse of the sequence proceeding it. We evaluate the outcomes of this sequence for increasing numbers of randomly sampled Clifford gates. We then fit a decaying exponential of the form

$$P_{\text{blockade}} = A\alpha^{N_C} + B,$$

where A represents the visibility of the system, α is the depolarizing parameter, N_c is the number of Clifford gates in the sequence, and B corresponds to the average signal of the $|00\rangle$ and $|01\rangle$ subspace (where the first index corresponds to the qubit being benchmarked) [26]. For a single qubit, the depolarizating parameter is related to the average Clifford fidelity according to

$$F_C = 1 - (1-\alpha)/2.$$

For comparison with GST we then convert the Clifford gate fidelity, F_C to a native gate fidelity F_N, this is achieved by dividing the Clifford infidelity by the average number of gates per Clifford, such that

$$1 - F_N = (1 - F_C)/n_C,$$

where n_C is the average number of native gates per Clifford, which in our case is 3.217. Single qubit benchmark of Q3 at the hyperfine noise sweet spot is shown in Figure 8.10a. We perform a bootstrapping analysis at the single-shot level to estimate the uncertainty in the fidelity F_N. For each Clifford depth, the single-shot data are repeatedly resampled with replacement, and the fitting routine is applied to each resampled dataset to obtain a distribution of F_N, shown in Figure 8.10b. The error bars correspond to the 2.5th and 97.5th percentiles of this distribution, representing a 95% confidence interval.

Operation	**Pulse Sequence**
Pauli I (Identity)	I
Pauli π rotations	$X_{90}X_{90}$ (X)
	$Y_{90}Y_{90}$ (Y)
	$Y_{90}Y_{90}X_{90}X_{90}$ (Z)
$2\pi/3$ rotations around $\sqrt{1/3}[\pm1,\pm1,\pm1]$	$X_{90}Y_{90}$
	$X_{90}Y_{90}Y_{90}Y_{90}$
	$X_{90}X_{90}X_{90}Y_{90}$
	$Y_{90}Y_{90}X_{90}Y_{90}$
	$Y_{90}X_{90}$
	$Y_{90}X_{90}X_{90}X_{90}$
	$Y_{90}Y_{90}Y_{90}X_{90}$
	$Y_{90}X_{90}Y_{90}Y_{90}$
$\pi/2$ rotations around $[\pm1,0,0]$, $[0,\pm1,0]$, $[0,0,\pm1]$	X_{90}
	$X_{90}X_{90}X_{90}$
	Y_{90}
	$Y_{90}Y_{90}Y_{90}$
	$Y_{90}X_{90}Y_{90}Y_{90}Y_{90}$
	$Y_{90}Y_{90}Y_{90}X_{90}Y_{90}$
Hadamard-like π rotations	$X_{90}X_{90}Y_{90}$
	$Y_{90}X_{90}X_{90}$
	$Y_{90}Y_{90}X_{90}$
	$X_{90}Y_{90}Y_{90}$
	$Y_{90}X_{90}Y_{90}$
	$Y_{90}X_{90}X_{90}X_{90}Y_{90}$

Table 8.1: RB Clifford gates decomposed into native X_{90} and Y_{90} pulses [18]. The gates are ordered from left to right to indicate their temporal sequence, as opposed to the operator notation where the first gate is the rightmost.

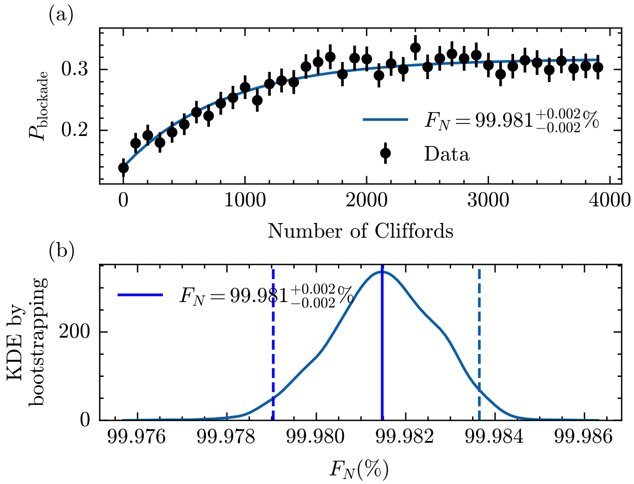

Figure 8.10: **(a)** Single-qubit randomized benchmarking (RB) of Q3 measured at the in-plane magnetic field. The solid blue line is a fit to the standard RB decay model, yielding an average Clifford gate fidelity of $F_{\mathrm{N}} = 99.981^{+0.002}_{-0.002}\%$. Black points show the measured blockade probability P_{blockade}, and the error bars represent the standard error of the mean over 20 random sequences. **(b)** Bootstrap kernel density estimate (KDE) of the extracted gate fidelity. The solid vertical line indicates the mean F_{N}, while the dashed lines mark the 68% confidence interval. The Clifford set used is listed in Table 8.1.

8.7.6. ADDITIONAL QUBIT COHERENCE AND FIDELITY DATA

This section presents additional datasets showing the coherence times and gate fidelities as functions of the external magnet's position. These measurements were acquired after the device had been fully retuned, resulting in gate voltages that differ from those used for the datasets presented in the main text.

Metric	**Slightly out of plane**	**In-plane**
External magnet x position (mm)	0	-29
Larmor frequency f_L (MHz)	98.3	58.8
Rabi frequency f_R (MHz)	0.48	0.41
X_{90} time (ns)	520	604
Dephasing time T_2^* (μs)	1.80	7.1
Hahn Echo coherence T_2^H (μs)	6.1	41
RB avg. Clifford fidelity F_N (%)	$99.772^{+0.025}_{-0.025}$	$99.973^{+0.001}_{-0.001}$
GST X_{90} fidelity (%)	99.593 ± 0.1484	99.955 ± 0.0461
GST Y_{90} fidelity (%)	99.535 ± 0.1446	99.961 ± 0.0389

Table 8.2: Qubit properties measured at two different magnet positions. The first corresponds to a few degrees out of plane and the second in plane.

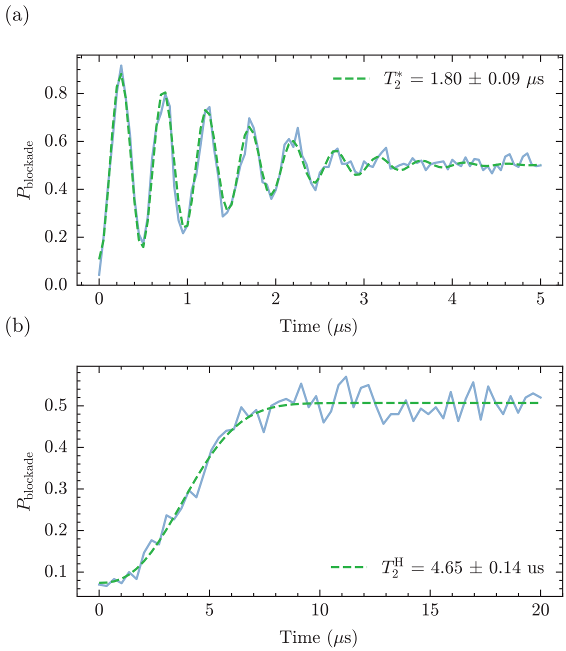

Figure 8.11: Ramsey and Echo coherence with the external magnet at $x = 0$.

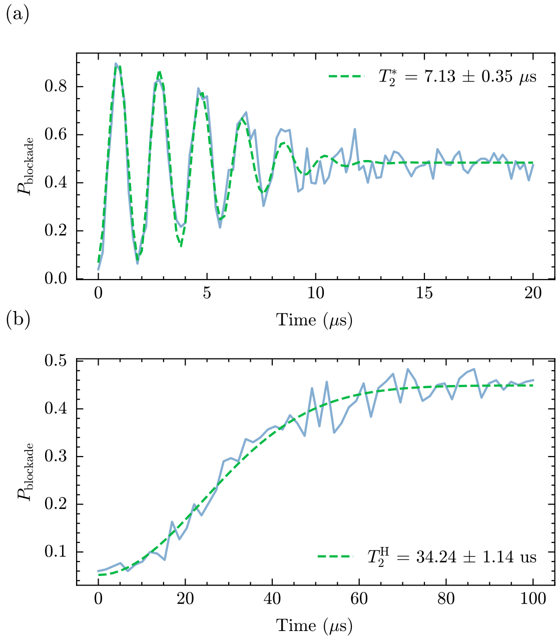

Figure 8.12: Ramsey and Echo coherence with the external magnet at $x = -29$.

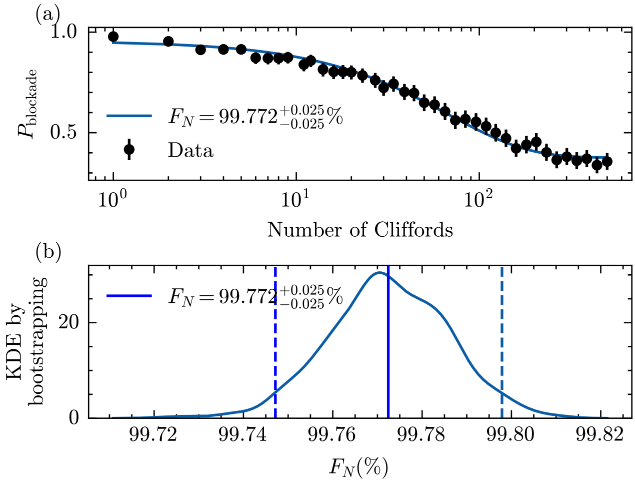

Figure 8.13: Randomised benchmarking with the external magnet at $x = 0$.

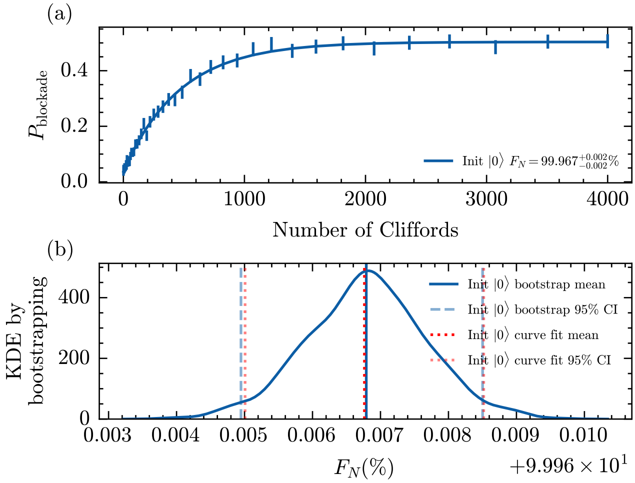

Figure 8.14: Randomised benchmarking with the external magnet at $x = -29$.

8.7.7. HYSTERESIS EFFECT IN THE MAGNET MOVEMENT

Here, we quantify the hysteresis effect observed in the magnet motion on three different qubits Q1, Q4 and Q8. The movement of the magnet is non-linear, which introduces hysteresis when repeating runs involving multiple start-and-stop motions. From Figure 8.15, we estimate an offset of 2.5 mm per run of 51 data points. This corresponds to an approximate offset of 50 μm per start-and-stop event during a magnet movement of 1 mm. We note that this 50 μm corresponds to the theoretical spatial resolution of the gantry system, so we expect to be roughly one step of the stepper motor off. Given the reproducibility of the offset, it could be compensated in software by a correction of 50 μm to each data point. The system can also be improved by replacing the motors with ones that include integrated calibration routines, similar to those used in 3D printers, or by incorporating a distance measurement system that provides real-time feedback on the magnet position to enable in-situ calibration of the existing setup.

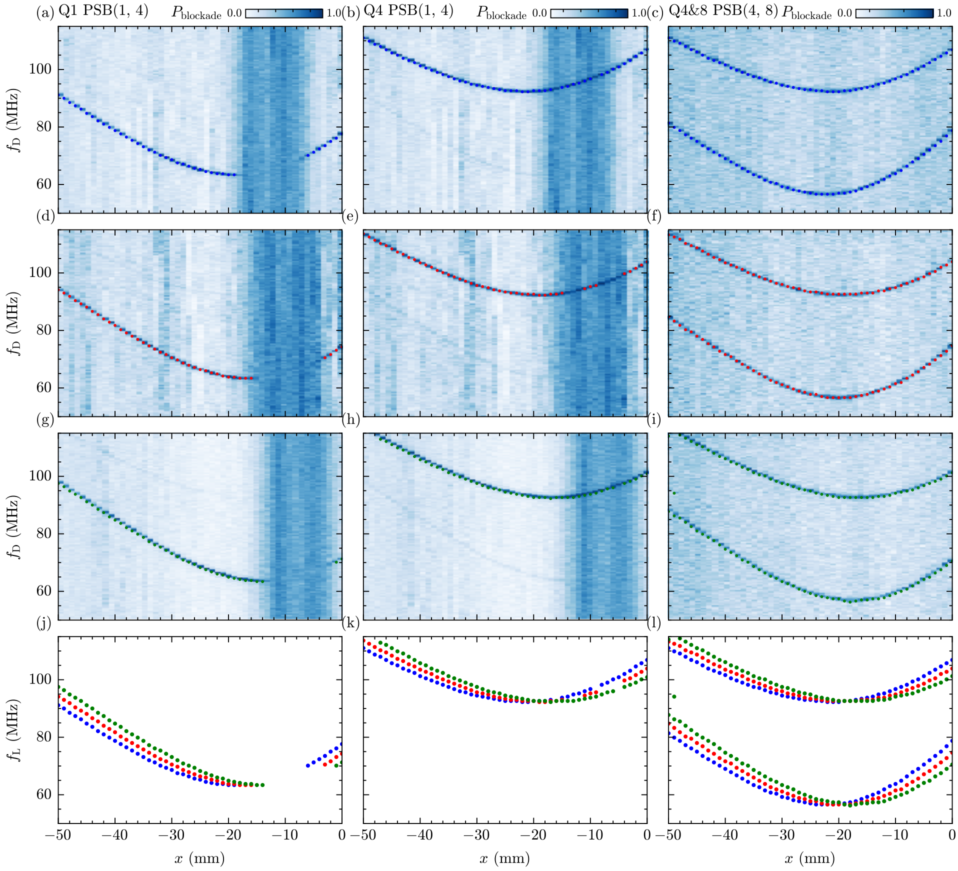

Figure 8.15: Hysteresis effect of the magnet movement probed over three different qubits Q1, Q4 and Q8. PSB(i, j) indicates that the readout is performed between qubits Qi and Qj. **a-c,** Microwave spectroscopy of qubits Q1, Q4, Q8 during the first magnet run. **d-f,** Second run **g-i,** Third run. **j-l,** Extracted Larmor frequencies for each qubit across the three runs (blue: first run, red: second run, green: third run) showing the run-to-run variation in qubit response to the external magnet position.

8.7.8. ZERO INTERNAL FIELD DATA

In Figure 8.16 randomised benchmarking at zero internal magnetic field is shown. All the magnetic field comes from the external magnet.

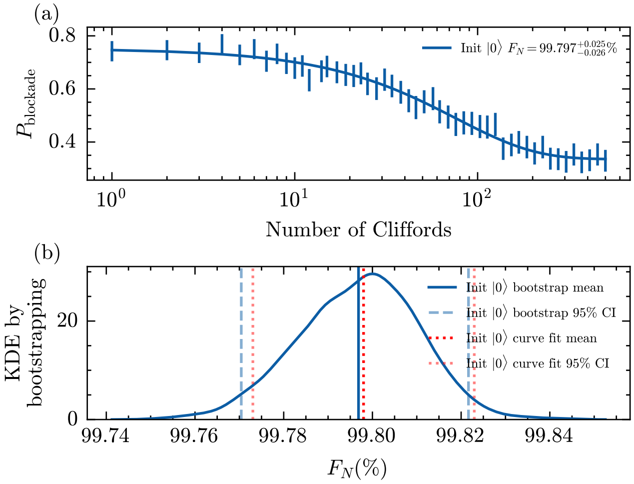

Figure 8.16: Randomised benchmarking of the qubit with magnet at $x, y, z = (-7, 0, -200)$ mm.

BIBLIOGRAPHY

[1] I. Kershner. *Star Wars: Episode V – The Empire Strikes Back*. 1980.

[2] G. Burkard et al. “Semiconductor spin qubits”. In: *Reviews of Modern Physics* 95.2 (June 2023), p. 025003. ISSN: 0034-6861. DOI: `10.1103/RevModPhys.95.025003`. URL: `https://link.aps.org/doi/10.1103/RevModPhys.95.025003`.

[3] H. Watzinger et al. “A germanium hole spin qubit”. In: *Nature Communications* 9.1 (Dec. 2018). ISSN: 20411723. DOI: `10.1038/S41467-018-06418-4`.

[4] N. W. Hendrickx et al. “A four-qubit germanium quantum processor”. In: *Nature* 591.7851 (Mar. 2021), pp. 580–585. ISSN: 0028-0836. DOI: `10.1038/s41586-021-03332-6`. URL: `https://www.nature.com/articles/s41586-021-03332-6`.

[5] C.-A. Wang et al. “Operating semiconductor quantum processors with hopping spins”. In: *Science* 385.6707 (July 2024), pp. 447–452. ISSN: 0036-8075. DOI: `10.1126/science.ado5915`. URL: `https://www.science.org/doi/10.1126/science.ado5915`.

[6] G. Scappucci et al. “The germanium quantum information route”. In: *Nature Reviews Materials* 6.10 (Dec. 2020), pp. 926–943. ISSN: 2058-8437. DOI: `10.1038/s41578-020-00262-z`. URL: `https://www.nature.com/articles/s41578-020-00262-z`.

[7] N. W. Hendrickx et al. “Sweet-spot operation of a germanium hole spin qubit with highly anisotropic noise sensitivity”. In: *Nature Materials* 23.7 (July 2024), pp. 920–927. ISSN: 1476-1122. DOI: `10.1038/s41563-024-01857-5`. URL: `https://www.nature.com/articles/s41563-024-01857-5`.

[8] L. Mauro et al. “Geometry of the dephasing sweet spots of spin-orbit qubits”. In: *Physical Review B* 109.15 (Apr. 2024), p. 155406. ISSN: 2469-9950. DOI: `10.1103/PhysRevB.109.155406`. URL: `https://link.aps.org/doi/10.1103/PhysRevB.109.155406`.

[9] J. Saez-Mollejo et al. “Exchange anisotropies in microwave-driven singlet-triplet qubits”. In: *Nature Communications 2025 16:1* 16.1 (Apr. 2025), pp. 3862–. ISSN: 2041-1723. DOI: `10.1038/s41467-025-58969-y`. URL: `https://www.nature.com/articles/s41467-025-58969-y`.

[10] V. John et al. “Robust and localised control of a 10-spin qubit array in germanium”. In: *Nature Communications* 16.1 (Nov. 2025), p. 10560. ISSN: 2041-1723. DOI: `10.1038/s41467-025-65577-3`. URL: `https://www.nature.com/articles/s41467-025-65577-3`.

[11] M. Bassi et al. “Optimal operation of hole spin qubits”. In: *arXiv* (Dec. 2024). URL: `http://arxiv.org/abs/2412.13069`.

[12] G. Da Prato et al. “Step-by-step design guide of a cryogenic three-axis vector magnet”. In: *Review of Scientific Instruments* 96.6 (June 2025). ISSN: 0034-6748. DOI: 10.1063/5.0270187.

[13] L. E. A. Stehouwer et al. “Exploiting strained epitaxial germanium for scaling low-noise spin qubits at the micrometre scale”. In: *Nature Materials* 24.12 (Dec. 2025), pp. 1906–1912. ISSN: 1476-1122. DOI: 10.1038/s41563-025-02276-w. URL: https://www.nature.com/articles/s41563-025-02276-w.

[14] M. Ortner and L. G. Coliado Bandeira. “Magpylib: A free Python package for magnetic field computation”. In: *SoftwareX* 11 (Jan. 2020), p. 100466. ISSN: 2352-7110. DOI: 10.1016/J.SOFTX.2020.100466.

[15] D. Jirovec et al. “Dynamics of Hole Singlet-Triplet Qubits with Large g-Factor Differences”. In: *Physical Review Letters* 128.12 (Mar. 2022), p. 126803. ISSN: 0031-9007. DOI: 10.1103/PhysRevLett.128.126803. URL: https://link.aps.org/doi/10.1103/PhysRevLett.128.126803.

[16] J. Fischer et al. “Spin decoherence of a heavy hole coupled to nuclear spins in a quantum dot”. In: *Physical Review B* 78.15 (Oct. 2008), p. 155329. ISSN: 1098-0121. DOI: 10.1103/PhysRevB.78.155329. URL: https://link.aps.org/doi/10.1103/PhysRevB.78.155329.

[17] C. X. Yu et al. “Optimising germanium hole spin qubits with a room-temperature magnet”. In: *arXiv* (July 2025). URL: http://arxiv.org/abs/2507.03390.

[18] W. I. L. Lawrie et al. “Simultaneous single-qubit driving of semiconductor spin qubits at the fault-tolerant threshold”. In: *Nature Communications* 14.1 (June 2023), p. 3617. ISSN: 2041-1723. DOI: 10.1038/s41467-023-39334-3. URL: https://www.nature.com/articles/s41467-023-39334-3.

[19] J. P. Dehollain et al. “Optimization of a solid-state electron spin qubit using gate set tomography”. In: *New Journal of Physics* 18.10 (Oct. 2016), p. 103018. ISSN: 1367-2630. DOI: 10.1088/1367-2630/18/10/103018.

[20] M. Mohseni et al. “How to Build a Quantum Supercomputer: Scaling from Hundreds to Millions of Qubits”. In: (Nov. 2024). URL: https://arxiv.org/abs/2411.10406v2.

[21] S. R. Katiraee-Far et al. “Unified evolutionary optimization for high-fidelity spin qubit operations”. In: (Mar. 2025). URL: https://arxiv.org/abs/2503.12256v1.

[22] C. Adambukulam et al. “An ultra-stable 1.5 T permanent magnet assembly for qubit experiments at cryogenic temperatures”. In: *Review of Scientific Instruments* 92.8 (Aug. 2021). ISSN: 0034-6748. DOI: 10.1063/5.0055318. URL: https://pubs.aip.org/rsi/article/92/8/085106/1032817/An-ultra-stable-1-5-T-permanent-magnet-assembly.

[23] J. Rooney et al. “Gate modulation of the hole singlet-triplet qubit frequency in germanium”. In: *npj Quantum Information 2025 11:1* 11.1 (Jan. 2025), pp. 15–. ISSN: 2056-6387. DOI: 10.1038/s41534-024-00953-3. URL: https://www.nature.com/articles/s41534-024-00953-3.

[24] O. Moutanabbir et al. “Nuclear Spin-Depleted, Isotopically Enriched 70Ge/28Si70Ge Quantum Wells”. In: *Advanced Materials* 36.8 (Feb. 2024), p. 2305703. ISSN: 0935-9648. DOI: `10.1002/adma.202305703`. URL: `https://onlinelibrary.wiley.com/doi/10.1002/adma.202305703`.

[25] E. A. Chekhovich et al. “Nuclear spin effects in semiconductor quantum dots”. In: *Nature Materials 2013 12:6* 12.6 (May 2013), pp. 494–504. ISSN: 1476-4660. DOI: `10.1038/nmat3652`. URL: `https://www.nature.com/articles/nmat3652`.

[26] X. Xue et al. “Benchmarking Gate Fidelities in a Si/SiGe Two-Qubit Device”. In: *Physical Review X* 9.2 (Apr. 2019), p. 021011. ISSN: 2160-3308. DOI: `10.1103/PhysRevX.9.021011`. URL: `https://link.aps.org/doi/10.1103/PhysRevX.9.021011`.

9

A GAPLESS SINGLE-SPIN QUBIT

When divine Art conceives a form and face,
she bids the craftsman for his first essay
to shape a simple model in mere clay
this is the earliest birth of Art's embrace. [1]

Michelangelo

All-electrical baseband control of qubits facilitates scaling up quantum processors by removing issues of crosstalk and heat generation. In semiconductor quantum dots, this is enabled by multi-spin qubit encodings, such as the exchange-only qubit. However, their performance is limited by unavoidable leakage states that are energetically close to the computational subspace. In this work, we introduce an alternative, scalable spin qubit architecture that leverages strong spin-orbit interactions of hole nanostructures for baseband qubit operations while completely eliminating leakage channels and reducing the overall gate overhead. This encoding is intrinsically robust to local variability in hole spin properties and operates with two degenerate states, removing the need for precise calibration and mitigating heat generation from fast signal sources. Finally, our architecture is fully compatible with current technology, utilizing the same initialization, readout, and multi-qubit protocols of state-of-the-art spin-1/2 systems. By addressing critical scalability challenges, our design offers a robust and scalable pathway for semiconductor spin qubit technologies.

Parts of this chapter have been published in Maximilian Rimbach-Russ, **Valentin John**, Barnaby van Straaten, and Stefano Bosco, **A gapless single-spin qubit**, *Phys. Rev. Lett. 135, 197001* (2025).

SEMICONDUCTOR quantum-dot-based spin qubits are a promising platform for large-scale and fault-tolerant quantum processors using industrial fabrication [2–7]. Among them, hole spin qubits in silicon (Si) and germanium (Ge) quantum dots are leading candidates for scaling [8–19]. Their strong spin-orbit interaction (SOI) enables ultrafast all-electric local operations [19–28] and long-distance interactions beyond the nearest neighbor [29–34]. Furthermore, SOI also provides a means to control the properties of the qubit performance in situ, offering sweet spots to improve the performance of the qubit [15, 35–45]. In analogy to superconducting qubits, most spin qubits are controlled using microwave pulses [21, 46–48], which introduce critical scaling challenges such as crosstalk and heating [49, 50] posing significant barriers to the development of large-scale devices [51, 52]. Progress has been made toward discrete baseband control of hole qubits through spin hopping in Ge quantum dots [19], but this approach still requires high-frequency signal generators and high-bandwidth pulses for diabatic gates, adding considerable technological constraints on electronic control.

The exchange-only (XO) qubit does not have such strict electronic requirements. The XO qubit uses multi-spin encoding with degenerate qubit states during idling, making phase tracking and dynamic pulse shaping obsolete and allowing electric two-axis control via inter-dot exchange interactions [10, 53–57]. While XO qubits have shown high-fidelity single- and two-qubit gates, readout, and state initialization [58], they are heavily impacted by leakage into close-in-energy states, requiring complex pulse sequences for high-fidelity quantum gates and large overhead in fault tolerance. Furthermore, readout and initialization are also limited by additional close-in-energy orbital leakage states [59].

In this work, we propose a novel qubit implementation by electrically tuning a hole spin qubit in the presence of strong SOI such that the qubit energy splitting, its Larmor frequency, can be tuned to zero[0]. Our resulting gapless single-spin (GS2) qubit combines the best features of XO and single spin qubits; simple and fast baseband controlled gates, no phase tracking, simple calibration, and the absence of leakage states. Remarkably, the GS2 qubit further enables a scalable architecture (See Fig. 9.1a)) suppressing additional crosstalk and observer errors, multiple read-out axes, and flexible high-fidelity two-qubit gates. By mitigating these key issues, our GS2 qubit encoding paves a path to scalable architectures for a full fault-tolerant quantum processors.

9.1. ARCHITECTURE

Fig. 9.1 a) shows our envisioned quantum processor architecture. Each qubit requires five gate electrodes for universal control, a central plunger gates surrounded by four control gates, thus, has a similar or smaller gate per qubit count than alternative implementations [10]. We note, that the double barrier design was already demonstrated in Ref. [16] and gives rise to a stronger suppression of residual exchange coupling and reduced electrostatic crosstalk due to the larger spacing. At the same time, the larger separation and sparser nature of the qubit array allows easier fabrication and fanout in contrast to dense 2D qubit arrays. By design, such a densely occupied design (with indi-

---

[0] We remark, that artificial spin-orbit interaction through micromagnets, nanomagnets, or magnetic textures can also be used instead [60].

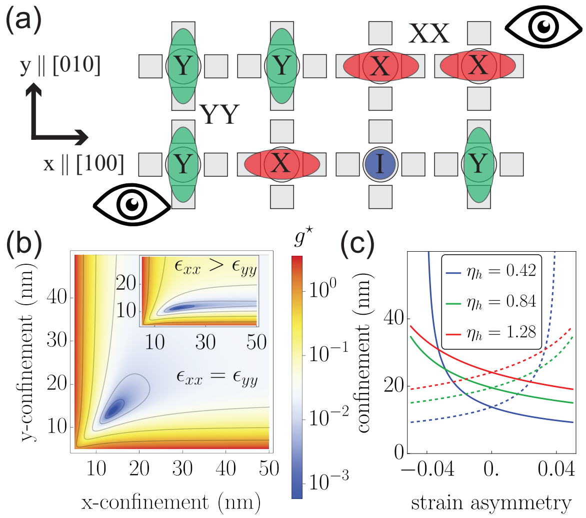

Figure 9.1: a) Proposed architecture for our novel single-spin spin-orbit qubit (GS2) qubit. Each qubit is controlled using five gate electrodes. Single-qubit gates are operated by electrically compressing and stretching the qubit. Readout, initialization, and two-qubit gates can be implemented along x and y directions. Readout and initialization uses Pauli-spin-blockade and either requires a close by charge sensor or readout resonator. During idling, qubit states are not subject to any dynamics. b) Effective g-tensor $g^\star = ||\mathcal{G}\boldsymbol{B}||/||\boldsymbol{B}||$ in the optimal optimal magnetic field direction $\boldsymbol{B} \parallel [110]$ (for $\boldsymbol{B} \parallel [1\bar{1}0]$ axes are flipped) as a function of characteristic confinement lengths of the groundstate wavefunction in X, Y-direction, assuming biaxial strain. The GS2 qubit condition is a dot radius ≈ 14 nm. The inset shows GS2 conditions assuming asymmetric strain. c) The GS2 qubit conditions for different heavy-hole light-hole coupling strengths as a function of strain asymmetry $(\epsilon_{xx} - \epsilon_{yy})/(\epsilon_{xx} + \epsilon_{yy})$.

vidual control) can be used to implement 2D quantum error corrections codes such as the surface code [61]. However, we note that using a sparse qubit occupation combined with hopping or shuttling interconnects [19, 62] or conveying the full qubit [63, 64], novel and more efficient codes may be implemented [65, 66].

9.2. GS2 QUBIT

For our qubit encoding, we consider a single Kramers doublet of a confined particle with half-integer spin in a semiconductor quantum dot. In the presence of a magnetic field, the Hamiltonian of such a system is given by

$$H = \frac{1}{2}\mu_B \boldsymbol{\sigma} \cdot \mathcal{G}\boldsymbol{B}. \tag{9.1}$$

Here, $B = (B_x, B_y, B_z)^T$ is the magnetic field vector, μ_B is Bohr's magneton, and $\mathcal{G}$ is the (anisotropic) gyro-magnetic matrix 3×3 [67], also called the g-tensor. For our qubit design, we use two properties. Firstly, at least two eigenvalues of the g-tensor, so-called principal values, can be electrically tuned to zero. Secondly, the magnetic field is not collinear with one of the principal axes of the g-tensor and is orthogonal to the principal axis with non-zero eigenvalue. While not exclusive, these requirements are often met in semiconductor hole qubits, e.g. hole qubits in silicon and germanium heterostructures [12, 68, 69].

Without loss of generality, we now consider for the reminder of the article planar germanium grown in [001] directions and prove that both requirements can be fulfilled in state-of-the-art materials. The g-tensor for planar strained germanium approximately consists of three parts [70, 71] $\mathscr{G} = \mathscr{G}_0 + \mathscr{G}_{\text{strain}} + \mathscr{G}_{\text{conf}}$. The first term is the bare g-tensor, which for heavy-hole ground states is given by $\mathscr{G}_0 = \text{diag}(3q, -3q, 6\kappa + 27q/2)$ and is highly anisotropic $|\kappa| \gg |q|$. The second and third expressions are g-tensor corrections arising from strain and confinement.

Explicitly, considering an in-plane magnetic field, the Hamiltonian of the ground doublet is approximately

$$H = \frac{1}{2}\mu_B(B_x\mathscr{G}_{xx} + B_y\mathscr{G}_{xy})\sigma_x + \frac{1}{2}\mu_B(B_y\mathscr{G}_{yy} + B_x\mathscr{G}_{yx})\sigma_y \tag{9.2}$$

with the electrically tunable g-tensor components [70–74]

$$\mathscr{G}_{xx} \approx 3q - \frac{6\tilde{\kappa}b_v(\langle\epsilon_{xx}\rangle - \langle\epsilon_{yy}\rangle)}{\Delta_{\text{HL}}} - \frac{6(\lambda\langle p_x^2\rangle - \lambda'\langle p_y^2\rangle)}{m_0\Delta_{\text{HL}}} \tag{9.3}$$

$$\mathscr{G}_{yy} \approx -3q - \frac{6\tilde{\kappa}b_v(\langle\epsilon_{xx}\rangle - \langle\epsilon_{yy}\rangle)}{\Delta_{\text{HL}}} + \frac{6(\lambda\langle p_y^2\rangle - \lambda'\langle p_x^2\rangle)}{m_0\Delta_{\text{HL}}}, \tag{9.4}$$

$$\mathscr{G}_{xy,yx} \approx \pm\frac{4\sqrt{3}\kappa d_v\epsilon_{xy}}{\Delta_{\text{HL}}} \mp \frac{12\tilde{\lambda}\langle p_x p_y\rangle}{m_0\Delta_{\text{HL}}}, \tag{9.5}$$

Here the average $\langle\cdot\rangle$ is with respect to the in-plane component of the groundstate wavefunction. The material dependent scaling parameters $\lambda = 2\eta_h\gamma_3^2 - \tilde{\kappa}\gamma_2$, $\lambda' = 2\eta_h\gamma_3\gamma_2 - \tilde{\kappa}\gamma_2$, $\tilde{\lambda} = 2\eta_h(\gamma_2\gamma_3 + \gamma_3^2) - \tilde{\kappa}\gamma_3$, and $\tilde{\kappa} = \kappa - 2\tilde{\eta}_h\gamma_3$ depend on the material dependent Luttinger parameters γ_1, γ_2, and γ_3, deformation parameters a_v, b_v, and d_v [75], and inter-band couplings, η_h and $\tilde{\eta}_h$ which depend on matrix elements between out-of-plane wave functions. Conveniently, η_h and $\tilde{\eta}_h$ and $\langle p_i p_j\rangle$ are electrically controllable. In principle, $\langle\epsilon_{ij}\rangle$ is also electrically tunable, although usually less predictable. In Figure 9.1 b) we show the energy splitting of Hamiltonian (9.2) without shear strain, $\langle\epsilon_{xy}\rangle = \langle\epsilon_{xz}\rangle = \langle\epsilon_{yz}\rangle = 0$, and separable wave-functions $\langle p_x p_y\rangle = \langle p_x p_z\rangle = \langle p_y p_z\rangle = 0$ with symmetric and asymmetric strain. Here, we introduced for better understanding the characteristic length of the in-plane wavefunction $\langle p_i^2\rangle = \hbar^2/(2L_i^2)$ with $i = x, y$. We can clearly identify the operation regime of our GS2 qubit at characteristic confinement lengths of 10 – 20 nm using parameters from Ref. [70]. The zero-crossings can be analytically expressed as

$$\langle p_x^2\rangle = p_{x,a}^2 = \frac{m_0}{2}\left[\frac{\Delta_{\text{HL}}q}{\lambda - \lambda'} - \frac{2b_v\tilde{\kappa}(\langle\epsilon_{xx}\rangle - \langle\epsilon_{yy}\rangle)}{\lambda + \lambda'}\right] \tag{9.6}$$

$$\langle p_y^2\rangle = p_{y,a}^2 = \frac{m_0}{2}\left[\frac{\Delta_{\text{HL}}q}{\lambda - \lambda'} + \frac{2b_v\tilde{\kappa}(\langle\epsilon_{xx}\rangle - \langle\epsilon_{yy}\rangle)}{\lambda + \lambda'}\right]. \tag{9.7}$$

While the required characteristic confinement lengths seem small, simulations and experimental demonstration show that they are feasible, see Figure 6.14 in chapter 6. In

Fig. 9.1-c), we show the GS2 condition for varying strain asymmetry $(\epsilon_{xx} - \epsilon_{yy})/(\epsilon_{xx} + \epsilon_{yy})$ that may arise from disorder [76] and for different heavy-hole light-hole coupling strengths [1]. Conveniently, typical strain fluctuations arising from dislocations are on length-scales multiple quantum dot radii [76], thus each GS2 qubit can be tuned to its own respective operation point. We also remark, that the GS2 condition is predicted to be possible in other material and device structures [38, 68, 69].

Shear strain from metallic top gates [70] or strong confinement [77] adds terms of the form $(B_x \mathscr{G}_{zx} + B_y \mathscr{G}_{zy})\sigma_z$ to Hamiltonian (9.2) giving rise to errors. However, due to the interplay of confinement and strain, there still exist a confinement that fulfills our requirements (see general expressions in Ref. [71]). In practice, one wants to avoid these shear contributions, for example, through deeper quantum wells, gate designs that minimize average shear strain, or materials with a smaller differential thermal expansion coefficient.

9.3. QUBIT STATES AND OPERATIONS

The qubit states are encoded in the two-fold degenerate doublet, defined as $|\Uparrow,\Downarrow\rangle$. The operation condition is visualised in Figure 9.2a, where by tuning the isotropic confinement potential the g-factor g^* can be tuned to zero. This typically requires to confine the spin tightly. Unlike conventional Loss-DiVincenzo qubits and similar to exchange-only qubits, the degeneracy ensures that our qubit has no dynamics during idling. Unlike exchange-only qubits, however, our qubit has no leakage states since only a single doublet is used and excited states are separated by more than 1 meV. Therefore, our design combines the best of both worlds. To the best of our knowledge, there is no equivalent encoding with a single particle in any quantum computing platform.

Single qubit operations Single qubit gates are enabled by small deviations from the degeneracy condition $\langle p_x^2\rangle = p_{x,a}^2 + \langle p_x^2\rangle_\Delta$ and $\langle p_y^2\rangle = p_{y,a}^2 + \langle p_y^2\rangle_\Delta$ that lead to the standard Hamiltonian

$$H_{1q} = b_x\sigma_x + b_y\sigma_y \tag{9.8}$$

with $b_{x,y} = \mp\frac{1}{2}\mu_B B_{x,y}\frac{6}{m_0\Delta_{\mathrm{HL}}}(\lambda\langle p_{x,y}^2\rangle_\Delta - \lambda'\langle p_{y,x}^2\rangle_\Delta)$ and neglecting out-of-plane tilts.

Using the layout shown in Fig. 9.1 a), $\langle p_x^2\rangle$ and $\langle p_y^2\rangle$ can be individually and electrically controlled, giving rise to arbitrary single qubit rotations. Orthogonal rotations around the X, Y-axis can be realized by pulsing $\frac{\langle p_{x,y}^2\rangle_\Delta}{\langle p_{y,x}^2\rangle_\Delta} = \frac{\lambda}{\lambda'}$ [2] as depicted in Figure 9.2b. In Ge/SiGe quantum wells $\lambda/\lambda' \sim \gamma_3/\gamma_2 \approx 4/3$. Notably, a misaligned magnetic field in the x, y-plane only affects the gate speed and not the rotation angle of the quantum gate. Consequently, the fastest operations are achieved if $\boldsymbol{B} \parallel [110]$ or $\boldsymbol{B} \parallel [1\bar{1}0]$. We remark that in realistic structures due to cross-capacitance coupling, orthogonal control might require an additional calibration step [79] or sufficient virtualization [80]. In addition,

---

[1] A value of $\eta_h = 0.42$ was reported in Ref. [77] assuming symmetric biaxial strain.

[2] Alternatively, rotations around the $\sigma_x \pm \sigma_y$-axes can be achieved by the condition $\langle p_y^2\rangle(\beta^2\lambda - \lambda') = (\beta^2\lambda' - \lambda)\langle p_x^2\rangle$ with $\beta = B_y/B_x$.

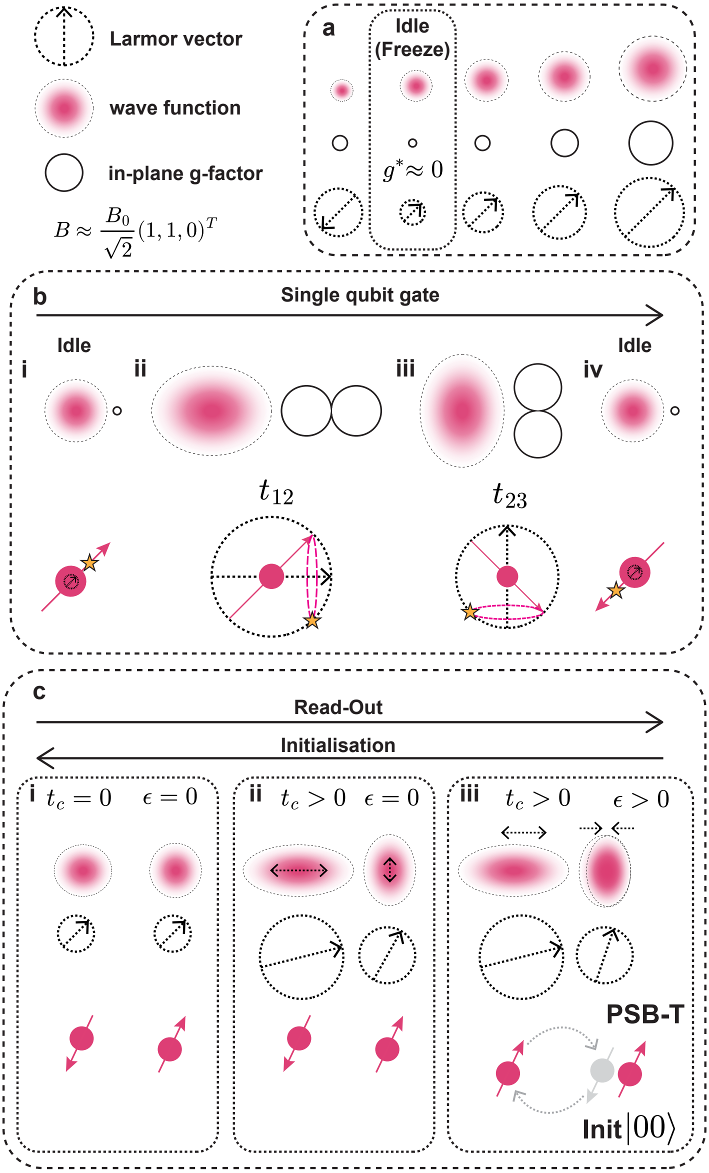

Figure 9.2: **Operation of the GS2 qubit. a.** The Larmor vector can be scaled isotropically by isotropically tightening the wavefunction confinement. Stronger confinement increases the g-factor, which eventually crosses zero, inverts its sign, and grows in magnitude upon further confinement. The configuration at which the g-factor vanishes defines the idle point, where no state evolution occurs. **b.** Single qubit gates are performed by squeezing the wavefunction in opposite directions starting from the idle point. The wait times t_{12} and t_{23}, during which the state evolves around the corresponding quantisation axes, can be calibrated to yield an arbitrary rotation before pulsing back to the idle point. **c.** Initialisation and readout protocol using g-tensor modulation to maximise the $|00\rangle - S(0,2)$ anticrossing.

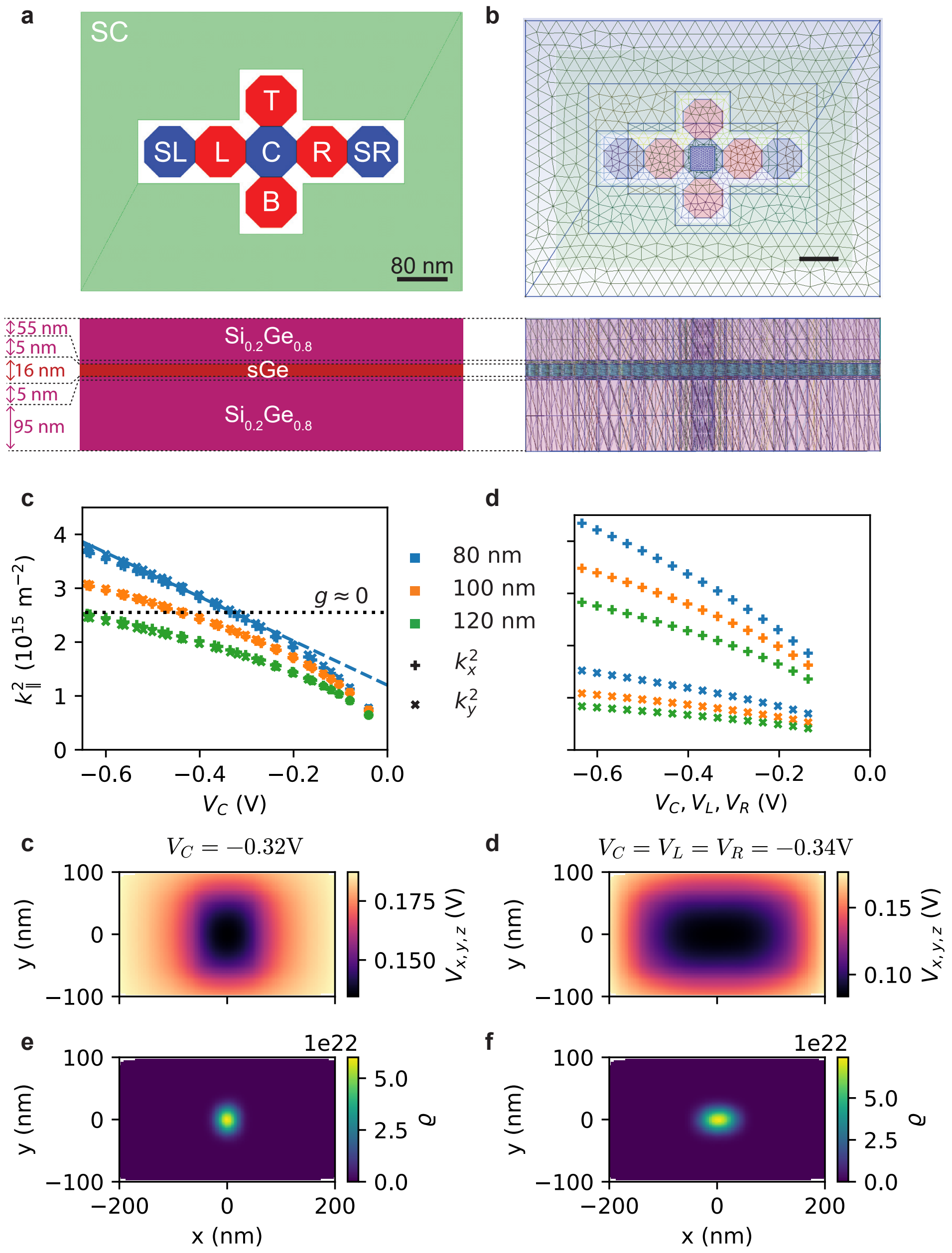

Figure 9.3: **Schrödinger-Poisson simulation using QTCAD** [78]. **a.** Simulated device structure with the indicated names of the gates. The GS2 qubit is made up of the gates C, L, R, T, B. Two additional gates at the side (SL, SR) and a screening gate (SC) are also included. The simulated heterostructure resembles a typical heterostructure used in experiment. The SiGe spacer has been increased from 55 nm to 60 nm to account for the difference in effective height due to the emittance of an additional gate oxide. b. Mesh generated with QTCAD. **c.** Confinement as function of the top gate for three different gate diameters (80, 100 and 120 nm). The black dash line is the target confinement with the g-factor approaching zero. The solid line is a linear regression with $\langle k_y^2 \rangle = 1.2 \times 10^{15}\,\mathrm{m}^{-2} + 4.1 \times 10^{15}\,\mathrm{m}^{-2}\mathrm{V}^{-1} V_g$ around the operation point at $g^* \approx 0$ for 80 nm gate diameter. **d.** Same as **c.**, but sweeping V_C, V_L and V_R all together. **c., d.** confinement potential at a given voltage setting. **e., f.** wavefunction at the same given voltage settings.

even with non-orthogonal rotation axes, arbitrary single-qubit gate can be calibrated similar to the ones with hopping spin [19].

We have performed Schrödinger-Poisson simulations of a gate layout similar to Fig. 1a) and a heterostructure as discussed in Ref. [19] to estimate the tunability of our GS2 qubit. The simulated device and the extracted data can be seen in Figure 9.3. We have simulated gate voltages ranging from zero to $-0.65\,\mathrm{V}$. For more negative voltages, the wave function escapes the quantum well. Generally, the simulated devices with smaller gate diameter have a larger tunability over the wavefunction confinement. Gate diameters of around 80 nm are therefore most promising in reaching an idle point with $g^* \approx 0$. Around the idle point, we estimate a local tunability of $4.1 \times 10^{15}\,\mathrm{m}^{-2}\mathrm{V}^{-1}\,V_g$ around the operation point, which should be sufficient to obtain sizable Zeeman splitting upon pulsing.

Readout and initialization The GS2 qubit can be read out using conventional Pauli-spin blockade (PSB) methods, where spin-selective charge transitions are observed. While PSB readout is generally used to read out any quantum dot spin-qubit, the unblocked spin state depends on the interplay of the Zeeman and the exchange interaction between spins in neighboring quantum dots. We distinguish three cases: i) For a uniform magnetic field and a uniform g-tensor without spin-orbit interaction, the spin singlet state $|S\rangle = (|10\rangle - |01\rangle)/\sqrt{2}$ is unblocked. We call this PSB-S and is typically used for electron spin qubits without micromagnet, singlet-triplet, and EO qubits. ii) For magnetic fields with a parallel gradient or a uniform magnetic field along a (common) principal axis of the g-tensors without spin-orbit interaction, the $|01\rangle$ or $|10\rangle$ state is unblocked. We call this the PSB-Z and is typically used for electron spin qubits with a micromagnet. iii) For magnetic fields with an orthogonal gradient, a uniform magnetic field along a (common) principal axis of the g-tensors, or spin-orbit interaction, the $|11\rangle$ is unblocked. We call this the PSB-T and is typically implemented for hole spin qubits.

We conceive a two-step high-fidelity PSB readout and initialization protocol, which is visualised in Figure 9.2c: i) We start from the idling position with $g^* \approx 0$. ii) We elongate the wave-functions such that they get closer and the tunnel coupling between the two dots is increased. Ideally, we elongate them orthogonal to each other, such that we increase the quantisation axis difference. iii) While tilting the two dots by sweeping the detuning ε from the charge symmetry point at $\varepsilon = 0$ towards the interdot transition at $\varepsilon > 0$, we additionally compress (stretch) the first (second) wavefunction such that $b_y^A \approx -b_y^B$ [3]. This ensures that we open the anti-crossing between the $|00\rangle$ and $|S_{02}\rangle$ states even in the presence of small spin flip tunnelling to ensure PSB-T.

In germanium, PSB-T readout and initialization protocols similar to our method achieves high fidelities [81]. We further remark, that faster pulses with higher fidelity can be achieved using optimal control, especially the QUAD protocol allows for consistently high transfer fidelity [82–85]. Consequently, high-fidelity state initialization can be achieved by reversing the upper protocol.

---

[3] In practice, maintaining the condition $b_y^A = b_y^B = 0$ during the readout process might be challenging. The only strict requirement for our protocol is to first turn on one axis and then maintain adiabaticity while turning on the other parameter.

Two qubit gates The two qubit gates are implemented similar to traditional spin qubits using the exchange interaction originating from the wavefunction overlap [18, 48, 86, 87].

9.4. GS2 QUBIT IN PRACTICE

To demonstrate the GS2 qubit experimentally, a shift in quantum dot array design is required. Traditionally, spin qubit arrays use a single dedicated plunger and barrier gate per site, which define the qubit potential and the coupling between sites. Typical plunger gate diameters are between 100 and 130 nm [21, 88]. The numerical estimates in Figure 9.3 indicate that smaller gate diameters of 80 nm would be advantageous, with five gates arranged in a cross pattern to define a single qubit. Although this increases the number of gates per qubit site, the approach fits naturally with sparse-array concepts and compares favourably to other encodings such as singlet triplet (S-T) and exchange-only qubits, which require a similar number of gate electrodes. Unlike these qubits, which operate exclusively in dense architectures, the GS2 qubit is inherently suited for sparse layouts and is compatible with conveyor-mode shuttling. This flexibility enables more efficient gate routing and reduces fabrication complexity at scale.

With these considerations, we propose the device shown in Figure 9.4a and b as a first proof-of-concept. It consists of a linear array with three GS2 qubit sites (Q1, Q2 and Q3) and a 250 µm-long conveyor with a repeating unit cell (×781). In the fanout, the elements of each repeating unit cell are shorted together, such that only four control lines are needed to operate the conveyor in a four phase scheme. A single-hole transistor is placed at each end of the array for read-out. Because the coupons are cut along the [110] crystallographic direction, the design must be rotated by 45 deg so that the GS2 qubit sites align along [100] and [010]. Ideally, this device allows the demonstration of:

1. tunability of the g-factor to zero at all three GS2 qubit sites
2. high-fidelity single-qubit gates by locally realigning the quantisation axis
3. high-fidelity initialization and read-out through the GS2 protocol, which controls the anticrossing between the $|00\rangle$ and $|S_{02}\rangle$ states
4. high-fidelity two-qubit gates
5. compatibility with conveyor-mode shuttling
6. spatial evaluation of strain effects on the g-factor
7. tunability of the g-factor at all three GS2 sites large enough to, in principle, tune all g-factors obtained in the conveyor to zero
8. coherent shuttling across a macroscopic distance (optional)

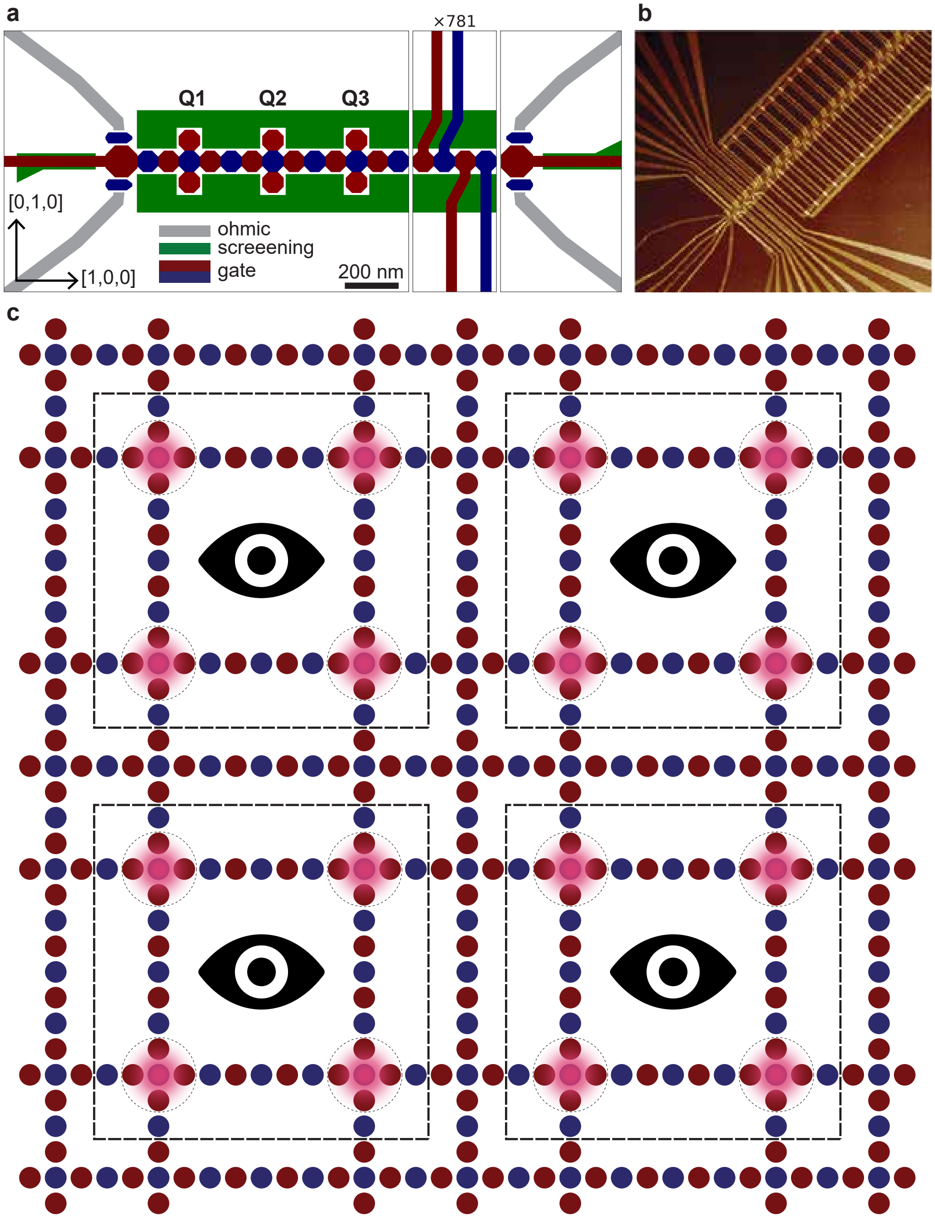

Figure 9.4: **GS2 device and architecture, a.** Proof-of-concept device to realise a GS2 qubit including three qubit sites and a coveyor. **b.** AFM image of a fabricated proof-of-principle device. The image is rotated by 45 deg since coupons are cut along the [110] crystallographic direction. **c.** GS2 architecture with unit cells consisting of four GS2 qubit sites each and a sensor in its centre. GS2 qubit unit cells are arranged on a grid and connected through a conveyor network.

9.5. GS2 QUBIT ARCHITECTURE

The most basic GS2 qubit architecture is shown in Figure 9.1a, featuring a dense array of GS2 qubits with sensors indicated at the periphery. For near-term devices, this layout yields the highest qubit count and supports coupling to up to four nearest neighbours. Its main limitations for further scaling are the required gate density and the absence of shuttling. The ability to shuttle spin qubits increases connectivity and enables the use of dedicated operation zones, where qubit gates, initialization and read-out can be performed depending on the zone type. As a result, shuttling offers much greater flexibility in quantum processor unit design. We therefore propose an alternative GS2 architecture shown in Figure 9.4c. It consists of a unit cell containing one sensor and four GS2 qubits, arranged in a sparse grid. This ensures sufficient separation between qubits such that chip-level crosstalk is strongly suppressed. Each unit cell is surrounded by a conveyor network that links all cells. In this scheme, every GS2 qubit can be initialized and read out locally while retaining full algorithmic flexibility through high connectivity enabled by shuttling. The conveyor network can be operated largely through shared control, while some degree of multiplexing is envisioned for the unit cells. A module may contain $n \times m$ such cells, with modules interconnected by long-distance shuttling lanes. This would make it possible to place cryogenic control electronics directly on the chip, as proposed in [89]. The architecture is flexible with respect to gate electrode density and requires only baseband pulses for full control. We therefore expect that this proposal can serve as a guiding blueprint for scaling the GS2 qubit beyond the initial proof-of-concept device.

9.6. CONCLUSION

We have introduced the GS2 qubit, a qubit encoding without the need for complex control electronics, that can be controlled fully using only baseband pulses, possess no noticeably leakage states, and allows fast and high-fidelity qubit gates. Our encoding fully leverages the potential of hole qubits and spin-orbit interaction through the g-tensor. Remarkably, our qubit can be implemented in state-of-the-art materials. This makes the GS2 qubit a truly promising encoding to realize a large-scale quantum processor.

BIBLIOGRAPHY

[1] J. A. Symonds. *The Sonnets of Michelangelo The Italian text with an English Translation and Introduction.* 2nd ed. London: Smith, Elder, & Co., 1904. URL: `https://publicdomainreview.org/collection/the-sonnets-of-michelangelo-1904-edition/`.

[2] R. Li et al. "A Flexible 300 Mm Integrated Si MOS Platform for Electron- and Hole-Spin Qubits Exploration". In: *2020 IEEE International Electron Devices Meeting (IEDM)*. 2020, pp. 38.3.1–38.3.4. DOI: `10.1109/IEDM13553.2020.9371956`.

[3] T. Bédécarrats et al. "A New FDSOI Spin Qubit Platform with 40nm Effective Control Pitch". In: *2021 IEEE International Electron Devices Meeting (IEDM)*. 2021, pp. 1–4. DOI: `10.1109/IEDM19574.2021.9720497`.

[4] A. M. J. Zwerver et al. "Qubits Made by Advanced Semiconductor Manufacturing". In: *Nat Electron* 5.3 (2022), pp. 184–190. ISSN: 2520-1131. DOI: `10.1038/s41928-022-00727-9`.

[5] H. C. George et al. "12-Spin-Qubit Arrays Fabricated on a 300 Mm Semiconductor Manufacturing Line". In: *Nano Letters* 25.2 (2025), pp. 793–799. ISSN: 1530-6984. DOI: `10.1021/acs.nanolett.4c05205`.

[6] P. Steinacker et al. "Industry-compatible silicon spin-qubit unit cells exceeding 99% fidelity". In: *Nature 2025 646:8083* 646.8083 (Sept. 2025), pp. 81–87. ISSN: 1476-4687. DOI: `10.1038/s41586-025-09531-9`. URL: `https://www.nature.com/articles/s41586-025-09531-9`.

[7] T. Huckemann et al. "Industrially Fabricated Single-Electron Quantum Dots in Si/Si—Ge Heterostructures". In: *IEEE Electron Device Letters* 46.5 (2025), pp. 868–871. ISSN: 1558-0563. DOI: `10.1109/LED.2025.3553672`.

[8] D. Loss and D. P. DiVincenzo. "Quantum Computation with Quantum Dots". In: *Phys. Rev. A* 57.1 (1998), p. 120. DOI: `10.1103/PhysRevA.57.120`.

[9] C. Kloeffel and D. Loss. "Prospects for Spin-Based Quantum Computing in Quantum Dots". In: *Annu. Rev. Condens. Matter Phys.* 4.1 (2013), pp. 51–81. DOI: `10.1146/annurev-conmatphys-030212-184248`.

[10] G. Burkard et al. "Semiconductor Spin Qubits". In: *Rev. Mod. Phys.* 95.2 (2023), p. 025003. DOI: `10.1103/RevModPhys.95.025003`.

[11] P. Stano and D. Loss. "Review of Performance Metrics of Spin Qubits in Gated Semiconducting Nanostructures". In: *Nat Rev Phys* 4.10 (2022), pp. 672–688. ISSN: 2522-5820. DOI: `10.1038/s42254-022-00484-w`.

[12] G. Scappucci et al. "The Germanium Quantum Information Route". In: *Nature Reviews Materials* (2020), pp. 1–18. ISSN: 2058-8437. DOI: `10.1038/s41578-020-00262-z`.

[13] Y. Fang et al. “Recent Advances in Hole-Spin Qubits”. In: *Mater. Quantum. Technol.* 3.1 (2023), p. 012003. ISSN: 2633-4356. DOI: 10.1088/2633-4356/acb87e.

[14] R. Maurand et al. “A CMOS Silicon Spin Qubit”. In: *Nat Commun* 7.1 (2016), p. 13575. ISSN: 2041-1723. DOI: 10.1038/ncomms13575.

[15] N. W. Hendrickx et al. “Sweet-Spot Operation of a Germanium Hole Spin Qubit with Highly Anisotropic Noise Sensitivity”. In: *Nat. Mater.* 23.7 (2024), pp. 920–927. ISSN: 1476-4660. DOI: 10.1038/s41563-024-01857-5.

[16] F. Borsoi et al. “Shared Control of a 16 Semiconductor Quantum Dot Crossbar Array”. In: *Nat. Nanotechnol.* (2023), pp. 1–7. ISSN: 1748-3395. DOI: 10.1038/s41565-023-01491-3.

[17] V. John et al. “Bichromatic Rabi Control of Semiconductor Qubits”. In: *Phys. Rev. Lett.* 132.6 (2024), p. 067001. DOI: 10.1103/PhysRevLett.132.067001.

[18] X. Zhang et al. “Universal Control of Four Singlet–Triplet Qubits”. In: *Nat. Nanotechnol.* (2024), pp. 1–7. ISSN: 1748-3395. DOI: 10.1038/s41565-024-01817-9.

[19] C.-A. Wang et al. “Operating Semiconductor Quantum Processors with Hopping Spins”. In: *Science* 385.6707 (2024), pp. 447–452. DOI: 10.1126/science.ado5915.

[20] D. V. Bulaev and D. Loss. “Electric Dipole Spin Resonance for Heavy Holes in Quantum Dots”. In: *Phys. Rev. Lett.* 98.9 (2007), p. 097202. DOI: 10.1103/PhysRevLett.98.097202.

[21] N. W. Hendrickx et al. “A Four-Qubit Germanium Quantum Processor”. In: *Nature* 591.7851 (2021), pp. 580–585. ISSN: 1476-4687. DOI: 10.1038/s41586-021-03332-6.

[22] F. N. M. Froning et al. “Ultrafast Hole Spin Qubit with Gate-Tunable Spin–Orbit Switch Functionality”. In: *Nat. Nanotechnol.* 16.3 (2021), pp. 308–312. ISSN: 1748-3395. DOI: 10.1038/s41565-020-00828-6.

[23] L. C. Camenzind et al. “A Hole Spin Qubit in a Fin Field-Effect Transistor above 4 Kelvin”. In: *Nat Electron* 5.3 (2022), pp. 178–183. ISSN: 2520-1131. DOI: 10.1038/s41928-022-00722-0.

[24] D. Jirovec et al. “A Singlet-Triplet Hole Spin Qubit in Planar Ge”. In: *Nat. Mater.* 20.8 (2021), pp. 1106–1112. ISSN: 1476-4660. DOI: 10.1038/s41563-021-01022-2.

[25] K. Wang et al. “Ultrafast Coherent Control of a Hole Spin Qubit in a Germanium Quantum Dot”. In: *Nat Commun* 13.1 (2022), p. 206. ISSN: 2041-1723. DOI: 10.1038/s41467-021-27880-7.

[26] D. Jirovec et al. “Dynamics of Hole Singlet-Triplet Qubits with Large g-Factor Differences”. In: *Phys. Rev. Lett.* 128.12 (2022), p. 126803. DOI: 10.1103/PhysRevLett.128.126803.

[27] S. D. Liles et al. “A Singlet-Triplet Hole-Spin Qubit in MOS Silicon”. In: *Nature Communications* 15.1 (2024), p. 7690. ISSN: 2041-1723. DOI: 10.1038/s41467-024-51902-9.

[28] H. Liu et al. “Ultrafast and Electrically Tunable Rabi Frequency in a Germanium Hut Wire Hole Spin Qubit”. In: *Nano Lett.* 23.9 (2023), pp. 3810–3817. ISSN: 1530-6984. DOI: 10.1021/acs.nanolett.3c00213.

[29] C. Kloeffel et al. “Circuit QED with Hole-Spin Qubits in Ge/Si Nanowire Quantum Dots”. In: *Phys. Rev. B* 88.24 (2013), p. 241405. DOI: 10.1103/PhysRevB.88.241405.

[30] P. M. Mutter and G. Burkard. “Natural Heavy-Hole Flopping Mode Qubit in Germanium”. In: *Phys. Rev. Res.* 3.1 (2021), p. 013194. DOI: 10.1103/PhysRevResearch.3.013194.

[31] S. Bosco et al. “Fully Tunable Longitudinal Spin-Photon Interactions in Si and Ge Quantum Dots”. In: *Phys. Rev. Lett.* 129.6 (2022), p. 066801. DOI: 10.1103/PhysRevLett.129.066801.

[32] V. P. Michal et al. “Tunable Hole Spin-Photon Interaction Based on g-Matrix Modulation”. In: *Phys. Rev. B* 107.4 (2023), p. L041303. DOI: 10.1103/PhysRevB.107.L041303.

[33] C. X. Yu et al. “Strong Coupling between a Photon and a Hole Spin in Silicon”. In: *Nat. Nanotechnol.* (2023), pp. 1–6. ISSN: 1748-3395. DOI: 10.1038/s41565-023-01332-3.

[34] F. De Palma et al. “Strong Hole-Photon Coupling in Planar Ge for Probing Charge Degree and Strongly Correlated States”. In: *Nat Commun* 15.1 (2024), p. 10177. ISSN: 2041-1723. DOI: 10.1038/s41467-024-54520-7.

[35] P. M. Mutter and G. Burkard. “All-Electrical Control of Hole Singlet-Triplet Spin Qubits at Low-Leakage Points”. In: *Phys. Rev. B* 104.19 (2021), p. 195421. DOI: 10.1103/PhysRevB.104.195421.

[36] S. Bosco, B. Hetényi, and D. Loss. “Hole Spin Qubits in Si FinFETs With Fully Tunable Spin-Orbit Coupling and Sweet Spots for Charge Noise”. In: *PRX Quantum* 2.1 (2021), p. 010348. DOI: 10.1103/PRXQuantum.2.010348.

[37] Z. Wang et al. “Optimal Operation Points for Ultrafast, Highly Coherent Ge Hole Spin-Orbit Qubits”. In: *npj Quantum Inf* 7.1 (2021), pp. 1–8. ISSN: 2056-6387. DOI: 10.1038/s41534-021-00386-2.

[38] S. Bosco and D. Loss. “Fully Tunable Hyperfine Interactions of Hole Spin Qubits in Si and Ge Quantum Dots”. In: *Phys. Rev. Lett.* 127.19 (2021), p. 190501. DOI: 10.1103/PhysRevLett.127.190501.

[39] N. Piot et al. “A Single Hole Spin with Enhanced Coherence in Natural Silicon”. In: *Nat. Nanotechnol.* (2022), pp. 1–6. ISSN: 1748-3395. DOI: 10.1038/s41565-022-01196-z.

[40] S. Bosco and D. Loss. “Hole Spin Qubits in Thin Curved Quantum Wells”. In: *Phys. Rev. Applied* 18.4 (2022), p. 044038. DOI: 10.1103/PhysRevApplied.18.044038.

[41] C.-A. Wang et al. “Modeling of Planar Germanium Hole Qubits in Electric and Magnetic Fields”. In: *npj Quantum Inf* 10.1 (2024), pp. 1–9. ISSN: 2056-6387. DOI: 10.1038/s41534-024-00897-8.

[42] A. Sen et al. “Classification and Magic Magnetic Field Directions for Spin-Orbit-Coupled Double Quantum Dots”. In: *Phys. Rev. B* 108.24 (2023), p. 245406. DOI: `10.1103/PhysRevB.108.245406`.

[43] M. J. Carballido et al. “Compromise-Free Scaling of Qubit Speed and Coherence”. In: *Nature Communications* 16.1 (2025), p. 7616. ISSN: 2041-1723. DOI: `10.1038/s41467-025-62614-z`.

[44] L. Mauro et al. “Geometry of the Dephasing Sweet Spots of Spin-Orbit Qubits”. In: *Phys. Rev. B* 109.15 (2024), p. 155406. DOI: `10.1103/PhysRevB.109.155406`.

[45] S. Bosco, J. Zou, and D. Loss. “High-Fidelity Spin Qubit Shuttling via Large Spin-Orbit Interactions”. In: *PRX Quantum* 5.2 (2024), p. 020353. DOI: `10.1103/PRXQuantum.5.020353`.

[46] H. Watzinger et al. “A Germanium Hole Spin Qubit”. In: *Nat Commun* 9.1 (2018), p. 3902. ISSN: 2041-1723. DOI: `10.1038/s41467-018-06418-4`.

[47] S. Bosco et al. “Phase-Driving Hole Spin Qubits”. In: *Physical Review Letters* 131.19 (2023), p. 197001. DOI: `10.1103/PhysRevLett.131.197001`.

[48] J. Saez-Mollejo et al. “Exchange Anisotropies in Microwave-Driven Singlet-Triplet Qubits”. In: *Nature Communications* 16.1 (2025), p. 3862. ISSN: 2041-1723. DOI: `10.1038/s41467-025-58969-y`.

[49] B. Undseth et al. “Nonlinear Response and Crosstalk of Electrically Driven Silicon Spin Qubits”. In: *Phys. Rev. Appl.* 19.4 (2023), p. 044078. DOI: `10.1103/PhysRevApplied.19.044078`.

[50] B. Undseth et al. “Hotter Is Easier: Unexpected Temperature Dependence of Spin Qubit Frequencies”. In: *Phys. Rev. X* 13.4 (2023), p. 041015. DOI: `10.1103/PhysRevX.13.041015`.

[51] M. Veldhorst et al. “Silicon CMOS Architecture for a Spin-Based Quantum Computer”. In: *Nature Communications* 8.1 (2017), p. 1766. ISSN: 2041-1723. DOI: `10.1038/s41467-017-01905-6`.

[52] L. M. K. Vandersypen et al. “Interfacing Spin Qubits in Quantum Dots and Donors—Hot, Dense, and Coherent”. In: *npj Quantum Information* 3.1 (2017), pp. 1–10. ISSN: 2056-6387. DOI: `10.1038/s41534-017-0038-y`.

[53] D. Bacon et al. “Universal Fault-Tolerant Quantum Computation on Decoherence-Free Subspaces”. In: *Phys. Rev. Lett.* 85.8 (2000), pp. 1758–1761. DOI: `10.1103/PhysRevLett.85.1758`.

[54] D. P. DiVincenzo et al. “Universal Quantum Computation with the Exchange Interaction”. In: *Nature (London)* 408.6810 (2000), p. 339. ISSN: 0028-0836. DOI: `10.1038/35042541`.

[55] A. Sala and J. Danon. “Exchange-Only Singlet-Only Spin Qubit”. In: *Phys. Rev. B* 95.24 (2017), p. 241303. DOI: `10.1103/PhysRevB.95.241303`.

[56] M. Russ and G. Burkard. “Three-Electron Spin Qubits”. In: *J. Phys. Condens. Matter* 29.39 (2017), p. 393001. DOI: `10.1088/1361-648X/aa761f`.

[57] S. Bosco and M. Rimbach-Russ. “Exchange-Only Spin-Orbit Qubits in Silicon and Germanium”. In: *ArXiv* arXiv:2410.05461 (2024). DOI: `10.48550/arXiv.2410.05461`. eprint: `arxiv:2410.05461`.

[58] A. J. Weinstein et al. “Universal Logic with Encoded Spin Qubits in Silicon”. In: *Nature* 615.7954 (2023), pp. 817–822. ISSN: 1476-4687. DOI: `10.1038/s41586-023-05777-3`.

[59] D. Buterakos and S. Das Sarma. “Spin-Valley Qubit Dynamics in Exchange-Coupled Silicon Quantum Dots”. In: *PRX Quantum* 2.4 (2021), p. 040358. DOI: `10.1103/PRXQuantum.2.040358`.

[60] M. Aldeghi et al. “Simulation and Measurement of Stray Fields for the Manipulation of Spin Qubits in One- and Two-Dimensional Arrays”. In: *Nano Letters* 25.5 (2025), pp. 1838–1844. ISSN: 1530-6984. DOI: `10.1021/acs.nanolett.4c05037`.

[61] D. Lidar and T. Brun. *Quantum Error Correction*. Cambridge University Press, 2013. ISBN: 978-0-521-89787-7.

[62] F. van Riggelen-Doelman et al. “Coherent Spin Qubit Shuttling through Germanium Quantum Dots”. In: *Nat Commun* 15.1 (2024), p. 5716. ISSN: 2041-1723. DOI: `10.1038/s41467-024-49358-y`.

[63] I. Seidler et al. “Conveyor-Mode Single-Electron Shuttling in Si/SiGe for a Scalable Quantum Computing Architecture”. In: *npj Quantum Inf* 8.1 (2022), pp. 1–7. ISSN: 2056-6387. DOI: `10.1038/s41534-022-00615-2`.

[64] M. De Smet et al. “High-Fidelity Single-Spin Shuttling in Silicon”. In: *Nature Nanotechnology* 20.7 (2025), pp. 866–872. ISSN: 1748-3395. DOI: `10.1038/s41565-025-01920-5`.

[65] S. Bravyi et al. “High-Threshold and Low-Overhead Fault-Tolerant Quantum Memory”. In: *Nature* 627.8005 (2024), pp. 778–782. ISSN: 1476-4687. DOI: `10.1038/s41586-024-07107-7`.

[66] B. Hetényi and J. R. Wootton. “Tailoring Quantum Error Correction to Spin Qubits”. In: *Phys. Rev. A* 109.3 (2024), p. 032433. DOI: `10.1103/PhysRevA.109.032433`.

[67] A. Abragam and B. Bleaney. *Electron Paramagnetic Resonance of Transition Ions*. Oxford Classic Texts in the Physical Sciences. Oxford: Oxford University Press, 2012. ISBN: 978-0-19-965152-8.

[68] S. Bosco et al. “Squeezed Hole Spin Qubits in Ge Quantum Dots with Ultrafast Gates at Low Power”. In: *Phys. Rev. B* 104.11 (2021), p. 115425. DOI: `10.1103/PhysRevB.104.115425`.

[69] P. Del Vecchio and O. Moutanabbir. “Light-Hole Gate-Defined Spin-Orbit Qubit”. In: *Phys. Rev. B* 107.16 (2023), p. L161406. DOI: `10.1103/PhysRevB.107.L161406`.

[70] J. C. Abadillo-Uriel et al. “Hole-Spin Driving by Strain-Induced Spin-Orbit Interactions”. In: *Phys. Rev. Lett.* 131.9 (2023), p. 097002. DOI: `10.1103/PhysRevLett.131.097002`.

[71] M. Rimbach-Russ et al. Supplemental Material. In the Supplemental Material, we report complete expressions for the effective qubit Hamiltonian including locally-varying quantum dot parameters, and the complete form of the two-qubit time-evolution operator and fildeilty discussed in the main text.

[72] B. Venitucci and Y.-M. Niquet. "Simple Model for Electrical Hole Spin Manipulation in Semiconductor Quantum Dots: Impact of Dot Material and Orientation". In: *Phys. Rev. B* 99.11 (2019), p. 115317. DOI: `10.1103/PhysRevB.99.115317`.

[73] V. P. Michal, B. Venitucci, and Y.-M. Niquet. "Longitudinal and Transverse Electric Field Manipulation of Hole Spin-Orbit Qubits in One-Dimensional Channels". In: *Phys. Rev. B* 103.4 (2021), p. 045305. DOI: `10.1103/PhysRevB.103.045305`.

[74] B. Martinez et al. "Hole Spin Manipulation in Inhomogeneous and Nonseparable Electric Fields". In: *Physical Review B* 106.23 (2022), p. 235426. DOI: `10.1103/PhysRevB.106.235426`.

[75] L. A. Terrazos et al. "Theory of Hole-Spin Qubits in Strained Germanium Quantum Dots". In: *Phys. Rev. B* 103.12 (2021), p. 125201. DOI: `10.1103/PhysRevB.103.125201`.

[76] C. Corley-Wiciak et al. "Nanoscale Mapping of the 3D Strain Tensor in a Germanium Quantum Well Hosting a Functional Spin Qubit Device". In: *ACS Appl. Mater. Interfaces* (2023). ISSN: 1944-8244. DOI: `10.1021/acsami.2c17395`.

[77] B. Martinez et al. "Hole Spin Manipulation in Inhomogeneous and Nonseparable Electric Fields". In: *Phys. Rev. B* 106.23 (2022), p. 235426. DOI: `10.1103/PhysRevB.106.235426`.

[78] P. Philippopoulos, F. Beaudoin, and P. Galy. "Analysis and 3D TCAD Simulations of Single-Qubit Control in an Industrially-Compatible FD-SOI Device". In: *Solid-State Electronics* 215 (2024), p. 108883. ISSN: 0038-1101. DOI: `10.1016/j.sse.2024.108883`.

[79] F. Martins et al. "Noise Suppression Using Symmetric Exchange Gates in Spin Qubits". In: *Phys. Rev. Lett.* 116.11 (2016), p. 116801. DOI: `10.1103/PhysRevLett.116.116801`.

[80] T.-K. Hsiao et al. "Efficient Orthogonal Control of Tunnel Couplings in a Quantum Dot Array". In: *Phys. Rev. Applied* 13.5 (2020), p. 054018. DOI: `10.1103/PhysRevApplied.13.054018`.

[81] E. G. Kelly et al. *Identifying and Mitigating Errors in Hole Spin Qubit Readout.* 2025. DOI: `10.48550/arXiv.2504.06898`. eprint: `arxiv:2504.06898`.

[82] D. Fernández-Fernández, Y. Ban, and G. Platero. "Quantum Control of Hole Spin Qubits in Double Quantum Dots". In: *Phys. Rev. Appl.* 18.5 (2022), p. 054090. DOI: `10.1103/PhysRevApplied.18.054090`.

[83] F. Fehse et al. "Generalized Fast Quasiadiabatic Population Transfer for Improved Qubit Readout, Shuttling, and Noise Mitigation". In: *Phys. Rev. B* 107.24 (2023), p. 245303. DOI: `10.1103/PhysRevB.107.245303`.

[84] C. V. Meinersen, S. Bosco, and M. Rimbach-Russ. *Quantum Geometric Protocols for Fast High-Fidelity Adiabatic State Transfer*. 2024. DOI: `10.48550/arXiv.2409.03084`. eprint: `arxiv:2409.03084`.

[85] C. V. Meinersen et al. "Unifying Adiabatic State-Transfer Protocols with (α, β)-Hypergeometries". In: *ArXiv* arXiv:2504.08031 (2025). DOI: `10.48550/arXiv.2504.08031`. eprint: `arxiv:2504.08031`.

[86] S. Geyer et al. "Anisotropic Exchange Interaction of Two Hole-Spin Qubits". In: *Nat. Phys.* 20.7 (2024), pp. 1152–1157. ISSN: 1745-2481. DOI: `10.1038/s41567-024-02481-5`.

[87] C.-A. Wang et al. "Operating semiconductor quantum processors with hopping spins". In: *Science* 385.6707 (July 2024), pp. 447–452. ISSN: 0036-8075. DOI: `10.1126/science.ado5915`. URL: `https://www.science.org/doi/10.1126/science.ado5915`.

[88] V. John et al. "Robust and localised control of a 10-spin qubit array in germanium". In: *Nature Communications* 16.1 (Nov. 2025), p. 10560. ISSN: 2041-1723. DOI: `10.1038/s41467-025-65577-3`. URL: `https://www.nature.com/articles/s41467-025-65577-3`.

[89] L. M. K. Vandersypen et al. "Interfacing spin qubits in quantum dots and donors—hot, dense, and coherent". In: *npj Quantum Information* 3.1 (Dec. 2017), p. 34. ISSN: 2056-6387. DOI: `10.1038/s41534-017-0038-y`. URL: `http://www.nature.com/articles/s41534-017-0038-y`.

10

CONCLUSION

"Da steh ich nun, ich armer Tor, und bin so klug als wie zuvor!" [1]
"And here, poor fool, I stand once more, no wiser than I was before!"

Dr. Heinrich Faust in Johann Wolfgang von Goethe's *Faust. Der Tragödie erster Teil*

It is encouraging to see the field advance, yet many scientific questions about the operation of hole spin qubits in germanium remain unresolved. A natural continuation of the current work is a systematic study of g-tensor variability as well as proof-of-concept demonstrations of extended sparse arrays and shuttling-based qubit operations. Beyond these directions, research into novel and improved qubit encodings and control schemes will become increasingly relevant and will likely delineate the roles of industrial R&D and academic groups. Industrial efforts will rather concentrate on established approaches such as single-spin qubits with microwave control and exchange-only qubits. These approaches still present significant challenges, which leaves ample space for academic research to contribute at the leading edge and to pursue more exploratory concepts.

10.1. G-TENSOR

Despite this progress, mastering the g-tensor remains one of the central obstacle to achieving truly large-scale quantum computation with germanium spin qubits. While experimental studies at scale are still missing, it appears reasonable that much of the spin qubit variability can be assigned to variability in the g-tensor [2–4]. Therefore a solid understanding of its emergence and variability are critical. Improvements in the material platform should go hand-in-hand with wafer scale g-tensor variability studies. The main barrier to such a study is the substantial overhead in qubit characterisation. A wafer scale investigation will require automated calibration and device tune-up beyond the level that is feasible today. It remains unclear to what extent the g-tensor can be predicted and matched, and it is likely to remain a major research question for the foreseeable future.

10.2. ADVANCING SCALABILITY

Scalability sits at the centre of all economic efforts toward large-scale quantum computing [5]. Yet the range of associated challenges is so broad that almost any incremental result can be framed as a step toward scalability, even when it neglects or contradicts other fundamental requirements. This risks turning the term into an empty label, invoked constantly but never truly realised. In practice, genuine scalability is a final objective relevant primarily to industry, and it is uncertain whether a fully scalable system can be engineered at economically acceptable cost. Ultimately, this question will depend on the willingness of governments, shareholders and venture capital to sustain long-term investment in the technology.

Academic research can and should address aspects of scalability, but with a clear understanding of the limitations and the specific facet being targeted. Many of these facets demand pushing far beyond what is currently feasible. It is essential to remain explicit about these limits and about how far each aspect can realistically be advanced.

On the device level, scaling challenges include g-tensor variability [2–4], noise, qubit-gate crosstalk, the number of required (individual) control lines per qubit [6], and the complexity of control pulses. On the fabrication side, the issues extend to gate pitch, routing density and the complexity of the back-end-of-line [7, 8]. Beyond fabrication lies the challenge of controlling the array itself. Current approaches rely heavily on arbitrary waveform generators and external microwave sources, which do not scale beyond small arrays. Dedicated cryo-CMOS hardware capable of handling most of the classical logic is therefore essential [8, 9]. Existing demonstrations remain limited in flexibility [10, 11], but increased industrial involvement and convergence toward a small set of architectures will facilitate further development.

Additional system-level constraints also matter, including the removal of bulky solenoid magnets [12], simplified cabling, reduced power consumption and increased refrigerator cooling power. The dominant challenge will be to address all these issues simultaneously and integrate them into a coherent and viable architecture.

10.3. GAPLESS SPIN QUBIT

After experiencing many of the challenges myself in over 4 years working in the field, the proposal of the gapless spin qubit in chapter 9 [13] constitutes a very promising direction in addressing many of the operation and scalability issues. If the encoding works as predicted, it opens up a lot of opportunities that can simplify operation and deal with variability. A first step should be to realise an experimental proof-of-concept, and evaluate the g-tensor variability across the tens of micrometre range.

10.4. SPIN QUBITS AT CROSSROADS

While the underlying physics is compelling and the ability to manipulate a single fundamental particle remains remarkable, spin qubits have reached technological crossroads. Scaling beyond few-qubit devices in an academic setting is not realistic, because academic institutions are not structured for sustained, large-scale device development that requires continuous and substantial engineering workforce. For many years, the dominant bottleneck in the field was reliable device fabrication with acceptable yields. A major shift occurred when industrial (and semi-industrial) actors such as Intel, HRL Laboratories and imec entered the field [14–16]. Intel, the most prominent example, has been active since 2015 [17]. After a decade, Intel is slowly advancing device technology to a point unreachable for academia, including the fabrication of a 12-dot linear array in a 300-mm line [14] and even larger devices shown at conferences. This progress is encouraging, yet their experimental demonstrations lag behind, particularly when compared to other quantum hardware platforms.

Similarly, after years of development, imec-based devices are beginning to show strong performance. In collaboration with imec, Diraq, an Australian quantum start-up, recently demonstrated high-fidelity operation across all relevant metrics [18]. The limitation is that the results were obtained on four double quantum dot devices, which are comparatively simple to operate and can host at most two qubits. While relevant and encouraging, this highlights a shift in the core bottleneck. As industrial fabrication improves and larger devices become available, the limiting factor is increasingly the ability to control these arrays at scale.

The next years will be critical for implementing and validating control strategies for large spin qubit systems that go significantly beyond the numbers we see today in the spin qubit community. It is exciting times seeing industrial efforts ramping up. It will be interesting to see how industrial fabs and start-ups are going to scale their operation, and how the economic landscape evolves. In particular, the emergence of Groove Quantum, which has spun out of TU Delft and is working exclusively on the Germanium platform, is exciting.

BIBLIOGRAPHY

[1] J. W. von Goethe. *Faust. Eine Tragödie.* 1st ed. 1808.

[2] B. Martinez and Y.-M. Niquet. "Variability of Electron and Hole Spin Qubits Due to Interface Roughness and Charge Traps". In: *Physical Review Applied* 17.2 (Feb. 2022), p. 024022. ISSN: 2331-7019. DOI: 10.1103/PhysRevApplied.17.024022. URL: https://link.aps.org/doi/10.1103/PhysRevApplied.17.024022.

[3] B. Martinez, S. de Franceschi, and Y.-M. Niquet. "Mitigating variability in epitaxial-heterostructure-based spin-qubit devices by optimizing gate layout". In: *Physical Review Applied* 22.2 (Aug. 2024), p. 024030. ISSN: 2331-7019. DOI: 10.1103/PhysRevApplied.22.024030. URL: https://link.aps.org/doi/10.1103/PhysRevApplied.22.024030.

[4] E. Valvo et al. "Electrically Tuneable Variability in Germanium Hole Spin Qubits". In: (Dec. 2025). URL: https://arxiv.org/abs/2512.12702v1.

[5] J. Preskill. "Quantum Computing in the NISQ era and beyond". In: *Quantum* 2 (Aug. 2018), p. 79. ISSN: 2521327X. DOI: 10.22331/q-2018-08-06-79. URL: https://quantum-journal.org/papers/q-2018-08-06-79/.

[6] D. Franke et al. "Rent's rule and extensibility in quantum computing". In: *Microprocessors and Microsystems* 67 (June 2019), pp. 1–7. ISSN: 01419331. DOI: 10.1016/j.micpro.2019.02.006. URL: https://linkinghub.elsevier.com/retrieve/pii/S014193311830293X.

[7] M. Veldhorst et al. "Silicon CMOS architecture for a spin-based quantum computer". In: *Nature Communications* 8.1 (Dec. 2017), p. 1766. ISSN: 2041-1723. DOI: 10.1038/s41467-017-01905-6. URL: http://www.nature.com/articles/s41467-017-01905-6.

[8] L. M. K. Vandersypen et al. "Interfacing Spin Qubits in Quantum Dots and Donors—Hot, Dense, and Coherent". In: *npj Quantum Information* 3.1 (2017), pp. 1–10. ISSN: 2056-6387. DOI: 10.1038/s41534-017-0038-y.

[9] E. Charbon et al. "Cryo-CMOS for quantum computing". In: *2016 IEEE International Electron Devices Meeting (IEDM)*. IEEE, Dec. 2016, pp. 1–13. ISBN: 978-1-5090-3902-9. DOI: 10.1109/IEDM.2016.7838410. URL: http://ieeexplore.ieee.org/document/7838410/.

[10] X. Xue et al. "CMOS-based cryogenic control of silicon quantum circuits". In: *Nature* 593.7858 (May 2021), pp. 205–210. ISSN: 0028-0836. DOI: 10.1038/s41586-021-03469-4. URL: https://www.nature.com/articles/s41586-021-03469-4.

[11] S. K. Bartee et al. "Spin-qubit control with a milli-kelvin CMOS chip". In: *Nature 2025 643:8071* 643.8071 (June 2025), pp. 382–387. ISSN: 1476-4687. DOI: 10.1038/s41586-025-09157-x. URL: https://www.nature.com/articles/s41586-025-09157-x.

[12] C. X. Yu et al. "Optimising germanium hole spin qubits with a room-temperature magnet". In: *arXiv* (July 2025). URL: http://arxiv.org/abs/2507.03390.

[13] M. Rimbach-Russ et al. "Gapless Single-Spin Qubit". In: *Physical Review Letters* 135.19 (Nov. 2025), p. 197001. ISSN: 0031-9007. DOI: 10.1103/mvtj-zhrl. URL: https://link.aps.org/doi/10.1103/mvtj-zhrl.

[14] H. C. George et al. "12-Spin-Qubit Arrays Fabricated on a 300 mm Semiconductor Manufacturing Line". In: *Nano Letters* 25.2 (Jan. 2025), pp. 793–799. ISSN: 1530-6984. DOI: 10.1021/acs.nanolett.4c05205. URL: https://pubs.acs.org/doi/10.1021/acs.nanolett.4c05205.

[15] W. Ha et al. "A Flexible Design Platform for Si/SiGe Exchange-Only Qubits with Low Disorder". In: *Nano Letters* 22.3 (Feb. 2022), pp. 1443–1448. ISSN: 1530-6984. DOI: 10.1021/acs.nanolett.1c03026. URL: https://doi.org/10.1021/acs.nanolett.1c03026.

[16] A. Elsayed et al. *Low Charge Noise Quantum Dots with Industrial CMOS Manufacturing*. 2022. DOI: 10.48550/arXiv.2212.06464. eprint: arxiv:2212.06464.

[17] Intel. *Intel Invests US$50 Million to Advance Quantum Computing*. Sept. 2015. URL: https://www.intc.com/news-events/press-releases/detail/316/intel-invests-us50-million-to-advance-quantum-computing.

[18] P. Steinacker et al. "Industry-compatible silicon spin-qubit unit cells exceeding 99% fidelity". In: *Nature 2025 646:8083* 646.8083 (Sept. 2025), pp. 81–87. ISSN: 1476-4687. DOI: 10.1038/s41586-025-09531-9. URL: https://www.nature.com/articles/s41586-025-09531-9.

SUMMARY

Is spin-orbit coupling a blessing or a curse? For the operation of spin qubits, the answer to this seemingly simple question is far from obvious. It provides convenient control mechanisms that are difficult to predict with precision, which leaves it unclear whether s-type electrons or p-type holes offer a simpler route to engineering quantum processing units.

At the start of my PhD, holes in germanium had only just established themselves as a promising alternative to electrons in silicon [1–5]. Prior experiments demonstrated that proof-of-principle quantum processors are feasible in germanium heterostructures, showing that spin-orbit interactions are not detrimental to device performance but can even be an important asset. While the potential of germanium quantum devices was clear, a pathway for scaling them up and a solid physical understanding of their behaviour were still missing.

Subsequent theoretical work [6–9] and experimental progress [10–13], including chapter 6, 7 and 9 of this thesis, have substantially advanced our understanding of hole spin qubit devices in germanium. The concept of spin quantisation axes has proved particularly effective in interpreting shuttle-induced dynamics and relating the g-tensor to spin evolution. This enabled hopping-based, high-fidelity single-qubit gates and the exploration of a ten-qubit array in chapter 6. In chapter 7, we tuned a ten-qubit array across several charge configurations, identified their driving mechanisms, and found promising operation points that support more reliable and local control at scale. Improved insight into the g-tensor also opened pathways to new qubit encodings and manipulation schemes, one of which is presented in chapter 9. Additional side gates shape the wave function and thereby tune the g-tensor, enabling access to distinct operation regimes. Experimental validation is ongoing.

Motivated by scalability challenges in large arrays, chapter 4 examines bichromatic driving, where two microwave signals applied to orthogonal lines locally mix to drive the qubit. This operation scheme is specifically designed for architectures with shared control lines. In chapter 5, a unit cell of such a shared control architecture has successfully been realised by showcasing the charge tune-up of a quantum dot array with shared control lines. While we brought the full array into the odd-charge configuration for the first time, device variability prevented progress toward qubit operation. In chapter 8, we explored qubit performance using an external magnet placed outside the dilution refrigerator. Despite the initially counter-intuitive idea of operating highly anisotropic spin qubits with a permanent magnet, we show that sufficient in- and out-of-plane tunability exists to reach favourable operating regimes, improve coherence times, and simplify system hardware.

In summary, we have demonstrated that spin-orbit coupling enables a wide range of opportunities for high-fidelity qubit control, from hopping-based gates to g-tensor engineering. We advanced germanium spin qubit devices from four-qubit systems to a ten-qubit array, while also identifying and applying strategies to further enhance scalability. Germanium hole spin qubits controlled through intrinsic spin-orbit interaction remain at the forefront of scientific and technological advancement in the field of semiconductor-based quantum processing units.

SAMENVATTING

Is spin-baan-koppeling een zegen of een vloek? Voor de werking van spinqubits is het antwoord op deze schijnbaar eenvoudige vraag allesbehalve duidelijk. Spin-baan-koppeling biedt handige controlemogelijkheden die moeilijk nauwkeurig te voorspellen zijn, waardoor onduidelijk blijft of s-type elektronen of p-type gaten een eenvoudigere route vormen voor het ontwikkelen van kwantumprocessoreenheden.

Aan het begin van mijn PhD hadden gaten in germanium zich nog maar net gevestigd als een veelbelovend alternatief voor elektronen in silicium [1–5]. Eerdere experimenten toonden aan dat proof-of-principle kwantumprocessors haalbaar zijn in germaniumheterostructuren en dat spin-baan-interacties niet schadelijk zijn voor de apparaatprestaties, maar juist een belangrijk voordeel kunnen bieden. Hoewel het potentieel van germaniumkwantumapparaten duidelijk was, ontbraken een opschaalbare route en een solide fysisch begrip van hun gedrag.

Vervolgwerk op theoretisch gebied [6–9] en experimentele vooruitgang [10–13], waaronder chapter 6, 7 en 9 van dit proefschrift, hebben ons begrip van gatenspinqubits in germanium aanzienlijk verdiept. Het concept van spin-kwantisatieassen bleek bijzonder effectief voor het verklaren van shuttle-geïnduceerde dynamica en het koppelen van de g-tensor aan spin evolutie. Dit maakte hopping-gebaseerde, hoog-fideliteit enkelqubitpoorten mogelijk en de verkenning van een tienqubitaray in chapter 6. In chapter 7 stemden we een tienqubitaray af over meerdere ladingsconfiguraties, identificeerden we hun aandrijfmechanismen en vonden we gunstige werkpunten die betrouwbaardere en lokaal schaalbare controle ondersteunen. Verbeterd inzicht in de g-tensor opende ook nieuwe routes naar qubit-encoderingen en manipulatieschema's, waarvan er een wordt gepresenteerd in chapter 9. Extra zijgates vormen de golffunctie en stemmen daarmee de g-tensor af, wat toegang geeft tot verschillende werkregimes. Experimentele validatie is nog aan de gang.

Gemotiveerd door schaalbaarheidsuitdagingen in grote arrays onderzoekt chapter 4 bichromatische aandrijving, waarbij twee microgolfsignalen op orthogonale lijnen lokaal mengen om de qubit aan te sturen. Dit schema is specifiek ontworpen voor architecturen met gedeelde controllijnen. In chapter 5 is een eenheidscel van zo'n gedeelde-controlearchitectuur succesvol gerealiseerd door de ladingsafstemming van een quantumdotarray met gedeelde controllijnen te demonstreren. Hoewel we de volledige array voor het eerst in de oneven-ladingsconfiguratie brachten, verhinderde apparaatvariabiliteit verdere vooruitgang richting qubitwerking. In chapter 8 onderzochten we qubitprestaties met een externe magneet buiten de verdunningskoelkast. Ondanks het op het eerste gezicht contra-intuïtieve idee om sterk anisotrope spinqubits met een permanente magneet te bedienen, laten we zien dat er voldoende instelbaarheid in en uit het vlak bestaat om gunstige werkregimes te bereiken, de coherentie te verbeteren en de systeemhardware te vereenvoudigen.

Samengevat hebben we aangetoond dat spin-baan-koppeling een breed scala aan mogelijkheden biedt voor hoog-fideliteit qubitcontrole, van hopping-gebaseerde poorten tot g-tensor-engineering. We hebben germaniumspinqubits ontwikkeld van vierqubitsystemen tot een array van tien qubits, terwijl we ook strategieën hebben geïdentificeerd en toegepast om de schaalbaarheid verder te vergroten. Germanium gatenspinqubits die worden aangestuurd via intrinsieke spin-baan-interactie blijven de voorhoede vormen van wetenschappelijke en technologische vooruitgang op het gebied van halfgeleidergebaseerde kwantumprocessoreenheden.

DATA AVAILABILITY

The PhD thesis is accompanied by a research data collection published on the 4TU platform under the following DOI: 10.4121/cc3cb254-6a92-4776-8117-cbfec2604212.v1. It links to the accompanying research data and underlying code of each chapter. The corresponding datasets are also given in the following table.

Chapter	Repository DOI
4	10.4121/bb43fe1d-f503-49e8-9f17-ce7d734f015d
5	10.5281/zenodo.8083119
6	10.4121/158ba07a-4375-4c17-bf7b-289726f5452a
7	10.4121/5ee5b0d3-e838-478e-990d-02c50b75eeab
8	10.4121/eb6053c1-e70c-401c-914e-576e612869a5
9	10.5281/zenodo.17137077

Table 10.1: The data repositories of individual chapters.

EDITORIAL METHODS

This PhD thesis has been edited using generative AI tools such as ChatGPT following the editorial policies of Springer Nature as in place in December 2025 (see `https://www.nature.com/nature-portfolio/editorial-policies/ai`).

ACKNOWLEDGEMENTS

After finishing my master's degree, I joined QuTech in autumn 2021. What can I say, I could have never imagined what a great time I would have here, not only scientifically but also with the people I would meet. It is difficult to fully express my gratitude, as I consider my PhD years the best period of my life, one that I will treasure in my memories forever. With so many people to acknowledge, I have probably forgotten some. If you do not find yourself mentioned in this section, it is likely a mistake and I can write a personal acknowledgement by hand into your hard copy.

At the centre of my time at QuTech has of course been you, **Menno**. I could not have imagined a better and more suitable promoter for my research. I still remember our very first online interview, after which I had to decide whether to decline another excellent PhD offer from imec. I had a good feeling about you from the beginning and have never been disappointed. On the contrary, I felt that our relationship improved steadily once I shed my initial shyness and treated you as an almost equal. I think we had a lot of fun together and I appreciate your humour. Besides our personal connection, you are a great scientist and group leader. It is rare to have someone so supportive and full of visionary ideas, who builds environments in which these ideas can flourish. At the same time, you give protégés the freedom to interpret those ideas in their own way and to find their own place. f I had to give one piece of advice to future generations on how to interact with you, it would be to be direct and above all, to be themselves, however foolish that may be at times. The reason the term 'Mennomagnet' stuck for the external magnet is not only your refusal to get us a vector magnet, but also a reflection of the affection the group has for you. This was perhaps best demonstrated by how uncomfortable the nickname made you and by your unsuccessful attempts to change it. I am sad to leave your group, but perhaps the term Mennomagnet will stick around and remind you of the time we had together. The same applies of course to our unofficial group name 'Mennoknights'. I will surely always stay a Mennoknight at heart!

I also want to acknowledge my second promoter, **Giordano**. I was very happy to be able to conduct all my experiments in collaboration with you and to first explore qubits on germanium heterostructures grown on the freshly available germanium substrates. I have always enjoyed our encounters over lunch and highly appreciate your genuine and honest opinions.

The three people I worked most closely with during my PhD were all postdocs. This has made me somewhat notorious for only "hiring" postdocs. Naturally, this comes with the risk of remaining the junior researcher throughout, but I believe I managed quite well to establish myself as a senior researcher within the projects I worked on. But then again, who am I to judge?

Upon arrival in the group, I was assigned to the project that was led by **Francesco**. I could not have been luckier. You taught me everything I needed on a daily basis to succeed in academia. In every aspect you were an example for me, and I always strived to follow your lead. I remember our joint struggles at the beginning of my PhD, with endless days dealing with the shared control of the 4x4, and designing and debugging the early faulty 3-4-3 devices with the unreliable dipstick. Even once we moved past device development, it still took months to get the first qubit because we did not expect the g factors to be so extraordinarily small. Of all people I have met, you were the best at tuning away charge noise. Without doubt, our time together laid the foundation for all experiments conducted with the 3-4-3, and it is your credit that the device features in many other publications. Outside the lab, you introduced me to the Quantum Warriors football team. I have many good memories cycling together to X and playing matches every Monday. Even there I strived to follow you by taking over the captain's band after you left to become a PI in Copenhagen. I am certain you will succeed and develop your own research line. You are a born leader and supervisor, but most importantly a great person.

Cécile, it is quite remarkable to reflect on the time we spent together over the past three years. Neither of us could have predicted how things would develop when we first met at CEA Grenoble. Back then, I was still shy and inexperienced, and my limited French meant that our working relationship and friendship truly began only once you came to Delft. What started by chance soon grew into a strong professional collaboration and a genuine friendship. Eventually, we have done all the measurements on the 3-4-3 array together. Even during my "PhD puberty" and stubborn phases, you handled me remarkably well, and it has always been a pleasure working with you. You are reliable, flexible, and exceptionally good at complementing others, which makes you the kind of missing link every team hopes to have. While you had to endure my directness, irony, and humour in full swing every single day, we always had plenty to joke and laugh about. I am also proud that some of my character traits seem to have, at least partially, rubbed off on you. Of course, it is still unheard that you had to wake me up the day of my presentation at SiQEW in Davos because I was sleeping with earplugs (we remain silent why I needed them in the first place). Outside the lab, you have grown into a true friend and I enjoyed all the times we met up. You are the person I trusted most and with whom I always felt welcome. Stay the way you are and I look forward to staying in touch for many years to come.

Lastly, to complete the golden trio there is **Barnaby**, or shall I rather call you Barnasheep? Despite trying I feel like I have never really teased you since you rather seem to enjoy it. You are a character impossible to forget: clever, funny and a bit dispersed. All ingredients to become either a genius or a supervillain. I hope you choose the good path. It was a pleasure working with you and you have given me great confidence in the gapless spin qubit. I was glad to share my excitement and have you join the project. Whenever you could not answer a theory question, I knew it was at the right level to ask our theorists. While some of your stories were too much for me and nearly made me faint, I cannot deny your talent for storytelling. You are a crazy and amiable person I have always enjoyed being around. I have always appreciated your advice despite you being a yes man, however, you have clearly shown that you can transform from Barnasheep to Barnasteel under certain circumstances! Outside the lab, I loved our bike rides. Under equal circumstances, you are slightly stronger, but I can compensate with more consistency and preparation. I hope we can still go on bike rides and perhaps even a proper bikepacking trip in the future even though our ways part. Stay true to who you are!

Corentin, you have been around me the longest, though technically we never worked on the same project. It does not feel that way since you were always rushing through the lab and helping wherever needed. You were truly the beating heart of the lab, always making sure everyone got along. I enjoyed our lunch conversations and the bike rides we did together. It was great sharing so much time with you and I wish you all the best for the future. **Sasha**, or should I call you Minnimenno? Nobody would deserve that title more. You combine all the attributes of a future successful researcher: smart, pragmatic, optimistic, visionary and team oriented. Seeing your progress throughout your PhD has been inspiring. Stay the way you are personally, while your professional path is essentially pre determined. I have enjoyed all our interactions and our trip to Budapest. I look forward to hearing from you in the future. **Chien-An** is a true legend. You have likely been the smartest person I worked with during my PhD, naturally spanning theory and experiment. Yet you remained down to earth and helpful to everyone you interacted with. This ability to complement anyone you work with is truly special. It was great to visit multiple conferences together and share accommodation almost every time. We could enjoy Kyoto for SiQEW and suffer together in Las Vegas at APS march meeting. It was an honour to be your paranymph during your defence. Stay true to yourself and find an environment that lets you flourish. I would have never guessed that you, **Damien**, would eventually become my heir to the fridge and project. I cannot deny that you surprised me. I did not know what to expect from you, but all doubt vanished once you joined and we started working together. You bring an excellent balance of professionalism and foolishness, which I greatly enjoyed, including during our trip to the ARO meeting in Boston. Keep the flag of the gapless spin qubit up in the years to come. It is surprising that **Marion** and I have (kind of) known each other for five years due to my time at CEA Grenoble. However, it is only since you joined us in Delft that we truly got to know one another. There are few people I have enjoyed being around as much as you (even though it is hard to pin down why). I have truly enjoyed all our lunch and coffee conversations, as well as our time in Budapest.

I hardly need to mention it, since everyone knows it by now, but I will say it anyway: **Sander** is the hero of the lab. You are incredibly easy to work with, regardless of whether someone is a fresh PhD candidate or an experienced postdoc. Your contributions to software development and debugging measurement setups set us apart from nearly all other labs. I was very lucky to have your support throughout my PhD. Another thing that sets us apart from other labs are our fabrication engineers. At the beginning I collaborated closely with **Stefan**. Looking back, it was an enormous ride we took together. Seven generations of 3-4-3 devices, with countless things to debug on both sides. We can be proud that we managed to get where we are now. This is in large part thanks to you. In my final year, **Setareh** stepped up the fabrication and kept things moving despite many odds working against her. I am excited to finally see the device you fabricated being measured. You did great and I am sure you will leave a lasting fingerprint on the group. I have enjoyed all our chats and I still hope that someday I can make the Ghormeh Sabzi for you! Another group of people that makes QuTech a special place are our technicians and **DEMO**. Special thanks goes to **Jason** and **Olaf**, who have supported me in several ways from device bonding to fridge operation. Thanks for always leaving the door open for us!

I had the pleasure to work with plenty of theorists during my PhD, internally and externally. From Budapest I want to acknowledge **Zoltán**, **Gabor** and **András**, with whom I collaborated for the bichromatic paper. Back than **Zoltán** was only a Bachelor student, but your work was already very advanced. I have been quite impressed with you! Now I wish you all best for your PhD in Basel. From CEA Grenoble I want to acknowledge **Esteban**, **Mauro** and **Yann-Michel**, with whom I collaborated on the ten-qubit work, but also **José** and **Biel**, with whom I have had great discussions along the way. I very much enjoyed your ability to give descriptive pictures of the theory at play. In general, your theory papers have been one of the most useful ones to better understand the hole spin qubit physics. Lastly, I still have to acknowledge **Max** and **Stefano**, who have established a theoretical base for multiple research projects that I have been part of. There is nothing more powerful than the case, when our experimental research efforts align with your theoretical understanding. I have enjoyed all our collaborations and I am particularly excited about how our GS2 qubit is going to unfold!

Floor, I enjoyed working with you during my early projects. Your advocacy for equality and fairness made a genuine impact and its legacy still remains within the group. **Marcel**, I enjoyed our small trip to the Grand Canyon. I am still amused that we saw tumbleweed rolling across the street while driving on Route 66. What could I possibly say about you, **Hanifa**. You are a special and funny person. I am sure you will find an exciting place for yourself. The person who can make the most adorable puppy face is undoubtedly **Dario**. It makes it hard to be mad at you but very tempting to tease you. I am sorry for triggering you at every possible occasion, but I could not resist. I always enjoyed going shopping and relaxing with you in Den Haag. I must have seen **Zarije** wandering around QuTech as a master student already early in my PhD, though you only joined us late in my PhD, but gladly so. You are a characterful and funny person and I genuinely enjoyed all the time we spent together. Despite our short time together, **Pietro**, I enjoyed being around you from day one and joking with you. I am sure you will have a great time ahead! Also **Harold**, **Alice** and **Naoual** joined recently. All of you had a great start and I am certain you will develop very well during your time here. There were many more Mennoknights with whom I had great interactions. Thanks to **Michael**, **Job** and **Will**.

Outside the Mennoknights, the person with the biggest impact on me has been **Yuta**. Our two weeks together in Japan created a bond that cannot be easily broken. I cannot sufficiently express my gratitude towards you. I experienced you as an incredibly warm, genuine and funny host. I will never forget our fancy dinners, research visits and onsen visits. I loved our time together and it is sad that we part rather than re-unite in Tokyo. I admire your scientific creativity and I am certain the world is open for you to conquer. For more than four years, **Maxim**, **Liza** and I have been office mates during almost the entire PhD. I enjoyed being around you very much and it was great to have occasional talks throughout the working day, and grow together side-by-side. **Brennan** completes our year of PhDs. I always admired your completeness. I feel like there is nothing you are not good at while staying fully down to earth. My go to expert for the semiconductor industry has always been **Asser**. Us having completed the same master programme gives a bond and intrinsic level of trust. I greatly value your judgement. **Pablo**, I always enjoyed your positivity and the energy you bring. It never gets boring with you! One of the funniest people I have been around was **Daniel**. I loved joking with you about all kinds of things and I also valued your scientific and personal advice. You have very much enhanced the atmosphere at QuTech! **Kenji** is another funny person I have to admit. I think one always has a good time when being around you! Also great that you have joined the Quantum Warriors! **Karina**, I enjoyed all our lunch encounters and I am glad that I could pass in my apartment to you. I am certain you will enjoy it as much as me. Most experiments I conducted relied on material grown by **Lucas**. You are without a doubt one of the most likeable and easy to work with people I encountered during my PhD. It has been great to see the spin qubit theorist groups grow over the last few years and I have to admit that they are almost as cool as the experimentalists. In particular **Edmondo** and **Chris**, the 'Social Maxists', who are noisy on one hand but funny and knowledgeable on the other. I enjoyed our scientific discussions and your foolishness. While technically not a Social Maxist, **Michèle** is undoubtedly on equal footing with them. I wish you all the luck in the world dealing with their unmatched energy, both for the good and for the bad. I also want to thank the remaining theorists **Patrick**, **Tess**, **Daniel** and **Minh** for the occasional chats that always brought new perspectives. In the last year, many people left and joined the spin qubit groups in Delft. With many of you I had great conversations and I am certain you will push the research far beyond what was achieved during my PhD. Thanks and good luck in the coming years to **Parsa**, **Nicola**, **Marcin**, **Stefano**, **Jaime**, **Elia**, **Yi-Hsien**, **Noah**, **Sam**, **Tobias** and **Vlad**. From those who left some time ago and with whom I interacted during the early stages of my PhD, I want to thank **Tzu Kan**, **Stephan**, **Oriol**, **Xiao** and **Alberto**. I also had the pleasure to interact with many more spin qubit colleagues and shared a significant time at QuTech with **Xin**, **Irene**, **Eline**, **Jurgen**, **Desa**, **Fede** and **Davide**. With **Florian** I had a great time in Boston and New York, where we accidentally shared the smallest possible hotel room one can imagine. Also with **Nico**, with whom I formally did not have any overlap, I have had several interactions and enjoyed our chats. Together with **Anne Marije**, I wish you all the best and success with Groove!

I also want to thank all my committee members for taking the time to read and evaluate my thesis: **Michael**, **Kristiaan**, **Natalia**, and **Dohun**! Next to being on my committe, **Lieven** has been a great coworker! I have enjoyed all our encounters and chats over lunch, and I appreciate that you are always open to discuss with anyone. We owe you the remarkable spin qubit eco-system that has formed around here in Delft and a great general work environment!

Even though spin qubits are obviously the centre of the universe, it turns out that there are indeed people working on other platforms as well. The person I have known the longest at QuTech is not a spin qubit person but a superconducting one: **Santi**. We met in 2018 during our Erasmus exchange year at Durham University. I never expected that our paths would cross again here in Delft, but they did. It was great to meet and chat occasionally and I would not be surprised if our paths cross once again. Even though we know each other for a much shorter time relatively, I likewise enjoy the company of **Ruggero** Together you make a great duo to hang around with!. Who would have thought there is life outside the QuTech bubble here in Delft. I very much enjoyed biking with **Baptiste**. Together with **Barnaby** we have formed an extraordinary trio, and it was a lot of fun every time we went on a ride or met with **Cécile**. I am still annoyed that I crashed the same way as you did, just a few months later, so I am afraid I am not any better than you. Particularly in the beginning I also enjoyed playing futsal at X with **Farzad**, and for three years I have been part of **Capoeira Mar Estradeiro** under the guidance of **contramestre Filósofo** in Den Haag. I have enjoyed playing Capoeira with you every week.

During my four years at QuTech, one of my favourite activities has been playing football with the **Quantum Warriors** in the TU Delft Monday league. I have countless memorable moments from my time with you. I was first introduced to the Quantum Warriors by **Francesco**, and soon after I was allowed to join the team permanently. After being captain myself, **Vincent** has become the new captain at the dawn of my departure. Hardly anyone has experienced such a great evolution since their start in our team. I also want to acknowledge **Gustavo**, who has invested enormous energy in building up the team over several years. Without you, the team would not exist in its current form. You are also an excellent central defender and leader. The most reliable and long-serving player has been **Alberto**. You are one of the most likeable people I have ever met and a strong, versatile all-rounder on the pitch. Our best player in recent years has likely been **Ema**, who has carried the team through difficult games with remarkable ball control and agility. You are challenged only by our little **Maroto**, who was always talking too much. For three years, our go-to striker was **Thijs**, one of my favourite players to play with. I always had the feeling that we understood each other blindly, knowing exactly what the other would do. It was a pleasure to play with you. On the wing, **Bas** has been a machine that runs tirelessly up and down the line. We could always rely on you. There are many more players who have shaped the Quantum Warriors over the last couple of years. I want to acknowledge in chronological order **Michael**, **Chris**, **Mark**, **Stefano**, **Sjoerd**, **Jorge**, **Fabrizio**, **João** , **Tom**, **Leo**, **Jared**, **Mattia**, **Marius**, **Rouven** and **Kenji**. I have not just enjoyed playing with all of the Quantum Warriors, but also enjoyed our joint post-game analyses at X, watching games together, and playing beach volley or football tennis together. Being with you in a team has made a big impact on me!

Next to the people I met during my time in Delft, there are also many from earlier stages of my life who had a significant influence on where I eventually ended up. From early on I was interested in exploring the world. The two most important people who strengthened my desire to be in an international environment are **Filipe**, whom I met during an exchange period in Brazil when I was fourteen, and **Kirill**, whose buddy I was while he was doing an exchange in Hamburg. Largely due to my experiences with both of you, as well as my subsequent exchange year at Durham University, I wanted to pursue an international career. This led me to the EMM Nano master programme, which connected me with many bright international minds and shaped the path that eventually brought me to QuTech. Thanks in particular to **Roozbeh** and **Stacy**. I hope I managed to convey my enthusiasm for Delft when you were visiting. During an educational journey one often relies on the support and endorsement of senior researchers when applying for scholarships or admission to a programme or research group. This was no different for me, and I want to acknowledge all those who believed in me, supported me and endorsed me. This includes my high school mathematics teacher **Friedrich**; my supervisors **Andy**, **Przemek**, **Christian** and **Ivan** when I was working on organic light emitting diodes at Durham University and Universidade Federal de Santa Catarina; my supervisors **Alex** and **Albert** during my project and internship on semiconductor devices at imec. I also want to thank **Romain** and **Simon**, from CEA Grenoble, who have first introduced me into the field of spin qubits during my PhD. The direct and indirect support of all of you has helped shape my career. I am happy with every decision I have taken along the way and proud of how things have unfolded. Thanks for your support!

Zuallerletzt möchte ich meiner Familie für ihre unerschütterliche Unterstützung danken. **Mama** und **Papa**, ihr habt mich in all meinen Entscheidungen stets bestärkt. Ohne euch wäre es deutlich schwieriger gewesen, meinen heutigen Karriereweg einzuschlagen. Ich weiß, dass ich mich im Zweifel immer auf euch verlassen kann, egal wo auf der Welt ich mich befinde. Besonders schätze ich, dass ihr mich immer ermutigt habt, Neues auszuprobieren und andere Länder zu erkunden, nicht nur innerhalb Europas, sondern auch darüber hinaus. Mein häufigster Besucher hier in Delft war natürlich meine Schwester **Marina**. Es macht immer Spaß, wenn du da bist, egal ob wir gemeinsam shoppen gehen oder an den Strand fahren. Ich wünschte, wir könnten uns häufiger sehen. Auch möchte ich meiner Halbschwester **Melanie** danken, deren Ratschläge zur Uni ich mir immer zu Herzen genommen habe. Ich bin sehr glücklich, dass im Frühling **Opa Manfred** zu Besuch war und ich ihm das Labor zeigen konnte. Dein Interesse an meiner Arbeit und deine Wissbegier beeindruckt mich. Ich erinnere mich noch gut daran, wie ich dir erklärte, dass unsere Qubits noch nicht sehr gut sind, und du meintest, man könne dann mehrere Qubits nutzen, um dieselbe Information zu speichern. Genau dies ist die Grundlage von Fehlerkorrekturcodes, und du hast es verstanden, bevor ich es selbst erwähnt hatte. Als ehemaliger Finanzbeamter ist das bemerkenswert. Zum Schluss möchte ich noch meinem besten Freund **Daniel** danken. Wir kennen uns seit der Grundschule, und obwohl sich unsere Wege später trennten, sind wir immer in Kontakt geblieben. Seit Beginn meiner Promotion in Delft sind wir gemeinsam über 2000 Kilometer mit dem Rad gefahren. Im ersten Jahr ging es von Hamburg nach Delft, im zweiten Jahr von Delft entlang der Küste bis nach Amiens, im dritten Jahr auf eine Skandinavienrunde durch Norwegen, Schweden und Dänemark, und im letzten Jahr auf die Spanienrunde durch die Sierra Nevada. Ich habe jede unserer Touren genossen. Mit Sicherheit kann ich sagen, dass sich unsere Bikepacking-Fähigkeiten genauso weiterentwickelt haben wie meine Forschung. Wir waren ziemliche Anfänger auf unserer ersten Tour mit Rädern, die alles andere als ideal waren. Das größte Highlight war natürlich, wie wir gemeinsam den Pico del Veleta auf 3.385 Metern Höhe erklommen haben. Besser lässt sich unsere Freundschaft und der steinige Weg der Promotion kaum beschreiben.

CURRICULUM VITÆ

Valentin JOHN

19-02-1997	Born in Bad Honnef, Germany.

EDUCATION

2007–2015	Grammar School Johanneum Lüneburg, Germany
2015–2019	BSc Physics Universität Hamburg, Germany (2015–2019) Erasmus Exchange at Durham University, United Kingdom (2017–2018) *Bachelor Thesis:* Study of TADF OLED Photophysics *Supervisor:* dr. Przemyslaw Data *Promotor:* prof. dr. Andrew Monkman
2019–2021	MSc Nanoscience and Nanotechnology Katholieke Universiteit Leuven, Belgium (2019–2020) Université Grenoble Alpes, France (2020–2021) *Master Thesis:* Circuit Quantum Electrodynamics with Silicon Hole Spin Qubits *Supervisor:* dr. Simon Zihlmann *Promotor:* dr. Romain Maurand
2021–2026	PhD Applied Physics Technische Universiteit Delft, The Netherlands *PhD Thesis:* Spin-Orbit Control of Spin Qubits in Germanium *Promotors:* prof. dr. ir. Menno Veldhorst dr. Giordano Scappucci

LIST OF PUBLICATIONS

10. *Optimising germanium hole spin qubits with a room-temperature magnet*
    Cecile X. Yu, Barnaby van Straaten, Alexander S. Ivlev, **Valentin John**, Stefan D. Oosterhout, Lucas E. A. Stehouwer, Francesco Borsoi, Giordano Scappucci, Menno Veldhorst
    arXiv:2507.03390 (2025)

9. *Towards autonomous time-calibration of large quantum-dot devices: Detection, real-time feedback, and noise spectroscopy*
    Anantha S. Rao, Barnaby van Straaten, **Valentin John**, Cécile X. Yu, Stefan D. Oosterhout, Lucas Stehouwer, Giordano Scappucci, M. D. Stewart Jr., Menno Veldhorst, Francesco Borsoi, Justyna P. Zwolak
    arXiv:2512.24894 (2025)

8. *Robust and localised control of a 10-spin qubit array in germanium*
    Valentin John$^{\hat{*}}$, Cécile X Yu$^{\hat{*}}$, Barnaby van Straaten, Esteban A Rodríguez-Mena, Mauricio Rodríguez, Stefan Oosterhout, Lucas EA Stehouwer, Giordano Scappucci, Stefano Bosco, Maximilian Rimbach-Russ, Francesco Borsoi, Yann-Michel Niquet, Menno Veldhorst
    Nat Commun 16, 10560 (2025)

7. *Gapless Single-Spin Qubit*
    Maximilian Rimbach-Russ, **Valentin John**, Barnaby van Straaten, Stefano Bosco
    Phys. Rev. Lett. 135, 197001 (2025)

6. *Modular Autonomous Virtualization System for Two-Dimensional Semiconductor Quantum Dot Arrays*
    Anantha S Rao, Donovan Buterakos, Barnaby van Straaten, **Valentin John**, Cécile X Yu, Stefan D Oosterhout, Lucas Stehouwer, Giordano Scappucci, Menno Veldhorst, Francesco Borsoi, Justyna P Zwolak
    Phys. Rev. X 15, 021034 (2025)

5. *Exploiting strained epitaxial germanium for scaling low-noise spin qubits at the micrometre scale*
    Lucas EA Stehouwer, Cécile X Yu, Barnaby van Straaten, Alberto Tosato, **Valentin John**, Davide Degli Esposti, Asser Elsayed, Davide Costa, Stefan D Oosterhout, Nico W Hendrickx, Menno Veldhorst, Francesco Borsoi, Giordano Scappucci
    Nat. Mater. 24, 1906–1912 (2025)

4. *Operating semiconductor quantum processors with hopping spins*
    Chien-An Wang, **Valentin John**, Hanifa Tidjani, Cécile X Yu, Alexander S Ivlev, Corentin Déprez, Floor van Riggelen-Doelman, Benjamin D Woods, Nico W Hendrickx, William IL Lawrie, Lucas EA Stehouwer, Stefan D Oosterhout, Amir Sammak, Mark Friesen, Giordano Scappucci, Sander L de Snoo, Maximilian Rimbach-Russ, Francesco Borsoi, Menno Veldhorst
    Science 385, 447-452 (2024)

3. *Bichromatic Rabi control of semiconductor spin qubits,*
   Valentin John$^{\hat{*}}$, Francesco Borsoi$^{\hat{*}}$, Zoltán György$^{\hat{*}}$, Chien-An Wang, Gábor Széchenyi, Floor van Riggelen-Doelman, William IL Lawrie, Nico W Hendrickx, Amir Sammak, Giordano Scappucci, András Pályi, Menno Veldhorst,
   Phys. Rev. Lett. 132, 067001 (2024)

2. *Shared control of a 16 semiconductor quantum dot crossbar array*
   Francesco Borsoi, Nico W Hendrickx, **Valentin John**, Marcel Meyer, Sayr Motz, Floor Van Riggelen, Amir Sammak, Sander L De Snoo, Giordano Scappucci, Menno Veldhorst
   Nat. Nanotechnol. 19, 21–27 (2024)

1. *Temperature Dependent Mismatch and Variability in a Cryo-CMOS Array with 30k Transistors,*
   Alexander Grill$^{\hat{*}}$, **Valentin John**$^{\hat{*}}$, Jakob Michl, Arnout Beckers , Erik Bury , Stanislav Tyaginov, Bertrand Parvais, Adrian Vaisman Chasin, Tibor Grasser, Michael Waltl, Ben Kaczer, Bogdan Govoreanu,
   IEEE International Reliability Physics Symposium (2022)

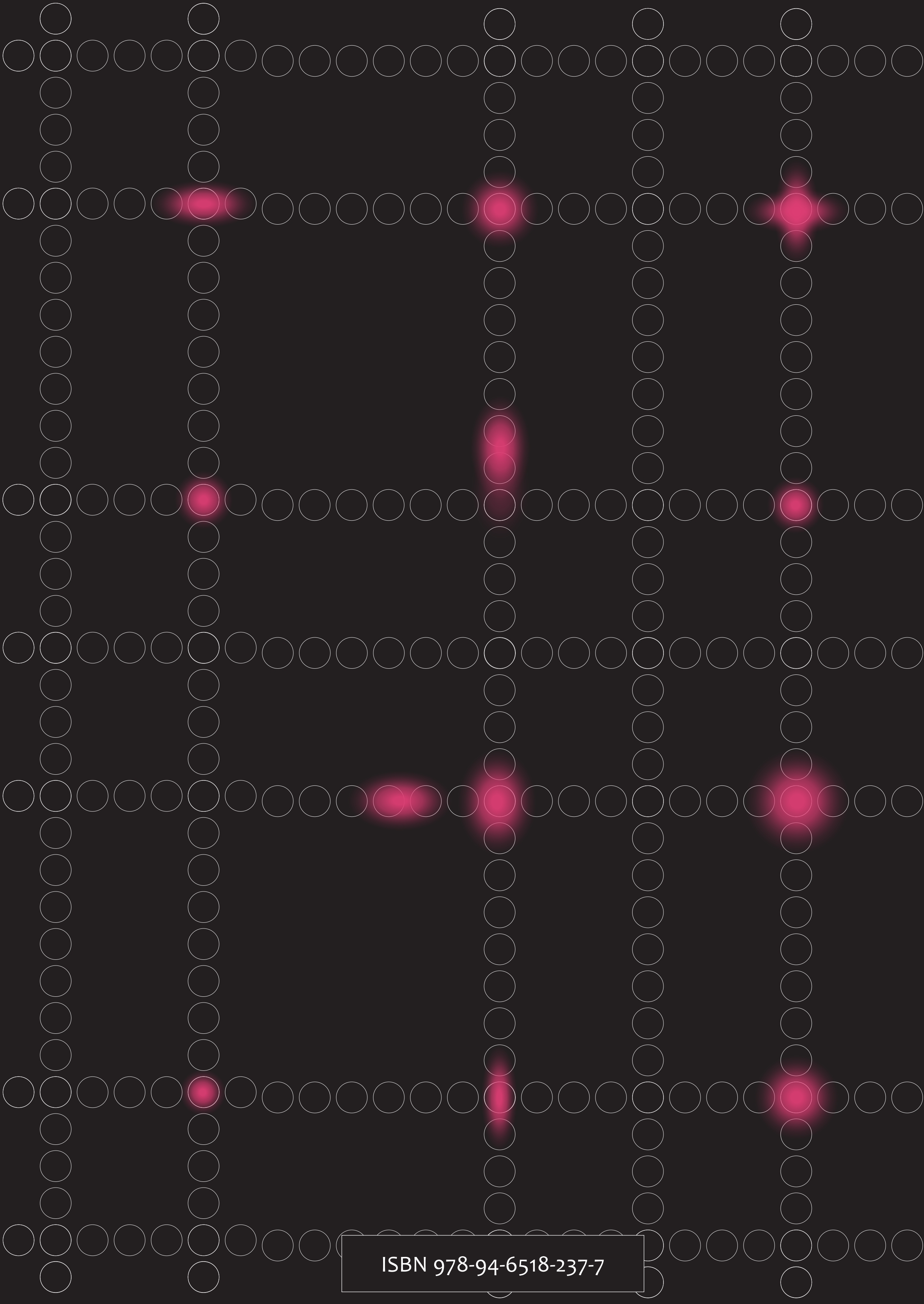

ISBN 978-94-6518-237-7